

THE UNIVERSITY *of* EDINBURGH

This thesis has been submitted in fulfilment of the requirements for a postgraduate degree (e.g. PhD, MPhil, DClinPsychol) at the University of Edinburgh. Please note the following terms and conditions of use:

- This work is protected by copyright and other intellectual property rights, which are retained by the thesis author, unless otherwise stated.
- A copy can be downloaded for personal non-commercial research or study, without prior permission or charge.
- This thesis cannot be reproduced or quoted extensively from without first obtaining permission in writing from the author.
- The content must not be changed in any way or sold commercially in any format or medium without the formal permission of the author.
- When referring to this work, full bibliographic details including the author, title, awarding institution and date of the thesis must be given.

A study of the Higgs boson decay $H \to ZZ^{(*)} \to 4\ell$ and inner detector performance studies with the ATLAS experiment

Karoline Elfriede Selbach
University of Edinburgh

Thesis submitted for the degree of Doctor of Philosophy

The known is finite, the unknown infinite; intellectually we stand on an islet in the midst of an illimitable ocean of inexplicability. Our business in every generation is to reclaim a little more land, to add something to the extent and the solidity of our possessions.

[Thomas H. Huxley]

Abstract

The Higgs mechanism is the last piece of the SM to be discovered which is responsible for giving mass to the electroweak $W^{\pm}$ and Z bosons. Experimental evidence for the Higgs boson is therefore important and is currently explored at the Large Hadron Collider (LHC) at CERN. The ATLAS experiment (A Toroidal LHC ApparatuS) is analysing a wide range of physics processes from collisions produced by the LHC at a centre-of-mass energy of 7-8 TeV and a peak luminosity of $7.73 \times 10^{33}\,\mathrm{cm}^{-2}\mathrm{s}^{-1}$.

This thesis concentrates on the discovery and mass measurement of the Higgs boson. The analysis using the $H \to ZZ^{(*)} \to 4\ell$ channel is presented, where ℓ denotes electrons or muons. Statistical methods with non-parametric models are successfully cross-checked with parametric models. The per-event errors studied to improve the mass determination decreases the total mass uncertainty by 9%. The other main focus is the performance of the initial, and possible upgraded, layouts of the ATLAS inner detector. The silicon cluster size, channel occupancy and track separation in jets are analysed for a detailed understanding of the inner detector.

The inner detector is exposed to high particle fluxes and is crucial for tracking and vertexing. The simulation of the detector performance is improved by adjusting the cross talk of adjacent hit pixels and the Lorentz Angle in the digitisation. To improve the ATLAS detector for upgrade conditions, the performance is studied with pile-up of up to 200. Several possible layout configurations were considered before converging on the baseline one used for the Letter of Intent. This includes increased granularity in the Pixel and SCT and additional silicon detector layers. This layout was validated to accomplish the design target of an occupancy $< 1\%$ throughout the whole inner detector.

The $H \to ZZ^{(*)} \to 4\ell$ analysis benefits from the excellent momentum resolution, particularly for leptons down to $p_T = 6\,\text{GeV}$. The current inner detector is designed to provide momentum measurements of low p_T charged tracks with resolution of $\sigma_{p_T}/p_T = 0.05\%\, p_T \oplus 1\%$ over a range of $|\eta| < 2.5$. The discovery of a new particle in July 2012 which is compatible with the Standard model Higgs boson included the 3.6σ excess of events observed in the $H \to ZZ^{(*)} \to 4\ell$ channel at 125 GeV.

The per-event error was studied using a narrow mass range, concentrated around the signal peak ($110\,\text{GeV} < m_H < 150\,\text{GeV}$). The error on the four-lepton invariant mass is derived and its probability density function (pdf) is multiplied by the conditional pdf of the four-lepton invariant mass given the error. Applying a systematics model dependent on the true mass of the discovered particle, the new fitting machinery was developed to exploit additional statistical methods for the mass measurement resulting in a discovery with 6.6σ at $m_H = 124.3^{+0.6}_{-0.5}(stat)^{+0.5}_{-0.3}(syst)\,\text{GeV}$ and $\mu = 1.7 \pm 0.5$ using the full 2011 and 2012 datasets.

Declaration

This dissertation is the result of my own work, except where explicit reference is made to the work of others, and has not been submitted for another qualification to this or any other university.

Karoline Selbach



Acknowledgements

I would like to express great thanks to my supervisor Prof. Philip J. Clark for giving me the opportunity to pursue this PhD and all the advice I received. I am also thankful to my second supervisor Dr. Victoria J. Martin who supported me throughout my PhD. Besides these, there are many people I worked with and I am grateful for all their support and ideas. I appreciate a lot being part of the ATLAS collaboration and the experimental particle physics group of the University of Edinburgh. I enjoyed superb collaborative work and am thankful for all the inspiring discussions with my colleagues. Furthermore, I want to thank for the financial support and development opportunities given to me by the Principal's Career Development PhD Scholarship offered by the University of Edinburgh. Last but not least, I want to thank my family and the people who stood by me.

Contents

1 Introduction **2**

2 Theory **4**

2.1 Standard Model 4
2.2 Spontaneous symmetry breaking and the Higgs mechanism 5
2.3 Discovering the Higgs boson and its properties 9
2.4 Production and decay modes of the Higgs boson 11
2.5 Beyond the Higgs discovery 18

3 ATLAS Overview **19**

3.1 Introduction and physics motivation 19
3.2 The Large Hadron Collider 19
3.3 The ATLAS experiment 21
3.3.1 Coordinate system 22
3.3.2 Magnet system 24
3.3.3 Inner Detector 26
3.3.4 Calorimetry 30
3.3.5 Muon Spectrometer 33
3.3.6 Forward detectors 35
3.3.7 Data acquisition, readout, trigger, and offline processing 36
3.4 Summary 38

4 Current and upgraded inner detector performance **40**

4.1 Current ATLAS inner detector tracker 40
4.1.1 Cluster size studies 40
4.1.2 Occupancy in ID 53
4.1.3 Occupancy in Jets 62
4.1.4 Track Separation in Jets 64

4.2 Future inner tracker . . . 70
4.2.1 Inner Detector Upgrade: outline . . . 70
4.2.2 Layout Conclusions . . . 74

5 Signal and background analysis of the H→ $ZZ^{(*)} \to 4\ell$ channel 77
5.1 Introduction . . . 77
5.2 Samples . . . 78
5.3 Event Selection . . . 78
5.3.1 Data quality selection . . . 78
5.3.2 Trigger . . . 78
5.3.3 Lepton pre-selection . . . 79
5.3.4 Quadruplet selection . . . 80
5.3.5 Z-mass constraint . . . 81
5.4 Background estimation . . . 83
5.5 m_{12} study . . . 83
5.6 Conclusion . . . 85

6 Statistical models and per-event error 87
6.1 Non-parametric signal model . . . 87
6.2 Parametric signal model . . . 88
6.2.1 Crystal ball resolution model . . . 89
6.2.2 Additional physically motivated models . . . 95
6.3 Categorisation by detector region . . . 103
6.4 Development of fitting framework . . . 105
6.4.1 Splitting into different channels . . . 106
6.5 Per-event error . . . 108
6.5.1 Per-event error calculation . . . 108
6.5.2 Per-event error pdfs . . . 113
6.6 Conclusion . . . 117

7 Fitting validation & results of the H→ $ZZ^{(*)} \to 4\ell$ mass measurement 118
7.1 Parametric models . . . 118
7.1.1 Results of the non-parametric model . . . 118
7.1.2 Results of the parametric model . . . 124
7.1.3 Detailed comparison of the results . . . 128
7.1.4 Conclusion . . . 131

7.2 Per-event error . . . 131
7.2.1 Applied models and their profile likelihood results . . . 132
7.2.2 Pseudo-experiments . . . 134
7.2.3 Comparison of per-event error to template approach . . . 136
7.2.4 Conclusion . . . 136

8 Statistical interpretation of the H$\to ZZ^{(*)} \to 4\ell$ analysis 137
8.1 Results and interpretation of the main non-parametric analysis . . . 137
8.2 Systematics . . . 141
8.2.1 Experimental systematic effects . . . 142
8.2.2 Theoretical systematic effects . . . 143
8.2.3 Modelling of systematics . . . 143
8.3 Comparison of (non-)parametric and per-event models . . . 146
8.4 Outlook . . . 148

9 Conclusion 150

A Appendices 154
A.1 Crystal ball model with all parameters floating . . . 154
A.2 Crystal ball model with n fixed . . . 154

Bibliography 162

List of Figures 172

List of Tables 181

Chapter 1

Introduction

Developed over the last 50 years, the Standard Model is based on the Glashow-Weinberg-Salam theory of electroweak processes finalised in 1967 and additionally incorporates quantum chromodynamics [1]. It has proven to describe the fundamental concepts of particle physics well, but one of the open questions is the principle of how masses are generated in this framework. A possible solution is the Higgs mechanism postulated by Peter Higgs, Emeritus Professor at the University of Edinburgh, and his colleagues Robert Brout, Franois Englert, Gerald Guralnik, Carl Richard Hagen and Tom Kibble [2–4].

Since then, researchers have put a lot of effort into the Higgs hunt to verify its existence building several world-leading experiments resulting in the development of the Large Hadron Collider (LHC) at CERN with two main experiments exploring the Higgs boson: the ATLAS and CMS experiments. Based on an international effort, physics beyond our current knowledge is studied at the ATLAS experiment and the mass generation mechanism of the vector bosons is investigated by testing the Higgs theory which addresses mass by the interaction of particles with the Higgs field. The ATLAS experiment has a total size of $25\,\mathrm{m} \times 25\,\mathrm{m} \times 45\,\mathrm{m}$ and has ~ 100 million electronic channels. Confronted with a luminosity of up to $7.73 \times 10^{33}\,\mathrm{cm}^{-2}\mathrm{s}^{-1}$, during the operation in 2012, the ATLAS experiment studied the SM Higgs particle which was expected to appear once per 10 billion collisions. In 2012, proton bunches collided with a centre-of-mass energy of 8 TeV every 50 ns in the ATLAS experiment with approximately 21 interactions per crossing.

On the 4th of July 2012, the discovery of a new particle consistent with the Higgs boson was announced and one of the significant contributions was provided by the ATLAS analysis studying the $\mathrm{H} \to ZZ^{(*)} \to 4\ell$ decay mode. It is a channel sensitive over a large mass range and provides with four leptons a very clean signature to detect Higgs candidates. This thesis presents the discovery in the $\mathrm{H} \to ZZ^{(*)} \to 4\ell$ channel and the subsequent mass measurements of the new particle which has resulted in the observation

of a Higgs boson with a significance of 6.6σ at a mass of $m_H = 124.3^{+0.6}_{-0.5}(\text{stat})^{+0.5}_{-0.3}(\text{sys})$ in the H$\to ZZ^{(*)} \to 4\ell$ channel [5].

This thesis furthermore describes the technical achievements of a high resolution silicon detecting device and studies about how to cope with even higher luminosities providing the opportunity to further explore the fundamental concepts of particle physics.

After this first chapter introducing the work presented, the second chapter explains the fundamental theoretical concepts underlying the search for the Higgs boson. It also describes the expected cross sections and branching ratios for the Standard Model Higgs boson.

In the third chapter the ATLAS detector and the challenges it faces at the LHC are presented. The different detectors and their functions are summarised and the processing chain of the gathered data and the simulated Monte Carlos (MC) samples are described.

The fourth chapter concentrates on the inner detector presenting its performance, starting by comparing the observed cluster size and channel occupancy to MC simulation. Following this, the track separation in jets is studied for the current and possible upgrade inner detector layouts. Several inner detector layouts are studied for an operation at ten times the current instantaneous luminosity which contributed information for the proposed Letter of Intent layout [6].

The fifth to eighth chapters explain the effort in the H$\to ZZ^{(*)} \to 4\ell$ channel. The selection cuts determining the signal and background contributions are given in the fifth chapter. The sixth chapter presents the contributions to the statistical analysis studying parametric and non-parametric models, the development of a new fitting framework, and the expansion of the analysis to include per-event errors.

The enhancements present in the sixth chapter are applied in the statistical analysis and results are discussed and validated in chapter seven using the obtained data and toy MC experiments. Chapter eight highlights the statistical achievements from the latest publication of the H$\to ZZ^{(*)} \to 4\ell$ mass measurement, it also describes the work on the systematics and presents an interpretation of the performed statistical analyses.

The accomplishments are then summarised and concluded in the ninth chapter including an outlook.

Chapter 2

Theory

The Standard Model of the strong and electroweak interactions is introduced. Additionally, spontaneous symmetry breaking and the Higgs mechanism are discussed, followed by a summary about the Higgs boson and its properties. Finally, a conclusion is drawn given the discovery of a Higgs boson in July 2012.

2.1 Standard Model

The Standard Model (SM) is a theory describing the strong, weak and electromagnetic interactions of particles. Strong interactions are modelled by Quantum Chromodynamics (QCD) [7] based on the symmetry group $SU(3)_C$ where C denotes colour. QCD describes the strong interaction between quarks with the 8 gauge bosons representing the massless spin-1 gluons with different colour-combinations. The weak and electromagnetic interactions are unified by the Glashow-Weinberg-Salam electroweak (EW) theory [8] based on $SU(2)_L \otimes U(1)_Y$ where L denotes left-handed chirality and Y hypercharge. In summary, the SM gauge group can be defined as

$$SU(3)_C \otimes SU(2)_L \otimes U(1)_Y. \tag{2.1}$$

It has been very successfully experimentally tested.

The Standard Model has two kind of fields: the bosons with integer spin and the fermions with half integer spin. On the fermionic side, there are three generations of leptons and quarks. Each family consists of a left-handed quark doublet $q_L = \begin{pmatrix} u_L \\ d_L \end{pmatrix}$, a

left-handed lepton doublet $\ell_L = \begin{pmatrix} \nu_L \\ e_L \end{pmatrix}$ and the right-handed singlets u_R, d_R and e_R [9][1]. It has been observed from β-decays that all emitted neutrinos are left-handed and all anti-neutrinos come out right-handed. Left- and right-handed fields couple to weak interactions differently, with $SU(2)_L$ denoting that it only acts on left-handed particles while $U(1)_Y$ acts on both. The hypercharge [8] is determined by the Gell-Mann–Nishijima equation $Y = 2(Q - T_3)$, where T_3 is the third component of the weak isospin and Q is the electric charge. Right-handed fermions have $T_3 = 0$ and left-handed $T_3 = \pm\frac{1}{2}$.

There are four gauge fields with spin-1, therefore bosons. The $U(1)_Y$ gauge group has one generator, the hypercharge, and therefore one gauge field B_μ. Additionally, $SU(2)_L$ has three generators and thus three fields $W_\mu^{1,2,3}$. The Lagrangian for these fields is

$$\mathcal{L}_B = -\frac{1}{4}B_{\mu\nu}B^{\mu\nu} - \frac{1}{4}W^i_{\mu\nu}W^{\mu\nu i} \tag{2.2}$$

where $B_{\mu\nu} = \partial_\mu B_\nu - \partial_\nu B_\mu$ and $W^i_{\mu\nu} = \partial_\mu W^i_\nu - \partial_\nu W^i_\mu - g_2\epsilon^{ijk}W^j_\mu W^k_\nu$, with g_2 as the coupling constant of $SU(2)_L$, and ϵ^{ijk} as the antisymmetric structure constant of SU(2) called totally anti-symmetric Levi-Civita symbol [7]. Equation 2.2 refers to four massless bosons, whereas in nature it is observed that the vector bosons of the weak interaction, $W^\pm$, and Z, are massive. Explicit mass terms in the Lagrangian would break gauge invariance. Giving mass to bosons can be achieved with spontaneous electroweak symmetry breaking where the interaction eigenstates $W_\mu^{1,2,3}$ and B_μ are rotated to the mass basis A, Z and $W^\pm$ [1].

2.2 Spontaneous symmetry breaking and the Higgs mechanism

To generate masses for the Z, W bosons, the electroweak symmetry is broken by the Higgs field. An additional $SU(2)$ doublet is defined with complex entries [10].

$$\Phi = \begin{pmatrix} \phi^+ \\ \phi^0 \end{pmatrix} = \frac{1}{\sqrt{2}} \begin{pmatrix} \phi_1 + i\phi_2 \\ \phi_3 + i\phi_4 \end{pmatrix} \tag{2.3}$$

[1] A right handed neutrino can be included for each family but it would be an isospin singlet and, being electrically neutral, it would have hypercharge 0. Therefore, it is called sterile neutrino as it does not have any gauge interactions.

Given the Lagrangian $\mathcal{L}_H = (D_\mu \Phi)^\dagger D^\mu \Phi - \mathcal{V}(\Phi)$, the potential is chosen to be

$$\mathcal{V}(\Phi) = -\mu^2 \Phi^\dagger \Phi + \lambda (\Phi^\dagger \Phi)^2 \tag{2.4}$$

where $\lambda > 0$ so the potential is bounded from below and $\mu^2 > 0$, giving the Mexican-hat potential shown in figure 2.1.

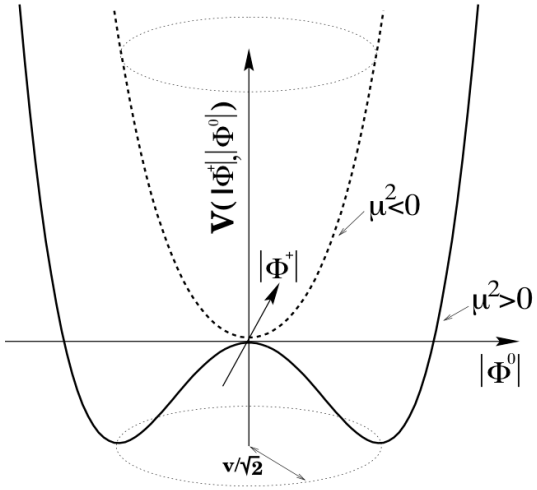


Figure 2.1: The Higgs potential is shown as a function of the magnitude of the two complex entries of the scalar field [11].

With $\Phi^\dagger \Phi = \frac{1}{2}(\phi_1^2 + \phi_2^2 + \phi_3^2 + \phi_4^2)$, the minimum of the potential can be calculated to be at

$$|\Phi| = \sqrt{\frac{\mu^2}{2\lambda}} \equiv \frac{v}{\sqrt{2}} \tag{2.5}$$

where we define the vacuum expectation value (v.e.v) v. Given the relative signs of the potential parameters (λ, μ), the minima occur at the v.e.v as shown in figure 2.1. Choosing a direction in the SU(2) space, we can define the minimum of the potential to be

$$\Phi = \frac{1}{\sqrt{2}} \begin{pmatrix} 0 \\ v \end{pmatrix}. \tag{2.6}$$

In this way $SU(2)_L \otimes U(1)_Y$ is spontaneously broken and charge is conserved, since only the field with zero electric charge ϕ^0 has a vacuum expectation value unequal to zero[2]

$$SU(2)_L \otimes U(1)_Y \longrightarrow U(1)_{EM} \tag{2.7}$$

where EM stands for electromagnetic.

Expanding ϕ_3 near the stable configuration by $\phi_3 = v + H(x)$, H being a real field, we can write the doublet as

$$\sqrt{2}\Phi = \begin{pmatrix} 0 \\ v + H(x) \end{pmatrix} + i \begin{pmatrix} -i\phi_1 + \phi_2 \\ \phi_4 \end{pmatrix}. \tag{2.8}$$

The general representation of a 2×2 complex unitary matrix using the Pauli matrices, σ^i, and the coefficients, ξ_i, is

$$\xi_i \sigma^i = \begin{pmatrix} \xi_3 & \xi_1 - i\xi_2 \\ \xi_1 + i\xi_2 & -\xi_3 \end{pmatrix}. \tag{2.9}$$

Neglecting terms with fields squared and higher orders when applying this to the Higgs doublet, it can be derived

$$(\xi_i \sigma^i) \begin{pmatrix} 0 \\ v + H(x) \end{pmatrix} = (v + H(x)) \begin{pmatrix} \xi_1 - i\xi_2 \\ -\xi_3 \end{pmatrix} \approx v \begin{pmatrix} \xi_1 - i\xi_2 \\ -\xi_3 \end{pmatrix}. \tag{2.10}$$

By taking into account the first two terms of the Taylor expansion of the exponential function, the following approximation can be made

$$e^{\frac{i}{v}\xi_i \sigma^i} \frac{1}{\sqrt{2}} \begin{pmatrix} 0 \\ v + H(x) \end{pmatrix} \approx \frac{1}{\sqrt{2}} \begin{pmatrix} 0 \\ v + H(x) \end{pmatrix} + \frac{i}{\sqrt{2}} \begin{pmatrix} \xi_1 - i\xi_2 \\ -\xi_3 \end{pmatrix}. \tag{2.11}$$

Equation 2.8 can be reparametrised using equation 2.11

$$\Phi = \frac{1}{\sqrt{2}} \begin{pmatrix} 0 \\ v + H(x) \end{pmatrix} + \frac{i}{\sqrt{2}} \begin{pmatrix} -i\phi_1 + \phi_2 \\ \phi_4 \end{pmatrix} = e^{\frac{i}{v}\alpha_i \sigma^i} \frac{1}{\sqrt{2}} \begin{pmatrix} 0 \\ v + H(x) \end{pmatrix}, \tag{2.12}$$

[2]The charged field ϕ^+ has a v.e.v of zero in contrast to the field ϕ^0.

where α_i are functions of the fields $\phi_{1,2,4}$. By gauge transformation $\Phi \to e^{-\frac{i}{v}\alpha_i\sigma^i}\Phi$, the three fields ϕ_1, ϕ_2 and ϕ_4 are no longer in the Lagrangian. They will reappear as the longitudinal degrees of freedom in the bosons. This leaves only one field, which is the Higgs field, $H(x) = H$ [10]. This is called the unitary gauge, where only the Higgs field as one of the four introduced fields remains in the Lagrangian [7].

The Lagrangian of the Higgs boson is $\mathcal{L}_H = (D_\mu\Phi)^\dagger D^\mu\Phi - \mathcal{V}(\Phi)$ with the potential $\mathcal{V}(\Phi) = -\mu^2\frac{1}{2}(v+H)^2 + \frac{\lambda}{4}(v+H)^4$ and the covariant derivative $D_\mu = \partial_\mu + ig_2\frac{\sigma^i}{2}W^i_\mu + ig_1\frac{1}{2}B_\mu$ where g_1 is the U(1) gauge coupling [9].

$$\mathcal{L}_H = \frac{1}{2}\left|\begin{pmatrix} \partial_\mu + \frac{i}{2}(g_2W^3_\mu + g_1B_\mu) & \frac{ig_2}{2}(W^1_\mu - iW^2_\mu) \\ \frac{ig_2}{2}(W^1_\mu + iW^2_\mu) & \partial_\mu - \frac{i}{2}(g_2W^3_\mu - g_1B_\mu) \end{pmatrix}\begin{pmatrix} 0 \\ v+H \end{pmatrix}\right|^2 - \mathcal{V}(\Phi) \quad (2.13)$$

$$= \frac{1}{2}(\partial_\mu H)^2 + \frac{g_2^2}{8}(v+H)^2((W^1_\mu)^2 + (W^2_\mu)^2) + \frac{1}{8}(v+H)^2(g_2W^3_\mu - g_1B_\mu)^2 - \mathcal{V}(\Phi)$$

In the following, only the quadratic terms in v are considered from the kinetic part of the Lagrangian, and only the quadratic terms in H from the potential part, to deduce the masses of the $W^\pm$, Z and photon.

$$\mathcal{L}_H = \frac{g_2^2}{8}v^2((W^1_\mu)^2 + (W^2_\mu)^2) + \frac{1}{8}v^2(g_2W^3_\mu - g_1B_\mu)^2 + \frac{\mu^2}{2}H^2 - \frac{\lambda}{2}3v^2H^2 \quad (2.14)$$

The first term of equation 2.14 is rearranged by using

$$W^\pm_\mu = \frac{1}{\sqrt{2}}(W^1_\mu \mp iW^2_\mu). \quad (2.15)$$

For the second term, the Weinberg rotation is used

$$\begin{pmatrix} W^3_\mu \\ B_\mu \end{pmatrix} = \begin{pmatrix} \cos\theta_W & \sin\theta_W \\ -\sin\theta_W & \cos\theta_W \end{pmatrix}\begin{pmatrix} Z_\mu \\ A_\mu \end{pmatrix} \quad (2.16)$$

where $W^\pm_\mu$ and Z_μ are the massive bosons, A_μ is the massless photon and the electroweak mixing (or Weinberg) angle is $\theta_W = \arctan(\frac{g_1}{g_2})$ [12].

Using the unitary gauge, the potential is expanded with the neutral component of the Higgs doublet. The last two terms of equation 2.14 are obtained keeping only the terms of the potential which are quadratic in H. The v.e.v, v, is calculated via the minimization of the Higgs potential given in the equation 2.5 and is substituted in the

Lagrangian:

$$\mathcal{L}_H = \frac{g_2^2}{4} v^2 W_\mu^+ W^{\mu-} + \frac{1}{8} v^2 \frac{g_2^2}{\cos^2\theta_W} Z_\mu Z^\mu - \lambda v^2 H^2. \tag{2.17}$$

The trigonometric equations $\cos(\arctan x) = \frac{1}{\sqrt{1+x^2}}$ and $\sin(\arctan x) = \frac{x}{\sqrt{1+x^2}}$ have been used to obtain 2.17. The kinetic term of the scalar Lagrangian shows the masses the $W^\pm$ and Z bosons acquire

$$m_{W^\pm} = \frac{g_2}{2} v \quad \text{and} \quad m_Z = \frac{g_2}{2\cos\theta_W} v = \frac{m_W}{\cos\theta_W}. \tag{2.18}$$

The Fermi constant, G_F, is obtained through the measurement of the muon life-time in the decay mode $\mu^- \to e^- \bar{\nu}_e \nu_\mu$ with $\tau = \frac{192\pi^3}{G_F^2 m_\mu^5}$, in natural units (neglecting the electron mass) [13]. The Fermi constant can be related to the W boson as this is the mediator of the muon decay

$$G_F = \frac{\sqrt{2}}{8} \left(\frac{g_2}{m_W} \right)^2 = 1.166 \times 10^{-5}\,\text{GeV}^{-2}\,[14]. \tag{2.19}$$

The v.e.v is calculated to be $v = (G_F\sqrt{2})^{-1/2} = 246\,\text{GeV}$ given the W mass dependence in equation 2.18 [1]. Below this energy scale of 246 GeV, no electroweak force is observed[3]. Given equation 2.17, the Higgs mass can be read out of the quadratic term in the H field, $m_H = \sqrt{2\lambda} v$. With the unitary gauge, three components of the Higgs doublet are subtracted. These three fields become the longitudinal polarizations of the $W^\pm$ and Z bosons and make them massive. The Higgs doublet now has only one real scalar field, the Higgs boson [15].

2.3 Discovering the Higgs boson and its properties

The Higgs mechanism predicts a particle with $m_H = \sqrt{2\lambda} v$, where λ is a free parameter. Given this last unknown parameter in the SM the exact mass of the Higgs boson is not predicted. This implies that finding the Higgs boson at a specific mass has to be accompanied by measuring its properties such as its well predicted couplings.

Theoretical and experimental constraints can be derived for the mass of the Higgs. Looking at the scattering of W bosons, the cross-section diverges neglecting the contributions by the Higgs boson. With the Feynman diagrams of the longitudinal W boson

[3] Despite the broken electroweak force, we still observe at low energies the effects of separate electromagnetic and weak forces such as beta decays.

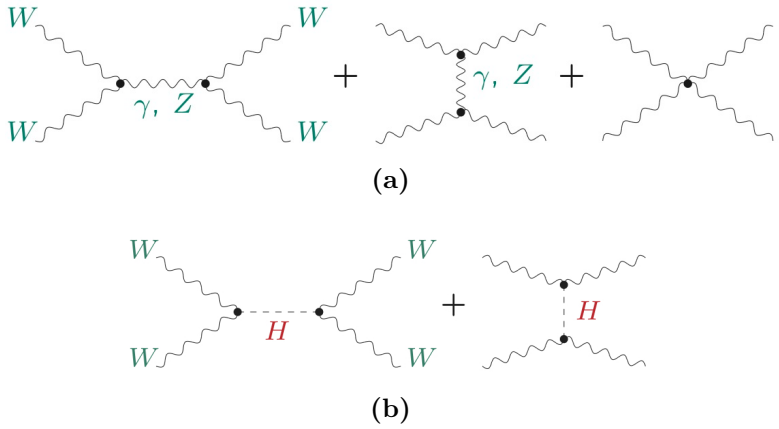


Figure 2.2: The Feynman diagrams for the scattering of longitudinal W bosons are shown without the contribution of the Higgs boson (2.2a) and the ones involving the Higgs boson (2.2b) [11].

scattering, shown in figure 2.2a, the invariant amplitude is derived $\mathcal{M}_V = -g_2^2 \frac{E^2}{m_W^2} + O(1)$. The amplitude diverges for $E \to \infty$ and, given the differential cross-section dependence $d\sigma \propto |\mathcal{M}|^2$, the cross section becomes infinite for $E \to \infty$. This violates unitarity and to prevent this a scalar particle has to be introduced to cancel the divergences.

This can be accomplished by the already introduced Higgs boson with the Feynman diagrams shown in figure 2.2b. The invariant amplitude for these contributions is calculated $\mathcal{M}_S = g_{WWH}^2 \frac{E^2}{m_W^4} + O(1)$, where the W and Z coupling to the Higgs boson can be derived from equation 2.13. Calculating $g_2^2 v H(W^\pm)^2 = g_2 m_W H(W^\pm)^2$, this results in $g_{WWH} = g_2 m_W$. These terms of the invariant amplitude compensate when calculating the total invariant amplitude:

$$\mathcal{M}_{Tot} = \mathcal{M}_V + \mathcal{M}_S = \frac{E^2}{m_W^4}(g_{WWH}^2 - g_2^2 m_W^2) + \ldots \quad \text{with} \quad g_{WWH} = g_2 m_W \,[11]. \tag{2.20}$$

Complying with unitarity conditions on the amplitudes and assuming perturbation theory holds for electroweak theory, the limit of $m_H < 2v\sqrt{\pi} \approx 870\,\text{GeV}$ can be derived [7, 16]. Additionally, a Higgs boson in the light mass range is predicted by precise electroweak fits. In the update for EPS 2011, the electroweak fits predict a most likely Higgs mass of $m_H = 125.2^{+8}_{-10}\,\text{GeV}$ including direct limits from LEP and Tevatron, but excluding direct searches for the Higgs boson from ATLAS and CMS [17]. In March 2012, further indications for a light Higgs were published as hints for a new particle with $m_H = 120\,\text{GeV}$ observed by the Tevatron experiment with a global significance of $\sim 2.2\,\sigma$ [18].

In July 2012, it was announced that a particle compatible with the Higgs boson was discovered at CERN. At the CMS experiment, an excess of events was observed with a significance of 5 standard deviations combining the results of the channels $H \to \gamma\gamma$, $H \to ZZ^{(*)}$, $H \to WW^{(*)}$, $H \to \tau^+\tau^-$ and $H \to b\bar{b}$ for $5.1\,\mathrm{fb}^{-1}$ collected at $\sqrt{s} = 7\,\mathrm{TeV}$ in 2011 and $5.3\,\mathrm{fb}^{-1}$ at $\sqrt{s} = 8\,\mathrm{TeV}$ in 2012 [19]. The largest significance was observed in the $H \to \gamma\gamma$ and $H \to ZZ^{(*)}$ channel at a best-fit mas of $m_H = 125.3 \pm 0.4(\mathrm{stat}) \pm 0.5(\mathrm{sys})\,\mathrm{GeV}$ for the combination of these two channels. At the ATLAS experiment, the excess was observed at $m_H = 126.0 \pm 0.4(\mathrm{stat}) \pm 0.4(\mathrm{sys})\,\mathrm{GeV}$ combining the results of $H \to \gamma\gamma$, $H \to ZZ^{(*)}$, $H \to WW^{(*)}$ (for $4.7 - 4.8\,\mathrm{fb}^{-1}$ collected at $\sqrt{s} = 7\,\mathrm{TeV}$ in 2011 and $5.8 - 5.9\,\mathrm{fb}^{-1}$ collected at $\sqrt{s} = 8\,\mathrm{TeV}$ in 2012) and using the 2011 data ($4.6 - 4.7\,\mathrm{fb}^{-1}$) for $H \to b\bar{b}$ and $H \to \tau^+\tau^-$ [20]. This observation with a significance of 5.9 standard deviations is compatible with the expected SM Higgs boson with the ratio of observed to SM cross-section: $\hat{\mu} = 1.4 \pm 0.3$. The discovery of a Higgs boson in July 2012 included the significant excess of 3.6σ observed by ATLAS in the $H \to ZZ^{(*)} \to 4\ell$ channel at 125 GeV. In this channel the SM Higgs boson was excluded with 95 % confidence level for 128-168 GeV and 174-580 GeV for $4.6\,\mathrm{fb}^{-1}$ collected at $\sqrt{s} = 7\,\mathrm{TeV}$ in 2011 and $13.0\,\mathrm{fb}^{-1}$ at $\sqrt{s} = 8\,\mathrm{TeV}$ in 2012 [21].

Since the discovery, intense work has been performed on studying the properties of this new particle to justify if it is indeed the SM Higgs boson. Using the full 2011 and 2012 dataset, the SM predicted spin and parity 0^+ is preferred. The exclusion limits obtained with the matrix element based likelihood analysis are 99.6% CL for 0^-, 99.4% CL for 1^+ and 96.9% CL for 1^- [21]. As shown in figure 2.3, the signal strength in the various Higgs decay channels studied at the ATLAS experiment is compatible with the expected SM Higgs boson couplings given the available number of events.

2.4 Production and decay modes of the Higgs boson

The cross section of a SM Higgs at $m_H = 120\,\mathrm{GeV}$ is 10 orders of magnitude smaller than the total cross section at the hadron collider LHC at its design centre-of mass $\sqrt{s} = 14\,\mathrm{TeV}$ [23].

The main production modes of the SM Higgs boson are the following ordered by their frequency in the LHC:

- gluon-gluon fusion (ggF)
- W/Z vector boson fusion
- W/Z-bremsstrahlung

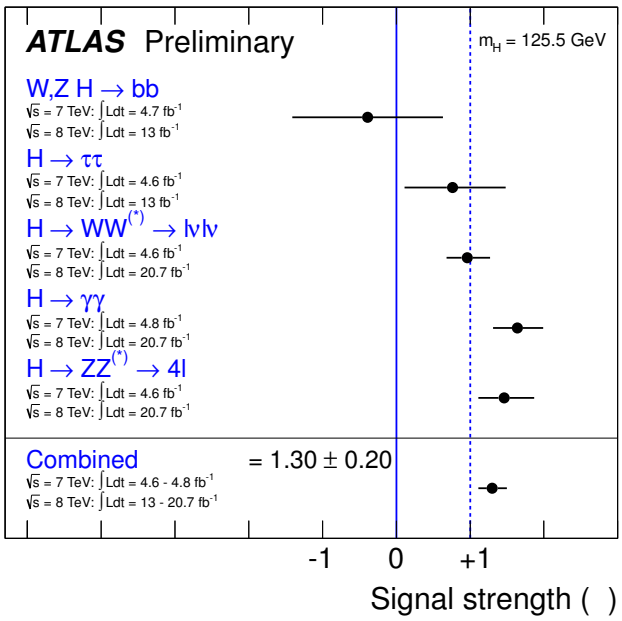


Figure 2.3: Signal strength shown for the different Higgs decay channels measured at the ATLAS experiment [22].

- associated production with heavy (top or bottom) quarks

The Feynman diagrams for these processes are shown in figure 2.4. These production mechanisms demonstrate that the Higgs boson couples preferably to heavy particles with the most frequent ggF coupling to the Higgs via a top-quark loop. There is no direct

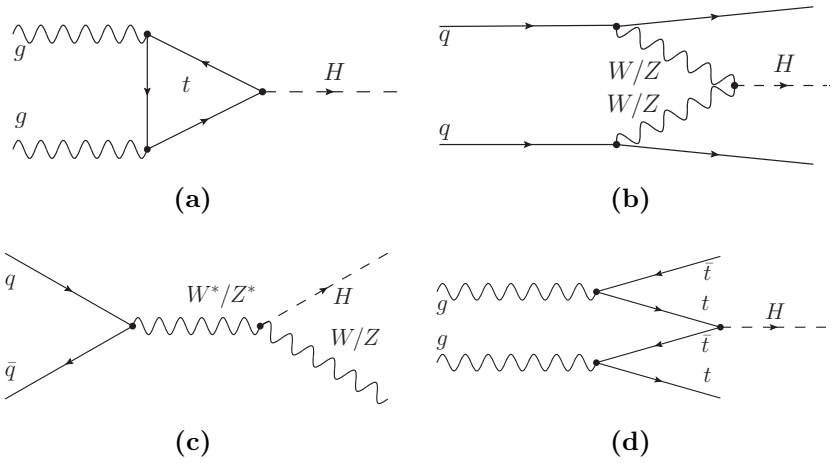


Figure 2.4: SM Higgs boson production modes with gluon-gluon fusion (ggF) 2.4a, vector-boson fusion (VBF) 2.4b, W/Z-bremsstrahlung 2.4c and associated production with a top-quark pair 2.4d [24].

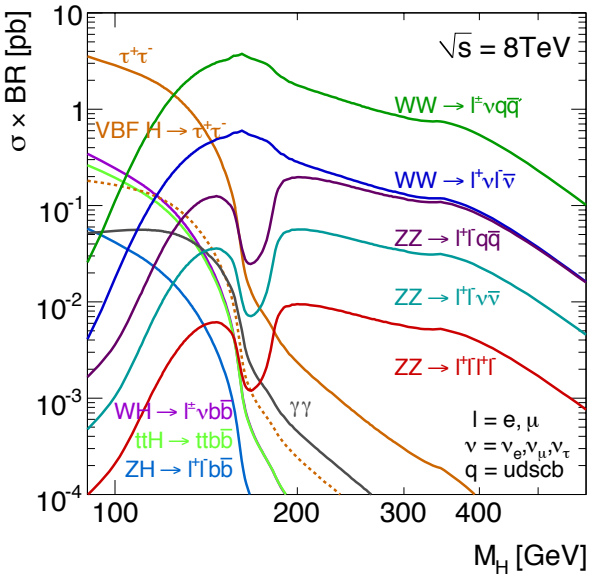


Figure 2.5: SM Higgs boson production cross section times branching ratio at E_{cm}= 8 TeV where $H \to ZZ^{(*)} \to 4\ell$ is given in red. Even though many channels have higher $\sigma \times \mathrm{BR}$, the $H \to ZZ^{(*)} \to 4\ell$ is a very sensitive channel due to its clean signature [25].

coupling to massless gluons and photons, but only through loops with massive charged or coloured particles is the interaction possible.

In figure 2.5, the production cross section times branching ratio (BR) for different channels is given as a function of the Higgs mass. The process $H \to \gamma\gamma$ is mediated by a W boson and a t quark loop. This channel has a low cross section times branching ratio, but a distinctive signature with two high p_T photons.

The decay into fermions, e.g., $H \to \tau^+\tau^-$ is common in the low mass region for $m_H < 130\,\mathrm{GeV}$ as shown in figure 2.5. With the Yukawa coupling, describing the interaction between the Higgs field and massless fermions, quarks and charged leptons gain mass via the spontaneous symmetry breaking. It is obtained that

$$g_{H\bar{f}f} = \frac{1}{v} m_f \tag{2.21}$$

which shows that the coupling is proportional to the fermion mass [26].

The Yukawa coupling constants, $g_{H\bar{f}f}$, are determined with fermion mass measurements since we know the Fermi constant is $1.166 \times 10^{-5}\,\mathrm{GeV}^{-2}$. The coupling constants vary over a large range from $g_{\nu_e} \sim 10^{-11}$, which is the maximal admissible value for g_{ν_e} as it is calculated for the upper limit of the electron-neutrino mass of $m_{\nu_e} = 2 \times 10^{-3}\,\mathrm{eV}$ given in reference [1], to $g_t \sim 1$. Using equation 2.21, the partial decay width for the

Higgs decaying to $\tau^+\tau^-$ is

$$\Gamma(H \to \tau^+\tau^-) = \frac{G_F m_\tau^2}{4\sqrt{2}\pi} m_H \left[1 - \frac{4m_\tau^2}{m_H^2}\right]^{\frac{3}{2}}. \tag{2.22}$$

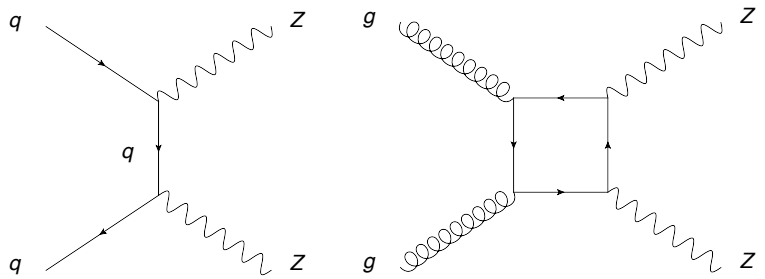
In equation 2.22, m_τ can be substituted by other fermion masses to determine the branching ratio of the other fermionic decay channels [27]. For decays into hadrons the partial decay width has to be multiplied by three due to the three colours of the quarks.

Given $m_W = \frac{g_2}{2}v$ and $g_{WWH} = g_2 m_W$ excerpted from equations 2.18 and 2.20 respectively, the coupling of the Higgs boson to the gauge bosons is $g_{HVV} = \frac{2M_V^2}{v}$ [15]. As this coupling is proportional to the square of the boson mass, $H \to ZZ$ and $H \to W^+W^-$ are the dominant decay channels in the high mass region $m_H > 2m_W/m_Z$. Below this mass threshold, at least one of the bosons in the pair has to be off-shell and the branching ratio peaks when both bosons come on-shell. The $H \to ZZ$ channel is less sensitive with softer lepton p_T at low mass and at $m_H \approx 2m_W$ where WW opens up. Over a large range of high m_H, the partial branching ratios tend to: $BR(H \to W^+W^-) = 2 \times BR(H \to ZZ) = \sim\frac{2}{3}$.

The WW channel with neutrinos in the final state is not sensitive for a precise mass determination of the observed particle in the low mass region. The final state of the $H \to ZZ^{(*)} \to 4\ell$ channel is fully reconstructed and provides a very good mass resolution which is in particular important for $m_H < 220\,\text{GeV}$ where the resonance is very small. For the $H \to ZZ^{(*)} \to 4\ell$ channel, also called "golden channel", the lepton detection and identification efficiency are crucial for a good mass measurement. Its branching ratio is at the level of 10^{-2} for $m_H = 125\,\text{GeV}$. The main background is the irreducible $ZZ^{(*)} \to 4\ell$ background. The Feynman diagrams of this process at leading order are shown in figure 2.6. Additionally, the Z+jets and $t\bar{t}$ with four leptons in the final state are an important background in the low mass region, where at least one of the Z bosons is off-shell. The Feynman diagrams at leading order are shown for Z+jets where the jets originate from $b\bar{b}$ in figure 2.7. The leptons from Z+jets are produced by the Z boson decaying into charged leptons and semileptonic b-decays or fake leptons from light flavour. In the $t\bar{t}$ background, shown by the Feynman diagrams in figure 2.8, the t quark decays into a W boson and a b quark which has a branching ratio of almost 100%. The leptonic decay of the W boson produces one charged lepton and another lepton originates from the semileptonic decay of the b quark.

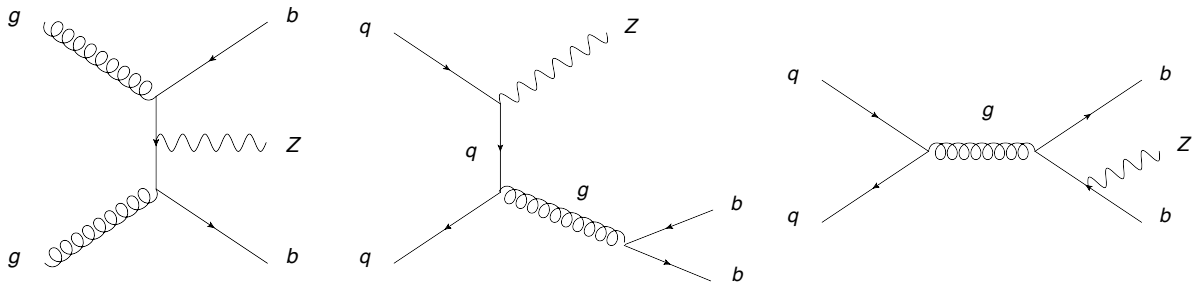
With the $H \to ZZ^{(*)} \to 4\ell$ channel the measurement of spin and parity of the observed particle is feasible using seven observables:

- the masses of the two Z bosons, m_{Z_1} and m_{Z_2}



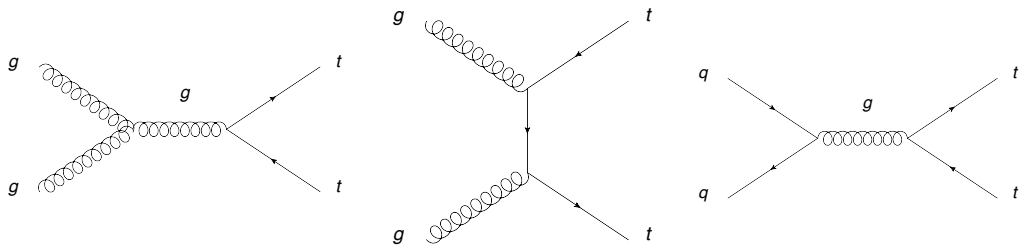
(a) (b)

Figure 2.6: The Feynman diagrams are shown for the production of $qq \to ZZ$ 2.6a and $gg \to ZZ$ 2.6b at LHC.



(a) (b) (c)

Figure 2.7: The leading order diagrams are given for the $Zq\bar{q}$ background with $q = b$.



(a) (b) (c)

Figure 2.8: The $t\bar{t}$ production is summarised for the LHC.

- the production angle θ^* between the $qq/qq \to X$ and $X \to Z_1 Z_2$ axis in the rest frame of the observed particle X
- the azimuthal angle Φ_1 between the plane of the $Z_1 \to \ell_1 \ell_2$ decay and the plane defined by the axis $qq/qq \to X$ and $X \to Z_1 Z_2$ in the X rest frame
- the azimuthal angle Φ between the planes defined by the lepton-pair of each Z decay in the X rest frame
- the decay angles θ_i with $i = 1, 2$ defined in the rest frame of Z_i between the a lepton from Z_i and the opposite direction of X.

These observables are shown in figure 2.9. In the SM, the $H \to ZZ$ coupling is even

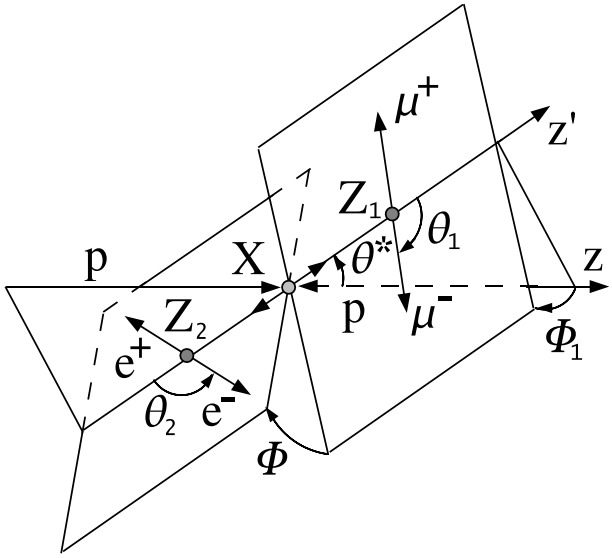


Figure 2.9: This diagram illustrates the process $qq/gg \to X \to ZZ \to 4\ell$ produced by proton-proton collision and defines the angles sensitive to the spin and parity measurement of X [28].

under charge and parity conjugation with the angular distribution of this process

$$\frac{d\sigma(ZH)}{d\cos\theta} \sim \beta^2 (\sin\theta)^2 + \frac{8m_z^2}{s}$$

where β is the two-particle phase space factor [29]. The SM Higgs boson is a scalar particle enabling Yukawa interactions and preventing unitarity violation in the scattering of the W bosons. The possible spins of a boson X decaying into two Z bosons are 0, 1 or 2. Assuming that the resonance observed by the $X \to ZZ$ and $X \to \gamma\gamma$ originates from the same particle, the spin-1 hypothesis of X can be excluded due to its decay to two massless spin-1 particles.

The amplitude for spin-1 is

$$A(X \to \gamma\gamma) = b_1[(\epsilon_1^* q_X)(\epsilon_2^* \epsilon_X) + (\epsilon_2^* q_X)(\epsilon_1^* \epsilon_X)] + b_2 \epsilon_{\alpha\mu\nu\beta} \epsilon_X^\alpha \epsilon_1^{*,\mu} \epsilon_2^{*,\nu} (q_1^\beta - q_2^\beta),$$

where ϵ_i are the polarisation vectors, q_i are the four-momenta and b_i are the dimensionless effective coupling constants [28]. As the photon has no longitudinal polarization, this amplitude is zero and therefore the particle X with a diphoton decay is not a vector which is also given in the Landau-Yang theorem [30, 31]. Hence, the spin-parity, J^P, scenarios studied with the $H \to ZZ \to 4\ell$ channel focus on 0^+, 0^-, 2^+ and 2^-.

The $\gamma\gamma$ and ZZ channel are the most important ones for the mass measurement due to their good mass resolution. Combined with the WW channel, they were the most significant channels for the discovery of the new boson. From the other channels which are sensitive to the observed particle and are studied in ATLAS, the $H \to b\bar{b}$ and $H \to \tau^+\tau^-$ channel were used for a signal strength measurement. Comparing the signal strength of the various decay channels is important to verify whether the new boson decays as predicted for a SM Higgs.

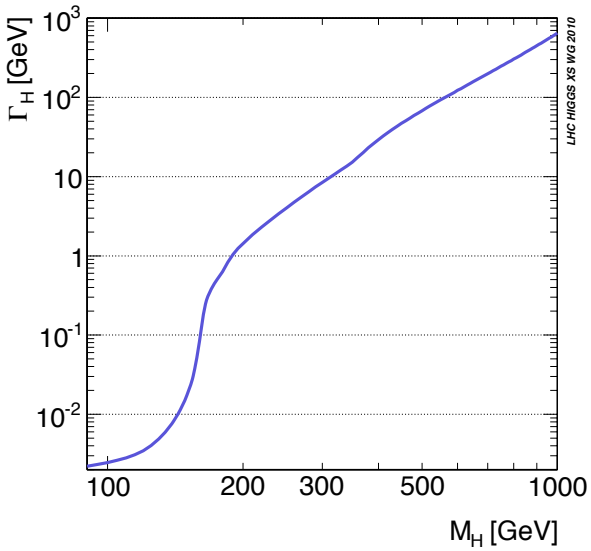


Figure 2.10: Total theoretical width of the Higgs boson shown on a Higgs mass range from 100 GeV to 1 TeV [32].

Finally, the total width of the Higgs decay is small for low Higgs masses, for example $\Gamma(m_H = 125\,\text{GeV}) = 4.03\,\text{MeV}$ [32]. The total width increases dramatically at about $m_H = 160\,\text{GeV}$ as shown in figure 2.10. For large Higgs masses, the total width is of about the same order of magnitude as the Higgs mass resulting in a very broad resonance, for example $\Gamma(m_H = 600\,\text{GeV}) = 123\,\text{GeV}$ [32].

2.5 Beyond the Higgs discovery

The SM has been a very successful theory which is further supported by the discovery of a Higgs boson. Though it still remains to be shown that the discovered particle is the SM Higgs boson with the couplings as expected for all particles including fermions. Assuming the SM Higgs properties will be validated, several open questions remain, which the SM cannot answer. One of these issues is the size of the Yukawa coupling constants mentioned in subsection 2.4. The Yukawa coupling constants to leptons range over 11 orders of magnitudes given $g_{\nu_e} \sim 10^{-11}$ and $g_t \sim 1$. Neglecting neutrinos the range is 6 orders of magnitude. The values of these couplings are not predicted by the SM known as the fermion hierarchy problem [33].

Besides that, there are several other questions related to the unification of the fundamental forces. The idea is to look for a group with a single coupling constant g_G that is equal to the coupling constants of U(1), SU(2) and SU(3) of the SM at a large-momentum scale to unify the electroweak and the strong coupling. At low energies the three coupling constants have very different values with a dependence on the energy. Extrapolating the coupling constants to high energies, they do not intersect at the same point. With a symmetry beyond the SM, the couplings can be unified at the Grand Unified Theories (GUTs) scale of $\sim 10^{16}\,\text{GeV}$ [34]. However, it is not clear at which energy scale to expect physics beyond the SM and if it can be reached with current experimental methods.

The gauge hierarchy problem arising from the radiative corrections to the Higgs mass has a possible solution at the TeV-scale. The quantum corrections from loops lead to a potential divergence with a quadratic sensitivity to the ultraviolet cutoff

$$m_H^2(p^2) = m_{0,H}^2 + Cg^2 \int_{p^2}^{\Lambda^2} dk^2 + \ldots \quad [35] \tag{2.23}$$

where $m_{0,H}$ is the bare Higgs mass or tree-level contribution and Λ is the scale up to which the SM is valid. The coefficient C and the coupling g are constants depending on the theory. A very good tuning of the bare mass is needed if it is assumed that the SM is valid up to the GUT scale, and if the Higgs mass is of the order $m_H \approx 125\,\text{GeV}$, as experimental evidence suggests. This unnatural fine tuning would not be needed if new physics is discovered at the TeV-scale as it would bring down Λ. A new symmetry with new particles at the TeV-scale could solve this gauge hierarchy problem and result in an unification of the coupling constants at the scale of $\sim 10^{16}\,\text{GeV}$. The ATLAS experiment is exploring this option with dedicated searches [36].

Chapter 3

ATLAS Overview

3.1 Introduction and physics motivation

To understand the fundamental physics and interactions our world is based upon, the world's largest scientific instrument, the Large Hadron Collider (LHC), has been built at the European Organization for Nuclear Research (CERN) near Geneva, Switzerland [37]. By accelerating protons with this machine to reach a design centre-of-mass energy of 14 TeV and a design luminosity of $10^{34}\,\mathrm{cm}^{-2}\mathrm{s}^{-1}$, conditions close to the birth of our universe are produced. This provides the possibility to study phenomena at the smallest scales and to test with precision measurements the Standard Model (SM) properties, e.g. electroweak cross-section measurements [38]. The importance of the results obtained by the LHC reaches up to astronomical processes including the search for dark matter which accounts for 23% of the mass of the universe [39].

3.2 The Large Hadron Collider

To accelerate protons to the highest energy (man-made), a hierarchy of several linear accelerators and synchrotrons is needed as shown in figure 3.1. The injected protons reach an energy of 1.4 GeV after going through the linear accelerator LINAC 2 and the circular accelerator Proton Synchrotron Booster. The following circular accelerators, the Proton Synchrotron (PS) and Super Proton Synchrotron (SPS) further increase the proton energy up to 450 GeV [37]. Protons are then injected in opposite directions into the largest synchrotron, the Large Hadron Collider (LHC), where they are accelerated to their final energy and collide [40].

The LHC is located within a circular tunnel with a circumference of 27 km, based 50 to 175 m deep underground. After tests since the middle of 2007, it started operating

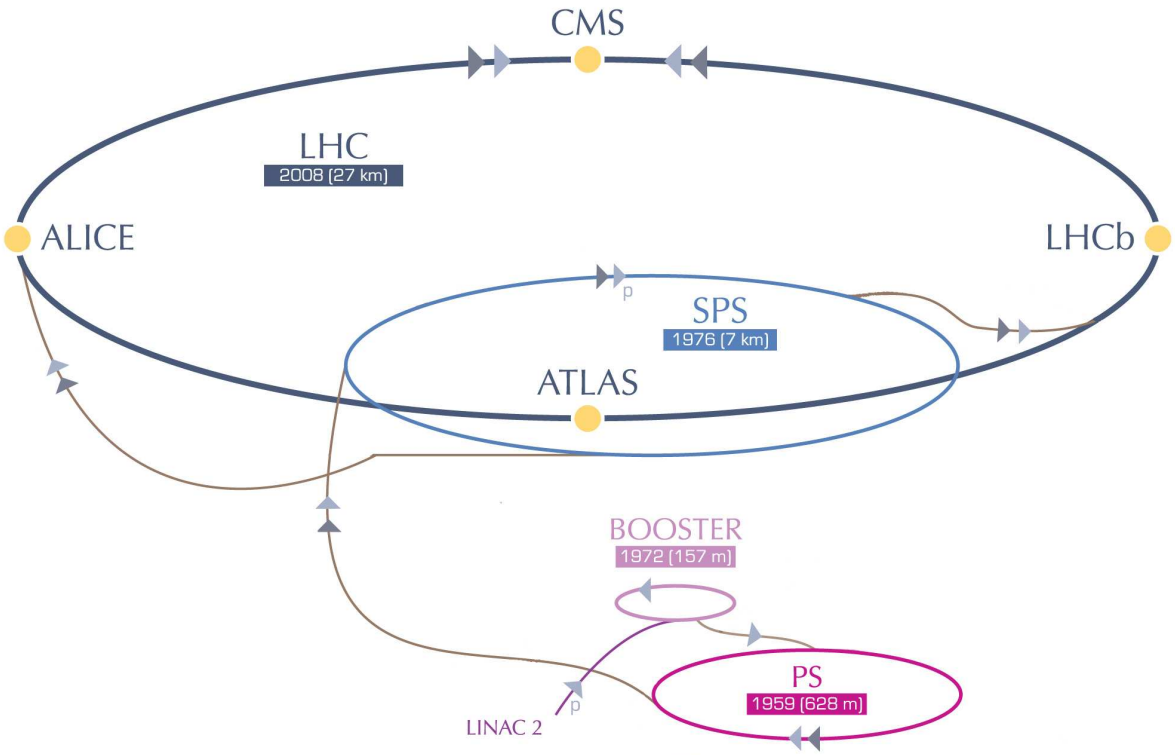


Figure 3.1: The chain of accelerators and synchrotrons that is used to produce proton-proton collisions at CERN is shown [41].

for physics data-taking in 2010, and supplies the following seven experiments: ATLAS (A Toroidal LHC Apparatus) [42], CMS (Compact Muon Solenoid) [43], LHCb (LHC-beauty) [44], ALICE (A Large Ion Collider Experiment) [45], TOTEM (Total Cross Section, Elastic Scattering and Diffraction Dissociation) [46], LHCf (LHC-forward) [47] and MoEDAL (Monopole and Exotics Detector At the LHC) [48].

The LHC consists of two rings to accelerate protons or ions in opposite directions. These rings intersect at 4 points to collide the beams which are equipped with detector setups. The ATLAS experiment is the largest detector, which is build to exploit the whole potential of the LHC during proton-proton runs and proton-ion runs [42]. The CMS detector has a very similar physics programme, but has a different detector design than the ATLAS detector. With the LHCb experiment, heavy flavour processes are studied in detail. The ALICE detector is specialised for ion collisions to study strongly interacting matter at LHC energies [45].

A total integrated luminosity of 5.61 fb^{-1} in 2011 and 23.3 fb^{-1} in 2012 was delivered by the LHC during the proton collision runs [49]. The amount of data-taken in 2010 (44.22 pb^{-1}) was negligible in comparison to the following two years, therefore it is often not included for physics analysis. As in the previous years, the annual integrated

luminosity is expected to further increase after the current and planned shutdowns [50]. The design parameters for the LHC are given in table 3.1.

Under nominal conditions each proton beam consists of 2808 bunches where each bunch contains 1.15×10^{11} protons [51]. The design bunch spacing is 25 ns, whereas during the latest data-taking runs, 50 ns was used. The instantaneous luminosity reached up to $7.73 \times 10^{33}\,\mathrm{cm^{-2}s^{-1}}$ in 2012. The mean number of interactions per crossing, so-called pileup, was 9.1 in 2011 and 20.7 in 2012. This high pileup is challenging at many levels in the experiment: for the trigger, computing, jets, track and vertex reconstruction [37].

LHC parameter	Design value	Unit
Circumference	26.7	km
Beam energy at collision	7	TeV
Beam energy at injection	0.45	TeV
Luminosity	10^{34}	$\mathrm{cm^{-2}s^{-1}}$
Number of bunches per beam	2808	
Intensity per bunch	1.15×10^{11}	p
Bunch spacing	24.95	ns
Operating temperature	1.9	K

Table 3.1: Table showing the main LHC design parameters [23, 37].

3.3 The ATLAS experiment

The ATLAS detector [52] is a general-purpose detector built to study a wide range of physics processes including precise measurement of Standard Model properties and the search for new particles. More than 2900 scientists from 172 institutes in 37 countries work in the ATLAS collaboration. At the centre-of-mass energy ($\sqrt{s}$) of 14 TeV, the detector is designed for 40 million bunch crossing per second. One hundred million electronic channels, with resolutions depending on the detector region, measure the momenta and energies of the produced particles. The detector is 25 m high and 45 m long and weighs 7×10^6 kg.

It has performed with a data taking efficiency of 93.5% in 2011 and 2012 [49]. ATLAS recorded integrated luminosities of 5.25 $\mathrm{fb^{-1}}$ collected at $\sqrt{s} = 7$ TeV in 2011 and 21.7 $\mathrm{fb^{-1}}$ at $\sqrt{s} = 8$ TeV in 2012. As shown in figure 3.2, the ATLAS detector consists of an inner tracking detector, calorimeters, a muon system, forward detectors and a system

of superconducting magnets [52]. A summary of the general performance goals of the subsystems is listed in table 3.2.

Detector component	Required resolution	η coverage
Tracking	$\sigma_{p_T}/p_T = 0.05\% p_T \oplus 1\%$	± 2.5
EM calorimetry	$\sigma_E/E = 10\%/\sqrt{E} \oplus 0.7\%$	± 3.2
Hadronic calorimetry		
barrel and end-cap	$\sigma_{p_T}/E = 50\%/\sqrt{E} \oplus 3\%$	± 3.2
forward	$\sigma_{p_T}/E = 100\%/\sqrt{E} \oplus 10\%$	$3.1 < \lvert\eta\rvert < 4.9$
Muon spectrometer	$\sigma_{p_T}/p_T = 10\%$ at $p_T = 1$ TeV	± 2.7

Table 3.2: The table contains the ATLAS performance goals for the different detector devices where the units for E and p_T are in GeV [52].

3.3.1 Coordinate system

The nominal interaction point (IP) is the origin of the coordinate system in ATLAS. In the Cartesian coordinate system the z-axis is the beam axis, the x-axis points horizontally to the centre of the LHC ring and the y-axis is vertical pointing upwards building a right handed coordinate system. The detector is symmetric about the perpendicular plane spanned by the x and y axis. The side of the detector at positive z values is called the A-side of the detector whereas the detector half with negative z values is defined as the C-side.

To describe the detector the spherical coordinate system is often preferred. The polar angle θ is measured from the beam-axis and the azimuthal angle ϕ is the angle in the perpendicular plane to the beam axis (z-axis). The parameter ρ is used to define the transverse radius from the beam axis ($\rho = \sqrt{x^2 + y^2}$). With these coordinates, the pseudorapidity, η, is defined as $\eta = -\ln(\tan(\theta/2))$. This dependence is derived from the definition of the rapidity, y, by assuming massless particles:

$$y = 0.5 \ln \frac{E + p_z}{E - p_z} \approx 0.5 \ln \frac{|p| + p_z}{|p| - p_z} = 0.5 \ln \frac{|p| + |p| \cos\theta}{|p| - |p| \cos\theta} = \ln \sqrt{\frac{1 + \cos\theta}{1 - \cos\theta}} = \eta^{1}. \quad (3.1)$$

[1] As the values for the energy and momentum of the particle are not needed in the pseudorapidity definition, it is an often used quantity to describe the detector in case the energy and momentum of particles are not known.

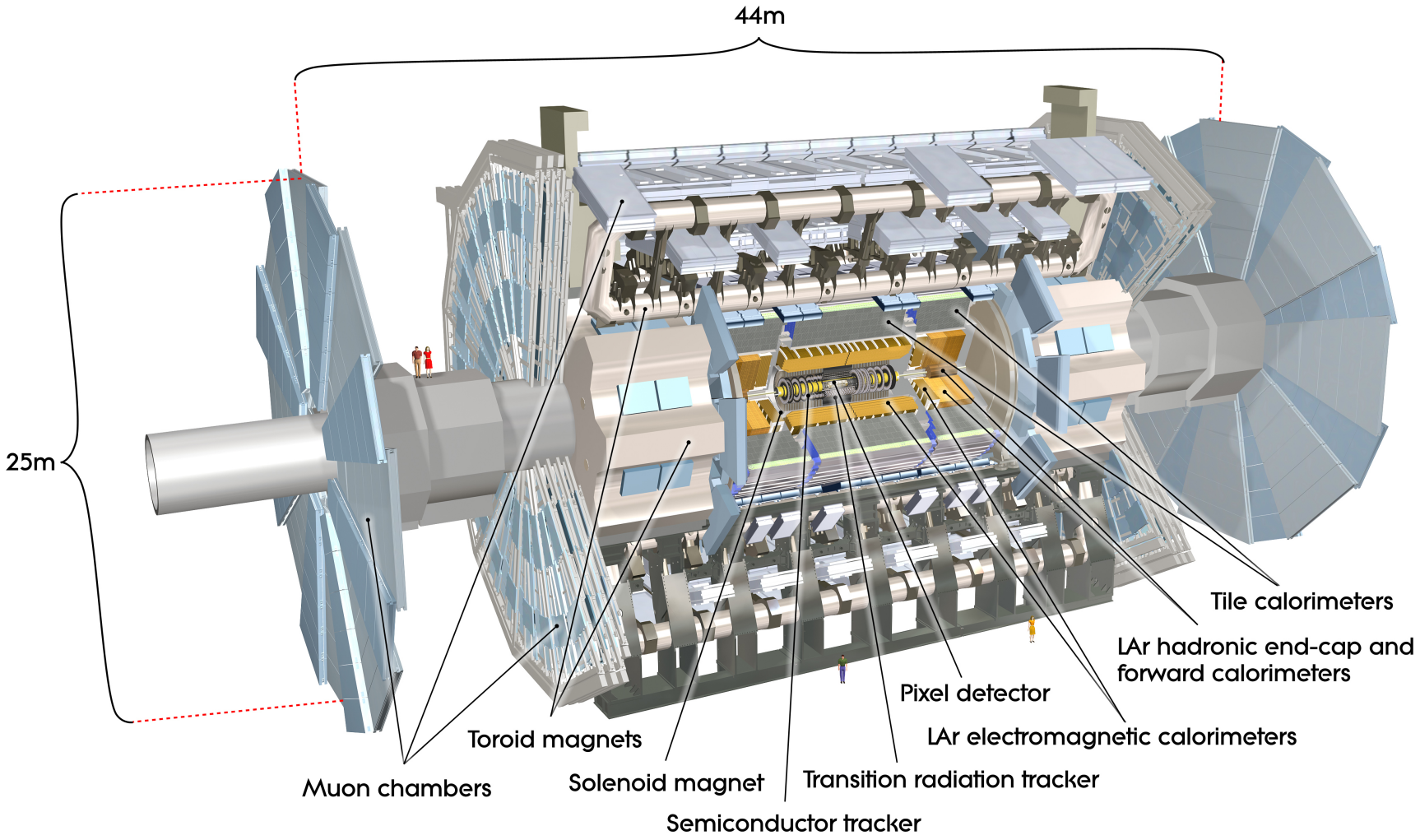


Figure 3.2: Schematic of the ATLAS detector [52].

Some additional quantities are used which are defined in the plane perpendicular to the beam. The transverse momentum, defined as $p_T = p \sin\theta$, is invariant under boosts along the beam axis. The starting conditions are well known in the perpendicular plane to the beam axis as the colliding protons have a trajectory parallel to the z-axis and have negligible momentum in the perpendicular plane [23]. This strongly motivates a detector coverage with high precision detectors in particular for small η.

The missing transverse energy is defined as $E_T^{miss} = -\sum_i p_T^i$ which is also named missing transverse momentum [53]. Given the conservation of momentum, a large hermetic detector is ideal to measure missing E_T.

The following example provides another main argument for the structure of the ATLAS detector and a detailed look into the coordinate system. Heavy particles are a main target to be studied. Their mass M depends on the momentum fraction of the two partons colliding, x_1, and, x_2, as given in the following formula: $M^2 = x_1 x_2 s$. To produce a heavy particle both momentum fractions have to be large.

With the definition of rapidity, y, the energy of the new particle, $E = 0.5\sqrt{s}(x_1 + x_2)$, and its momentum in the direction of the beam axis, $p_z = 0.5\sqrt{s}(x_1 - x_2)$, the following dependence can be derived:

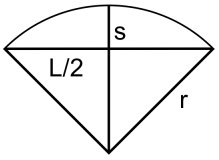
$$e^y = \sqrt{x_1/x_2} \Rightarrow y \to 0 \quad \text{for} \quad x_1 \approx x_2.$$

This shows that if x_1 and x_2 are similar, the rapidity is close to zero. In conclusion, heavy particles are produced centrally motivating a high quality detector coverage for small η and an overall large hermetic coverage for missing E_T.

3.3.2 Magnet system

The momentum and charge of particles is measured with the trajectories of charged particles curving in the magnetic field. The following formula determines the momentum, p, in GeV, depending on the radius, r, of the track in metres and the magnitude of the magnetic field, B, in Tesla: $p = 0.3rB$. The momentum resolution is determined by the sagitta $s = L^2/(8r)$ for $r \gg L/2$, where L is the length of the detector region in the perpendicular plane. The relative momentum resolution, δp, can be derived from the relative sagitta resolution, δs:
To enable a good momentum resolution, a large value for L^2B is preferred. This is realised in ATLAS by a two-magnet system: a solenoid at $r = 1.2\,\text{m}$ (internal radius of $1.23\,\text{m}$ and external radius of $1.28\,\text{m}$) with a magnetic field of $2\,\text{T}$ and three air-core toroids

$$p = \frac{0.3L^2B}{8s} \Rightarrow \frac{\delta p}{p} = \frac{\delta s}{s} = \frac{8}{0.3}\frac{1}{L^2B}p\delta s \qquad (3.2)$$



around the calorimeter with a strength ranging between 0.2 and 3.5 T [54]. The solenoid coil is located in the boundary between the tracker and the calorimeter. To minimize the number of soft particles curling in the ID but not reaching the calorimeter, the radius of the solenoid is required to be small. The radius of the magnet is recommended to be $R_M = 2r = p/(0.15B)$ so particles with $p > 0.35\,\text{GeV}$ reach the calorimeter. The maximal radius of the ATLAS solenoid with a magnetic field of $B = 2\,\text{T}$ is therefore $R_M = 1.2\,\text{m}$. A higher magnetic field would result in a higher occupancy in the tracker due to charged particles curling in the inner detector ("loopers") which makes tracking harder.

The solenoid has an axial length of 5.283 m and is placed in front of the electromagnetic and hadronic calorimeter [55]. In the CMS detector, the solenoid is positioned outside the calorimeter. This however restricts the space for the CMS calorimeter which is essential to measure the energy of particles with high p_T and jets. In the ATLAS detector the material in front of the calorimeter is minimised by using the same cryostat (cooling device) for the liquid-argon calorimeter and the solenoid to ensure a small impact on the calorimeter resolution [56].

The steel yoke at $r \sim 4.25\,\text{m}$ is the return for the solenoid field and leaves the calorimeter with a negligible magnetic field. Enough space for the calorimeter is available to allow good containment of jets. Muons with their small interaction with matter travel through the calorimeter reaching the muon system as the only charged particles from the IP. The muon system is embedded in a magnetic field from the toroids covering the region $|\eta| < 2.7$. The bending power is 1.5-5.5 $\text{T}\cdot\text{m}$ in the barrel ($0 < |\eta| < 1.4$) and 1-7.5 $\text{T}\cdot\text{m}$ in the end-caps ($1.6 < |\eta| < 2.7$) [52]. In the regions between the barrel and end-caps, the field is very inhomogeneous and the bending power is lower. The toroids produce a complex magnetic field which is important to map for tracking. For the toroid no return yoke is required which leaves less material to cause multiple scattering and increases the momentum resolution.

The toroid system consisting of eight coils allows the very large size of the ATLAS detector. Separating the muon and ID magnet system ensures the necessary space for the calorimeters to contain a large fraction of hadron showers from high energetic particles.

The magnet system of ATLAS provides a magnetic field with a large coverage of $|\eta| < 2.7$ and is monitored by three-dimensional Hall probes.

3.3.3 Inner Detector

The inner detector (ID) measures positions along the trajectory of passing charged particles. By combining these positions tracking is accomplished and the momentum is determined. It is also essential to find primary and secondary vertices and determine the impact parameter to identify long-lived particles often originating from heavy flavour particles. Particle identification can be supported by measuring specific ionization (dE/dx). The energy loss of particles described by the Bethe-Bloch function can be used in combination with the momentum measurement to identify the particle. The use of the specific ionization method for particle identification is restricted to low momentum regions as the specific ionization is the same for different particles at high momentum. The performance of the ATLAS Pixel detectors shows that the resolution of specific ionization dE/dx for a track is about 10% [57]. The TRT also measures the specific ionization dE/dx [58] and for the SCT measuring dE/dx is currently investigated [59].

Additionally, transition radiation produced by particles travelling through the boundary between two materials provides particle identification particularly e/π separation which is further discussed later [60].

The design momentum resolution for the ATLAS tracker is $\sigma_{PT}/p_T = 0.05\% p_T \oplus 1\%$ for charged tracks with $p_T > 0.5\,\text{GeV}$ and $|\eta| < 2.5$ given in table 3.2. Electron identification is provided for $0.5\,\text{GeV} < p_T < 150\,\text{GeV}$ over a range of $|\eta| < 2$ [52].

The infrastructure to support the inner detector with readout and cooling requires dead material to be placed in front of the calorimeter. This restricts the resolution of the calorimeter as mentioned in sub-section 3.3.2. However, for precise tracking several measured points along the trajectory are needed with sufficient bending radius. Therefore, reducing fakes, many tracking layers are recommended which increases the amount of infrastructure. Regarding the amount of material in the ID in front of the calorimeter, a balance between the tracking and calorimeter performance has to be found in the detector layout. The highest particle flux is close to the interaction point and decreases with r^{-2}. The occupancy is minimized and the impact parameter resolution maximised by placing the detector with the highest resolution, and accordingly the smallest cells closest to the IP. This will decrease the fake hit assignment and improve hit reconstruction resolution. Considering these performance issues, the innermost part of the ATLAS detector is a pixel detector consisting of three layers with a total of 80.4 million pixels [61]. Further

out the Semiconductor Tracker (SCT) with larger granularity, and even further out the Transition Radiation Tracker (TRT), are placed illustrated in figure 3.3.

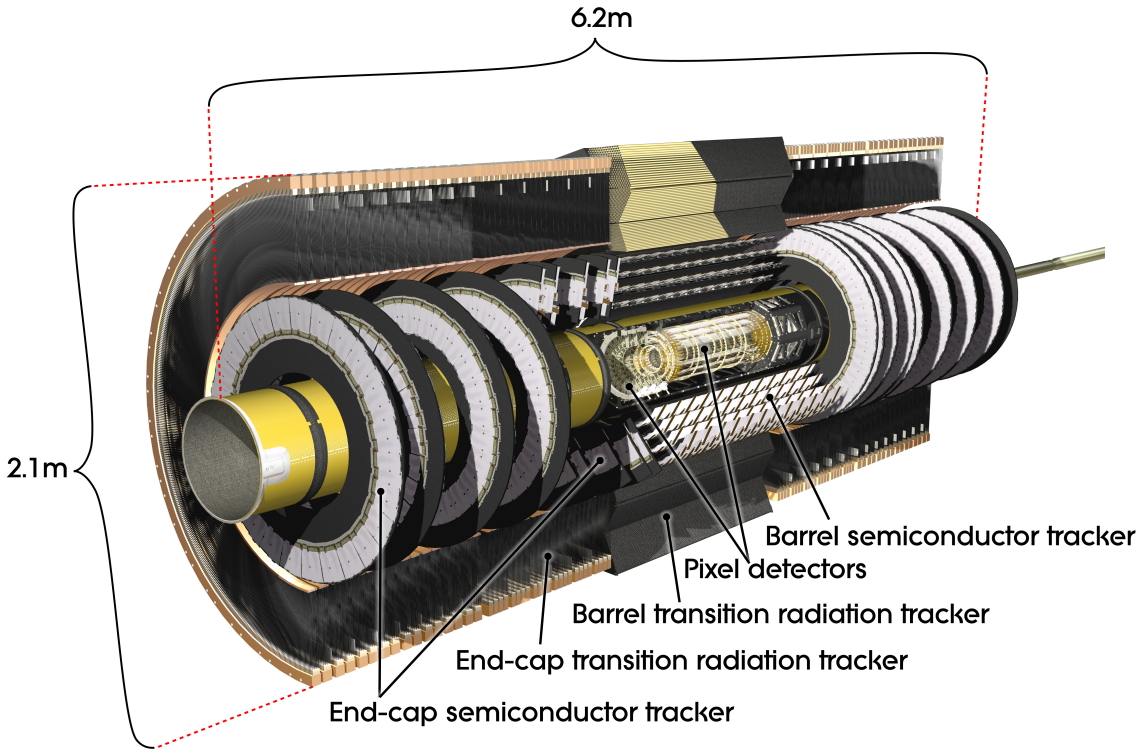


Figure 3.3: The ATLAS inner detector is shown as a 3D model with detector sections cut away for a view inside [52].

As shown in figure 3.4, the ID has a coverage of $|\eta| < 2.5$. The two silicon detectors (Pixel and SCT) provide a minimum of 7 position measurements of passing particles, whereas the TRT operates continuous tracking with 32-45 measurements for typical track measurements with the channels specified in table 3.3 [61, 62].

Pixel detector

The pixel detector contains three layers in the barrel and three disks on the A and C side with $\sim 98\,\%$ of the pixels having a size of $50\,\mu\text{m} \times 400\,\mu\text{m}$. The rest of the pixels are larger ($50\,\mu\text{m} \times 600\,\mu\text{m}$) to complete a continuous sensitive area between front-end chips. The charge deposited in each pixel is determined by measuring the time over threshold (ToT) by the sensors. The amplified current of the signal pulse is compared with the discriminator to give the ToT. Up to a pseudorapidity of $|\eta| \leq 2.5$ a particle passes at least three pixel layers.

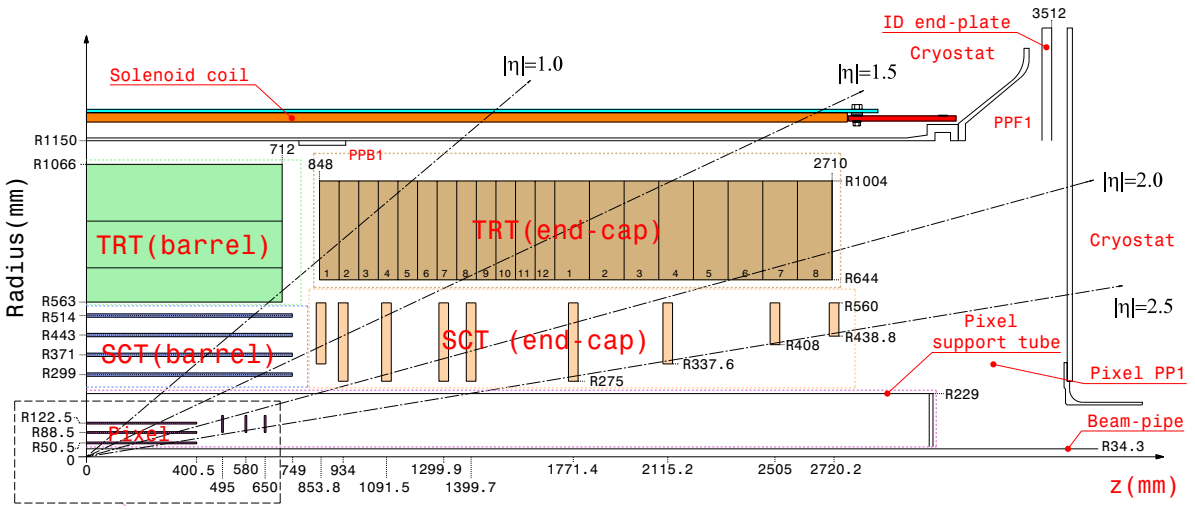


Figure 3.4: Schematic of the ATLAS inner detector [52].

The free charge carriers produced by passing charged particles drift towards the electrodes. Due to the presence of a magnetic field, the charge carriers in the silicon detector are deflected in the rϕ plane. The angle of this deflection is called Lorentz angle. This increases the charge sharing and is partly counterbalanced by tilting the modules to obtain a staggered silicon detector layout [63].

Semiconductor Tracker

The Semiconductor Tracker (SCT) consists of four barrel layers and nine disks with each having up to three rings. Each layer consists of two layers of silicon microstrips which are arranged with a stereo angle measuring one space point. Instead of using an angle between the back-to-back strips of $\frac{\pi}{2}$ rad, it is 40 mrad increasing the spatial resolution in one direction at the expense of decreasing the resolution in the orthogonal direction. This is chosen to fulfil the required of the intrinsic resolution of 17 μm ($r\phi$) and 580 μm (z) for the barrel and 17 μm ($r\phi$) and 580 μm (r) for the disks. The SCT is constructed so that on average four space points are measured for particles up to a pseudorapidity of $|\eta| \leq 2.5$ as shown in figure 3.4. In the barrel all strips have a 80 μm pitch. In the barrel strips are wire-bonded to build a length of 12.8 cm. The pitch of the strips is between 57 μm and 90 μm in the end-cap [52] and the length of the strips varies between 6 and 7 cm [64]. In the pixels and the SCT the readout time is less than 25 ns (design bunch spacing) to distinguish between hits from different bunch crossings. In comparison to the planar silicon n^+-in n sensors of the pixel detector, the SCT consists of a single-sided p-in-n microstrip sensors.

Inner Detector			Position [mm]	Channels
Pixel:	3 barrel layers:	B-Layer	$r = 50.5$	$\mathbf{13.2 \cdot 10^6}$
		Layer 1	$r = 88.5$	$\mathbf{22.8 \cdot 10^6}$
		Layer 2	$r = 122.5$	$\mathbf{31.2 \cdot 10^6}$
	3 end-cap disks:	Disk 1	$\lvert z\rvert = 495$	$\mathbf{4.4 \cdot 10^6}$
		Disk 2	$\lvert z\rvert = 580$	$\mathbf{4.4 \cdot 10^6}$
		Disk 3	$\lvert z\rvert = 650$	$\mathbf{4.4 \cdot 10^6}$
SCT:	4 barrel layers:	Layer 0	$r = 299$	**589,824**
		Layer 1	$r = 371$	**737,280**
		Layer 2	$r = 443$	**884,736**
		Layer 3	$r = 514$	**1,032,192**
	9 end-cap disks:	Disk 1	$\lvert z\rvert = 853.8$	**141,312**
		Disk 2	$\lvert z\rvert = 934.0$	**202,752**
		Disk 3	$\lvert z\rvert = 1091.5$	**202,752**
		Disk 4	$\lvert z\rvert = 1299.9$	**202,752**
		Disk 5	$\lvert z\rvert = 1399.7$	**202,752**
		Disk 6	$\lvert z\rvert = 1771.4$	**202,752**
		Disk 7	$\lvert z\rvert = 2115.2$	**141,312**
		Disk 8	$\lvert z\rvert = 2505.0$	**141,312**
		Disk 9	$\lvert z\rvert = 2720.2$	**79,873**
TRT:	continuous barrel:	3 rings	$554 < r < 1082$	**52,544**
	continuous end-cap:	20 rings	$827 < z < 2744$	**245,760**

Table 3.3: The table shows the position and number of channels of the ID components.

Transition Radiation Tracker

In the Transition Radiation Tracker (TRT), relativistic charged particles emit transition radiation passing through boundaries of media with different dielectric constants. The radiated photons interact with the molecules of the gas by freeing electrons.

The TRT consists of thin-walled drift tubes with a radius of 2 mm and a central wire. The electrons which are accelerated towards the wire due to a electric field between the wire and the cylinder wall might cause further ionization ending up in an avalanche close to the wire. As the drift tube is operating in a proportional mode the amount of charge carriers produced is proportional to the energy loss [65].
Particles cross 35-40 straws for $|\eta| < 2$ producing two-dimensional space points [66]. The TRT has a resolution of 130 μm by design. Xenon, which is the main component of

the gas mixture in the ATLAS TRT straws, has a high atomic number which allows an efficient detection of the transition radiation [62].

3.3.4 Calorimetry

The calorimeter is an essential detector to determine the energy of photons, electrons or hadronic jets. The stochastic error on the calorimetry scales as:

$$\frac{\delta E}{E} \propto \frac{1}{\sqrt{E}}.$$

The relative resolution improves with energy which is very useful for measuring particles with high p_T. For particles with low- and medium-transverse momentum the spectrometer provides a good momentum resolution. The spectrometer is characterised by the following resolution dependence: $\frac{\delta p}{p} \propto p$.

The calorimeter of the ATLAS detector consists of an active medium, liquid argon (LAr), and a passive material which differs between the different detector sections. This structure is called sampling calorimeter, whereas calorimeters which consist of a single material combining the tasks of the active signal generation and the passive particle absorption are called homogeneous calorimeters. A sampling calorimeter can provide information about the longitudinal shower development with the different active material sectors. A homogeneous calorimeter has usually a better energy resolution as most of the energy deposited can be measured, whereas in a sampling calorimeter only the energy deposited in the active material will be experimentally measured.

Besides the stochastic sampling error, $\delta E/E = a/\sqrt{E}$, mentioned above, an additional error describing the electronic noise and pileup has to be considered, b/E. Furthermore, a constant relative error, c, accounting for the nonuniformities in the detector has to be added resulting in the following total relative error of calorimetry:

$$\frac{\delta E}{E} = \frac{a}{\sqrt{E}} \oplus \frac{b}{E} \oplus c. \tag{3.3}$$

The calorimetry in the ATLAS detector consists of an electromagnetic (ECAL) and a hadronic calorimeter (HCAL) as shown illustrated in figure 3.5 [61]. The electromagnetic shower in the ECAL produced by electromagnetic interactions is compact and dense. The on average larger hadronic shower in the HCAL is dominated by hadronic interactions while locally also electromagnetic showers can occur when π^0 mesons decay into two photons [67].

The performance goals are $\sigma_E/E = 10\%/\sqrt{E} \oplus 0.7\%$ over a range of $|\eta| < 3.2$ for the ECAL as given in table 3.2. The resolution requirement for the HCAL is

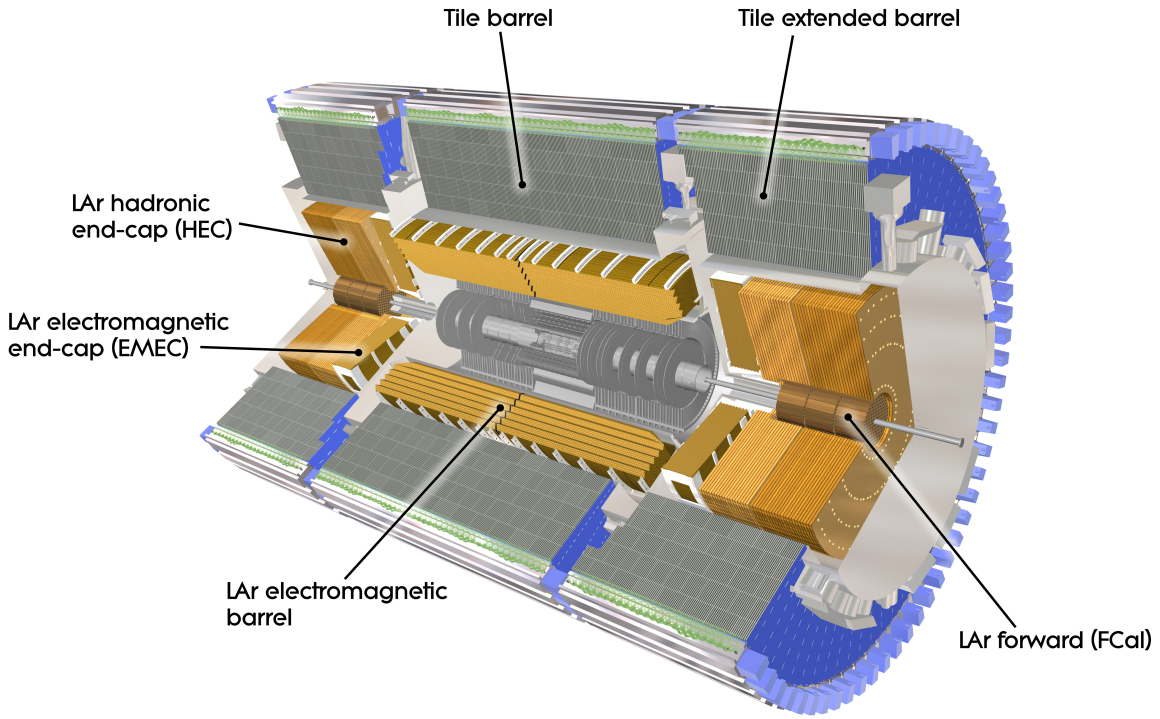


Figure 3.5: A simulated geometry of the ATLAS calorimetry system is shown as a 3D model [52].

$\sigma_{p_T}/E = 50\%/\sqrt{E} \oplus 3\%$ in the barrel and end-cap and $\sigma_{p_T}/E = 100\%/\sqrt{E} \oplus 10\%$ in the forward region.

LAr electromagnetic calorimeter

In the electromagnetic calorimeter, electrons, positrons and photons produce showers by alternating phenomena of pair-production and bremsstrahlung. The energy loss in the mean longitudinal profile in an electromagnetic shower is described by $dE/dt \propto t^a \exp(-bt)$ where $t = x/X_0$ with the position in the shower, x, and the radiation length depending on the media X_0 [68]. The parameters a and b depend on the particle, its energy and the media. It takes into account the dominating physical principles in the electromagnetic cascade of the bremsstrahlung and the impact of the ionisation [69].

The electromagnetic calorimeter of the ATLAS detector consists of a barrel covering $|\eta| < 1.475$ and two end-caps capturing $1.375 < |\eta| < 3.2$. The active medium LAr is a noble gas cooled down to its liquid state by the surrounding cryostat. As an advantage, it is radiation resistant, but as a disadvantage, it processes the signal relatively slowly.

The thickness of the ATLAS electromagnetic calorimeter varies between $24\,X_0$ at $\eta \approx 0$ and $35\,X_0$ at $\eta \approx 2.5$. The passive material of the electromagnetic calorimeter is lead ($X_0 = 0.56\,\text{cm}$) whereas the active liquid argon material has a radiation length of $X_0 = 14.0\,\text{cm}$. The electromagnetic calorimeter can contain electromagnetic showers with about 1 TeV which are around 25 radiation lengths [56].

A significant amount of energy of the passing particles is already lost before the calorimeter mainly due to the inner detector and the solenoid coil. With higher pseudo-rapidity, the material that the particles pass through is considerably higher, resulting in an increased energy loss [70].

A sampling term of 10%, a constant term of 0.2-0.35% and a noise per cluster of 250 MeV were measured for the electromagnetic calorimeter [56].

Hadronic calorimeter

In the hadronic calorimeter, hadronic jets interact by inelastic hadronic interactions producing showers. The hadronic calorimeter consists of three detectors: Tile calorimeter, LAr hadronic end-cap calorimeter and LAr forward calorimeter.

The Tile calorimeter includes a barrel and on each side an extended barrel reaching up to a coverage of $|\eta| = 1.7$. The absorber material of the tile calorimeter is steel whereas it is copper in the LAr hadronic end-cap calorimeter. The two independent wheels of the LAr hadronic end-cap calorimeter have a coverage of $1.5 < |\eta| < 3.2$. The LAr forward calorimeter increases the calorimeter coverage by $3.1 < |\eta| < 4.9$ and consists of three modules in each end-cap. The innermost module is optimised for electromagnetic calorimetry with copper as the absorber material. The other two modules are specialised for hadronic measurements with tungsten being the absorber material.

As discussed for the electromagnetic calorimeter, the hadronic calorimeter is influenced by the energy loss of the particles in the material in front of the calorimeter. The hadronic calorimeter is built to contain a hadronic jet of about 1 TeV. This corresponds to an effective interaction length of $11\,\lambda_0$ [71].

The performance of the combined barrel LAr and Tile calorimeter is a stochastic term of $55\%/\sqrt{E}$, a constant term of 2.3% and noise of 3.2 GeV [56]. For the combined end-cap LAr a stochastic term of $85\%/\sqrt{E}$, a constant term of $< 1\%$ and noise of 1.2 GeV was measured [56].

3.3.5 Muon Spectrometer

The muon spectrometer (MS) is expected to resolve stand-alone muons of about 1 TeV with a resolution better than 10%. To analyse this goal, the equation 3.2 gives an understanding of the experimental implications. The average field of the large air-torroid is 0.5 T and the distance between the innermost and outermost of the three barrel layers of the muon spectrometer is ~ 5 m. For muons with 1 TeV this results in a sagitta of $\sim 500\,\mu$m. To achieve a resolution of 10%, the precision of the sagitta is required to be $\sim 50\,\mu$m. As the sagitta is inversely proportional to the momentum, very high momentum muons need a very precise sagitta measurement. This limits the maximum momentum of muons that can be resolved to a few TeV. For low momentum muons up to 300 GeV the precision is limited to a few percent by the uncertainty on the energy loss in the calorimeter and multiple scattering. Additionally, the precision of the alignment strongly affects the resolution of the muon spectrometer [56].

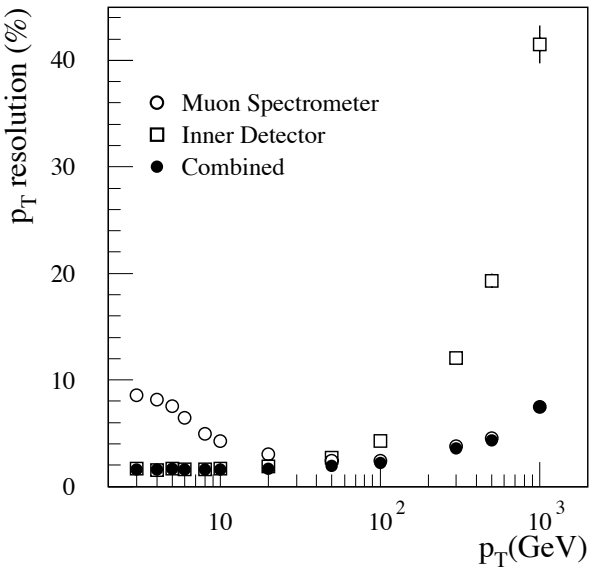


Figure 3.6: Momentum resolution shown as a function of p_T for the ID, MS and combined for $|\eta| < 2.5$ [72].

In figure 3.6, the momentum resolution depending on the transverse momentum is given for the inner detector, the muon spectrometer and a combined measurement. The interplay of the ID vs. MS shows a better momentum resolution at low p_T for the ID. For $p_T > 50$ GeV, the resolution of the MS dominates [72].

Structure of the muon spectrometer

The muon spectrometer covers a large rapidity up to $|\eta| < 2.7$ and is located partly within the air-toroid super-conducting magnet as the outermost detector in the ATLAS experiment shown in figure 3.7. The multiple scattering of muons by material is minimized by the open structure of the toroid. The toroid consists of a complex magnetic field as mentioned in section 3.3.2 which affects the detector resolution. For a precise modelling of the detector resolution a good understanding of the magnetic field map is crucial. Furthermore, the alignment is challenging as it needs to react sensitively to movements, which is difficult considering the complexity of the magnetic field and the size of the total experiment. Muons have to be reconstructed over a large distance of about 14 m from the muon system to the interaction point [61].

The ATLAS muon system consists of a barrel inside the magnetic field and an end-cap outside the magnetic field. The barrel consists of three layers of the Monitored Drift Tubes (MDTs) for tracking. These layers are positioned at a radius of 5 m, 7.5 m and 10 m. The middle layer is surrounded by Resistive Plate Chambers (RPCs) for triggering. On one side of the third layer a further RPC is located. Each of the two end-caps has four disks. The end-caps consist of MDT tracking detectors except the innermost disk which consists of tracking detectors with higher granularity, Cathode Strip Chambers (CSCs), motivated by the higher occupancy. The middle MDT disk is surrounded by the trigger detector used in the end-caps, Thin Gap Chambers (TGCs). A further TGC is placed in front of the innermost disk [73].

Muon tracking detector

The main tracking detectors in the muon system are MDTs with in total 400,000 tubes. Each MDT module has 3 layers of tubes on both sides. The tubes are between 1 m and 6 m long and are characterised by a very precisely positioned wire in the middle of the tube with a diameter of 30 mm [74]. The precision is essential for the accuracy of the MDT measurements. Besides the wire, the tubes are filled with Ar-CO_2 gas (with a ratio 93:7). The wire is made of gold-plated tungsten-rhenium and has a diameter of 50 μm [52, 73].

The gas mixture shows almost no effects from irradiation, but has a relatively slow drift time so that the maximal drift path of 15 mm takes about 700 ns. Furthermore, the drift time is non-linear and this has to be taken into account when analysing the signal [61].

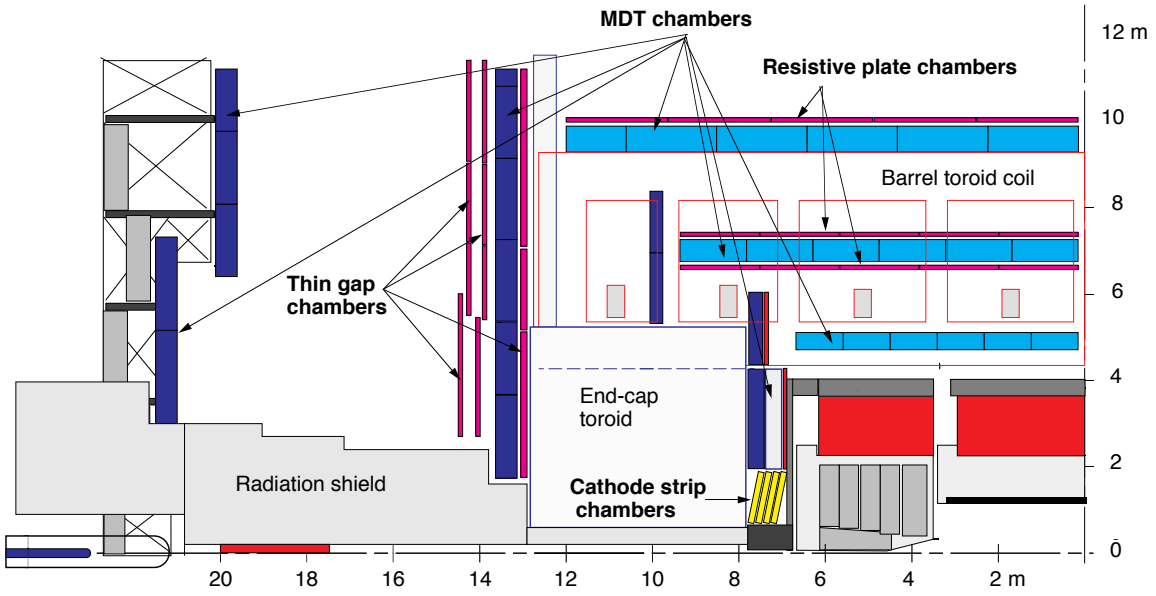


Figure 3.7: Two dimensional model of the muon spectrometer showing all four technologies: RPC, MDT, CSC and TGC [16].

In the CSC tracking detector, 16 four-layer packages are built into each end-cap of the muon system. The CSC is a multiwire proportional chamber consisting of cathode planes and anode wires.

Muon trigger detector

Besides the tracking detectors, which determine the bending coordinate of the muons with high precision, trigger detectors are needed. They determine which bunch crossing the muon came from. This is difficult with the tracking detector due to the long drift time. Furthermore, trigger detectors determine the azimuthal coordinate of the muons with an accuracy of $8-10\,\text{mm}$. The trigger detector also detects muons with a transverse momentum beyond the threshold of the tracking detector. The trigger detectors used in ATLAS are RPCs with a coverage of $|\eta| < 1.05$ and TGCs with a coverage of $1.05 < |\eta| < 2.4$ [52].

3.3.6 Forward detectors

Three forward detectors belong to the ATLAS experiment. One of these is the detector called LUminosity measurement using Cherenkov Integrating Detector (LUCID). It measures the instantaneous luminosity at $z = \pm 17\,\text{m}$. This information is combined

with the measurements of the detector called Absolute Luminosity For ATLAS (ALFA) at $z = \pm 240\,\text{m}$. Using the accelerator properties the luminosity can be calculated to a precision of $5 - 10\%$ [75]. The precision of accelerator parameters, such as the transverse beam dimensions, makes it difficult to determine the luminosity more accurately. The required precision of $2 - 3\%$ can be obtained with LUCID and ALFA. The third forward detector Zero-Degree Calorimeter, ZDC, at $z = \pm 140\,\text{m}$ determines the centrality of collisions during heavy-ion and proton-proton runs [76].

3.3.7 Data acquisition, readout, trigger, and offline processing

The data taken has to be moved, selected and controlled. As only a limited amount of data can be recorded in permanent storage, a selection of the events has be made so that the essential data can be recorded in real time. This data is then accessible for offline reconstruction and analysis.

Data acquisition & readout

This task is performed by a complex trigger and data acquisition system (TDAQ). One of the challenges of TDAQ is the large size of the detector. It takes particles originating in the interaction point up to 75 ns to reach the far end of the detector. It takes altogether $2.5\,\mu\text{s}$ for the signal from the detectors to reach the first level of selection called level-1 Trigger (L1 trigger) and to be processed until a first decision of the L1 trigger. As the detector operates at 40 MHz, during $2.5\,\mu\text{s}$ 100 other bunch crossings will have taken place (when operating with design bunch spacing). This data has to be stored during the time until a L1 trigger decision is made. Therefore, detectors have buffers as part of their front-end electronics.

The rejection power required of the TDAQ can be determined by the ratio of the expected rate of data from the experiment, 40 MHz, and the amount of data possible to store in real time, $\sim 200 - 300\,\text{Hz}$. This leads to a rejection power of about 10^5 leaving a large enough fraction to store interesting events of each bunch crossing. Besides these challenges, the system must be ready for operation at any time. It also has to work on a very large scale and a modular approach is essential to allow selective usage of the system.

One of the three main aims of the TDAQ system is the minimization of detector dead time arising after measurement and not prolonging the time needed until a new measurement is possible. Dead time can be avoided by parallel processing. Even when the information of the whole event is needed, systems as the event filter are based on

parallel processing. Furthermore, the smooth transport of the large amount of data and successful controls are goals of the TDAQ system so that the system operates continually and reliably.

Trigger

The online selection consists of three main trigger levels which refine the decision: Level 1, Level 2, and the Event Filter. Higher levels need more information to filter events effectively. The decision latencies are inversely proportional to the amount of data required. Buffers on different levels are required to absorb the latencies.

To select physically interesting events, the L1 trigger looks for high transverse-momentum particles, large transverse and missing energy, decreasing the rate from 40 MHz to 75 kHz. The L2 trigger reduces the rate further to 3.5 kHz and the event filter condenses it to about 200 Hz [52]. These events are then stored permanently at the CERN computer centre.

At this frequency, an order of 10^9 events per year have to be stored where each event has a size of 1.3 MB [52]. This results in about a Petabyte per year which is initial processed at CERN and then distributed to the LHC Computing Grid (LCG). In this worldwide network of computing centres the data gets stored on a local site to be analysed further. In the ATLAS computing model, the computing centres are grouped by their responsibilities in Tiers. CERN builds the central Tier-0, and a group of ten computing centres worldwide form the Tier-1s which hold, besides Tier-0, a second copy of the RAW data files. All Tier-2s are associated to a Tier-1 giving access to the data for individual analysis and provide the capacities for simulation production. The largest use of the grid bulk is done in Tier-2s. Tier-3s build the end of the Tier chain with computing resources for users to process their analysis [77, 78]. The University of Edinburgh builds together with the University of Glasgow and the University of Durham, ScotGRID, a Tier-2 site [79].

Offline processing

From the RAW data files, the Event Summary Data (ESD) file is produced as an output after the reconstruction. It contains all variables required for further analysis and has a size of 0.5 MB per event. A format produced with less detail is the Analysis Object Data (AOD) file comprising about 0.1 MB per event. Additionally, a format with a further reduced size is the Derived Physics Data (DPD), which has further slimmed down versions, e.g. D3PDs and ntuples, produced with contents required for the analysis [80].

The chain for the simulated data starts with the EVGEN format as an output of the Monte-Carlo generators. The events are further processed through the GEANT4 simulation of the ATLAS detector, which contains a detailed geometry and material description. The obtained output in the HITS format is passed through the digitization modelling the detector response. The events are transformed into a Raw Data Object (RDO) format which is the input for the reconstruction process following thereupon the same chain as data [78, 81].

3.4 Summary

The ATLAS detector is a general-purpose particle physics detector with a cylindrical geometry consisting of the magnet system, the inner detector, the calorimeters, the muon spectrometer and the forward detectors. The ATLAS experiment provides a sophisticated combination of detectors to reconstruct events of all types at centre-of-mass energy ($\sqrt{s}$) of 14 TeV. Figure 3.8 shows an example of a simulated $H \to ZZ^{(*)} \to e^+e^-\mu^+\mu^-$ event detected in the ATLAS detector.

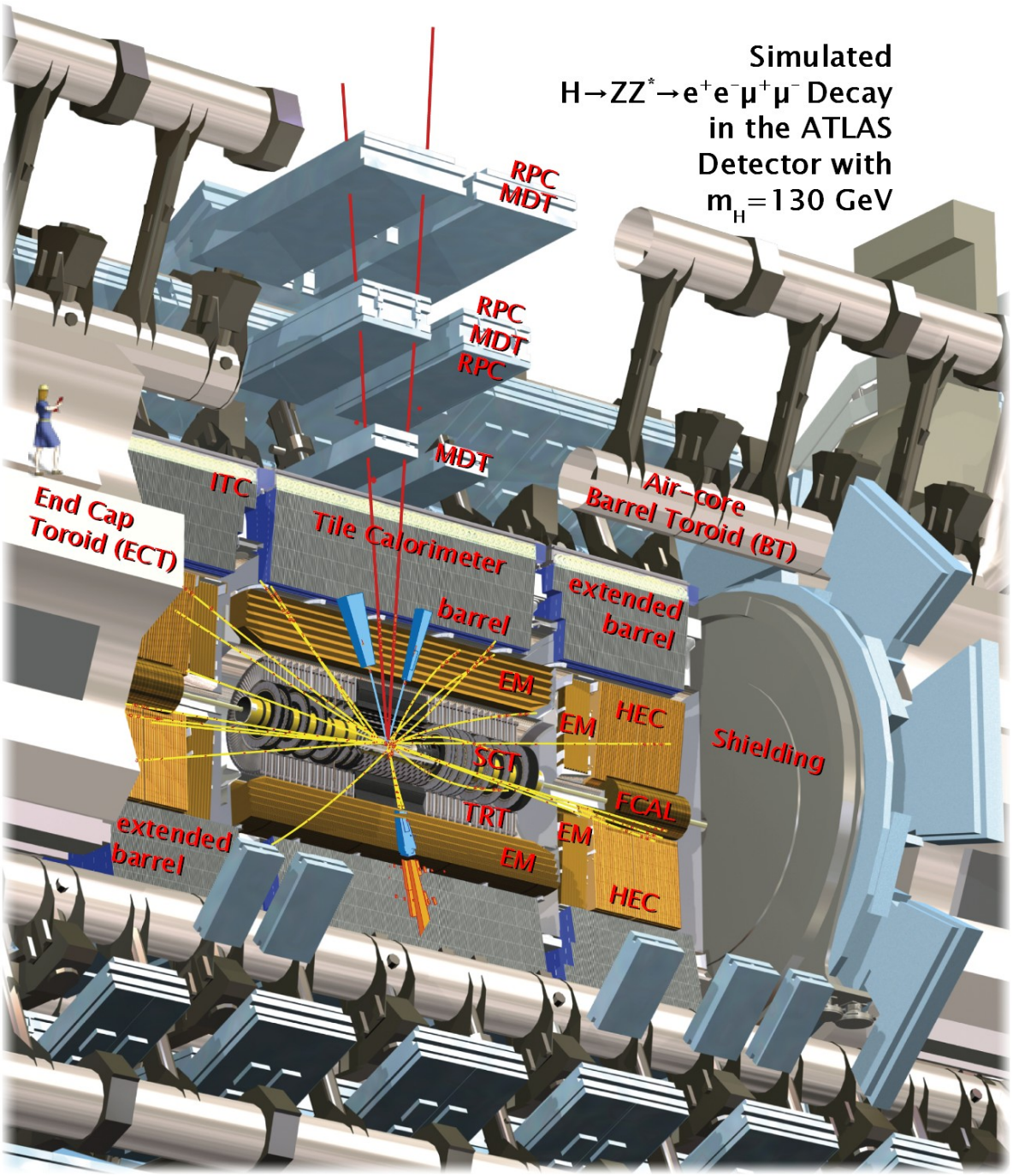


Figure 3.8: Simulated Higgs event at $m_H = 130\,\text{GeV}$ is shown in the ATLAS detector [64].

Chapter 4

Current and upgraded inner detector performance

In this chapter, performance studies of the current and possible upgraded inner detector layouts are presented. The first part concentrates on the challenges faced by the current ID detector given the high pileup environment. In the second half the future tracker layouts are discussed concluding with the proposed Letter of Intent ID upgrade layout.

4.1 Current ATLAS inner detector tracker

The inner detector at the heart of the ATLAS experiment is built to measure the trajectory of charged particles. To ensure good operation and improved understanding of the performance of this detector, studies comparing the expected and actual behaviour were conducted. Pixels with deposited charge above threshold are grouped into clusters if they have a common edge or a common corner. The size of these clusters is studied. In addition, the occupancy is analysed as a measure of the fraction of channels which are hit during a bunch crossing. Furthermore, studies about the separation of tracks within high p_T jets are presented.

4.1.1 Cluster size studies

Introduction

By comparing simulation and data, the understanding of the detector and its response to particle interactions can be checked. The cluster size is a detector parameter which can be used for this comparison. It is simulated in the digitization as part of the simulation software which models the detector response to hits caused by passing particles [81].

When comparing the simulated and the measured average cluster size in ϕ as a function of the track incidence angle on the module in the $r\phi$ plane, a discrepancy was observed as displayed in figure 4.1. Studies to understand this discrepancy and improve the digitization of the pixel hits are presented.

Datasets

The study has been done by looking at inelastic collisions of protons which are contained in minimum bias samples. All samples are summarised in table 4.1. A data sample from 2010 data-taking at $\sqrt{s} = 7\,\text{TeV}$ (sample 1) with an integrated luminosity of $2630\,\text{nb}^{-1}$ during stable beams of run 167844 is compared with Monte-Carlo (MC) samples for this data run(sample 2 and sample 3). The sample 3 has been generated and simulated with with an updated releases and minor changes in the pixel service description in the ATLAS geometry in comparison to the sample 2.

Number	Sample name
sample 1	data10_7TeV.00167844.physics_MinBias.merge.ESD.r1774_p327
sample 2	mc09_valid.105001.pythia_minbias.simul.HITS.e517_s899
sample 3	mc10_7TeV.105001.pythia_minbias.simul.HITS.e577_s964
sample 4	data11_7TeV.00180614.express_express.merge.NTUP_TRKVALID.x117_m810
sample 5	data11_7TeV.00184130.physics_MinBias.recon.ESD.r2603
sample 6	mc11_valid.108351.Pythia8_minbias_Inelastic.recon.ESD.e816_s1310_s1300_r2721
sample 7	mc11_valid.108351.Pythia8_minbias_Inelastic.recon.ESD.e816_s1310_s1300_r2767
sample 8	mc11_valid.108351.Pythia8_minbias_Inelastic.recon.ESD.e816_s1310_s1300_r2719
sample 9	mc11_valid.108351.Pythia8_minbias_Inelastic.recon.ESD.e816_s1310_s1300_r2720
sample 10	mc09_valid.105001.pythia_minbias.recon.ESD.e517_s896_d347_r1479

Table 4.1: Samples used for the cluster size study are listed with their full names.

These MC samples are produced with the generator Pythia 6 [82] and the detector response is modeled with GEANT4 (G4). Pythia 6 and Pythia 8 are Monte Carlo event generators used in ATLAS. Pythia 6 is based on Fortran and Pythia 8 is written in C++ with an improved model of diffraction [83]. As the generated primary particles are simulated passing through the ATLAS geometry secondary particles can be induced. These secondaries are only simulated if they propagate beyond the minimal threshold distance defined as the G4 Range Cut. This cut-off is defined to save CPU time. The

default delta ray range cut is 50 μm, corresponding to a delta ray energy of $\sim$150 keV in silicon with an approximately linear dependence between the range and energy [84].

Validation plots have also been produced for the comparison of a dataset collected in 2011 (sample 4) with an integrated luminosity of 4341 nb^{-1} during stable beam of run 180614 and the perviously mentioned MC sample (sample 3). The studies presented in section 4.1.1 were conducted with a 2011 data sample 5 with an integrated luminosity of 62.1 pb^{-1} during stable beam of run 184130, which is not as sample 4 from the express stream, but a minimum bias sample. This dataset is compared to MC samples with pileup of 0μ, 10μ, 20μ and 40μ (sample 6 - sample 9).

Selection

Only the Pixel barrel is used for these studies and only clusters associated to tracks are selected (so-called clusters on track). Tracks are required to have a significant amount of hits in the inner detector with at least one hit in the Pixel detector. The sum of the TRT hits and the SCT hits multiplied by five is required to be larger than 29, to avoid a bias from low quality tracks. Edge effects occur in clusters consisting of pixels which are at a module border. This bias is avoided by rejecting these clusters. Additionally, the clusters are required to be crossed by the associated track. In the tracking procedure the fitted track can miss one or more clusters along its path. Requiring all clusters to be crossed maximises the probability that the studied clusters belong to the track. The avoided, associated clusters which are not crossed by the track originate from randomness, fakes, delta rays or splitting [85].

G4 Range Cut

In data the cluster width is larger than in the MC simulation. This could be the consequence of low range secondaries, which were not propagated in simulation. The G4 range cut determines the threshold below which secondaries are not propagated in simulation. The influence of the G4 range cut on the cluster size has been studied using a Pythia sample digitized with different G4 range cuts: 5 μm, 10 μm, 20 μm, 50 μm and 100 μm (sample 10).

However, no significant difference in the cluster size could be observed as shown in figure 4.2. Therefore, further studies to understand the discrepancy used the ATLAS default cut of 50 μm.

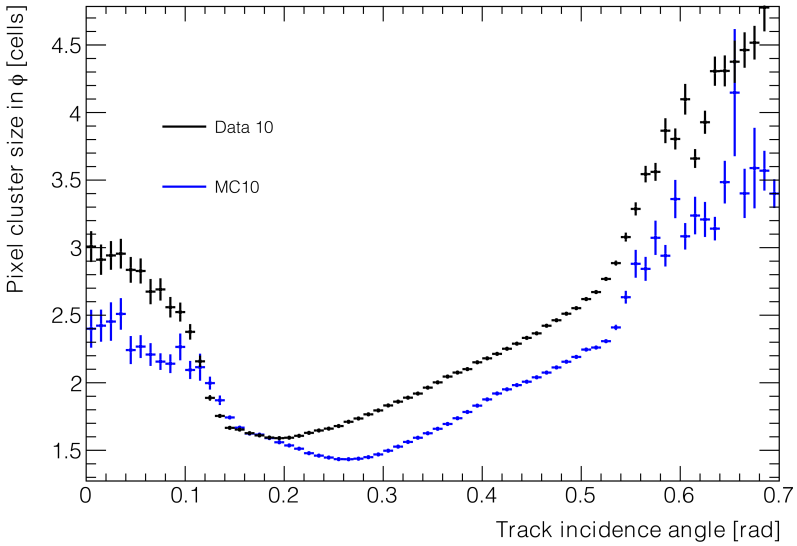


Figure 4.1: Average cluster size versus transverse incidence angle of the track using 2010 data and Monte Carlo showing the discrepancy in the Pixel cluster size; the minimum cluster size corresponds to the Lorentz angle.

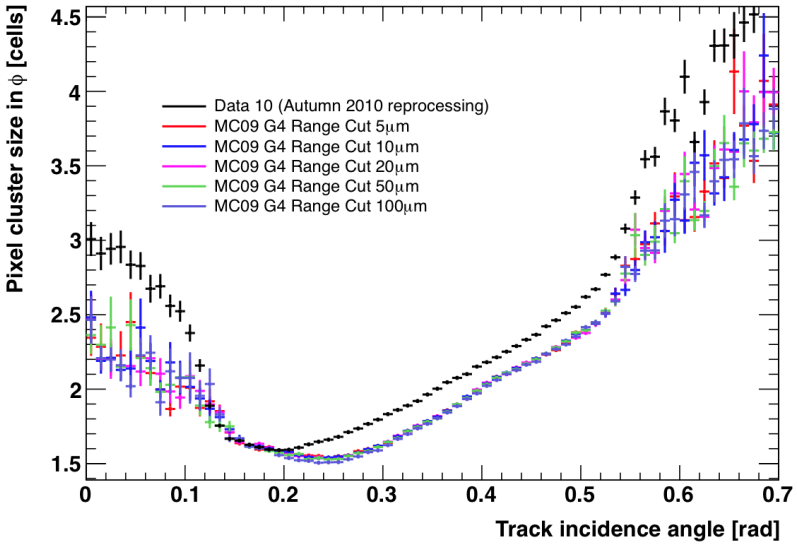


Figure 4.2: Average cluster size versus transverse incidence angle of the track using 2010 data and Monte Carlo samples with different G4 range cuts.

Bragg-peak modelling

The Bragg-peak modelling is a study of the energy deposition of secondaries produced by particles passing through the detector material. So far the energy loss profile used in the Pixel digitization is a uniform distribution and does not resemble the more realistic Bragg-peak shape as shown in figure 4.3. In the Pixel detector the secondary charged

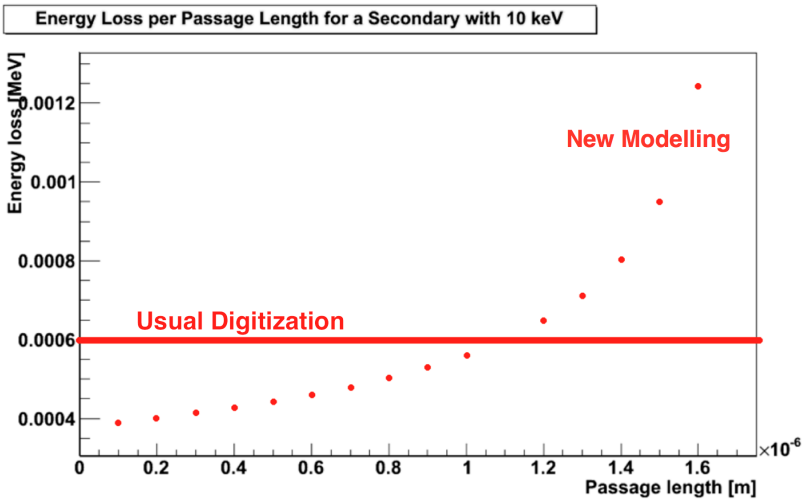


Figure 4.3: Shape of energy deposition of secondaries as it is implemented in usual digitization and the new Bragg-peak modelling.

particles mainly consist of low energy electrons ($< 0.1\,\text{MeV}$). The energy deposition of these electrons has two components: the collision stopping power and the radiative stopping power [86]. This results in an energy loss profile with the occurrence of a Bragg-peak at the end of the path. As shown in figure 4.4, the energy deposition increases exponentially for low energetic electrons below 1 MeV. Therefore, the energy loss of the electron peaks at the end of its passage length.

The Bragg-peak modelling was found to increase the number of clusters per event as shown in figure 4.5. A possible explanation is that the Bragg-peak modelling decreases the energy loss at the start of the path of the secondary as shown on figure 4.3. Therefore, it is more likely that the energy loss at the beginning of the path of the secondary is too small and stays below the threshold to trigger the Pixel detector to measure the signal pulse. In the Pixels where also the primary is present (at the origin of the path of the secondary), the probability of triggering a measurement is very high. If the secondary particle loses more energy at the end of its path, and the energy loss rises over the threshold, it can happen that it is recognised as a new separate cluster. Therefore, the Bragg-peak modelling can cause cluster breaking which may particularly affect large

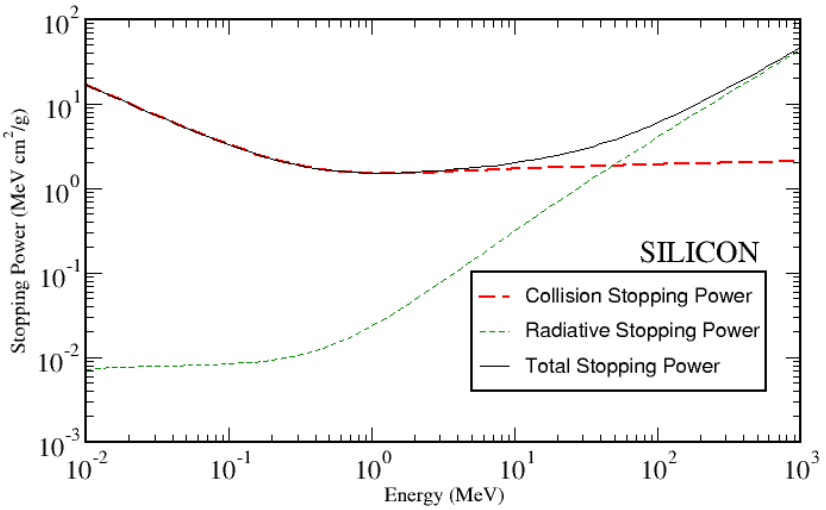


Figure 4.4: The energy deposition of electrons in silicon is shown as a function of the energy of the passing through electron for the total stopping power and its two components, the collision and radiative stopping power [87].

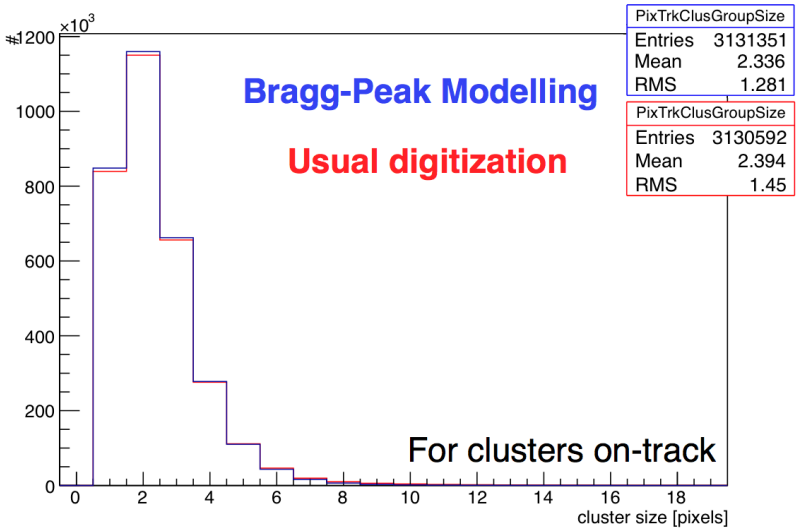


Figure 4.5: Cluster size of Monte Carlo 10 samples digitized with the flat profile and with Bragg-peak modelling.

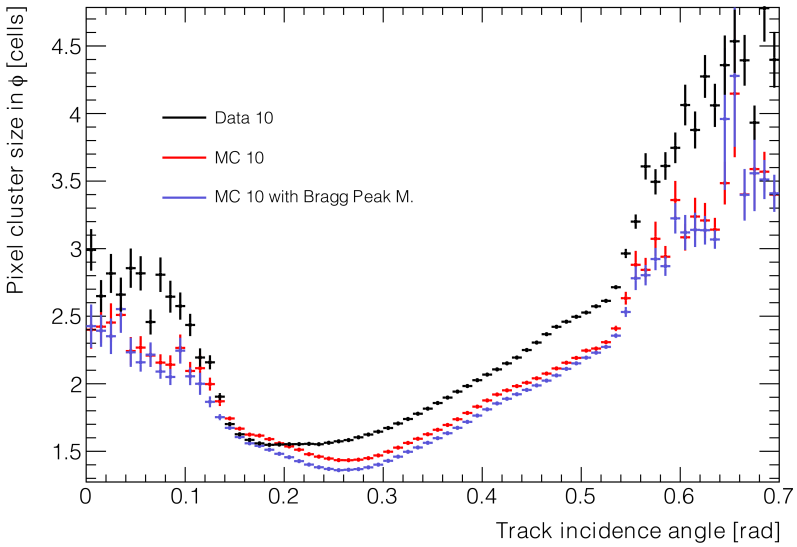


Figure 4.6: Average cluster size versus track incidence angle of data 10 and Monte Carlo 10 samples provided by default digitization and with the Bragg-peak modelling.

clusters. This decreases the average cluster size as illustrated in figure 4.5 from 2.39 to 2.34 cells. This is also shown in figure 4.6 with the dependence on the track incidence angle. The conclusion is that the Bragg-peak modelling unfortunately makes the MC data disagreement worse 4.5.

Fitting the Lorentz angle

Particles passing through the Pixel detector produce electron-hole pairs which drift in accordance with the Lorentz angle induced by the combination of the electric field due to the bias voltage and the magnetic field due to the ATLAS solenoid. As shown in figure 4.7, the particle incidence angle determines predominantly the cluster size produced. If the particle incidence angle corresponds to the Lorentz angle, the Lorentz Angle will keep the electron-hole pair in the direction of the incident particle. This results in a minimal cluster size for an incidence angle equal to the Lorentz angle shown in figure 4.6[1].

The function $F(\alpha)$ predicts the dependence of the average cluster size as a function of the incidence angle and is used to obtain the Lorentz angle, α_L:

$$F(\alpha) = \left[a \cdot (\tan\alpha - \tan\alpha_L) + \frac{b}{\sqrt{\cos\alpha}} \right] \oplus G(\alpha) \ , \tag{4.1}$$

[1]This is also one reason why the pixel barrel staves are tilted. They overlap with a tilt angle of $-20°$, i.e. 0.35 rad, relative to the radial axis [52].

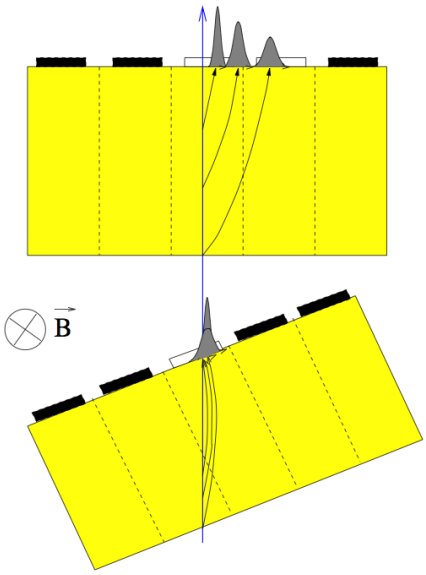


Figure 4.7: Drift of charge carriers in the magnetic and electric field for a particle passing perpendicularly through the detector (upper figure) and with an incidence angle equal to the Lorentz angle (lower figure) [88].

where a convolution with a Gaussian function, $G(\alpha)$, depending on the incidence angle α, is applied. The Gaussian smearing models the distribution of the cluster size for a fixed incidence angle defining the studied average cluster size [88]. The slope is fitted by the free parameter a and the minimal cluster size is described by the free parameter b. The term $\frac{b}{\sqrt{\cos\alpha}}$ accounts for the effect of diffusion on the cluster size and defines the minimal average cluster size which is not exactly one pixel due to diffusion. The term $a \cdot (\tan\alpha - \tan\alpha_L)$ represents the projection of the charge carriers onto the sensor surface.

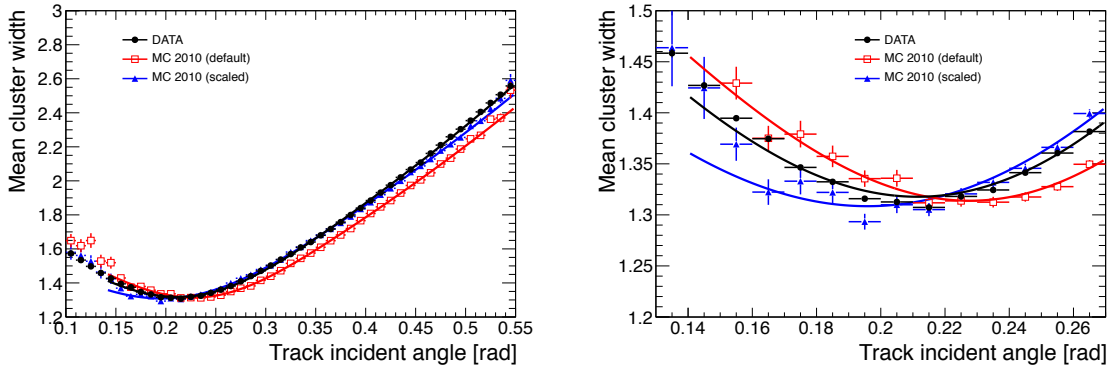
This function (4.1) is fitted to the Data10 and MC09 samples separately to obtain the Lorentz angle:

$$\alpha_L^{\text{Data}} = 0.2100 \pm 0.0004 \tag{4.2}$$

$$\alpha_L^{\text{MC}} = 0.233 \pm 0.001^{2}. \tag{4.3}$$

Both Lorenz angles are determined very precisely and vary from each other. The ratio of the two Lorentz angles, $r = \frac{0.210}{0.233}$, is applied as a scale factor to the MC sample during the digitization and reconstruction process. In figure 4.8 this scaled MC sample is plotted together with the original MC and data.

[2]These are the statistical errors determined by the fit.



(a) Full range of incidence angle fitted **(b)** Range zoomed close to minimum

Figure 4.8: The average cluster width as a function of the track incidence angle. The distribution is plotted for 2010 data, the default MC09 sample, and the improved MC09 sample with the scaled Lorentz angle.

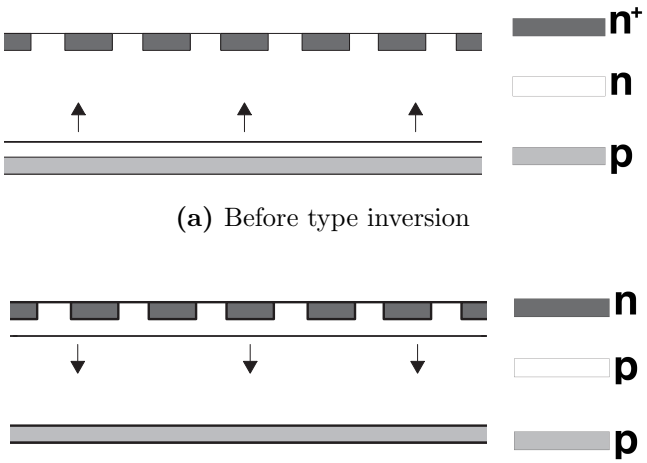
The minimum of the distribution of MC sample is shifted by the Lorentz angle scaling to smaller values. The minimum of the scaled MC and data agree well and the shift has improved the agreement of data and MC.

Changing the cross-talk

Further studies concentrated on the effect of the cross-talk, which describes the creation of new charges in the neighbouring sensors due to capacitive coupling and charge leakage from the main pixel to the neighbours caused by resistive coupling. The cross-talk is defined as the fraction of charge generated in the neighbouring pixels per contact length of the two neighbouring pixels.

To determine the cross-talk, a scan is performed where a signal is injected into a pixel, and the charge in the neighbouring pixels is measured. The Pixel sensor is produced with n^+ pixels within n substrate which is on the opposite side bordered by a p bias as shown in figure 4.9a. The pn junction is on the side of the non-segmented electrode and with increasing depletion voltage the depletion zone grows towards the pixels. If the silicon is not fully depleted the pixels are coupled and the cross talk is maximal. The depletion zone is increased by increasing the reversed-bias voltage. As soon as the reverse-bias voltage creates full depletion, the cross talk plummets. Therefore, the cross talk is used to determine the depletion voltage in the ATLAS Pixel detector [89].

In 2012 some type inversion of the Pixel detector was caused by radiation. The bulk changes from n to p doped, the pixels change from n^+ to n and the bias side stays p as shown in figure 4.9b. This results in a pn junction on the side of the pixels so they are



(a) Before type inversion

(b) After type inversion

Figure 4.9: The Pixel sensor design is shown before 4.9a and after 4.9b type inversion. The depletion zone grows from the bias side in an n^+np^+-type sensor as indicated by the arrows. After type inversion the bulk is p-doped and the depletion zone develops from the pixel side [90].

immediately decoupled and the cross talk can no further be used as a measure of the depletion voltage [64].

It is expected that the cross talk changes with time as the bias and the resistivity of the sensors will change due to radiation. The original cross-talk is $0.03\,\mathrm{mm}^{-1}$ and was determined from lab measurements at the time of the construction of the ATLAS detector. Figure 4.10 shows the impact of increasing the cross-talk by studying a set of cross-talk values. Therefore, due to the illustrated dependence, it was checked whether the cross-talk in the simulation is modelling the cross-talk observed in data well. From the latest cross-talk measurements performed *in-situ* it was recommended to update the cross-talk to $0.06\,\mathrm{mm}^{-1}$ which doubles the original cross-talk number.

The enhancement of the cross-talk increases the average cluster size which can be seen in the rϕ plane in figure 4.10. The contact length of pixels in rϕ is $400\,\mu\mathrm{m}$ [52]. The increase of the cross-talk in the digitization improves the agreement between the MC simulation and data. However, the doubling of the cross-talk with a new value of $0.06\,\mathrm{mm}^{-1}$ does not explain the full residual difference between data and MC. The main motivation for modifying the cross-talk value is to ensure it is more realistic given the *in-situ* measurements.

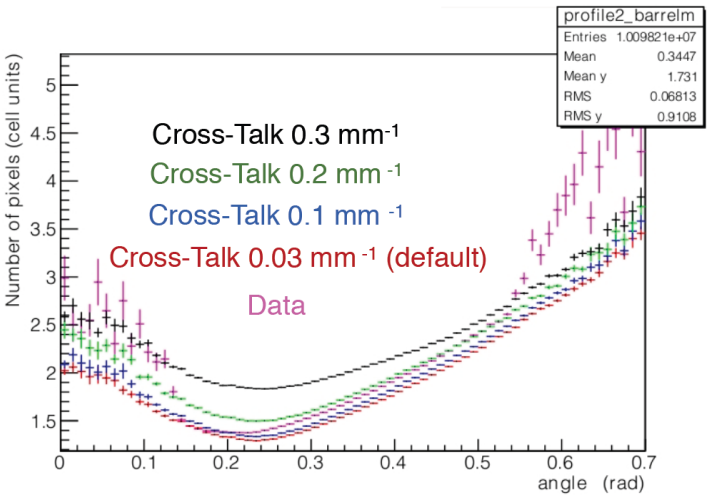


Figure 4.10: Average cluster size in ϕ is shown versus the track incidence angle in the $r\phi$ plane for data10 and Monte Carlo samples digitized with different cross-talk.

Improved cluster size modelling in the ATLAS software

The ATLAS software framework Athena was updated for the MC11 simulation campaign with the improvements resulting from these cluster size studies. The updates were submitted in form of tags[3] to include the new Lorentz Angle scaling by 0.9 and the doubling of the cross-talk ($0.06\,\mathrm{mm}^{-1}$) as the measurement of these two parameters indicated these modifications. Previously, to save CPU time, the cross-talk was only generated if the charge deposited by the primary particle exceeded three times the threshold. This threshold was removed so that the cross-talk is generated for all pixels hit. Pixels which need the cross-talk to pass the threshold to measure a signal are gained by removing the cut. This increases the average cluster size slightly as shown in figure 4.11.

In figure 4.12, the effect of the three changes (new value for cross-talk, Lorentz angle scaling, removal of threshold for cross-talk) is studied by running the digitization of the same MC10 sample each time with one of the improvements not applied. It is visible that the Lorentz angle scaling causes the largest increase of the average cluster size in comparison to the other changes studied. Comparing the average cluster size of data from 2010 with the simulation as demonstrated in figure 4.11 the agreement was dramatically improved.

[3]Three new tags were created with these changes and were first used for release 17.0.1: PixelDigitization-00-10-20, SiLorentzAngleSvc-00-00-30 and SiPropertiesSvc-00-00-06.

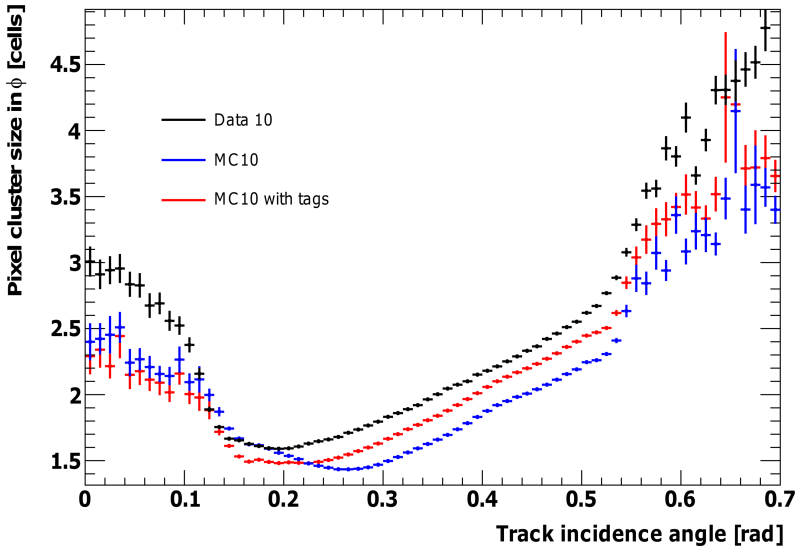


Figure 4.11: The average cluster size versus track incidence angle is shown with MC processed with and without new tags. The modelling of the average cluster size is clearly improved with the new value for the cross-talk, the Lorentz angle scaling and the removal of threshold for the cross-talk.

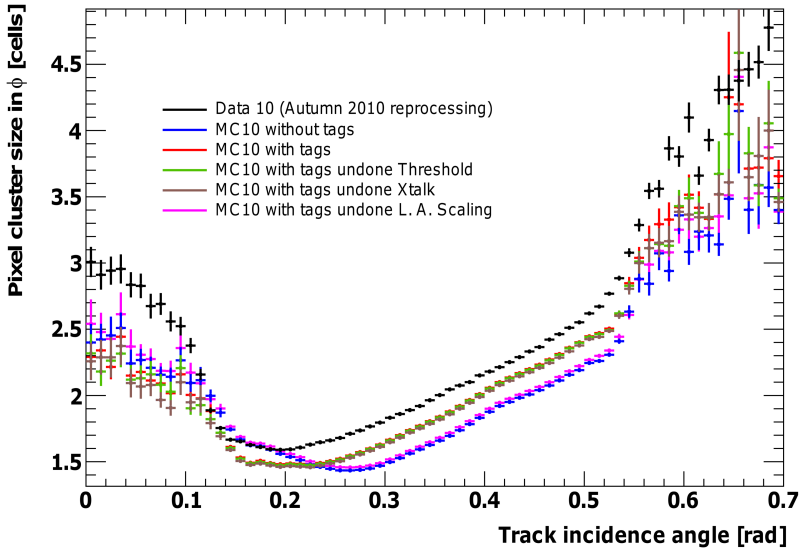
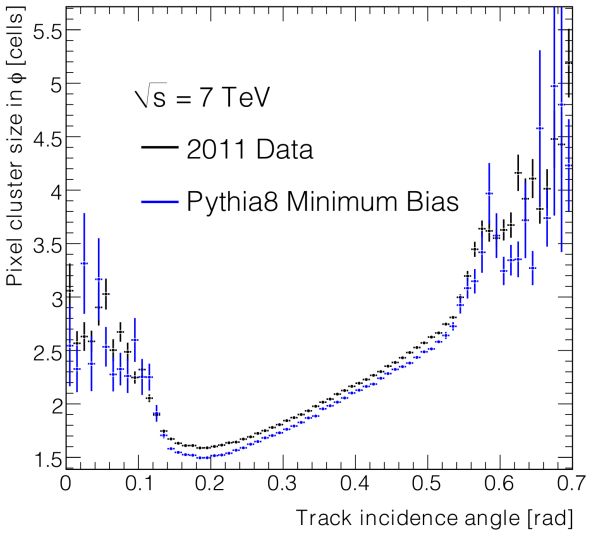


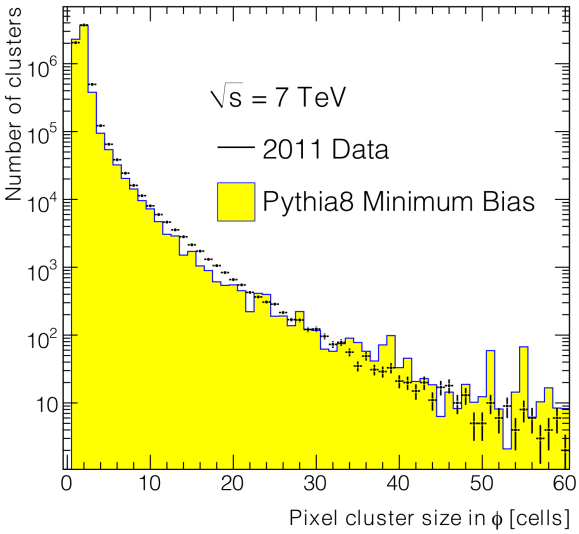
Figure 4.12: The average cluster size versus track incidence angle is shown with MC processed with each change of the new tags undone.

Validation plots with large samples

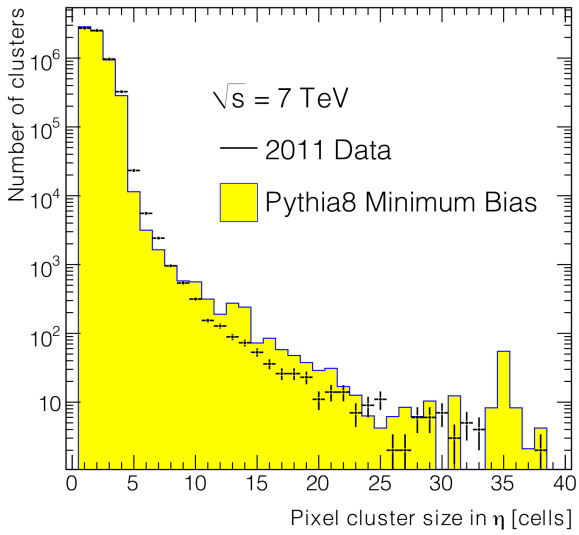
The following plots (figure 4.13) show the average cluster size in ϕ for clusters on track and their dependence on the track incidence angle. A data sample (sample 5) from 2011 with an integrated luminosity of $62.1\,\mathrm{pb}^{-1}$ is compared to the combined MC samples, sample 6 - sample 9, with the studied modifications applied.



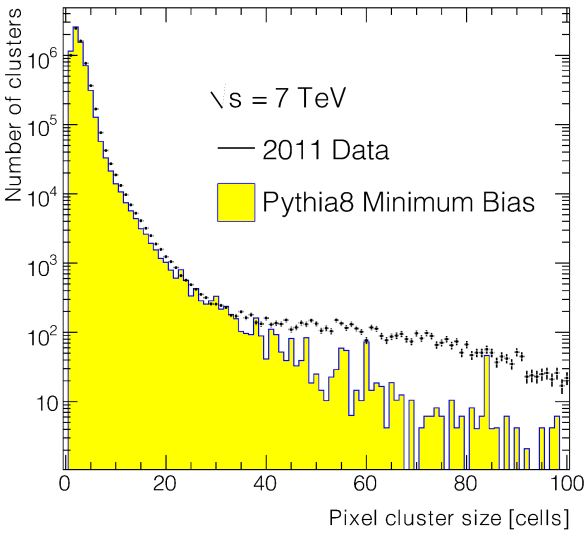
(a) Average cluster size versus track incidence angle in the $r\phi$ plane



(b) Average cluster size in Φ



(c) Average cluster size in η



(d) Overall average cluster size

Figure 4.13: Size of clusters on track for 2011 data and Pythia 8 MC simulation.

Figure 4.13a shows that clusters are wider in data than in simulation for all azimuthal incidence angle. The width distribution in ϕ (figure 4.13b), the width distribution in η (figure 4.13c) and the overall shape (figure 4.13d) are approximately reproduced by the simulation. MC is underestimating the average number of clusters with a large size of 10 and 20 cells projected in ϕ.

Figure 4.13c shows the η-projection of the average cluster size. The distribution is dominated by small cluster sizes up to 5 cells. The tail of this projection coming from secondaries is not well reproduced in the simulation. The differences in cluster widths in both projections propagate to the total cluster size modelling as illustrated in figure 4.13d. A clear difference in the tail shapes is observed for MC and data for very large clusters.

Conclusion

Several studies have been performed to investigate the difference of the average cluster size in data and MC. By applying a Lorentz angle scaling of 0.9, the minimum of the average cluster size depending on the track incidence angle of the simulation was shifted to now agree with the observed minimum in data. Besides the shift of the minimum, the overall simulated cluster size was increased by doubling the cross-talk and generating the cross-talk for every pixel. These changes are implemented in the simulation framework and are motivated by experimental observations showing a change of the Lorentz angle and the cross-talk over time. Further changes of the cross-talk and the Lorentz angle are expected, e.g., due to radiation damage. Therefore, the addition of these variables to the condition database is recommended. For this further studies to determine the development of the cross-talk and the Lorentz angle over time are required.

4.1.2 Occupancy in ID

Approximately 20.7 inelastic proton-proton interactions take place per crossing as an average for the 2012 data-taking period with a typical bunch spacing of 50 ns and a peak instantaneous luminosity of $7.73 \cdot 10^{33}\,\mathrm{cm}^{-2}\mathrm{s}^{-1}$ [49]. High pileup makes it important to monitor the occupancy, which is a measure of how many detector channels are occupied during a bunch crossing. A high occupancy in the inner detector can lead to loss of significant information for the reconstruction of particles as cluster merging complicates track separation.

The descriptions of quantities such as noise, particle multiplicities and the p_T spectrum in simulation can be cross checked by occupancy studies. In the following sections, the occupancy of the inner detector (subdivided into the Pixel detector, Semiconductor

Tracker and Transition Radiation Tracker) is compared between MC and data for different pileup levels. Analysis such as the H$\rightarrow ZZ^{(*)} \rightarrow 4\ell$ analysis use the MC predictions, for example to determine the momentum scale, motivating a high accuracy of the simulation modelling the ID performance.

Pileup

Pileup is the number of interactions per crossing, μ, and is particularly large at the start of a proton run with the peak value, μ^{peak}. The number of interactions per bunch crossing is distributed with a Poisson function. Pileup is defined as:

$$\mu = \frac{\mathrm{L} \times \sigma_{\text{inel}}}{n_{\text{bunch}} f_r}$$

where n_{bunch} is the number of bunches injected and f_r is the revolution frequency calculated as the frequency at which collisions of one bunch take place evaluated by the speed of light and the circumference of the collider. The mean over all bunch crossings of a dataset is denoted $\langle\mu\rangle$.

The luminosity, L, is measured with an uncertainty of 3.9% by forward detectors [91]. High pileup runs have an additional luminosity uncertainty of 1% because the luminosity is extrapolated from the measurements from lower intensity runs. The total inelastic cross-section, σ_{inel}, is the other variable governing the uncertainty on pileup. The value used for the pileup calculation in the event generator Pythia 6 and 8 is $\sigma_{\text{inel}} = 71.5\,\text{mb}$ [83]. The value measured by TOTEM is $\sigma_{\text{inel}} = 73.5 \pm 1.9\,\text{mb}$ [92], whereas with ATLAS a value of $\sigma_{\text{inel}} = 69.1 \pm 2.4(\text{exp.}) \pm 6.9(\text{extr.}^{4})\,\text{mb}$ is extrapolated using the cross-section measurement of events detected by scintillation counters located in the forward region at $z = \pm 3.56\,\text{m}$ [94]. These Minimum Bias Trigger Scintillator (MBTS) detectors consist of a total of 16 counters covering $2.09 < |\eta| < 3.84$ [93]. The difference between the measurements and the value used by Pythia 6 and 8 of about 3% is a systematic uncertainty affecting the comparisons of data and MC simulation in this section 4.1.2.

Samples

The samples used for this study are for MC Pythia 6 (sample 11) and Pythia 8 (sample 12) as given in table 4.2. As a data sample the special high pileup run 190728 from 10th October 2011 is used (sample 13). The dataset was recorded with only one bunch in each

[4] extr.=extrapolation uncertainty. Only a fraction of the inelastic cross-section is measured which is used to extrapolate to the full inelastic cross-section [93].

direction circulating in the LHC and has a $\mu^{peak} = 30$ and $\langle\mu\rangle = 26$. The full integrated luminosity used from the dataset is $\sim 482\,\mu\mathrm{b}^{-1}$.

Number	Sample name
sample 11	group.det-slhc.mc11_7TeV.105000.pythia_minbias_inelastic.recon.D3PD .e816_s1364_s1367_r2978
sample 12	group.det-slhc.mc11_7TeV.108351.Pythia 8_minbias_Inelastic.recon.D3PD .e816_s1364_s1367_r2979
sample 13	group.det-slhc.data11_7TeV.00190728.physics_MinBias.recon.ESD.f411
sample 14	data11_7TeV.00182726.physics_JetTauEtmiss.merge.DESD_CALJET .r2603_p659_p662

Table 4.2: Samples used for the occupancy studies are listed with their full names.

The MC samples were produced to match the data sample, so that the luminous size of the collision region and the luminosity profile of the data fill were modelled consistently. Limits of the comparison of MC and data are due to the uncertainty on the number of vertices which are managed to be reconstruct in the ID acceptance. This results in an uncertainty of about 10% on the pileup measured in data which has to be taken into account when comparing to simulations depending on the number of inelastic interactions.

Average occupancy

This study compares the average occupancy in different ID subdetector regions between Pythia 6, Pythia 8 and data. In figures 4.14, 4.15 and 4.16 all clusters are used, i.e. not only clusters which are associated to a track. The mean occupancy plotted for each detector segment is defined by

$$\text{Occupancy} = \frac{1}{\mathrm{N_{event}}} \cdot \sum_{i}^{N_{event}} \frac{\text{Number of pixels [strips] hit in a detector section}_i}{\text{Total number of pixels [strips] in a detector section}}, \quad (4.4)$$

where N_{event} is the number of events. The table 3.3 contains the number of pixels and strips in the studied detector sections. For each figure, 300 events are used from the corresponding sample. On the data sample the requirement of at least one actual interaction per crossing is applied to remove events recorded from empty trains.

Figure 4.14 shows the mean occupancy of detector regions in the SCT and Pixel detector. The SCT disks are subdivided into their rings for determining the occupancy

which are three rings for disk 1-5, two rings for disk 0, 6 and 7 and one ring for disk 8. This results in relatively scattered points at each z-position of the disks. The rings of the SCT disks consist of four different module types with an active length ranging from 52.48 mm to 126.09 mm created by the same number of strips. The SCT occupancy given as the ratio of occupied strips does not take into account the different strip types used for the SCT endcap. The occupancy values are therefore not evenly spaced for the SCT endcap. To obtain a more detailed dependence, the Pixel disks are subdivided into smaller structures: 144 points which consists of 8 chips in η, each with 18 columns of pixels. The error bars of the Pixel disk data points which are overlapping have a relative uncertainty in the occupancy measurement of about 10% due to the limited number of events of the available samples. Overall, the occupancy distribution has a strong radial dependence which is in particularly clear from the Pixel and SCT barrel layers. In each of the three Pixel and the four SCT barrel layers the occupancy is distributed evenly between the modules within the given uncertainties. In contrast, the occupancy in each end-cap ranges over about half an order of magnitude. The occupancy distribution is affected by two main principles: the distribution of the generated particles and the distribution of the cluster size.

The number of generated particles in the rapidity, $d\sigma/dy$, is constant, if the matrix element, $|M|^2$, is approximately constant in rapidity: $d\sigma = |M|^2 d\tau$ where the single

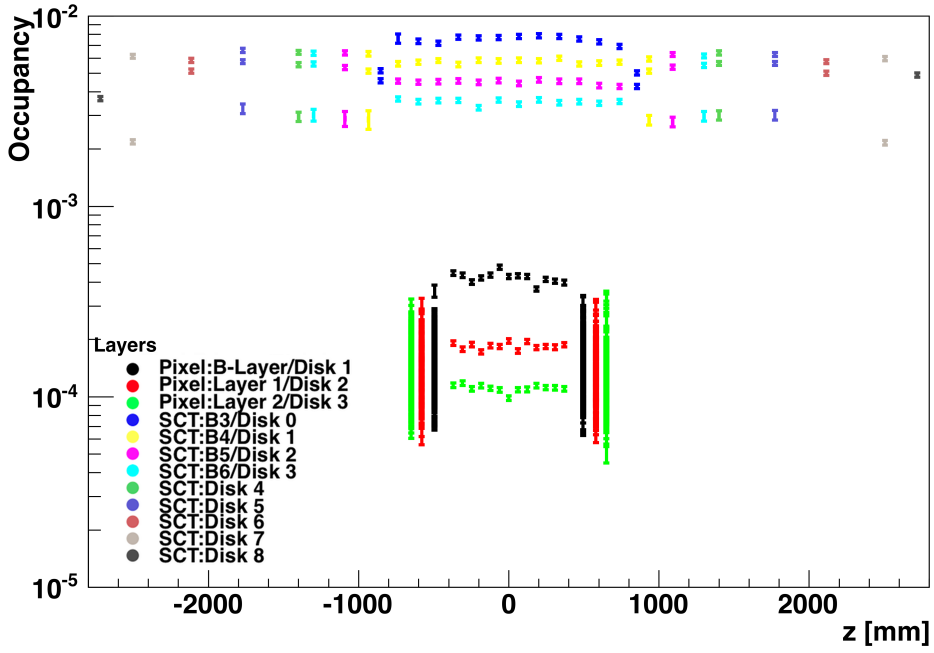


Figure 4.14: Distribution of the mean occupancy obtained from data is shown for different silicon detector sections of the current ATLAS detector.

particle relativistically invariant phase space is $d\tau = 1/2 dp_T^2 d\phi dy$ [95]. Experimentally, it is observed that the number of generated particles is flat in the region around $\eta \approx 0$ [61]. The inner detector lies well within the rapidity-plateau of $\eta = 0 \pm \Delta\eta$ with $\Delta\eta \sim 5$.

Taking into account the dependence of pseudorapidity and the z-coordinate, the number of clusters per module in the barrel layers is expected to be particularly large in the modules close to the interaction point (at small z values).

$$\eta = -\ln\left(\tan\left(\frac{\arctan\left(r/z\right)}{2}\right)\right) \tag{4.5}$$

Besides this dependence, the cluster size distribution has a large impact on the hit occupancy shown in figure 4.14. The magnetic force in the ID influences the cluster size in $r\phi$ but not in z direction. Therefore, the cluster size in z, depending on the position in z, is approximately

$$\frac{1}{\sin\left(\theta\right)} = \sqrt{1 + \left(\frac{z}{r}\right)^2} \tag{4.6}$$

according to the geometrical dependence, where r is the shortest distance between the beam axis and the track incidence point. The cluster size increases as a function of $|z|$ due to the larger track incidence angle θ.

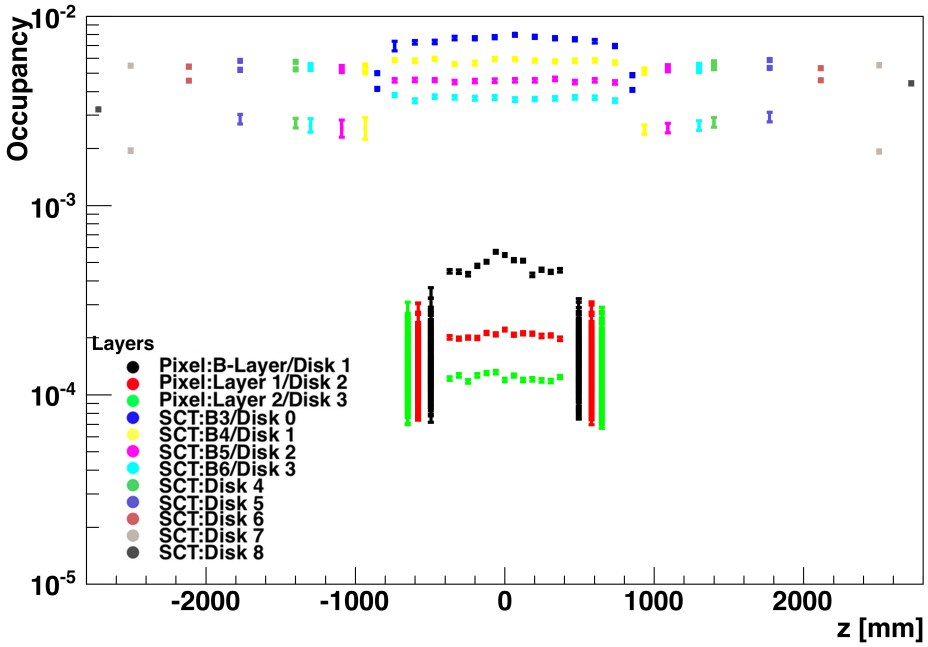


Figure 4.15: The mean occupancy is shown for different silicon detector sections of the current ATLAS detector modelled with Pythia 6.

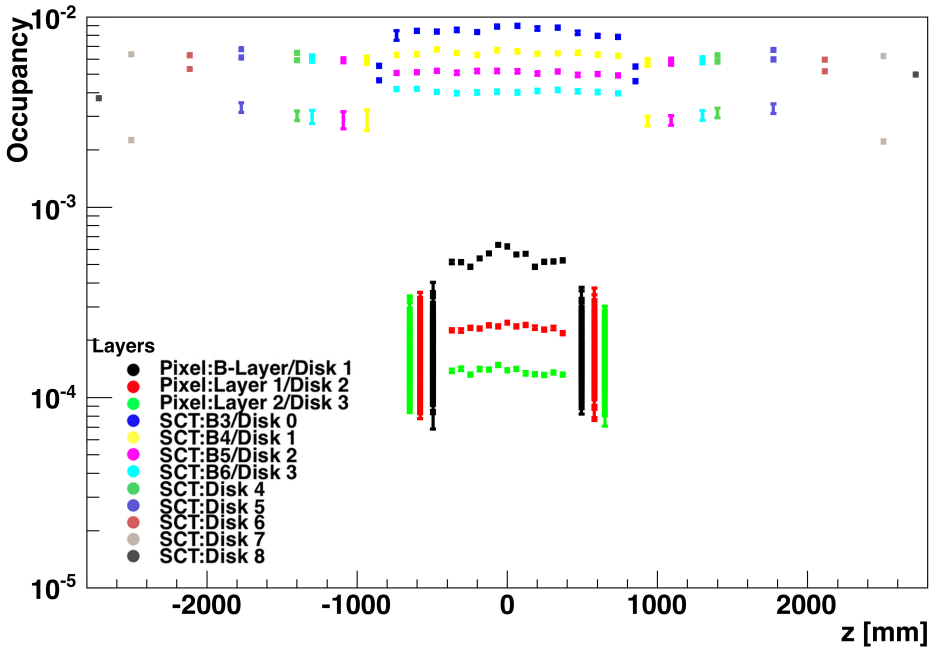


Figure 4.16: The mean occupancy modelled with Pythia 8 is shown for different silicon detector sections of the current ATLAS detector.

The two dependencies of the particle distribution (equation 4.5) and the cluster size (equation 4.6) combined are the main underlying theoretical concepts of the occupancy distribution and act as a counterbalance resulting in the approximately evenly distributed occupancy in the barrel layers of the Pixel and SCT detector.

The results from both Pythia 6 and Pythia 8 show similar occupancy distributions in the Pixel and SCT detector given in figures 4.15 and 4.16. The occupancy in the Pixel B-layer is approximately constant for all modules studying the data. For the Pythia 6 and Pythia 8 samples the occupancy increases in the middle of the Pixel B-layer. The statistical error on the Pixel B-layer occupancy is about 3% for the Pythia samples which is given by error bars in the figures 4.14 - 4.16. Due to the logarithmic y-axis spanning over three order of magnitudes, the bar appears very small as rectangles. There is an increased occupancy in the centre of the barrel which is observed for both Pythia 6 and 8 in the Pixel B-layer, which suggests the possibility that a systematic difference is underlying, for example the mean cluster size in η, which we know to be too small in MC, would be an interesting starting point for further studies. It can also be affected by too many low p_T tracks in simulation from Pythia 6 and 8 causing loopers which would peak here[5].

[5]The effect is also greater in Pythia 8 where we know to be too many low p_T tracks.

A selection of occupancy values is summarised in table 4.3. All occupancies in the table are given in per mill and the resolution uncertainty of the occupancy values are of the order of 5% due to the limited number of events of the available samples. Furthermore, a systematic uncertainty of 3% has to be taken into account given the total inelastic cross-sections used to determine the pileup of the MC samples as discussed in section 4.1.2. Due to the uncertainty of the reconstructible interactions within the ID as discussed in the same section 4.1.2, an uncertainty of 10% has to be additionally considered.

	Pixel B-Layer	Pixel Disk 1	SCT Barrel 3	SCT Disk 0
Data	0.43 ± 0.01	0.15 ± 0.01	7.55 ± 0.22	4.65 ± 0.12
MC Pythia 6	0.48 ± 0.01	0.16 ± 0.01	7.50 ± 0.17	4.53 ± 0.08
MC Pythia 8	0.54 ± 0.01	0.18 ± 0.01	8.43 ± 0.19	5.07 ± 0.10

Table 4.3: Summary of the mean occupancy in different detector regions of the Pixel and SCT detector for data, Pythia 6 and Pythia 8 shown in figures 4.14, 4.15 and 4.16. The mean occupancy is given in per mill.

In general the occupancy of Pythia 6 is smaller than for Pythia 8 comparing the last two rows of the table 4.3. Comparing the modelling of the Pythia generators to data, the accuracy of the modelling depends on the detector section. In the Pixel detector, Pythia 6 overestimates the occupancy about 10% as shown in yellow but models the occupancy in the SCT well highlighted in blue.

For Pythia 8 the occupancy is about 20% higher in the Pixels than in data with an example highlighted in orange in the table 4.3. Shown in green the occupancy in the SCT is about 10% overestimated by Pythia 8. In general, the occupancies simulated with Pythia 8 are a few per cent higher than the occupancies for the same pileup from Pythia 6.

Pile-up dependence of the occupancy

For high pileup, the vertex reconstruction efficiency decreases due to vertices which are so close to each other that they cannot be resolved. This can be seen in figure 4.17 showing the number of reconstructed vertices as a function of pileup. The dependence starts to deviate from the linear extrapolation at pileup of ~ 15. This efficiency drop is observed when applying the default track requirements in 2011. The track requirements are at least seven silicon hits and maximal two holes in the Pixel detector. Hits are

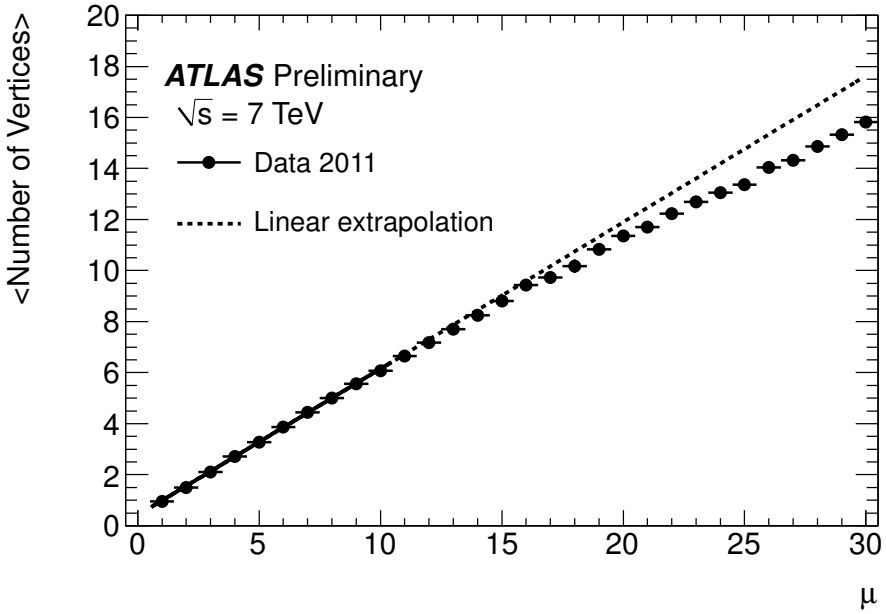


Figure 4.17: The mean number of reconstructed primary vertices shown as a function of the pileup for data taken in 2011 (consisting of three datasets with $\langle\mu\rangle = 15$, 29 and 32) using the default track requirements [96].

measured points associated to a track and holes are defined as missing points in the trajectory where measurements are expected. If a track passes through a dead module this does not count as a hole, but as a hit. More robust track requirements consist of at least nine silicon hits and zero holes in the Pixel detector resulting in approximately no track efficiency drop due to pileup in the range studied in figure 4.17. The overall vertex reconstruction efficiency decreases with the robust track requirements[6]. The vertex reconstruction efficiency drop versus pileup observed with the default tracking requirement is modelled in simulation, so that the number of reconstructed vertices is a good measure of the in-time pileup.

In these simulation samples only the in-time pileup was modelled[7]. Due to small bunch spacing, interactions from prior or subsequent bunch crossings can be read out if the read-out window is large enough. This effect is referred to as out-of-time pileup. With the typical bunch spacing of 50 ns in 2012 data-taking, the measurements of the silicon detectors with a short deadtime were not significantly affected by the out-of-time pileup. The Pixel and SCT have a readout window of 25 ns with an excellent time resolution. The readout window of the TRT is 75 ns as the maximum drift time of charge carriers

[6]The vertex reconstruction efficiency with robust track requirements is 5% smaller at low pileup ($\mu \sim 5$) and 1% higher at high pileup ($\mu \sim 40$) than the efficiency with default track requirements [96].
[7]Intense work takes place to implement the modelling of the out-of-time pileup.

to the straw cathodes can be up to 50 ns [61]. Additional time to allow for electronic shaping is needed and the readout window has to be in units of 25 ns to measure the complete response of a bunch crossing. Dedicated studies presented in reference [96] have shown that an occupancy increase by 3% is expected at 50 ns bunch spacing for the TRT due to out-of-time pileup. In general the out-of-time pileup has a much smaller impact than the in-time pileup and the number of reconstructed vertices describes the in-time pileup well. As the used data sample defined in 4.1.2 is from a special dedicated high pileup run with only one bunch, out-of-time pileup has no effect on these results. Therefore, the comparison of the data sample to the simulation sample containing only in-time pileup is performed.

A cut on the primary vertices requires at least three tracks attached to each reconstructed vertex to avoid fake vertices. In figure 4.18 the occupancy for the different subdetectors is shown for data and MC Pythia 8 using all clusters.

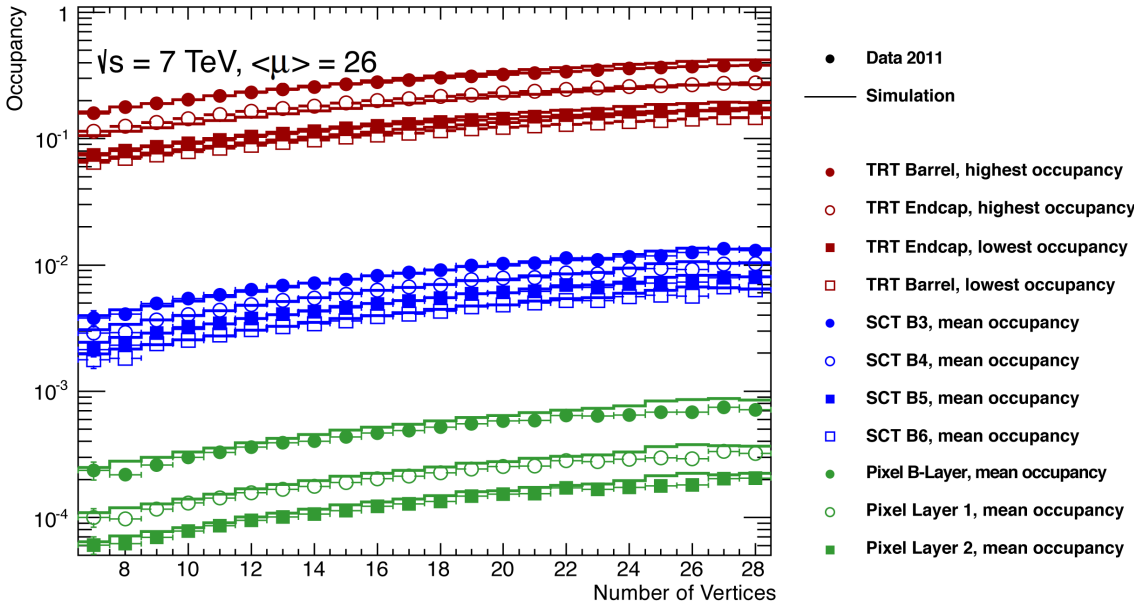


Figure 4.18: The occupancy in the inner detector is shown separately for the Pixel, SCT and TRT using all clusters. The dependence on the number of reconstructed vertices is displayed for the data taken during a high-pileup run in 2011 with $\langle\mu\rangle = 26$ (solid markers) and MC Pythia 8 simulation samples (line). The mean occupancy of each barrel layer is shown for the Pixel and SCT. For the TRT, the average over the three straws with the highest and the lowest occupancy is determined indicating the occupancy range observed.

Figure 4.18 shows the dependence of the occupancy in the ID on the number of reconstructed vertices. In the Pixel detector the simulation slightly overestimates the

occupancy in all barrel layers. The occupancy in the SCT is modelled very well. The TRT simulation slightly underestimates the occupancy when there is low number of vertices (< 20) whereas at a higher number of vertices ($\gtrsim 20$) the occupancy is overestimated. In the TRT the occupancy reaches up to 40% during a run with a mean pileup of 26. The high occupancy of the TRT results in less precision measurements at high pileup. This decreases the observed resolution of the successful track reconstruction.

The dependence of the occupancy and the number of pileup interactions was also studied for the technical design report of the Insertable B-layer [97]. This was studied using MC simulation samples for the current silicon detectors which will be facilitated by the Insertable B-layer currently being installed. As shown in figure 4.19 the occupancy in the Pixel detector reaches up to 0.02% for the Pixel and 2% for the SCT at a pileup of 50 consistent with the expectation from the recent studies presented.

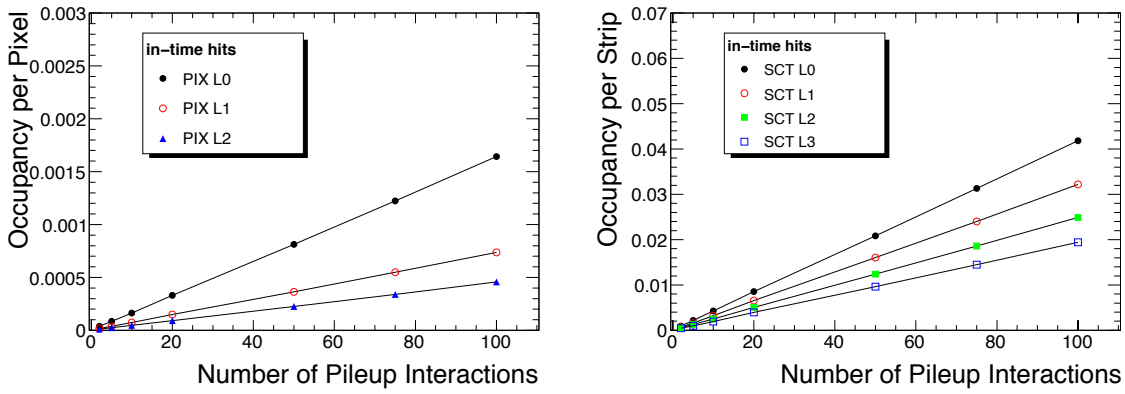


Figure 4.19: The occupancy simulated for the technical design report of the Insertable B-layer is shown depending on the pileup in the three Pixel barrel layers (left) and the four SCT barrel layers (right) of the current detector. The pileup conditions of up to hundred interactions are expected after inserting the Insertable B-layer [97].

Pileup is a large challenge in the data-taking, particularly in 2012 affecting the performance. The occupancy studies show a strong dependence on pileup, but also demonstrate that this dependence is modelled by simulation. A saturation of the inner detector due to occupancy has not been observed for the pileup range of the data taken.

4.1.3 Occupancy in Jets

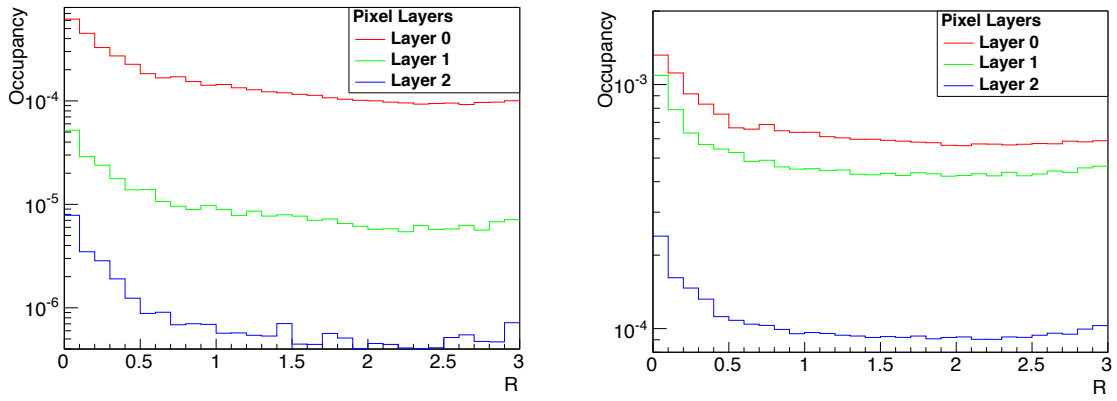
Jets are a common phenomena in hadronic colliders and need to be well reconstructed. Since they produce dense cones of particles the occupancy is expected to be significantly higher in jets. The occupancy is studied as the distance from the jet axis for the Pixel

detector. The distance R is defined by

$$R = \sqrt{(\eta_{\text{Jet axis}} - \eta_{\text{Cluster position}})^2 + (\phi_{\text{Jet axis}} - \phi_{\text{Cluster position}})^2}$$

A data sample (sample 14) from 2011 is used with $\mu \approx 8$ as given in table 4.2.

Very high p_T jets with $p_T > 280\,\text{GeV}$ are studied for the three layers of the Pixel barrel providing 3971 jets from 2415 events using a JetTauEtmiss stream. The full integrated luminosity used from the dataset is $6504\,\text{nb}^{-1}$. These high p_T jets are also called boosted jets as the particles in the jet cone are boosted with respect to the laboratory frame. The number of pixels hit as a function of the distance R from the jet axis is determined for all clusters and for clusters on track at different cylinder radii corresponding to the three Pixel barrel layers. Additionally, the total number of pixels available at different distances from the jet axis are calculated. The R-dependence of the number of hit pixels is divided by the R-dependence of the number of available pixel. Hence, the occupancy in jets is obtained as a function of R for clusters on track and all clusters, shown in figure 4.20.



(a) Clusters on track **(b)** All clusters

Figure 4.20: Occupancy in boosted jets ($p_T > 280\,\text{GeV}$) as a function of the distance R from the jet axis is shown for the three Pixel barrel layers for a selection of events using the run 182726 of the 2011 data taking.

An order of magnitude difference between the occupancy close to the centre of high p_T jets ($>280\,\text{GeV}$) and further away at R$>$ 1 is observed. The occupancy increase in the centre of jets is caused by the small track separation. The shape of the occupancy dependence for clusters on and off track is similar. The occupancy of clusters on track is of the order of a percent of the occupancy observed of all clusters.

4.1.4 Track Separation in Jets

In a densely populated track environment (e.g. a jet) shared clusters are a common feature. Figure 4.21 shows the minimal spatial separation between the closest charged particles in the innermost pixel layers as found in simulated dijet events. Pythia 6 evgen samples at $\sqrt{s} = 7\,\text{TeV}$ (samples 15a−15i) are used which have different jet p_T slices (different p_T of leading jets) as shown in table 4.4.

Number	p_T range [GeV]	Sample name
sample 15a	$8 - 17$	mc11_7TeV.105009.J0_pythia_jetjet.evgen.EVNT.e815
sample 15b	$17 - 35$	mc11_7TeV.105009.J1_pythia_jetjet.evgen.EVNT.e815
sample 15c	$35 - 70$	mc11_7TeV.105009.J2_pythia_jetjet.evgen.EVNT.e815
sample 15d	$70 - 140$	mc11_7TeV.105009.J3_pythia_jetjet.evgen.EVNT.e815
sample 15e	$140 - 280$	mc11_7TeV.105009.J4_pythia_jetjet.evgen.EVNT.e815
sample 15f	$280 - 560$	mc11_7TeV.105009.J5_pythia_jetjet.evgen.EVNT.e815
sample 15g	$560 - 1120$	mc11_7TeV.105009.J6_pythia_jetjet.evgen.EVNT.e815
sample 15h	$1120 - 2240$	mc11_7TeV.105009.J7_pythia_jetjet.evgen.EVNT.e815
sample 15i	> 2240	mc11_7TeV.105009.J8_pythia_jetjet.evgen.EVNT.e815

Table 4.4: Samples used for the track separation studies in jets are listed with their full names.

The mean minimal separation in the $r\phi$ [z] plane is shown in blue [green]. It is required that the minimal separation in the orthogonal direction z [$r\phi$] is less than 400 μm [50 μm]. This is the size of the ATLAS pixels. The binning in jet p_T is non-uniform to insure similar number of entries per bin to avoid statistical fluctuations due to the different jet p_T slices.

This study describes the track separation on a generator level and does not include the detector response e.g. modelling of cluster size which increases strongly in detector regions at $z \gg 0$. Therefore, the results are valid for the jet separation at $z \sim 0$. This study does not apply a cluster algorithm and splitting with which the reconstruction of tracks in jets can be improved.

Figure 4.21 shows that in the innermost Pixel layer the tracks of high p_T jets become very close to each others as they often lie within one pixel.

This study has also been performed for the second and third pixel layers. The distribution of the minimal separation in $r\phi$ and z is very asymmetric around the average separation for each jet p_T slice with a long tail to minimal separations of up to the order of millimetres. Therefore, the mean of this distribution is biased by a long tail towards

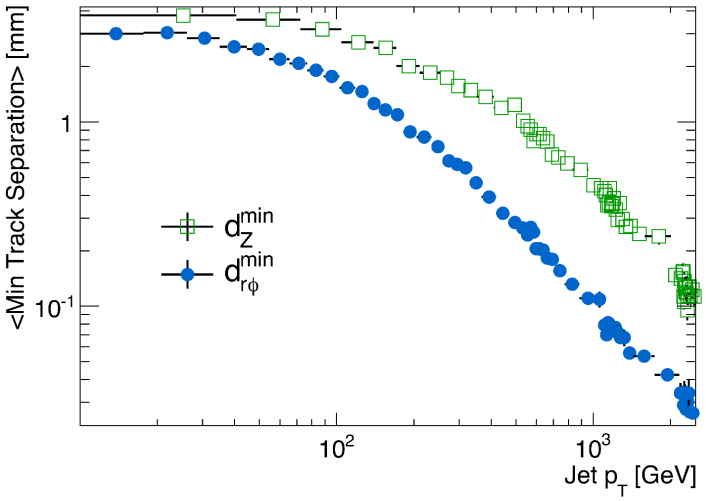


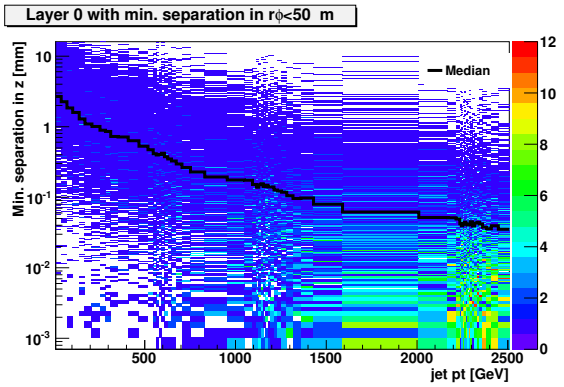
Figure 4.21: Simulated mean minimum separation between two charged particles in a jet for the innermost layer of the current ATLAS pixel barrel ($|\eta|$<2.77 with 50 µm × 400 µm pixels) in simulated dijet events. The mean minimum particle separation in z, d_Z^{min}, is shown after requiring the separation in $r\phi$<50 µm. The mean minimum particle separation in $r\phi$, $d_{r\phi}^{min}$, is shown after requiring the separation in z<400 µm.

larger particle separation. The median is used instead in figure 4.22 as it is closer to the frequently obtained values of the minimal track separations. The median is applied to determine the critical jet p_T dependence for layer 0,1 and 2.

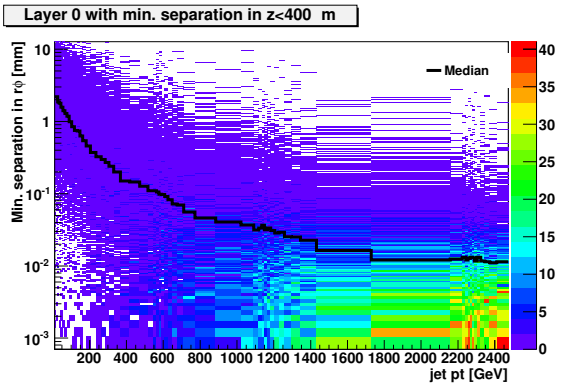
	Critical jet p_T value with mean min. sep. in z =400 μm & requiring min. sep. in $r\phi$ <50 μm	Critical jet p_T value with mean min. sep. in $r\phi$ =50 μm & requiring min. sep. in z <400 μm &
B-layer	1.1[0.6] TeV	1.4[0.7] TeV
Layer 1	2.0[0.9] TeV	>2.5[1.4] TeV
Layer 2	>2.5[1.4] TeV	>2.5[1.8] TeV

Table 4.5: Summary of critical jet p_T values for a mean [median] calculation of the minimal separation in $r\phi$ and z.

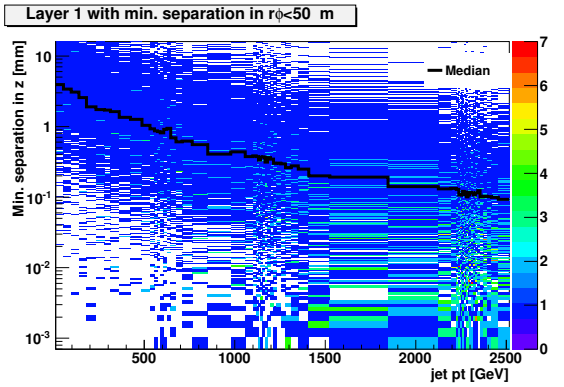
The results are summarised for the whole Pixel barrel in table 4.5. Due to the long tails they are sensitive to the choice of performing the studies with either a mean or median. The critical jet p_T value is defined as the jet p_T value at which the median or mean minimal separation is equal to the pixel size. This is the p_T value at which the reconstruction of the closest tracks becomes challenging. The critical jet p_T value for the mean minimal separation in the B-layer is 0.6/0.7 TeV. At $\sqrt{s} = 14$ TeV the cross-section



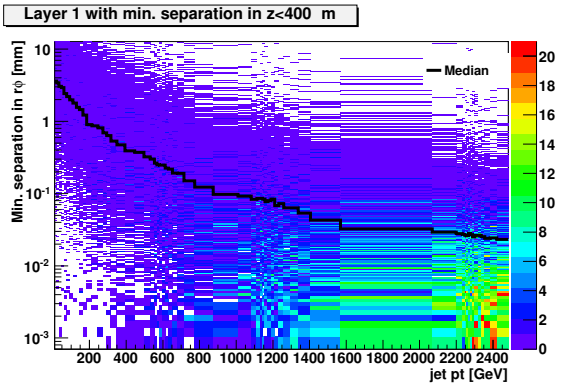
(a) Min. separation in $r\phi$ of Pixel layer 0



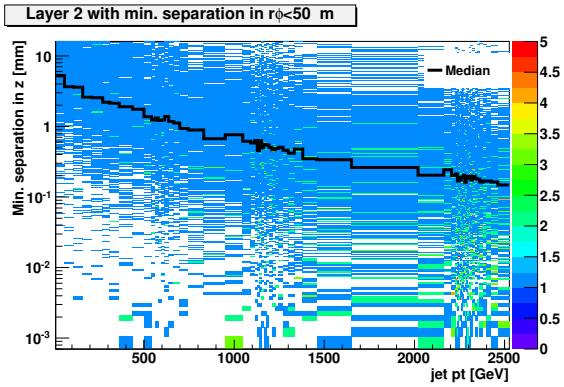
(b) Min. separation in z of Pixel layer 0



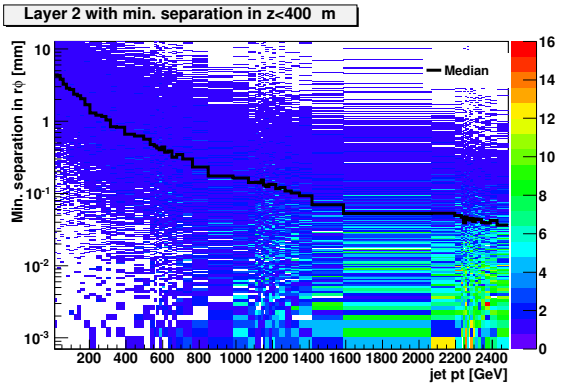
(c) Min. separation in $r\phi$ of Pixel layer 1



(d) Min. separation in z of Pixel layer 1



(e) Min. separation in $r\phi$ of Pixel layer 2



(f) Min. separation in z of Pixel layer 2

Figure 4.22: Distribution of the minimal track separation in jets as a function of the jet p_T where the number of entries is shown with a colour code. The median for each column is displayed with black data points. The results are obtained for the current three Pixel barrel layers with radius 50.5 mm, 88.5 mm and 122.5 mm using simulation.

of jets with a transverse energy of 0.7 TeV is 0.1 nb [23]. Due to the relatively high cross section it is important that the IBL has finer granularity and also that the reconstruction can split merged clusters.

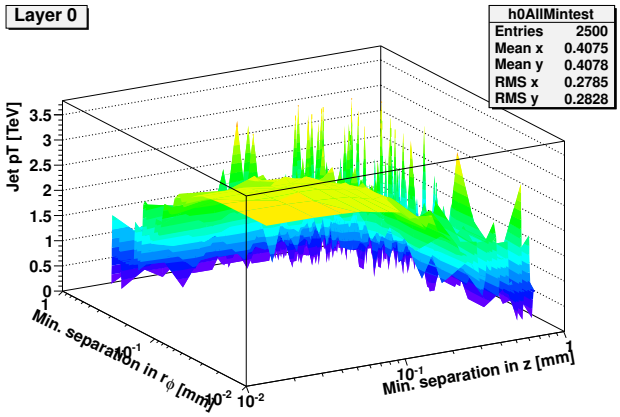


Figure 4.23: 3D approach showing the dependence of the track separation on the position in a jet cone.

A 3D approach is applied in figure 4.23 showing the mean jet p_T as a function of the minimum separation in z and rϕ. The studies show the particle separation in the centre of high p_T jets is often smaller than the minimum pixel size ($50\,\mu\text{m} \times 400\,\mu\text{m}$). This results in merged clusters produced by nearby particles in high p_T jets. The cluster algorithms to disentangle these particle tracks can be optimised by applying a Neural Network (NN).

The aim of the Neural Network (NN) application to the cluster reconstruction is to identify merged clusters produced by nearby particles and split them. Additionally, it is targeted to determine more precisely their positions by using detailed cluster shape information.

Neural network implementation of a cluster algorithm

A NN has the ability to solve pattern recognition problems and handle input variables with non-linear correlations. The inputs are weighted differently in the hidden layers of the NN to determine the output. The properties of the NN help meet the requirements of the cluster reconstruction, which has to deal with many cluster properties which do not by themselves give the position of the particle, but only a specific quantity of the measurement (e.g. the charge deposited in a single pixel). By combining the cluster properties and putting them in context (e.g. knowing the charges of the adjacent pixels) the particle position can be determined better. The following inputs are used by the NN:

- A matrix of 7×7 pixels containing the deposited charges around the original cluster. The cluster is centred in the matrix by using the charge weights determined by their ToT.
- A vector containing information of the longitudinal size of the pixel. It distinguishes between pixels with a standard length of 400 µm and long pixels of 600 µm.
- The estimated angle of incidence of the track with respect to the pixel sensor.

Different NNs are used to determine the particle multiplicity, the particle position and the errors on the particle position. All the NNs use the same inputs specified above. In the first case the NN algorithm outputs are trained to provide an estimate of the probability of the number of charged particles passing through each cluster. In the other cases, the NN outputs provide an estimate of the cluster positions and their associated uncertainties, as determined in two dimensions (rϕ and z). An example of a merged cluster and outputs of the NN algorithm are shown in figure 4.24.
The NNs were trained using simulated mixed samples of $t\bar{t}$ and high p_T dijet events (140 GeV < jet p_T < 560 GeV).

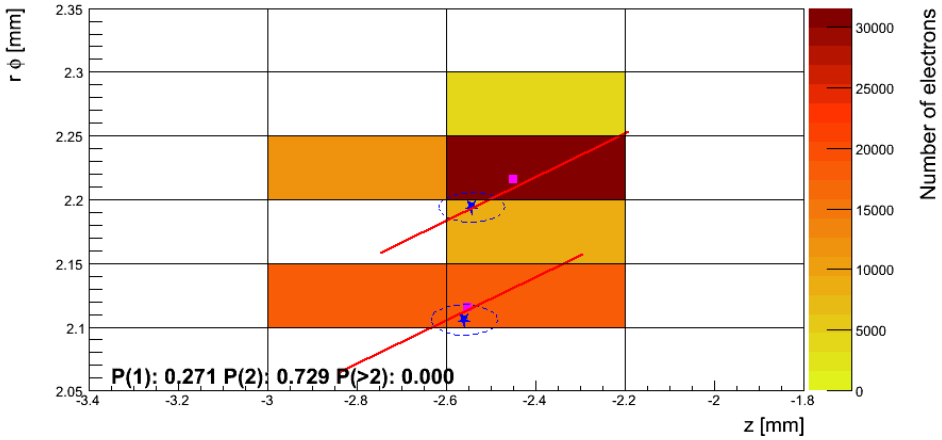


Figure 4.24: A cluster shown with charges deposited in each pixel represented by the colour scale and with the particle's true positions (pink marker) and their true directions (red line). Additionally, the NN probabilities for the particle multiplicity (lower left corner) and the estimated positions (blue marker) and their uncertainty (blue dotted line) are displayed [98].

The NN algorithm demonstrates its best potential in the innermost pixel layer because the two-particle separation is very small there. Furthermore, for high p_T tracks, the intrinsic detector resolution is critical and it can be improved by the NN algorithm. The number of tracks with p_T>100 GeV, and more than one shared cluster, can be reduced by an order of magnitude in the innermost pixel layer by the NN algorithm. The most evident improvement on the cluster residual, defined as the difference between the cluster

position and the extrapolated track position, is seen for clusters with a transverse size of 4 pixels, shown in figure 4.25. These clusters are mainly produced by the emission of delta rays. Due to the non-linear treatment, the NN algorithm can deal significantly

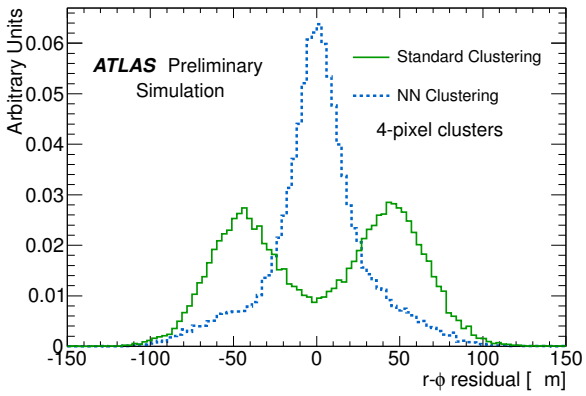


Figure 4.25: The cluster residual in the rϕ-direction for 4-pixel clusters reconstructed with the standard algorithm and the NN clustering algorithm for $t\bar{t}$ events [98].

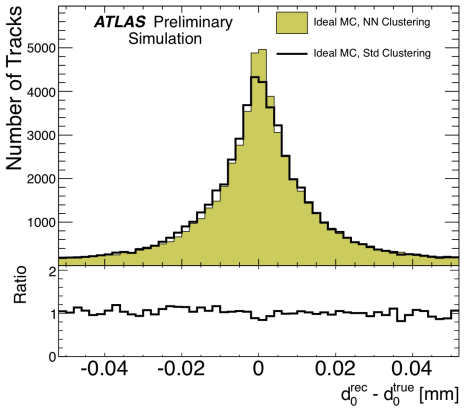


Figure 4.26: Simulated transverse impact parameter resolution with and without NN-based clustering for tracks with p_T>100 GeV for $t\bar{t}$ events [98].

better with the merged clusters: the double-peak vanishes and, in addition, the width of the cluster residual distribution is reduced, demonstrating an improved resolution. An overall improvement of the cluster resolution is also seen for other cluster sizes.

The improved cluster position resolution has a direct consequence on the transverse impact parameter resolution, which is improved by $\sim$15 % for tracks with high p_T, as shown in figure 4.26. The longitudinal impact parameter shows a similar improvement. This also results in an improved primary and secondary vertex resolution especially relevant for heavy flavour tagging.

The improvements coming from the NN reconstruction will be even more important when reaching the design luminosity of the LHC, and in future upgrades, because of the higher particle density and the greater emphasis on high p_T jets. During the current shutdown, the ATLAS Pixel detector will be upgraded with the insertion of a new layer closer to the interaction point (R=33.25 mm) [97], decreasing further the average track separation. In this extremely dense environment the improved two particle separation power of the NN algorithm will boost the detector capability extending the physics potential of the ATLAS experiment.

4.2 Future inner tracker

For the High Luminosity LHC scheduled to start in 2024 an instantaneous luminosity of $5 \times 10^{34}\,\mathrm{cm}^{-2}\mathrm{s}^{-1}$ is expected. As the LHC delivers higher luminosity, ATLAS Pixels must cope with larger radiation damage and keep a satisfactory hit efficiency. Furthermore, they have to stay with a high tracking efficiency even when many charged particles pass through the detector. For the upgrades of the ATLAS detector, advantage will also be taken of the new sensor technology developments since the ATLAS construction.

The dose of the ionizing radiation in the detector material will increase and will cause more noise. The ionized material can make the detector dangerously radioactive, for example, much installed copper can turn into cobalt-60. In this case it loses two of its protons and becomes a radioactive isotope with a half life of 5.27 years [99]. The Pixel detector is built to handle a fluence[8] of $10^{15}\,\mathrm{n_{eq}cm}^{-2}$ and a radiation dose of 500 kGy [100]. With the delivered $28\,\mathrm{fb}^{-1}$ the fluence in the innermost Pixel layer is $7 \times 10^{13}\,\mathrm{n_{eq}cm}^{-2}$ corresponding to about two times the amount needed to cause type inversion [101].

4.2.1 Inner Detector Upgrade: outline

Currently the regular data-taking at the LHC is paused. For safety reasons the magnets are being modified to reach the 14 TeV design energy after the current shutdown. A beam pipe closer to the interaction point with an inner radius of 25 mm[9] will be installed to give space for a new innermost Insertable B-Layer (IBL) with a radius of 33.25 mm (distance to the centre-of-mass of the sensors) [97]. Besides this, the machine development and other actions of the first long shutdown, LS1, are being completed in 2013 and 2014. Beyond the current shutdown, upgrades are also scheduled for later[10] where a replacement of the whole inner detector is planned [37]. The data-taking period after the planned shutdown around 2017 is called phase I and after 2021 it is denoted as phase II. The damage of the LHC magnets in 2008 showed that plans have to be adjusted given the complexity of the machine extending the frontiers of research. All the more, it is of great importance to study the possible conditions and conclude different upgrade opportunities.

A suggested layout for the inner detector is the Utopia layout shown in figure 4.27 [102]. It consists of only silicon detectors and does not include a TRT-like component. In

[8] 1 MeV neutron equivalent per square centimetre

[9] The current beam pipe has an inner radius of 29 mm.

[10] Two further long shutdowns are planned to start in 2017 and 2021. The exact years and the following specifications for possible upgrades have to be taken with care since they are still under investigation as the upgrade depends on the performance and development of the current detector.

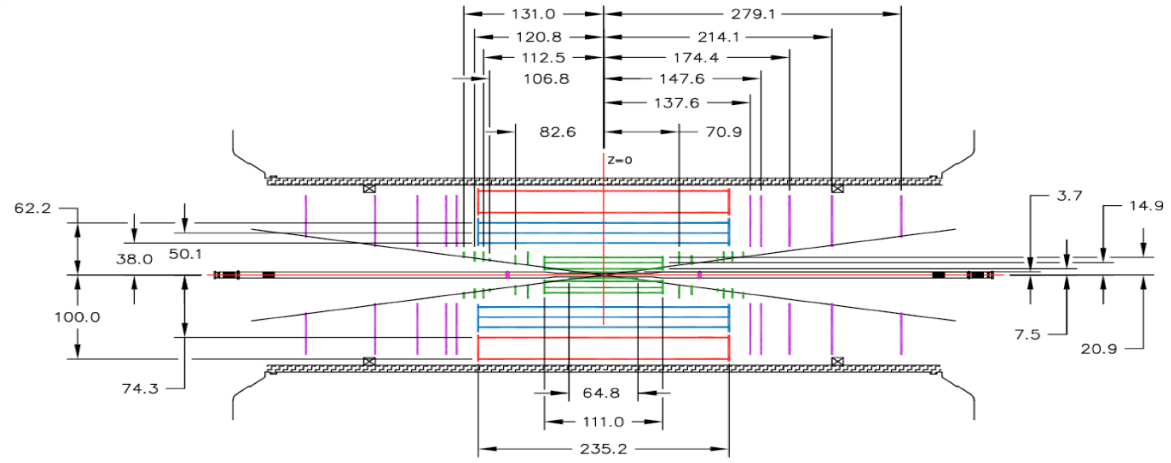
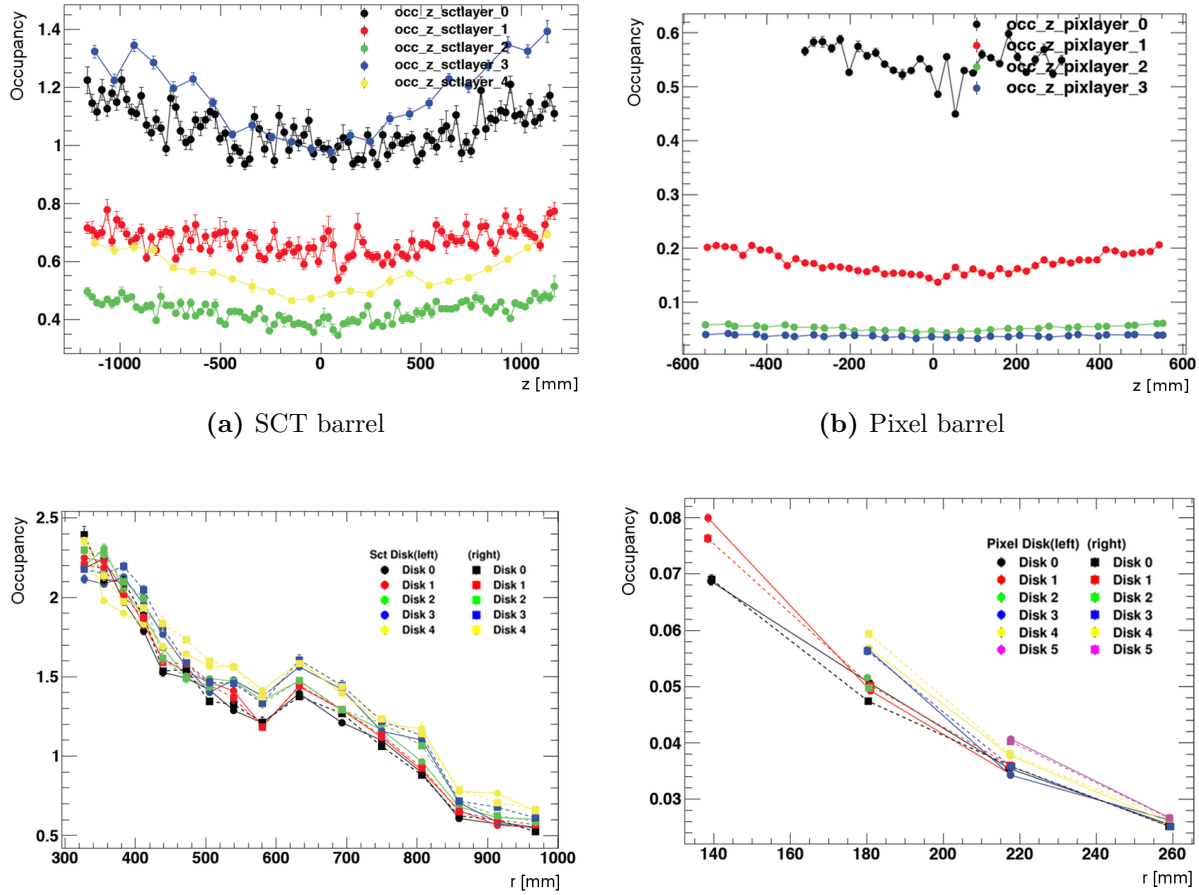


Figure 4.27: Projection in r-z of the ATLAS inner detector Utopia design given in cm. The Pixel detector is shown in green, the short strips in blue, the long strips in red and the micro-strip disks in purple. [102].

the barrel, the innermost detector components are 4 pixel layers with a granularity of $50\,\mu\text{m} \times 400\,\mu\text{m}$, followed by 3 short silicon strip and then 2 long silicon strip layers. These micro-strip layers have a size of $80\,\mu\text{m} \times 24000\,\mu\text{m}$ and $80\,\mu\text{m} \times 96000\,\mu\text{m}$ respectively.

For the IBL the new beam pipe implemented has an internal radius of 25 mm, but for phase II the size of the beam pipe will be increased with an expected minimal radius of 29 mm [103]. For phase II the closest pixel layer can be implemented at an active radius of about 37 mm. The maximal outer radius of the inner detector is restricted by the solenoid cryostat wall at $r = 1153\,\text{mm}$. An additional requirement is the replaceability of the innermost layers due to radiation. The expected replacement of 1-2 layers, must be possible with the arrangement of the disks. The position of the disks is constrained to $z \sim 2900\,\text{mm}$ to stay within the gas and thermal enclosure. The financial aspect has to be taken into account especially when planning the arrangement of the Pixel detector as it is a costly device. The large cost restricts the possible area of Pixelated silicon. This limits the maximal radius and number of Pixel barrel layers. An important criterion for the layout design is an equal spacing of position measurements for an acceptance as large as possible [102]. The occupancy distribution of the Utopia layout is shown in figure 4.28 for the different detector sections. The Pythia 8 sample used (sample 16) as given in table 4.6 is simulated with 200 in-time pileup interactions and the occupancy is given in percent in figure 4.28.

The three innermost SCT barrel layers consist of short strips with four times the number of strips per module as the two outermost barrel layers with long strips. This increases the occupancy of the two outermost layers drastically as shown by the high



(a) SCT barrel

(b) Pixel barrel

(c) SCT disks

(d) Pixel disks

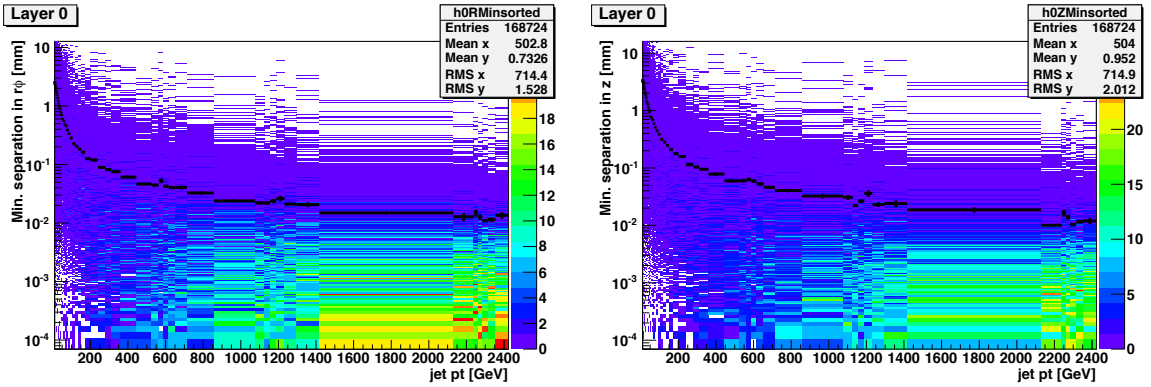
Figure 4.28: The occupancy given in % of the Utopia is shown for pileup 200 as a function of z [mm] for the SCT (4.13a) and Pixel (4.13b) barrel and as a function of the radius [mm] for the SCT (4.13c) and Pixel (4.13d) disks.

occupancy of the SCT layer 3 and 4 in figure 4.28a. The occupancy reaches up to 0.6% in the innermost Pixel layer at $r = 37\,\text{mm}$ and up to 1.2% in the innermost SCT layer. To

Number	Sample name
sample 16	user.silviam.group.det-slhc.mc11_14TeV.4907443.multi_muons.reco.ESD. LowPtMinbiasOnly
sample 17	group.det-slhc.mc12_14TeV.119995.Pythia8_A2MSTW2008LO_minbias _inelastic_low.ESD.D3PD.010300.clus.v3_EXT2

Table 4.6: Samples used for the ID upgrade studies are listed with their full names.

reduce the occupancy a change of the granularity is considered. In figure 4.29 the minimal



(a) Min. separation in $r\phi$ **(b)** Min. separation in z

Figure 4.29: Distribution of the minimal track separation in jets as a function of the jet p_T where the number of entries (colour code) and the mean (black data points) are shown. The results are obtained for the innermost Pixel layer in the Utopia layout with a radius of 37 mm.

track separation in jets is shown at the radius of the innermost Utopia barrel layer. The critical value of p_T for which the reconstruction of the closest tracks is challenging for the mean minimal separation is 0.5 TeV(figure 4.29a)/0.1 TeV(figure 4.29b). These studies

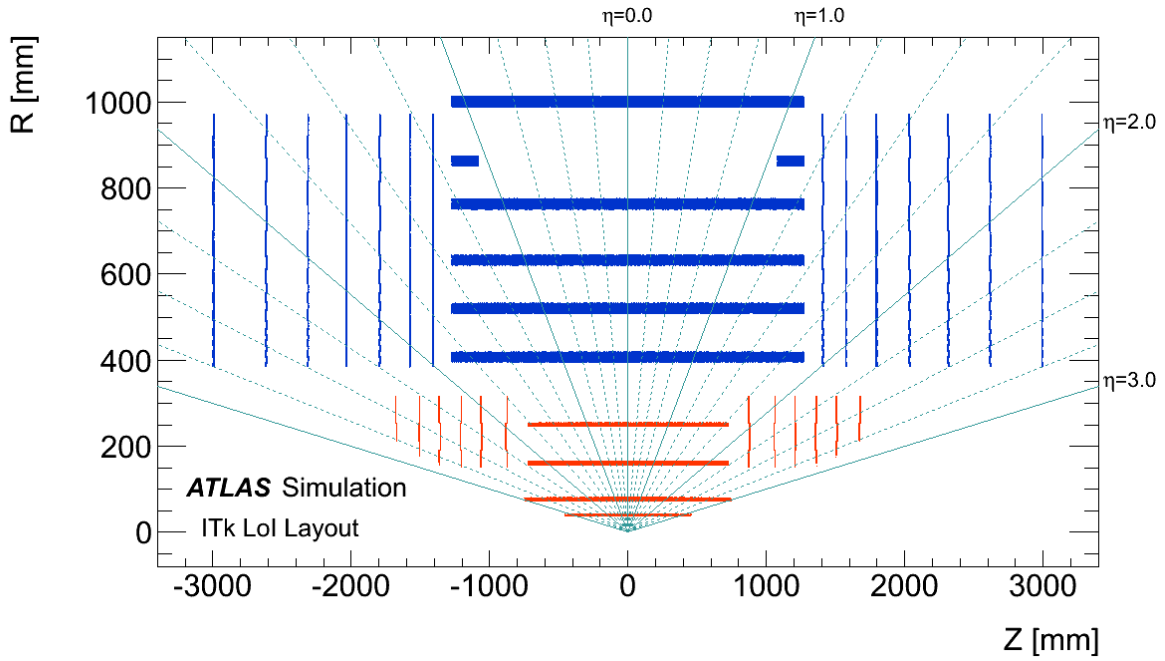


Figure 4.30: Projection in r-z of the inner detector design for the LoI for phase II consisting of the Pixels detector (red) and the SCT (blue) [103].

confirm the recommendation of reducing the pixel size to support a high reconstruction efficiency in high p_T jets.

The reduced pixel size is realised in the latest layout proposal for the inner detector replacement presented in the Letter of Intent (LoI) for phase II [6]. The so-called Letter of Intent (LoI) layout shown in figure 4.30 comprises of a Pixel and silicon strip detector. The Pixel detector has four barrel layers and six endcap disks [104]. The proposed pixel size is $25\,\mu\text{m} \times 150\,\mu\text{m}$ for the two innermost pixel layers and $50\,\mu\text{m} \times 250\,\mu\text{m}$ for the rest. The SCT consists of five barrel layers, seven endcap disks and two stub cylinders at either end of the barrel. The stub cylinders placed between the fourth and fifth layer are implemented to support an even spacing of position measurements with no gap in the intermediate region between the barrel and endcap. For the barrel layers, the strip size is $75\,\mu\text{m} \times 23.82\,\text{mm}$ for the three innermost layers and $75\,\mu\text{m} \times 47.64\,\text{mm}$ for the remaining layers. In the endcap the strip size is $(8.1\text{-}58.3)\,\text{mm} \times (0.0192\text{-}0.0085)\,\text{mrad}$ in ϕ.

The occupancy results shown in figure 4.31 are produced with the MC sample (sample 17) with 200 pileup. The highest occupancy is observed in the centre of the SCT disks and the innermost SCT barrel layer. Overall, the SCT occupancy of this layout is below 1% and the pixel occupancy is below 0.25%.

4.2.2 Layout Conclusions

These initial studies of proposed layouts for the inner detector replacement were performed with the first simulated samples where only the ID is simulated. To study more involved parameters (e.g. reconstruction of combined muons) samples with the full detector geometry are being produced.

In the design phase the criterion was set to accept a maximal occupancy of 1% in the inner detector for pileup of 200 [103]. This target was not met by the Utopia layout. Even after optimising the SCT disk position according to the occupancy values obtained, the maximal occupancy remained above 2%. Revising the layout structure resulted in the LoI layout with an increased granularity in the Pixel and SCT. For this layout the design target of an occupancy $\leq 1\%$ is accomplished.

The performance of the LoI layout keeps the quality of the measurement of all the physics objects the same as they currently are, or even improves them under upgrade conditions. The tracking efficiency of electrons and muons, particularly important for the $H \rightarrow ZZ^{(*)} \rightarrow 4\ell$ analysis, is shown in figure 4.32. A very high efficiency can be maintained over a large pseudorapidity range at a pileup of 140. The electron efficiency

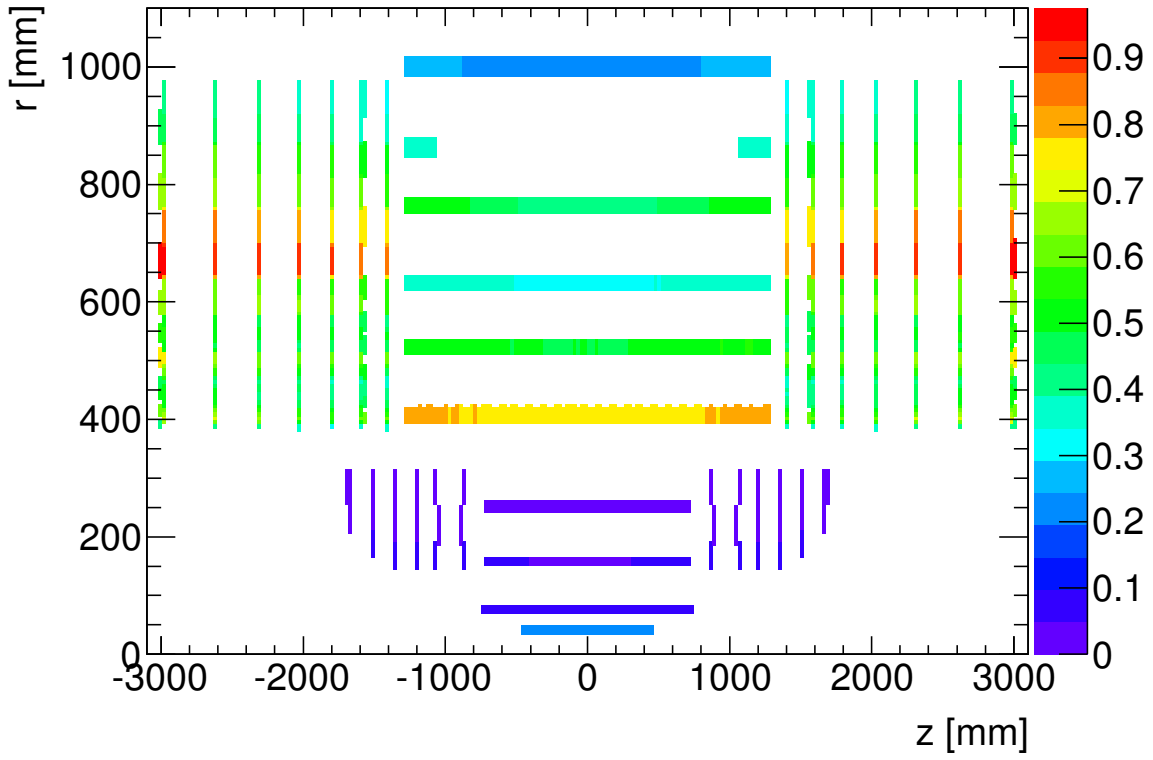


Figure 4.31: Occupancy map of the inner detector design for the LoI for phase II.

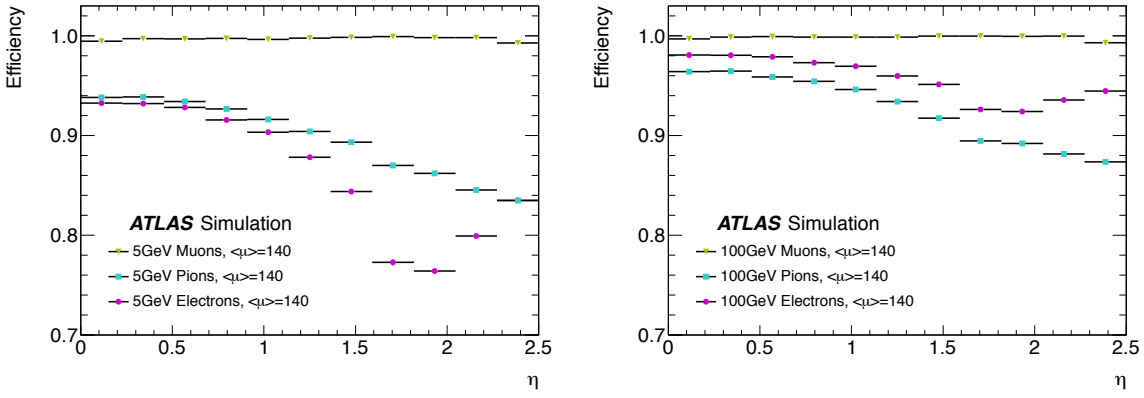


Figure 4.32: The tracking efficiency of muons, pions and electrons is shown depending on the pseudorapidity at upgrade conditions with 140 pileup for the LoI layout. The efficiency is shown for 5 GeV on the left and for 100 GeV on the right [6].

is improved by the bremsstrahlung refitting during reconstruction. The challenging transition region between the barrel and the endcap is moved to higher pseudorapidity in the LoI layout given the long barrel layer reaching up to $|z| = 1276.5\,\text{mm}$ for the SCT and $|z| = 750.6\,\text{mm}$ for the Pixel except of the innermost layer[11]. The material in the upgraded tracker layout is $0.7X_0$ for $|\eta| \leq 2.7$ except a few small regions. This is a large improvement for the tracking compared to the current inner detector with greater than $1.2X_0$ for $|\eta| > 1$. The performance of the LoI layout results in an electron and muon efficiency of over 90% for $p_T = 100\,\text{GeV}$ up to $|\eta| \leq 2.5$ at 140 pileup offering great prospects for physics analysis at $\sqrt{s} = 14\,\text{TeV}$ [6]. The electron and muon efficiency is of great importance for the H$\rightarrow ZZ^{(*)} \rightarrow 4\ell$ analysis discussed in the following chapter.

[11] The coverage of the current detector layout is up to $|z| = 749.0\,\text{mm}$ for the SCT and $|z| = 400.5\,\text{mm}$ for the Pixel barrel.

Chapter 5

Signal and background analysis of the H$\rightarrow ZZ^{(*)} \rightarrow 4\ell$ channel

5.1 Introduction

The $H \rightarrow ZZ^{(*)} \rightarrow 4\ell$ analysis is sensitive over a large mass range and is performed in ATLAS for a possible Higgs mass range from 80 GeV to 1 TeV. For $m_H \leq 182$ GeV at least one of the Z bosons is off-shell. The final state $\ell^+\ell^-\ell'^+\ell'^-$ is abbreviated as 4ℓ, where ℓ denotes electrons or muons in this analysis.

The main background comes from the continuum $(Z^{(*)}/\gamma^*)(Z^{(*)}/\gamma^*)$ production [105]. The Z+jets and $t\bar{t}$ backgrounds also contribute in the region below 400 GeV. In the low Higgs mass range ($m_H \lesssim 150$ GeV) the $H \rightarrow ZZ^{(*)} \rightarrow 4\ell$ analysis is one of the channels which are most sensitive. For example at $m_H = 120$ GeV, the sensitivity $(S/\sqrt{B})$ for the $H \rightarrow ZZ^{(*)} \rightarrow 4\ell$ channel is 2.8 at 30 fb^{-1} from sensitivity studies using MC prior to data taking [36]. The events were counted within the region $m_H \pm 2\sigma_{m_H}$. The expected significance for the discovery of a Higgs at $m_H = 120$ GeV is 5.7 for the $H \rightarrow \gamma\gamma$ channel at 30 fb^{-1}. The cross-section times branching ratio is shown in figure 2.5.

The latest measurement by ATLAS in March 2013 with a new particle at $m_H = 124.3^{+0.6}_{-0.5}(\text{stat})^{+0.5}_{-0.3}(\text{syst})$ GeV observed in the $H \rightarrow ZZ^{(*)} \rightarrow 4\ell$ channel is compatible with the SM Higgs boson [5]. The Higgs boson is produced most often by two initial gluons (ggF) as shown in figure 5.1. The $H \rightarrow ZZ^{(*)} \rightarrow 4\ell$ channel is ideal for the mass measurement due to its excellent mass resolution. Its clean signature is clearly distinguished from the large backgrounds common to other LHC analysis.

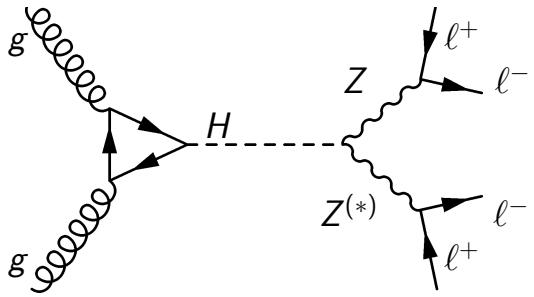


Figure 5.1: Feynman diagram with Higgs produced by gluon-gluon fusion and the decay channel $H \to ZZ^{(*)} \to 4\ell$.

5.2 Samples

The datasets used have integrated luminosities of $4.6\,\text{fb}^{-1}$ at $\sqrt{s} = 7\,\text{TeV}$ in 2011 and $20.7\,\text{fb}^{-1}$ at $\sqrt{s} = 8\,\text{TeV}$ in 2012. Signal samples for the ggF and VBF production modes are produced with PowHeg [106], interfaced with Pythia to model the parton shower and hadronization [82, 83]. The production modes VH and $t\bar{t}H$ are modeled by Pythia.

The generator used for the $ZZ^{(*)}$ background is gg2ZZ [107], when produced by two gluons, and PowHeg [106] when produced by a quark-antiquark pair. The generator ALPGEN is used to estimate the Z+jets background [108]. The $t\bar{t}$ background is modelled by MC@NLO [109]. The generators ALPGEN, MC@NLO and gg2ZZ, are interfaced with Herwig for the parton showering and all PowHeg samples are interfaced with Pythia [110].

5.3 Event Selection

5.3.1 Data quality selection

A run of proton-proton beams is subdivided into luminosity blocks (LB) each with approximately similar instantaneous luminosity. Data are only analysed from LB where stable beams are declared by the LHC and all detector components performed well (good run list).

5.3.2 Trigger

The trigger menu is used for data and MC including either the single or di-lepton trigger as summarised for 2011 and 2012 in table 5.1. The threshold required in the single-muon trigger is $p_T = 18\,\text{GeV}$ in 2011 and $p_T = 24\,\text{GeV}$ in 2012. For the single-electron trigger, events are selected with at least $E_T = 25\,\text{GeV}$ in 2012. In 2011, the E_T threshold of

the single-electron trigger varied between 20 GeV and 22 GeV depending on the data period. In the di-muon trigger, both muons are required to have at least $p_T = 13\,\text{GeV}$ in 2012 and $p_T = 10\,\text{GeV}$ in 2011. For 2012 an additional asymmetric option was included with the threshold requirement of $p_T = 18\,\text{GeV}$ for the first and $p_T = 8\,\text{GeV}$ for the second muon. The thresholds are $E_T = 12\,\text{GeV}$ in 2012 and 2011 for each electron in the di-electron trigger. For the electron-muon trigger the electron has a minimal $E_T \geq 12\,\text{GeV}$ or $E_T \geq 24\,\text{GeV}$ depending on the electron identification requirements and the muon is characterised by $p_T \geq 8\,\text{GeV}$ in 2012. The corresponding requirements for 2011 are $E_T \geq 10\,\text{GeV}$ and $p_T \geq 6\,\text{GeV}$ [5].

Trigger Type	Threshold(s) [GeV]	
	$\sqrt{s} = 7\,\text{TeV}$	$\sqrt{s} = 8\,\text{TeV}$
single-muon	$p_T > 18$	$p_T > 24$
single-electron	$E_T >$20 to 22 varies over data-taking periods	$E_T > 24$
di-muon (symmetric)	$p_{T1} > 10$ and $p_{T2} > 10$	$p_{T1} > 13$ and $p_{T2} > 13$
di-muon (asymmetric)	- added for 2012	$p_{T1} > 18$ and $p_{T2} > 8$
di-electron	$E_{T1} > 12$ and $E_{T2} > 12$	$E_{T1} > 12$ and $E_{T2} > 12$
electron-muon	$E_T > 10$ and $p_T > 6$	$E_T > 12$ or 24 and $p_T > 8$ two trigger with different requirements

Table 5.1: The trigger types used for the H→ $ZZ^{(*)} \to 4\ell$ analysis are summarised where p_{T1}/E_{T1} [p_{T2}/E_{T2}] means first [second] lepton in di-lepton pair.

5.3.3 Lepton pre-selection

The electron reconstruction suffers from bremsstrahlung due to which electrons lose $20-50\%$ of their energy, on average, before leaving the SCT [36]. With the Gaussian-sum filter (GSF) some of the energy losses can be recovered before the electron reconstruction. The radiation losses in the silicon detector are refitted with the Gaussian-sum filter. If photons are emitted in close proximity to the primary vertex, the energy recovery is not possible. The dependence of the resolution on η can be reduced with the GSF as the energy loss in material is taken into account by the GSF. For low p_T electrons ($\lesssim 15\,\text{GeV}$) the improvement gained by the GSF is particularly important as the resolution is more severely affected by bremsstrahlung losses [111].

For the electron selection it is required that at least three tracks are attached to each primary vertex. The pseudo-rapidity range is $|\eta| < 2.47$ for electrons and $|\eta| < 2.70$ for muons. The impact parameter of the leptons along the beam axis is required to be within 10 mm from the reconstructed primary vertex. This requirement is loosened for muons in the forward region without an ID track.

5.3.4 Quadruplet selection

In the $H \to ZZ^{(*)} \to 4\ell$ analysis, events are selected with two same-flavour opposite-sign lepton pairs. The leptons in the quadruplet, ordered by p_T, are required to have a $p_T^{1,2,3,4} > 20, 15, 10, 7\,\text{GeV}$ (6 GeV for μ). The leading di-lepton pair is defined as the di-lepton pair of the quadruplet with the mass, m_{12}, closest to the nominal Z boson mass and the sub-leading di-lepton pair is the second di-lepton pair of the quadruplet with a mass, m_{34}. The mass of the leading di-lepton pair is required to be $50\,\text{GeV} < m_{12} < 106\,\text{GeV}$ and the mass of the sub-leading di-lepton pair is selected with $m_{min} < m_{34} < 115\,\text{GeV}$ where m_{min} depends on m_{4l}. For $m_{4l} < 140\,\text{GeV}$, the threshold is $m_{min} = 12\,\text{GeV}$ rising linearly to $m_{min} = 50\,\text{GeV}$ at $m_{4l} = 190\,\text{GeV}$. For $m_{4l} > 190\,\text{GeV}$, the threshold remains constant at $m_{min} = 50\,\text{GeV}$. In the region where at least one Z boson is off-shell the mass threshold of the sub-leading boson reduces with the expected mass [112].

For all combinations of possible same-flavour opposite-charge lepton pairs the mass threshold is $m_{ll} > 5\,\text{GeV}$ to remove $J/\psi \to \ell\ell$ events. The required separation is $\Delta R > 0.1$ for same-flavour leptons, and $\Delta R > 0.2$ for different-flavour leptons, where $\Delta R = \sqrt{(\Delta\phi)^2 + (\Delta\eta)^2}$. For bunch-crossings where more than one quadruplet remains, only one is kept with the preference given to the quadruplet with m_{34} closest to the Z boson mass. Further requirements on tracking and calorimeter isolation and the impact parameter (IP) significance are applied to reduce the background of the $H \to ZZ^{(*)} \to 4\ell$ analysis [5].

The track isolation is determined by the ratio of the p_T within a cone of $\Delta R < 0.2$ around the lepton over the p_T of the lepton, $\frac{\sum p_T}{p_T}$. The $\sum p_T$ within the cone is calculated by adding the p_T of all charged tracks coming from the primary vertex. The p_T of the lepton is not included in the sum of p_T in the cone. Also, if any of the other leptons of the quadruplet are within the cone, they are not included in the summation. Furthermore, only good quality tracks are selected for the p_T sum. For muon tracks, this requires $p_T > 1.0\,\text{GeV}$ and more than three hits in the Pixel and SCT subsystem denoted as silicon hits. For the electron tracks, the selection is $p_T > 1.0\,\text{GeV}$ and more than seven silicon hits including one hit in the innermost silicon layer (Pixel b-layer) in 2011. For

2012, this changed to more than eight silicon hits including one hit in the Pixel b-layer and $p_T > 0.4\,\text{GeV}$. The normalised track isolation is required to be $\frac{\sum p_T}{p_T} < 0.15$ for all leptons [5].

The calorimeter isolation discriminant sets a threshold on the ratio of the E_T sum of calorimeter clusters with a barycentre in a cone of $\Delta R < 0.2$. In 2011 cell-based clusters were used whereas in 2012 clusters determined by a 'topological' algorithm were selected, which only keeps clusters with a significant signal in comparison to energy equivalent of the electronics noise [113]. For electrons, the calorimeter isolation cut is $\frac{\sum E_T}{p_T} < 0.3$ in 2011 and $\frac{\sum E_T}{p_T} < 0.2$ in 2012. Muons are selected with $\frac{\sum E_T}{p_T} < 0.3$ except for muons without a corresponding track in the ID which are required to have $\frac{\sum E_T}{p_T} < 0.15$. As for the track isolation, the p_T of any of the leptons in the quadruplet is excluded from the summation in the numerator of the calorimeter isolation.

The impact parameter significance defined by the impact parameter over the corresponding uncertainty is required to be $\frac{|d_0|}{\sigma_{d_0}} < 3.5$ for muons and for electrons $\frac{|d_0|}{\sigma_{d_0}} < 6.5$.

In addition, a selection requirement is applied to correct for the effect of final state radiation (FSR). For $66\,\text{GeV} < m_{12} < 89\,\text{GeV}$, photons are added to the reconstructed mass if they are close to one of the muon tracks. The E_T of the photon has to be at least 1 GeV and uses the longitudinal segmentation of the LAr calorimeter. The energy deposited in a cluster in the front segment of the calorimeter is divided by the total energy to define the fraction $f1$. By using the discrimination power of the fraction $f1$, fake photon clusters from energy loss of the muon are reduced. For $1.0\,\text{GeV} < E_T < 3.5\,\text{GeV}$, photons with $f1 > 0.2$ and $\Delta R < 0.15$ are added to the reconstructed mass. For $E_T > 3.5\,\text{GeV}$, the FSR correction is applied given $f1 > 0.1$ and $\Delta R <$0.15. The FSR correction is only applied if the requirement $m_{12} < 106\,\text{GeV}$ is satisfied after the correction. In this fiducial region, 70% of the FSR candidates are recovered and 4% of the H→ $ZZ^{(*)} \to 4\mu$ candidates are expected to be corrected for FSR [5, 114].

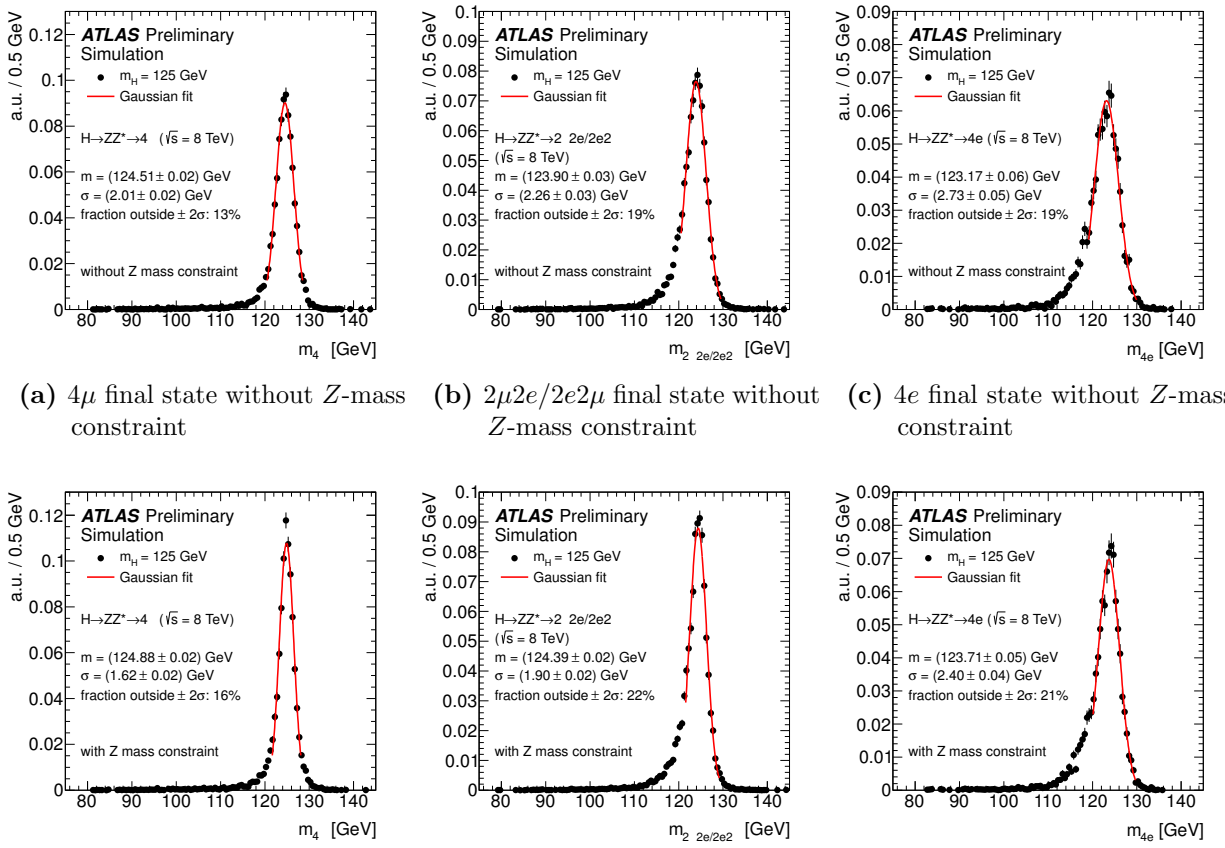
5.3.5 Z-mass constraint

The Z-mass constraint is a kinematic fit to the leading lepton pair for $m_{4l} < 190\,\text{GeV}$ and reweights the leptons to give a mass consistent with the mass and width of the Z boson. The probability density function $F(m_{12}, \mu_{12})$ for a measured di-lepton mass m_{12} given the true value of the di-lepton mass, μ_{12}, is

$$F(m_{12}, \mu_{12}) = R(m_{12}|\mu_{12})G(\mu_{12}),$$

where $G(\mu_{12})$ is the generator level distribution and $R(m_{12}|\mu_{12})$ is the response function. A Breit-Wigner function is used to model the Z-line shape of $G(\mu_{12})$ and a Gaussian function describes the dependence of the measured and the true di-lepton mass $R(m_{12}|\mu_{12})$ with a mean μ_{12} and a sigma $\sigma_{m_{12}}$. The parameter $\sigma_{m_{12}}$ is the uncertainty on the measured di-lepton mass which can be calculated by error propagation using the lepton momentum resolution. Given the measured value for the di-lepton mass and the corresponding uncertainty, the most likely true di-lepton mass is determined and the di-lepton mass is corrected to the value of the most likely true di-lepton mass evaluated from $F(m_{12}, \mu_{12})$.

For $m_{4\ell} > 190\,\text{GeV}$ the Z-mass constraint is applied to m_{12} and m_{34} [5]. In figure 5.2, the mass resolution is shown without (5.2a - 5.2c) and with the Z-mass constraint (5.2d - 5.2f) applied. The improved resolution with Z-mass constraint is 1.9% in the $4e$ channel, 1.3% in the 4μ channel and 1.5% in the mixed channels at 125 GeV determined by a Gaussian fit [5].



(a) 4μ final state without Z-mass constraint

(b) $2\mu 2e/2e2\mu$ final state without Z-mass constraint

(c) $4e$ final state without Z-mass constraint

(d) 4μ final state with Z-mass constraint

(e) $2\mu 2e/2e2\mu$ final state with Z-mass constraint

(f) 4μ final state with Z-mass constraint

Figure 5.2: Signal resolution for a simulation of $m_H = 125\,\text{GeV}$ without Z-mass constraint applied 5.2a - 5.2c and with Z-mass constraint applied 5.2d - 5.2f [5].

5.4 Background estimation

The estimate for the irreducible background $ZZ^{(*)}$ background is taken from MC and normalised to the theoretical cross section. In 2011, the measurement of the ZZ cross section has been a bit larger ($\sigma^{tot}_{ZZ} = 6.7 \pm 0.5(\text{stat})^{+0.4}_{-0.3}(\text{syst}) \pm 0.3(\text{lumi})$ pb) than expected by the SM ($5.9^{+0.2}_{-0.2}$ pb) [115]. The measurement $\sigma^{tot}_{ZZ} = 7.1^{+0.5}_{-0.4}(\text{stat}) \pm 0.3(\text{syst}) \pm 0.2(\text{lumi})$ pb in 2012 is very close to the SM expectation of $7.2^{+0.3}_{-0.2}$ pb [38]. Both respective CMS measurements have been a larger than expected with $6.24^{+0.86}_{-0.80}(\text{stat})^{+0.41}_{-0.32}(\text{syst}) \pm 0.14(\text{lumi})$ pb at $\sqrt{s} = 7$ TeV and $7.7^{+0.5}_{-0.5}(\text{stat})^{+0.5}_{-0.4}(\text{syst}) \pm 0.4(\text{theo}) \pm 0.3(\text{lum})$ pb at $\sqrt{s} = 8$ TeV [116, 117]. The errors are of significant size, therefore all the measurements are compatible with the cross sections expected by the SM.

The normalisation for the reducible background, including Z+jets and $t\bar{t}$, is evaluated by data-driven procedures, where the Higgs signal is suppressed with isolation and impact parameter cuts. Different procedures are used to determine the normalisation for the background to a $\ell\ell$+$\mu\mu$ and a $\ell\ell$+ee signal. In the former case, the background consists mainly of $t\bar{t}$ and $Zb\bar{b}$. The $b\bar{b}$ control region is enhanced by removing the isolation requirement for the sub-leading lepton pair and requiring at least one of the sub-leading leptons to fail the impact parameter significance. The m_{12} distribution is fitted by a 2nd order Chebychev polynomial for the flat $t\bar{t}$ component and a convolution of a Breit Wigner function and a Crystal Ball resolution function for the Z+jets contribution. With this fit, the yields are determined and extrapolated to signal region.

The reducible background to a $\ell\ell$+ee signal is mainly Z+jets where the electrons come from heavy flavour semi-leptonic decays (E), from photon conversions (C) or light jets misidentified as electrons (F). The $\ell\ell$+ee background control region is created by relaxing the electron selection criteria for the sub-leading pair. The events are classified into the reconstruction categories E, C or F e.g. by studying suitable variables as the fraction of high threshold hits in the TRT categories [5]. By comparing this to MC the efficiency is determined to extrapolate the yield to the signal region.

5.5 m_{12} study

The m_{12} distributions are studied by comparing MC simulation to data as shown in figure 5.3 to cross-check the selections applied in the analysis. For large m_{4l}, the Z_1 and Z_2 mass are very similar. Due to this the leading and the sub-leading lepton-pair might be confused so that the leading lepton pair is assigned to be the sub-leading lepton-pair. This would mean that some events appearing in the Z_1 mass plot of the

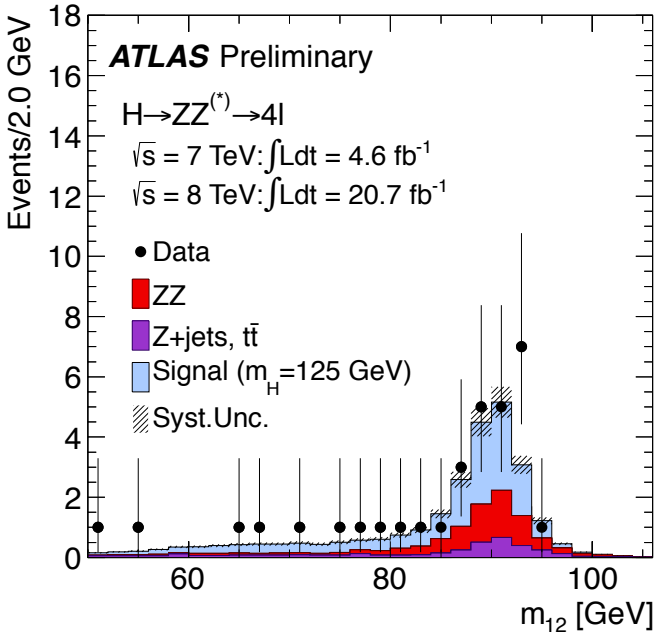


Figure 5.3: The m_{12} distribution of the events is shown after the full selection for simulation using a signal sample at $m_H = 125\,\text{GeV}$ and the combined dataset [5].

$2\mu 2e$ channel actually belong to the $2e2\mu$ category. The difference between Z_1 mass and the Z_2 mass gets larger when restricting m_{4l} to the low mass range. This reduces the possible confusion of the events classification in the mixed channels. As shown in figure 5.3, the m_{12} shape of the MC simulation is consistent with the data given the limited number of events. Applying the cut $m_{4l} < 200\,\text{GeV}$ does not influence the m_{12} shape of the mixed channels.

Another cross-check to study the possible mismatching of the leading and sub-leading lepton pair in the mixed channels can be performed with the energy scale systematic. The electron energy scale is the main source of systematic errors for electrons (whereas the key systematic for the muons is the muon momentum scale). The impact of the electron energy scale has been studied for the Z_1 mass peak. If the electron energy scale is underestimated, events might be identified as $2\mu 2e$ events which actually belong to the $2e2\mu$ category. On the contrary, if the energy scale for electrons is too high, $2\mu 2e$ events might be identified as $2e2\mu$. It was found to have no effect on the Z_1 mass peak observed in the 4μ channel when changing the electron energy scale up and down by one standard deviation. The mean of the Z_1 mass distribution fitted by a Crystal Ball also stays constant in the electron channels when changing the energy scale. This demonstrates that the identification of four different final states is robust using the analysis selection.

5.6 Conclusion

With the signal and background selection cuts presented in this chapter, the expected number of signal and backgrounds is obtained which is summarized in table 5.2. The loosened electron identification (see subsection 5.3.2) and the changes in the calorimeter isolation (see subsection 5.3.4) are only applied for 2012 in the combined dataset and for the dataset containing only 2012 data. The 2011 component of the combined dataset uses the 2011 electron identification and calorimeter isolation cuts.

	signal	ZZ^*	Z + jets, $t\bar{t}$	S/B	expected	observed
$\sqrt{s} = 8\,\text{TeV}$						
4μ	5.3 ± 0.7	2.3 ± 0.1	0.50 ± 0.13	1.9	8.1 ± 0.9	11
$2\mu 2e$	2.6 ± 0.4	1.2 ± 0.1	1.01 ± 0.21	1.2	4.8 ± 0.7	4
$2e2\mu$	3.4 ± 0.4	1.7 ± 0.1	0.51 ± 0.16	1.5	5.6 ± 0.7	6
$4e$	2.3 ± 0.3	1.0 ± 0.1	0.62 ± 0.16	1.4	3.9 ± 0.6	6
total	13.7 ± 1.8	6.2 ± 0.4	2.62 ± 0.34	1.6	22.5 ± 2.9	27
$\sqrt{s} = 7\,\text{TeV}$						
4μ	0.97 ± 0.13	0.49 ± 0.02	0.05 ± 0.02	1.8	1.5 ± 0.2	2
$2\mu 2e$	0.39 ± 0.05	0.21 ± 0.02	0.55 ± 0.12	0.5	1.0 ± 0.1	1
$2e2\mu$	0.57 ± 0.08	0.33 ± 0.02	0.04 ± 0.01	1.6	0.9 ± 0.1	2
$4e$	0.29 ± 0.04	0.15 ± 0.01	0.49 ± 0.12	0.5	0.9 ± 0.1	0
total	2.2 ± 0.3	1.17 ± 0.07	1.12 ± 0.17	1.0	4.3 ± 0.5	5
$\sqrt{s} = 8\,\text{TeV}$ and $\sqrt{s} = 7\,\text{TeV}$						
4μ	6.3 ± 0.8	2.8 ± 0.1	0.55 ± 0.15	1.9	9.6 ± 1.0	13
$2\mu 2e$	3.0 ± 0.4	1.4 ± 0.1	1.56 ± 0.33	1.0	6.0 ± 0.8	5
$2e2\mu$	4.0 ± 0.5	2.1 ± 0.1	0.55 ± 0.17	1.6	6.6 ± 0.8	8
$4e$	2.6 ± 0.4	1.2 ± 0.1	1.11 ± 0.28	1.2	4.8 ± 0.8	6
total	15.9 ± 2.1	7.4 ± 0.4	3.74 ± 0.93	1.6	27.0 ± 3.4	32

Table 5.2: The number of events are summarised the expected signal with $m_H = 125\,\text{GeV}$, the expected background and the observed data for $120\,\text{GeV} < m_{4\ell} < 130\,\text{GeV}$. Additionally, the ratio of expected signal over background events is given by S/B. The results are listed for $20.7\,\text{fb}^{-1}$ at $\sqrt{s} = 8\,\text{TeV}$, $4.6\,\text{fb}^{-1}$ at $\sqrt{s} = 7\,\text{TeV}$ and the combined dataset [5].

The ratio of signal over background is in almost all cases larger than one in particular after optimising the electron identification for the 2012 data taking. The $ZZ^{(*)}$ background

contribution is larger than the reducible background which has been suppressed well by the applied selection.

Chapter 6

Statistical models and per-event error

The distributions obtained by the signal and background analysis are fitted using statistical models. Features of the distributions can be better understood and quantitative conclusions can be drawn from the statistical analysis. For this, histogram approaches or more advanced non-parametric signal models can be used. Fitting the distributions allows the underlying shape to be used to give discrimination between signal and background. Given a fundamental understanding of the distributions, parametric models can be applied. In this chapter the different approaches are discussed for the H$\rightarrow ZZ^{(*)} \rightarrow 4\ell$ channel.

6.1 Non-parametric signal model

The expectation for the signal and background components is obtained from Monte Carlo (MC) simulation. The SM Higgs signal is simulated for different masses in the range of 80 GeV to 1 TeV. For each mass generated point the m_{4l} distribution consists of a binned histogram which is produced from unbinned MC samples. Furthermore, the signal MC samples are only generated for discrete m_H values. To obtain a continuous estimate and reduce the binning effect, a non-parametric method is applied for each simulated mass point with its parameters depending on m_H.

Non-parametric representations are defined to have the ability to describe a variety of distributions [118]. They have many parameters which can diverge with the number of data points. The histogram can be used as a very basic non-parametric estimator. A simple non-parametric estimation technique to minimize the influence of the binning is to create N histograms with a bin-width h where the i-th histogram begins at $x_0 + \frac{ih}{N}$. By averaging over the N histograms, a non-parametric estimator is obtained, the so-called Average Shifted Histogram (ASH). In the limit of $N \rightarrow \infty$, a kernel density estimation is obtained with a isosceles triangle for each data point [119]. Kernel Density Estimates

$\hat{f}_K(x)$ are a type of non-parametric estimator and are built from the sum of kernel functions, K, for each component centred around each data point x_i:

$$\hat{f}_K(x) = \frac{1}{nh}\sum_{i=1}^{n} K\Big(\frac{x - x_i}{h}\Big), \tag{6.1}$$

where n is the number of data points and h is a smoothing parameter. Different distributions can be used as a kernel function which are then summed up. For histograms, rectangles are used as a kernel function which are not centred around the data points.

For the non-parametric model of the H$\to ZZ^{(*)} \to 4\ell$ channel, the kernel density estimator uses a Gaussian function centred around each data point with variable width depending on the data point density called adaptive Kernel Density Estimates [119]. Each data point is influenced by several independent processes. Among these is the detector response which determines strongly the point to point variation. Each of these underlying phenomena might not be Gaussian shaped, but combined they are modelled by a Gaussian distribution motivated by the central limit theorem.

The Kernel Density Estimate is applied to each $m_{4\ell}$ distribution for each m_H mass point with signal samples available and then interpolated to build a signal model dependent on m_H. The MC signal shapes can be shifted in m_{4l} to determine a weighted combination for signal expectations falling between two mass points with simulated signal samples.

This signal model is later referred to as the standard template approach. As the H$\to ZZ^{(*)} \to 4\ell$ analysis moves from a discovery to a mass measurement, a high resolution on the mass measurement is the aim. To achieve this, the signal model is a key input in the fitting machinery to optimise the resolution. In the following section a refined signal model is studied.

6.2 Parametric signal model

For parametric estimator models, the parameters are optimized to values that meet best-fit requirements. An analytical function is chosen which describes a physical process, e.g. a Gaussian function might be used with the width σ representing the resolution so that values for experimental quantities can be directly obtained from the fitted parameter values.

Using a parametric model, the parameter values and shapes can be obtained for any mass point. Discontinuities are avoided in the whole statistical analysis, for instance,

smooth likelihood scans and multidimensional contours can be expected. The energy and momentum scale systematics are implemented as a shift of the mean of the signal distribution. The analytical model is also a stepping stone towards more involved statistical analysis methods, for instance, using per-event error models.

6.2.1 Crystal ball resolution model

With a parametric model additional knowledge about the underlying physics processes can be used to help choose the function. This provides possibilities to implement the experience and recommendation of the groups studying the performance of the ATLAS detector. In the $Z \to \mu\mu$ performance analysis, the convolution of a Breit-Wigner function, describing the intrinsic Z boson width with a Crystal ball function, as the detector resolution function, is used [120].

The Crystal ball function (CB) consists of a Gaussian central part and a power law tail. There are two parameters describing the asymmetric tail of the CB: the parameter a determines the position where the transition from Gaussian function to power law takes place and n is the free parameter of the power law. For positive a, the power law (non-Gaussian tail) is on the left hand side of the peak. For negative a, it is on the right hand side.

The Crystal ball function is defined as

$$f(x; a, n, \bar{x}, \sigma) = N \cdot \begin{cases} \exp\left(-\frac{(x-\bar{x})^2}{2\sigma^2}\right) & \text{if } \frac{x-\bar{x}}{\sigma} > -a \\ A\left(B - \frac{x-\bar{x}}{\sigma}\right)^{-n} & \text{if } \frac{x-\bar{x}}{\sigma} \leq -a \end{cases} \tag{6.2}$$

$$\text{with the coefficients } A = \left(\frac{n}{|a|}\right)^n \exp\left(-\frac{|a|^2}{2}\right) \text{ and } B = \frac{n}{|a|} - |a|, \tag{6.3}$$

where N is the normalizing factor, $\bar{x}$ is the expected value and σ is the standard deviation of the Gaussian function.

The Crystal ball function was used as the detector response function by the Crystal ball collaboration when studying Charmonium spectroscopy from radiative decays of the J/ψ and ψ' [121]. The Crystal ball function with its power law tail at low energies describes well the energy losses due to bremsstrahlung which affects in particular the electron channels of the H$\to ZZ^{(*)}$ analysis.

The Crystal ball function is fitted to signal MC samples where the gluon-gluon fusion is the production mode of the SM Higgs boson. The signal samples (sample 18) given in

table 6.1 are studied in 5 GeV steps between 110 GeV and 150 GeV[1]. The event selection, discussed in section 5.3, is applied including the Z-mass constraint. The samples are divided into the four final states: 4μ, $2e2\mu$, $4e$ and $2\mu2e$. The fit of the Crystal ball function for $m_H = 125$ GeV is shown in figure 6.1 with a linear scale and in figure 6.2 with a logarithmic scale.

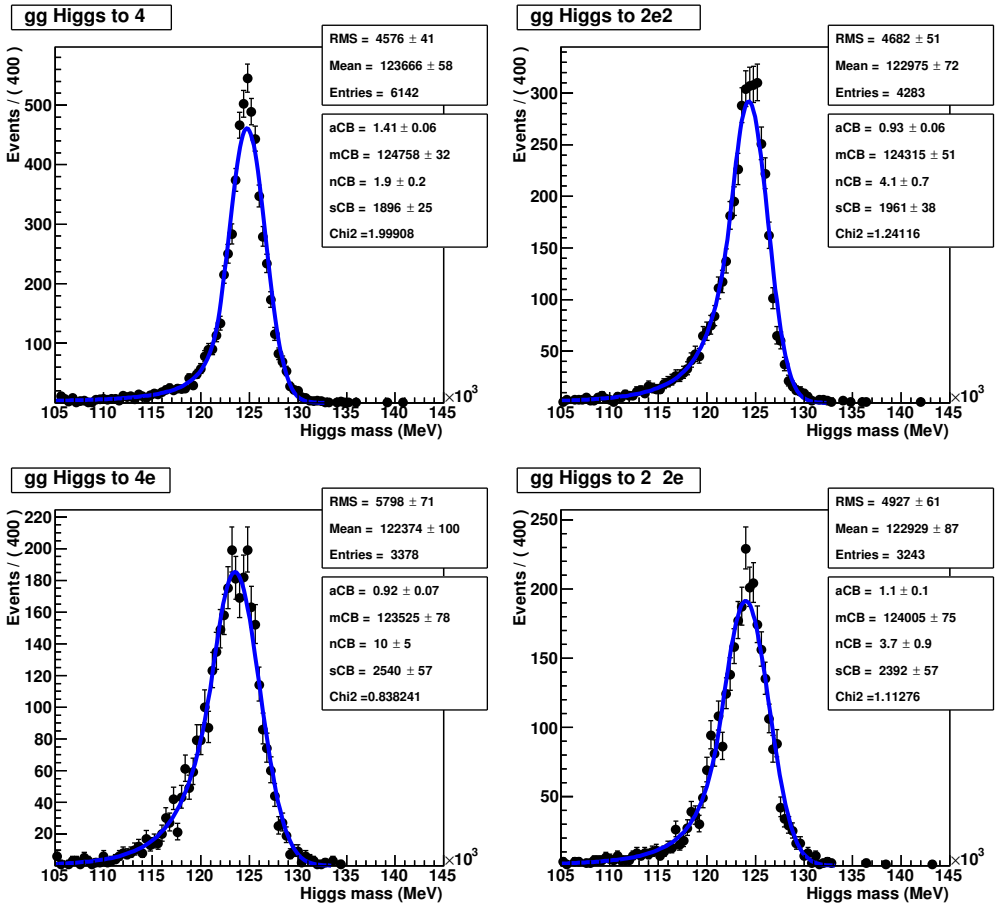


Figure 6.1: A Crystal ball function is fitted to the MC SM Higgs signal samples produced with ggF.

The four parameters of the Crystal ball ($\bar{x}$, σ, a, n) are fitted for each signal sample with a different hypothesised Higgs mass and the results for the 4μ final state are shown in figure 6.3. The plots for the others modes are in the appendix A.1. It is shown in figure 6.3 that the mean of the Crystal ball is modelled well by a linear function $(p_0 + p_1 m_H)$ depending on the hypothesised Higgs mass. It is expected that the measured mean is slightly shifted to a lower mass due to energy losses in the detector.

[1]Later signal samples in 1 GeV steps became available between 120 GeV and 130 GeV.

Number	Sample name
sample 18:	user.vippolit.H4l000022.*PowhegPythia8*ggH*2012 campaign.*
sample 19:	user.vippolit.H4l000022.*PowhegPythia8*VBFH*2012 campaign.*
sample 20:	PowhegPythia8_AU2CT10_ggH*_ZZ4lep*
sample 21:	PowhegPythia8_AU2CT10_VBFH*_ZZ4lep*

Table 6.1: Samples used for the $H \to ZZ^{(*)} \to 4\ell$ signal studies are listed with their full names.

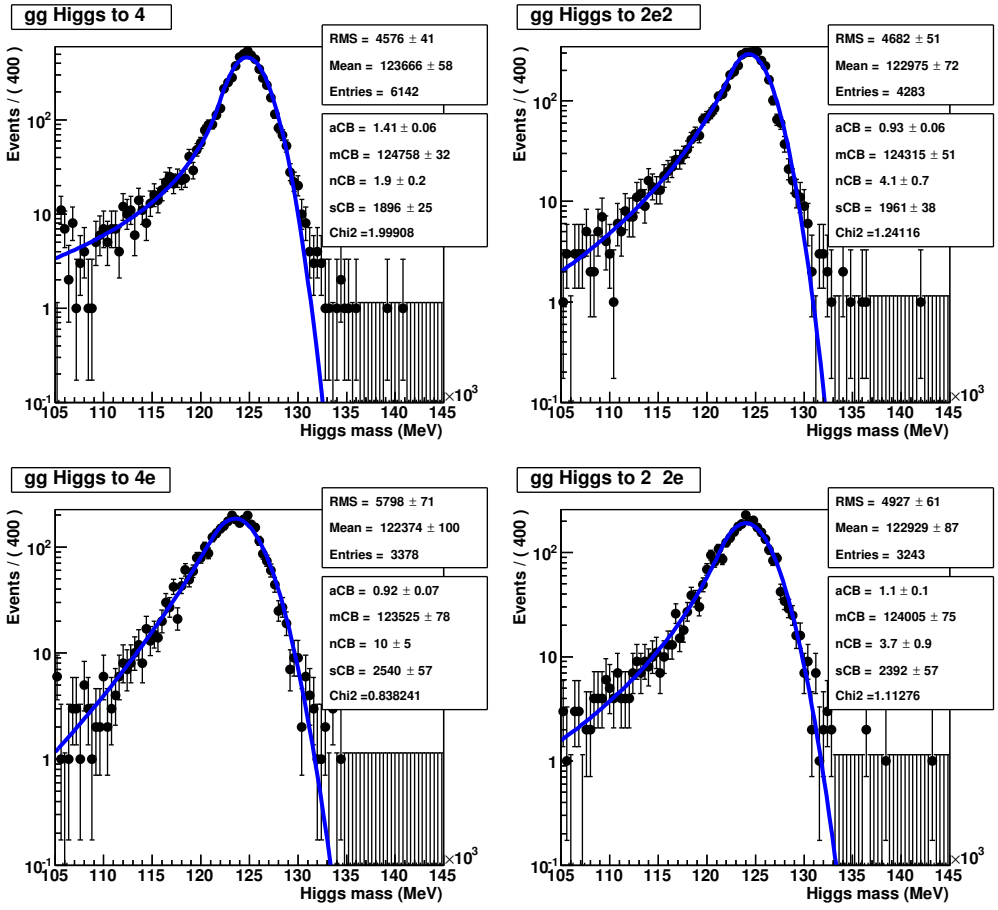


Figure 6.2: The results of the Crystal ball fit are shown with the MC SM Higgs signal samples on a logarithmic scale.

The sigma is fitted by $p_0 + p_1\sqrt{m_H}$. This dependence is chosen due to the resolution of the ATLAS calorimeter after noise subtraction: $\frac{\sigma(E)}{E} = \frac{10.1\%\,GeV}{\sqrt{E(GeV)}} \oplus 0.17\%$ [52]. This dependence is particularly important for the electron channels as the electron reconstruction strongly depends on the calorimeter resolution. The mass resolution is approximately proportional to the Higgs mass shown in figure 6.3 for 4μ and in figures A.1 - A.3 in

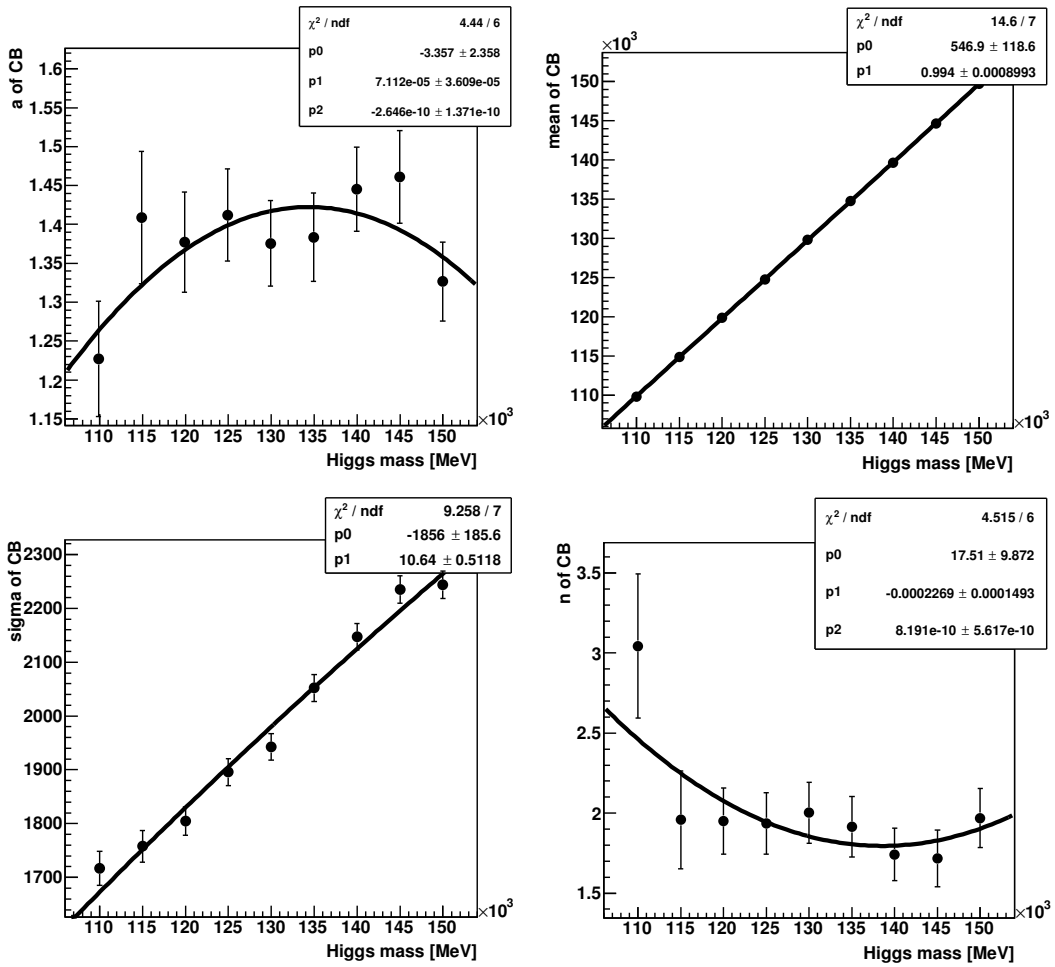


Figure 6.3: Fit results for the Crystal ball parameters shown for 4μ final state as a function of the Higgs mass. Besides the mean and the sigma describing the Gaussian component of the Crystal ball function, n, is the free parameter of the power law and a determines the transition between the power law and the Gaussian component.

the appendix for the other channels. Therefore, a linear model to describe the sigma dependence could be considered, too. Using figure 6.3, the ratio of the resolution over the Higgs mass decreases with higher Higgs mass.

In previous studies from 2009, the resolutions of the H$\rightarrow ZZ^{(*)} \rightarrow 4\mu$ and H$\rightarrow ZZ^{(*)} \rightarrow 4e$ channel were studied to determine the expected performance of the ATLAS experiment [36]. The H$\rightarrow ZZ^{(*)} \rightarrow 4e$ mass resolution for 120 GeV$< m_H <$ 180 GeV was expected to be between 2$-$2.8 GeV with, and 2.1$-$3.2 GeV without, the Z-mass constraint applied. For H$\rightarrow ZZ^{(*)} \rightarrow 4\mu$ the resolution was expected to be $1.7 - 2.7$ GeV with, and $2.0 - 3.0$ GeV without, the Z-mass constraint applied using the same mass range. The results obtained with the Crystal ball fit, for example shown in figure 6.3, are compatible

with these studies from 2009 [36]. For instance, the resolution at $m_H = 120\,\text{GeV}$ was expected to be approximately $\sigma = 1.75 \pm 0.5\,\text{GeV}$ [36], and the studies shown in figure 6.3 given $\sigma = 1.83 \pm 0.4\,\text{GeV}$.

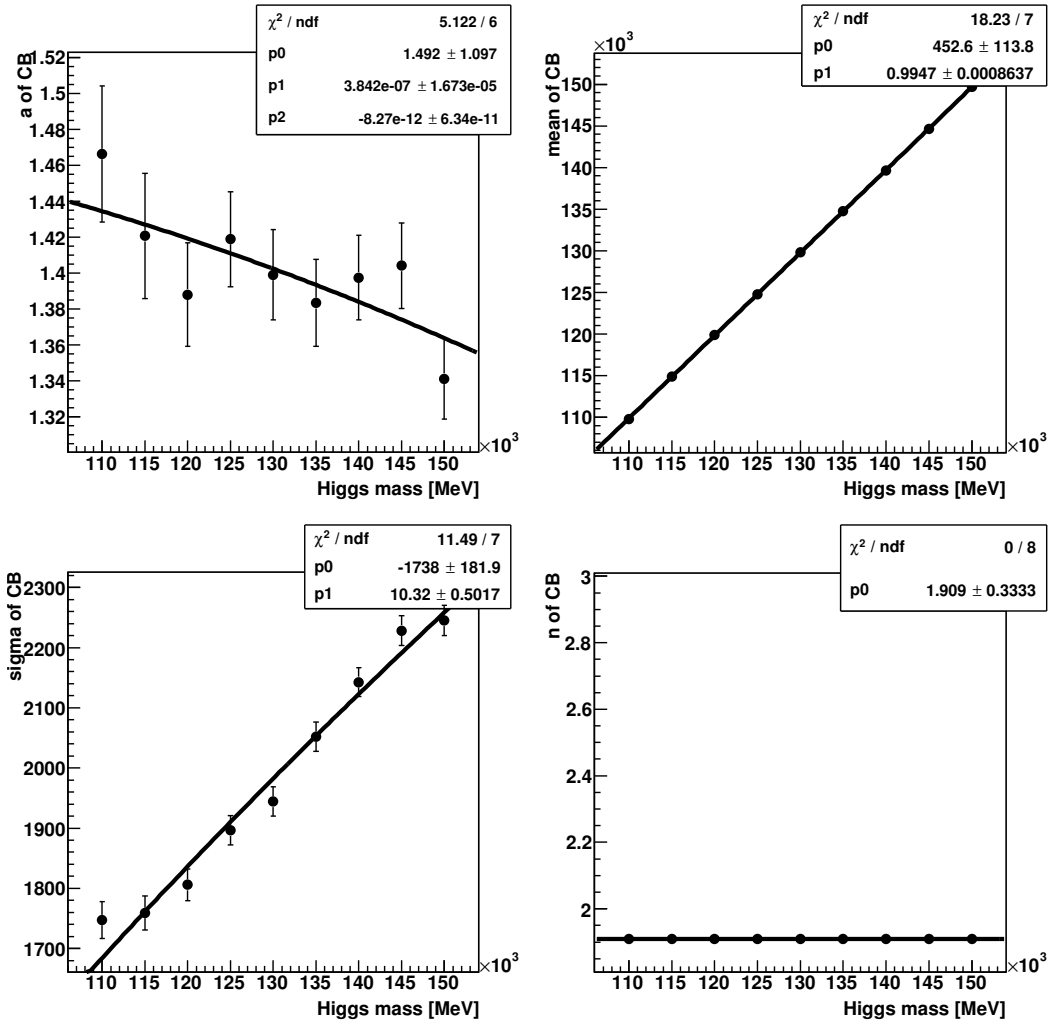


Figure 6.4: Fit results for the Crystal ball parameters shown for 4μ with n set to constant.

The parameters a and n describing the non-Gaussian tails of the Crystal ball are fitted by a second order polynomials $(p_0 + p_1 m_H + p_2 m_H^2)$. The parametric m_H dependence of the Crystal ball parameters is:

$$\begin{aligned}
\mu_{CB}(m_H) &= p_0 + p_1 m_H \\
\sigma_{CB}(m_H) &= p_0 + p_1 \sqrt{m_H} \\
a_{CB}(m_H) &= p_0 + p_1 m_H + p_2 m_H^2 \\
n_{CB}(m_H) &= p_0 + p_1 m_H + p_2 m_H^2,
\end{aligned} \tag{6.4}$$

where the ten parameters which are fitted to MC are highlighted in red.

The uncertainties on the best-fitted values for a and n are very large as shown in figure 6.3 and the choice of a second order polynomial is questionable. In figure 6.4, the parameter n is fixed for a Crystal ball function fitted to the signal MC samples. The value for n is determined by calculating the mean of the values obtained when keeping n floating in the fit. Therefore, after the fit to determine n, the seven remaining parameters are fitted to MC. Figure 6.4 shows the results for the 4μ channel and the figure for the other channels can be found in the appendix (A.4-A.6).

The parameter a decreases as a function of the Higgs mass. This shows that the transition region from the power law tail to the Gaussian component shifts[2] to smaller $\frac{x-\bar{x}}{\sigma}$. For the resulting CB pdf the probability of events in the non-Gaussian tail increases with m_H. A possible explanation for this enhancement of the tail for muons is the observed probability increase of the FSR depending on m_H. The FSR is mainly observed for on-shell Z bosons. As the percentage of on-shell Z bosons increases with $m_{4\ell}$, the effects of FSR becomes more sizeable. This increases the ratio of events in the lower energetic tail [122]. The FSR photons are corrected for $E_T > 1.0\,\text{GeV}$ which improves the resolution in the Z measurement as discussed in section 5.3.4 although 80% of the FSR photons have $E_T < 1.0\,\text{GeV}$ which are not corrected for [123]. Another possible explanation for the enhancement of the events in the non-Gaussian tail as a function of m_H is the increase of bremsstrahlung affecting mainly electrons. The CB function has also been studied with the vector boson fusion production modes using specific signal samples (sample 19).

[2]The parameter σ increases faster with m_H than the parameter a decreases. Therefore, the absolute distance of the transition region to the mean increases. However, the probability of the Gaussian component of the CB decreases as the transition to a power law happens at a smaller fraction of σ.

6.2.2 Additional physically motivated models

For low hypothesised Higgs masses $110\,\text{GeV} < m_H < 150\,\text{GeV}$, the natural width is at the order of $10^{-3} - 10^{-2}\,\text{GeV}$ as shown in figure 2.10 and is negligible in comparison to detector effects. The Breit Wigner (BW) function can be used to model the theoretical width of the Higgs boson [13]. For the detector effects, the BW function can be convoluted with a detector response function, for example, the Gaussian or Crystal ball function. A discrete convolution with the fast Fourier transformation (FFT) is applied as there is no analytical form for the convolution of a Crystal ball and a BW function [124].

This procedure results in the fits shown in figure 6.5 where the mean of the BW function is set to the true Higgs mass. In the first row the width of the BW function gBW is determined by the fit whereas in the second row the width is set to the theoretical expectation shown in figure 2.10. As the width of the BW function is at the order of $10^{-3} - 10^{-2}\,\text{GeV}$ for $110\,\text{GeV} < m_H < 150\,\text{GeV}$, it almost behaves like a delta function in the convolution. The FFT convolution takes too much CPU time to be applied when fitting to data.

The procedure can be refined by fitting the BW parameters to the distribution at the generator level instead of to the reconstructed Higgs mass. Due to high p_T photon emission, given the final state radiation, an asymmetric shape with a lower energetic tail is expected at the generator level which can be modelled by an asymmetric BW function. The convolution of a BW and a CB function can also be used to model the signal including per-event errors which are further discussed in section 6.5. The CB function modelling the detector response is then a conditional pdf with sigma proportional to the error on $m_{4\ell}$. Tests for this signal model are currently in progress.

Besides the minor impact of the natural width of the Higgs boson in the low mass region, a variety of detector effects govern the m_{4l} distribution. As shown in figure 3.6, the uncertainty on the momentum measurement of muons and electrons varies over the range of their momentum.

Many detector effects cause outliers in the $m_{4\ell}$ distribution, e.g., the poor reconstruction efficiency in the calorimeter crack region causes Higgs candidates to be measured with a larger uncertainty. This combination of effects is, given the central limit theorem, Gaussianly distributed so that besides the Crystal ball function an additional Gaussian function can be considered to describe the underlying physics processes. A model consisting of a sum of a Crystal ball and a Gaussian function has been employed by the $H \to \gamma\gamma$ analysis at the ATLAS experiment [125].

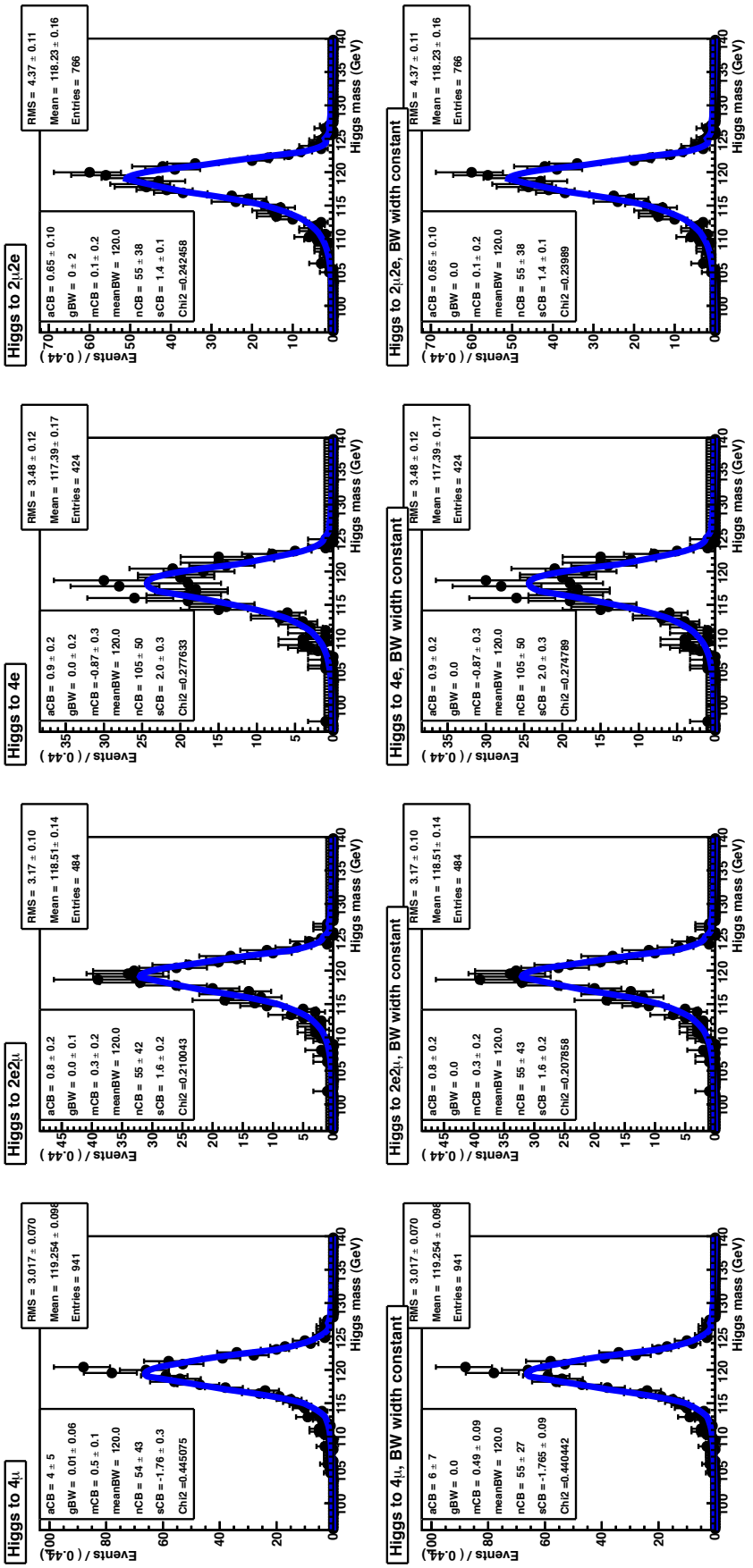


Figure 6.5: The convolution of a Crystal ball and a Breit-Wigner function is fitted to signal MC with $m_H = 120\,\text{GeV}$.

In figure 6.6, the residuals are shown for the fit of the Crystal ball function to the signal sample at $m_H = 110\,\text{GeV}$. A systematic oscillation is observed in the residuals. This oscillating structure shown at $m_H = 110\,\text{GeV}$ is representative for the systematic oscillation in the residual at other mass points between 110 GeV and 150 GeV. It shows the difficulties of modelling the simulated signal with a Crystal ball function. The periodic fluctuation can be observed where the pdf underestimates MC in the peak region and overestimates MC in region of the steep tails. In figure 6.7, the residual is shown for a fit of a sum of a Crystal ball and a Gaussian function. Comparing figure 6.6 with figure 6.7, the systematic effect in the residuals decreases when adding a Gaussian function. This motivates the use of an additional Gaussian function to improve the signal modelling.

In the following, the sum of a Crystal ball and a Gaussian function is fitted to a reprocessed version of the mc12a signal samples (sample 20) applying the full selection. Additional signal samples with mass points between 120 GeV and 130 GeV are used and MC weights, e.g., the pileup reweighting are applied.

All mass points are fitted simultaneously by a conditional fit where each parameter is described by a function of the hypothesised Higgs mass m_H. The total pdf $P(m_H, m_{4\ell})$ is defined as

$$P(m_H, m_{4\ell}) = R(m_{4\ell}|m_H)Y(m_H).$$

The resolution function $R(m_{4\ell}|m_H)$ consists of a sum of a Crystal ball and a Gaussian function in $m_{4\ell}$ where their parameters are dependent on m_H. The resolution function is multiplied by the function describing the yield $Y(m_H)$ modelling the number of signal events per mass point from MC.

The same fitting procedure has been conducted by the $H \to \gamma\gamma$ analysis [126]. The observable m_H is subtracted by 125 GeV so that the fitted parameters have a direct physical meaning. An example is the y-axis intercept of the linear uncertainty dependence $\sigma_{CB_{125}}$. It resembles the sigma of the CB at 125 GeV shown in equation 6.6. The resolution model is

$$\begin{aligned} &R(m_{4l}, \mu_{CB}, \sigma_{CB}, \alpha_{CB}, n_{CB}, f_{CB}, \mu_{GA}, \sigma_{GA}) \\ &= f_{CB} \cdot CB[m_{4l}, \mu_{CB}, \sigma_{CB}, \alpha_{CB}, n_{CB}] + (1 - f_{CB}) \cdot GA[\mu_{GA}, \sigma_{GA}] \end{aligned} \tag{6.5}$$

where M is the true Higgs mass in GeV. The model is summarised in figure 6.8.

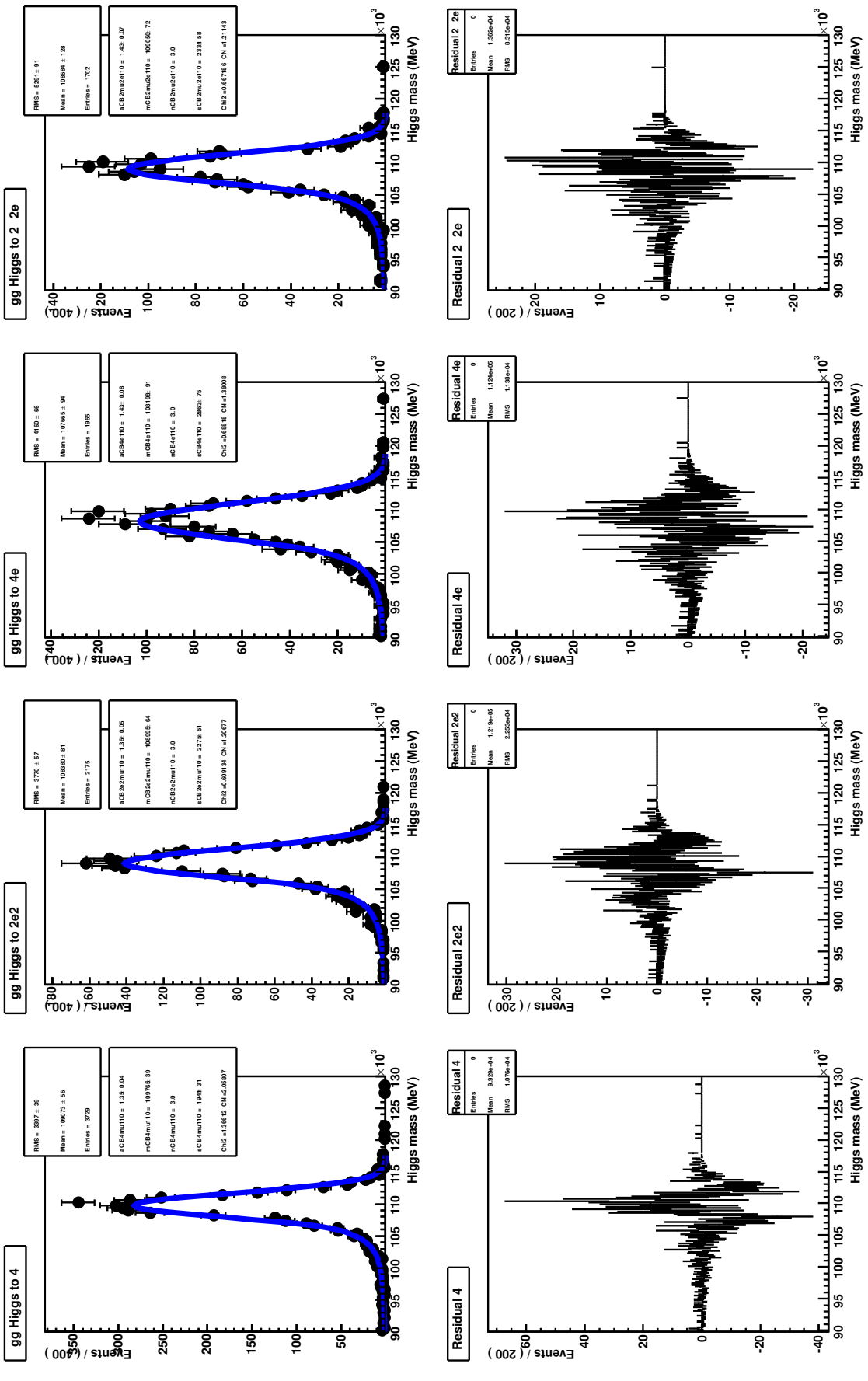


Figure 6.6: Fit results and residual of a Crystal ball function fitted to signal MC at $m_H = 110\,\text{GeV}$. In the residuals a periodic fluctuation can be observed where the pdf underestimates MC in the peak region and overestimates MC in region of the steep tails.

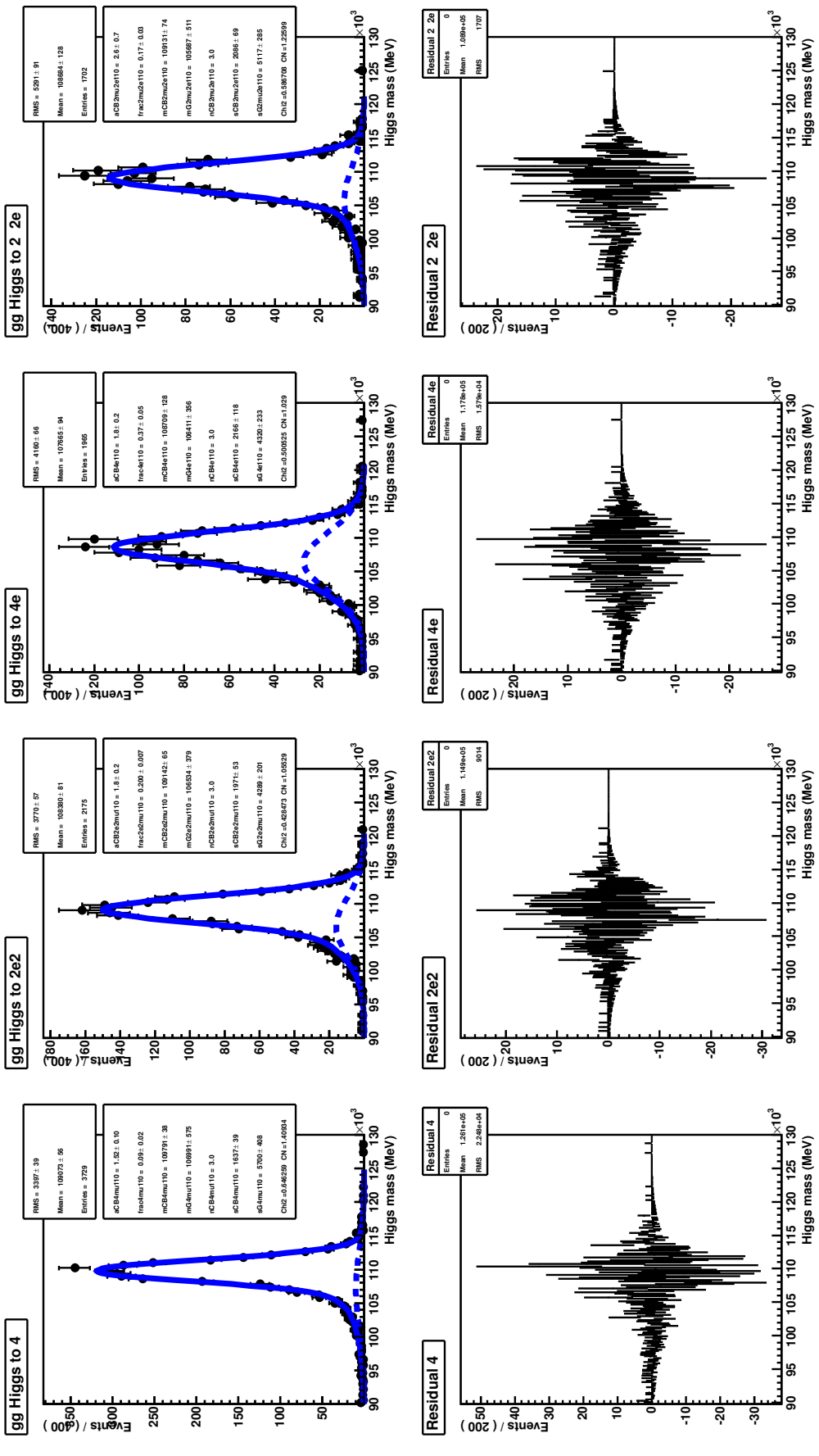


Figure 6.7: The fit of the sum of a Crystal ball and a Gaussian function is shown at $m_H = 110\,\text{GeV}$. The residual of the fitted function and the signal MC is well distributed without a systematic effects.

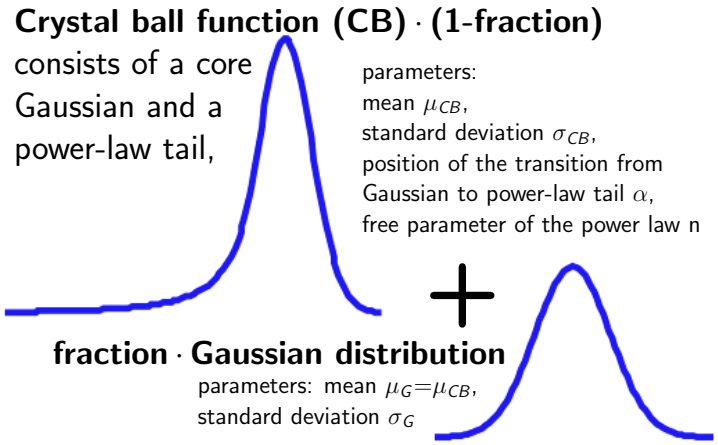


Figure 6.8: The signal model discussed consists of the sum of a Crystal ball and a Gaussian function.

Linear dependencies on M are assumed for the following parameters with the parameters to be fitted marked in red.

$$\begin{aligned}
\mu_{CB}(M) &= M + \mu_{CB_{125}} + \Delta_{\mu_{CB}}(M - 125\,\text{GeV}) \\
\sigma_{CB}(M) &= \sigma_{CB_{125}} + \Delta_{\sigma_{CB}}(M - 125\,\text{GeV}) \\
\alpha_{CB}(M) &= \alpha_{CB_{125}} + \Delta_{\alpha}(M - 125\,\text{GeV}) \\
\sigma_{GA}(M) &= \sigma_{GA_{125}} + \Delta_{\sigma_{GA}}(M - 125\,\text{GeV}) \\
n_{CB}(M) &= n_{CB_0} \\
f_{CB}(M) &= f_{CB_0}
\end{aligned} \tag{6.6}$$

The fraction of the Crystal ball contribution, f_{CB}, is fitted to a constant and the free parameter of the power law component of the Crystal ball, n_{CB}, is also fitted to a constant. The mean of the Gaussian and Crystal ball function are set to be equal. This results in a final 10 parameters of the model to be obtained from the fit:

$$\mu_{CB_{125}}, \Delta_{\mu_{CB}}, \sigma_{CB_{125}}, \Delta_{\sigma_{CB}}, \alpha_{CB_{125}}, \Delta_{\alpha}, n_{CB_0}, \sigma_{GA_{125}}, \Delta_{\sigma_{GA}}, f_{CB_0}. \tag{6.7}$$

These parameters have been determined in the simultaneous conditional fit and the resulting resolution model is shown depending on $m_{4\ell}$ and the true Higgs mass m_{truth} in figure 6.9 as an example for the 4μ final state.

Figure 6.10 shows the final CB+GA model plotted together with the MC simulation for several mass points of the 4μ final state. The fraction of the Gaussian function is

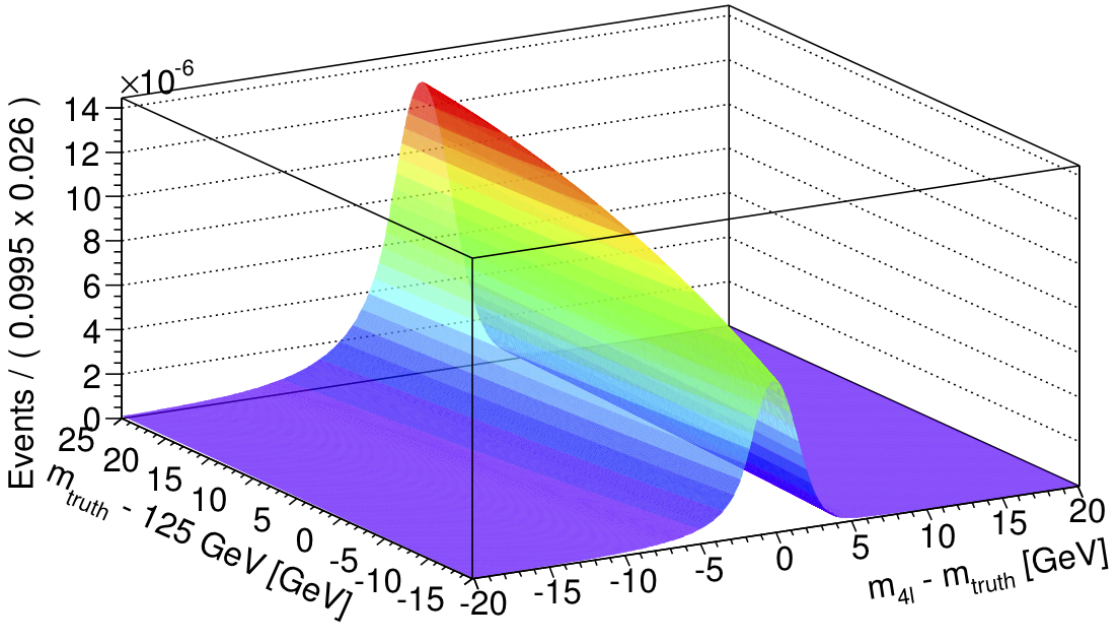


Figure 6.9: The composition of a signal model is shown consisting of the sum of a Crystall ball and a Gaussian function where the colours represent the changes on the z-axis.

largest in channels with electrons, but never exceeds 10%. The electron channels gain more significantly from an additional Gaussian function than the 4μ channel. As shown in figure 6.7, the systematic effect seen in the residuals of the fit is reduced by the additional Gaussian function, particularly in the electron channels. This parametric model (CB+GA) describes the signal simulation well over a mass range of $110\,\text{GeV} \leq m_H \leq 150\,\text{GeV}$. In the peak region the probability is slightly underestimated using the sum of a Crystal ball and Gaussian function as shown in figure 6.10 (particularly at 125 GeV).

It has been studied whether the quality of the signal description can be improved by keeping the mean of the Gaussian and Crystal ball function independent. The percentage error on the fitted mean and sigma of the CB have been measured for three different scenarios ($\mu_{GA} < \mu_{CB}$, $\mu_{GA} > \mu_{CB}$, $\mu_{GA} = \mu_{CB}$), shown in table 6.2 for $m_H = 125\,\text{GeV}$.

The parameter σ_{GA} is determined with a precision of about 2% in all three scenarios ($\mu_{GA} < \mu_{CB}$, $\mu_{GA} > \mu_{CB}$, $\mu_{GA} = \mu_{CB}$) and therefore not sensitive to the dependency between mean of the Crystal ball and the Gaussian function. As shown in table 6.2, the mean of the signal model is most precisely determined when the mean of the Crystal ball and Gaussian function are equal. This assumption simplifies the model, resulting in two less parameters and reduces the statistical error on μ. In addition, biases from the Gaussian distribution in the fit are avoided and the treatment of the systematics is

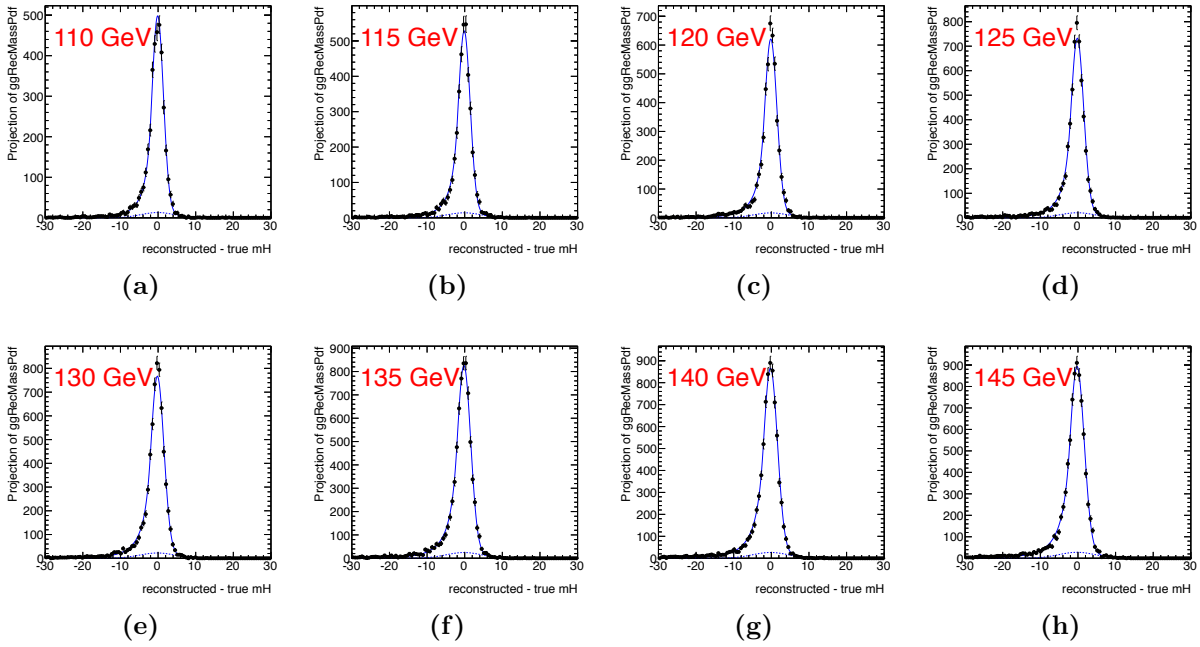


Figure 6.10: Signal resolution for a simulation of $m_H = 125\,\text{GeV}$ without Z-mass constraint applied using the sum of a Crystal ball and a Gaussian function. This signal model describes the MC simulated samples well over the mass range $110\,\text{GeV} \leq m_H \leq 150\,\text{GeV}$.

Error at 125 GeV [%]	**CB+GA**	
	μ_{CB}	σ_{CB}
$\mu_{GA} < \mu_{CB}$	4.4%	0.51%
$\mu_{GA} > \mu_{CB}$	5.3%	0.72%
$\mu_{GA} = \mu_{CB}$	2.0%	0.67%

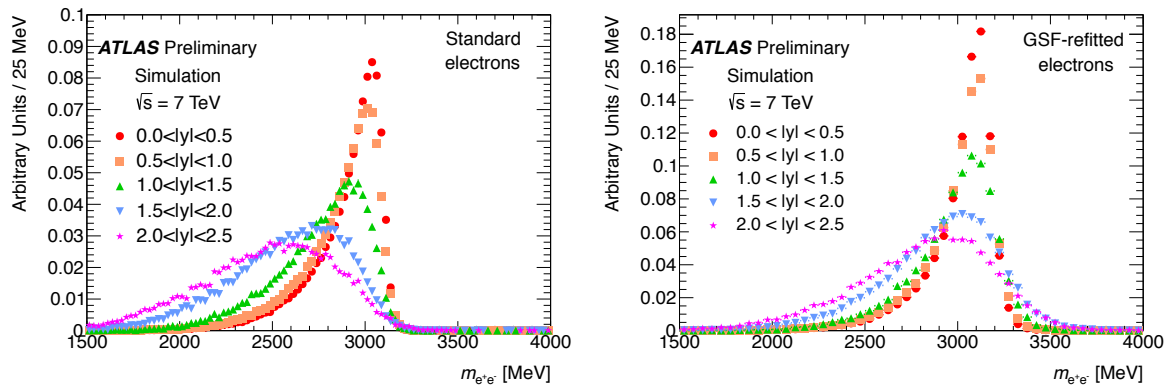
Table 6.2: Percentage error at 125 GeV for a gluon-gluon fusion signal model of the sum of a Crystal ball and a Gaussian function for the 4μ channel as a representative example.

simplified as correlations are avoided and the mean has the correct uncertainties.

The other production modes have been studied with the model of a sum of a Crystal ball and a Gaussian function. The second most common production mode after gluon-gluon fusion, is vector boson fusion. This can also be well modelled by a sum of a Crystal ball and a Gaussian function as studied with signal samples (sample 21) generated by Powheg [106]. The other production modes were difficult to model given the limited number of events of the samples. A simplified model of a double Gaussian was studied as a signal shape but the lower energetic tail could not be described well.

6.3 Categorisation by detector region

A large number of detector effects can influence the signal shape and to overcome part of the complexity of this mixture, the categorization of events can help to analyse the signal shape. The detector region where the leptons are detected plays a major role. This is shown for $J/\psi \to e^+e^-$ at different rapidity regions in reference [111]. Different CB shapes are applied for the different detector categories divided into rapidity regions of $\Delta y = 0.5$ in the range $0 < \eta < 2.5$. The width of the Crystal ball increases strongly for larger pseudorapidity as shown in figure 6.11. The improvement using the GSF is shown, which is used in the H$\to ZZ^{(*)} \to 4\ell$ analysis as described in section 5.3.3.



(a) **(b)**

Figure 6.11: The invariant mass distribution is shown for the $J/\psi \to e^+e^-$ analysis using the standard reconstruction (6.11a) and using GSF-refitted electrons (6.11b) for the simulated signal samples. The signal shape depends strongly on the detector region and the mean is stabilised applying the GSF algorithm [111].

The peak region shifts to lower energies in the forward region without applying the GSF. For GSF-refitted electrons, the peak region remains approximately at the same energy over all detector regions. The width of the Crystal ball decreases when the GSF is applied.

To include the resolution differences in pseudorapidity in the $H \to ZZ^{(*)} \to 4\ell$ analysis, the resolution has been studied depending on the detector region. For muons the best resolution is obtained in the pseudorapidity region $|\eta| < 1.05$ as shown in reference [127]. This detector region, in the following referred to as the muon barrel region, is covered by the ID barrel which is the ID region with the best alignment. Outside the muon barrel region, the muon momentum resolution degrades, affected by a large amount of dead material [52]. For the electrons, the region $|\eta| < 1.37$ is most sensitive,

in the following referred to as the electron barrel region. This region is confined by the calorimeter crack region at $1.37 < |\eta| < 1.52$. The crack region suffers from a lot of material in front of the electromagnetic calorimeter, in particular from ID services [111].

Each of the four final states is subdivided into four categories, for instance, for the 4μ final state the categories depend on the number of muons detected in the muon barrel region (all four muons in the barrel, three muons in the barrel, two muons in the barrel, all remaining events). All 16 categories are summarised in table 23 in reference [128].

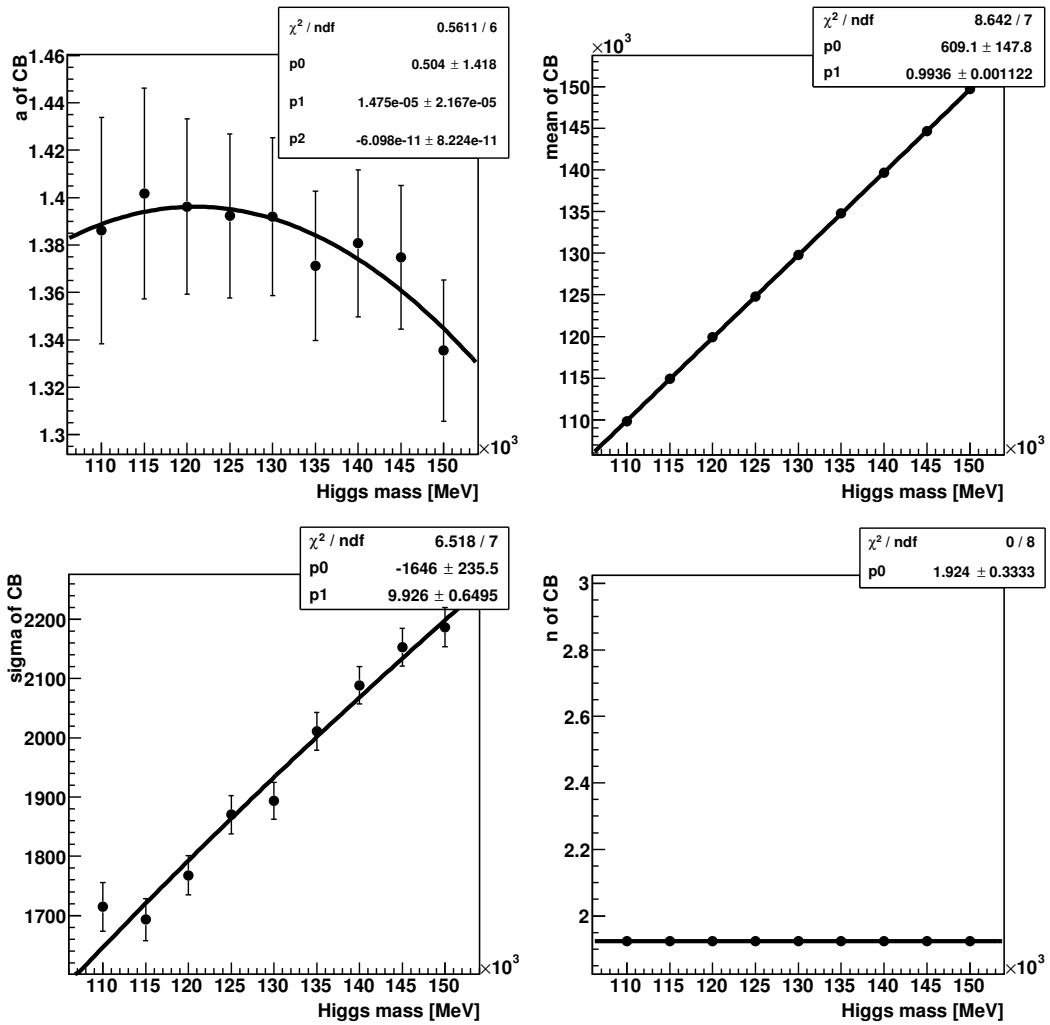


Figure 6.12: Fits results for the Crystal ball parameters are shown for 4μ with n set to constant and all muons detected at $|\eta| < 1.05$.

The mass resolution depends strongly on the detector categories. For example, the resolution improves by 50 MeV for $m_H = 125\,\text{GeV}$ studying the final state with all 4μ detected in the barrel region. This is shown in figure 6.12 in comparison to the result for 4μ without detector categorisation (figure 6.4). By using the 16 detector categorisations

the available number of events of the MC samples is subdivided to determine the CB+GA parameters. This resulted in a subset which had too limited number of events to develop a robust model.

A better option to improve the signal model is to use the errors on the reconstructed mass on an event by event basis. For this the errors calculated for the momentum measurement of each electron are propagated to the reconstructed mass error. The obtained distribution of the errors can then be used to subdivide the events into slices with a similar uncertainty on the reconstructed mass. To each of these slices, a separate CB function can be fitted integrating additional information about the error distribution. The slices, keeping the statistical analysis simplified and saving CPU-time, can be also avoided with a full per-event error implementation as further discussed in subsection 6.5.

6.4 Development of fitting framework

Using the shapes determined for the different event classes (signal and background), the percentage of data belonging to each category is determined by a maximum-likelihood fit [129]. For this, the total likelihood function is the product of the pdf, f, evaluated for the quantities $\vec{x_i}$ of each event $L(\vec{\theta}) = \prod_i^N (f(\vec{x_i}; \vec{\theta}))$ where $\vec{\theta}$ is a set of parameters [14]. Note that k variables are observed, $\bar{x} = x_{1,..,k}$, where N observations of the same variable are made and each component x_i refers to a different variable, but the density function is the same [130]. Maximising the Log-Likelihood leads to the estimators of θ for which the likelihood function is maximised where $\hat{\theta}$ can be the results for the parameter of interest. The likelihood term is multiplied by a Poissonian probability determining the total number of events:

$$L(\vec{\theta}) = \frac{\exp \nu(\vec{\theta}) \nu(\vec{\theta})^n}{n!} \prod_i^N (f(\vec{x_i}; \vec{\theta})). \tag{6.8}$$

The total number of events can also depend on the same set of parameters as denoted by $\nu(\vec{\theta})$. Assuming two event classes k, signal s and background b, the likelihood function can be written as the sum of the components:

$$L(\vec{\theta}) = \prod_i^N \left(\sum_{k=s,b} N_k f_k(\vec{\theta}) \right) \text{[131]}. \tag{6.9}$$

Taking into account the Poissonian term to obtain the extended likelihood, the expected total number of events ν consists of the signal events s with the signal strength μ and

the background events b: $\nu = \mu s + b$. The pdfs $f_k(\vec{\theta})$ are weighted by the number of events expected for the class k resulting in the extended likelihood function:

$$L(\mu, \vec{\theta}) = \frac{e^{-\mu s(\vec{\theta})+b(\vec{\theta})}}{n!} \prod_{i=1}^{n} \left(\mu s f_s(\vec{x_i}; \vec{\theta}) + b f_b(\vec{x_i}; \vec{\theta}) \right) \text{ [132]}. \tag{6.10}$$

A new fitting machinery has been developed to accomplish the statistical analysis. It consists of a "workspace" which is a RooFit[3] [133] object containing data events, systematics and all the pdfs. It is created for the needs of this analysis and is flexible to use additional models. It also helps facilitates the Higgs combination results. It was rigorously validated against the results published at ICHEP 2012 and used for the publications since then. This allows the implementation of various signal models in the fitting. An initial study accomplished with the new machinery was the determination of the gain by splitting the analysis into four final states according to the type of lepton (electrons or muons).[4]

6.4.1 Splitting into different channels

To set limits on the Higgs hypothesis, the upper exclusion limits were studied. The background-only and signal+background hypothesis are studied where μ is the signal strength. The test statistic is defined as

$$Q = \frac{L(data|\mu = \mu_{test}, \hat{\hat{\theta}}(\mu_{test})}{L(data|\mu = 0, \hat{\theta}(0))} \tag{6.11}$$

where μ_{test} is fixed to the probed signal strength and $\vec{\theta}(\mu_{test})$ is optimised given the probed signal strength which is denoted by two hats. In the denominator the likelihood is evaluated for a signal strength of zero and the remaining parameters are optimised for a signal strength of zero denoted by $\hat{\theta}(0)$. The test statistic is a discriminant that serves as a continuous scale to order results between background-like and signal-like.

The confidence level of a signal exclusion is defined as

$$CL_{s+b} = P_{s+b}(Q \leq Q_{obs}),$$

[3] RooFit is a library containing fitting objects to support the statistical analysis.

[4] The analysis was already split into four channels according to the four final states before the data taking started to optimize the analysis technique increasing its sensitivity of the search. With this study the improvement on the exclusion limit is cross-checked obtained by splitting into four channels.

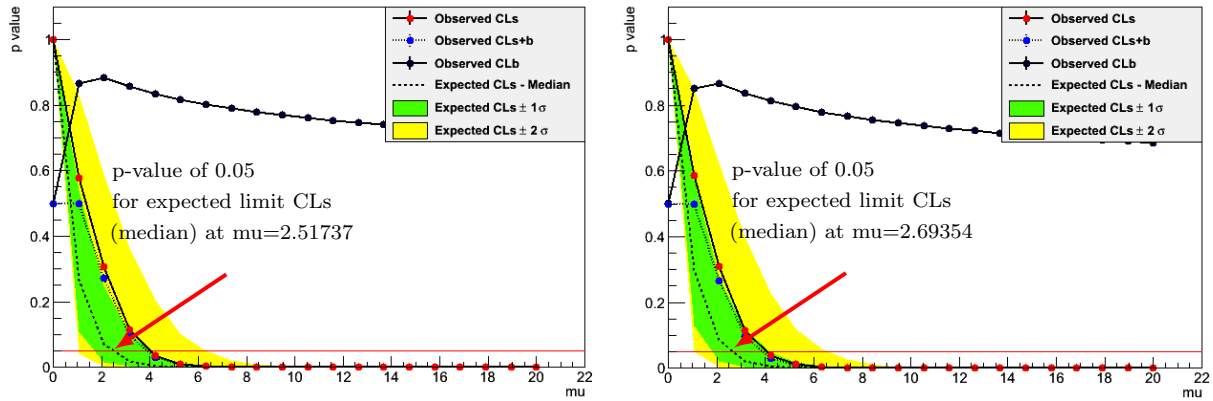
where $P_{s+b}(Q \leq Q_{obs})$ is the probability that the test statistics is smaller than the observed test statistics assuming the signal+background hypothesis. The confidence level for excluding the background-only hypothesis, also known as local p-value, is defined as

$$1 - CL_b = P_b(Q \geq Q_{obs})$$

giving the probability that the background-only hypothesis results in a test statistic at least as signal-like as the observed test statistic. To evaluate the probability distributions depending on the test statistics, pseudo-experiments are generated assuming the signal+background and background only hypothesis. The probability $P_{s+b}(Q \leq Q_{obs})$ and $P_b(Q \geq Q_{obs})$ are then determined by integrating over the according test statistic range [134]. To avoid signal exclusions in case there is no sensitivity [135], CL_{s+b} is regulated by dividing by CL_b resulting in

$$CL_s = \frac{CL_{s+b}}{CL_b}. \tag{6.12}$$

Given $P_b(Q \geq Q_{obs}) \leq 1$, the CL_s method is more conservative than CL_{s+b} with $CL_s \leq CL_{s+b}$. These quantities are given in figure 6.13 for $m_H = 125\,\text{GeV}$ using $4.8\,\text{fb}^{-1}$. Already with this amount of data taken in 2011, an upward fluctuation of the observed signal strength exclusion at a 95% CL with respect to the expected signal strength



(a) separate fit for 4μ, $2e2\mu$, $4e$ and $2e2\mu$ **(b)** combined fit

Figure 6.13: Expected and observed exclusion limit shown for a SM Higgs boson at $m_H = 125\,\text{GeV}$ using $4.8\,\text{fb}^{-1}$. The expected exclusion limit is 7% smaller if the combined exclusion limit is determined by fitting the four final states separately 6.13a than without this discrimination 6.13b.

exclusion can be observed for $m_H = 125\,\text{GeV}$. The shift of the observed exclusion limit lies within the one σ band of the expected exclusion limit.

The expected signal strength to be excluded at 95% CL reduced by 7% from a signal strength of 2.7 to 2.5 by splitting the analysis into four different channels. This is shown in figure 6.13 where the dashed line crosses the red horizontal line. The study confirms the sensitivity optimisation by splitting the analysis into four channels, corresponding to their final states.

6.5 Per-event error

The resolution of the ATLAS detector varies in the detector regions and depends on the momentum, energy and type of the detected particle. Therefore, the resolution changes on an event-by-event basis and each candidate can be characterised by the measurement of its mass and associated error [131]. Using these two observables in the final fit, events get more weight than others when the error on their mass measurement is small. Exploiting this additional information can lead to a better measurement with the same data [133].

6.5.1 Per-event error calculation

The error on the invariant four-lepton mass is derived from the detector resolution measuring the four leptons and the shift occurring from final state radiation.

The Higgs mass

$$m^2 = (E_1 + E_2 + E_3 + E_4)^2 - (\vec{p_1} + \vec{p_2} + \vec{p_3} + \vec{p_4})^2$$
$$= \left(\sum_{i=1}^{4} E_i^2 + \sum_{i=1}^{3}\sum_{j>i}^{4} 2E_iE_j\right) - \left(\sum_{i=1}^{4} \vec{p_i}^2 + \sum_{i=1}^{3}\sum_{j>i}^{4} 2\vec{p_i}\cdot\vec{p_j}\right)$$

can be simplified with the approximation that the mass of the muons and electrons is a negligible contribution to their energy E_i. Therefore, the energy terms can be simplified using $E = \sqrt{m^2 + \vec{p}^2} \approx |\vec{p}|$ resulting in

$$
\begin{aligned}
m^2 \approx \sum_{i=1}^{4} p_i^2 + \sum_{i=1}^{3}\sum_{j>i}^{4} 2p_i p_j - \sum_{i=1}^{4} \vec{p_i}^{\,2} - \sum_{i=1}^{3}\sum_{j>i}^{4} 2\vec{p_i}\cdot\vec{p_j} \\
= \sum_{i=1}^{3}\sum_{j>i}^{4} 2p_i p_j(1-\cos\theta_{ij}) \\
= \sum_{i=1}^{4}\sum_{j=1,j\neq i}^{4} p_i p_j(1-\cos\theta_{ij}),
\end{aligned}
$$

where p_i is the modulus momentum of the lepton and θ_{ij} is the angle between a lepton pair ij. The error in θ_{ij} is negligible in comparison to the error on the momentum. Therefore, applying the error propagation for the mass

$$
\sigma_m = \sqrt{\sum_{i=1}^{4}\left(\frac{\partial m(p_1,p_2,p_3,p_4,\theta)}{\partial p_i}\right)^2 \sigma_{pi}^2 + \left(\frac{\partial m(p_1,p_2,p_3,p_4,\theta)}{\partial \theta}\right)^2 \sigma_\theta^2} \tag{6.13}
$$

$$
\approx \sqrt{\sum_{i=1}^{4}\left(\frac{\partial m(p_1,p_2,p_3,p_4,\theta)}{\partial p_i}\right)^2 \sigma_{pi}^2}, \tag{6.14}
$$

we can derive its associated error as a function of the momentum resolution by taking the derivative of $m(p_1,p_2,p_3,p_4,\theta) = \sqrt{\sum_{i=1}^{4}\sum_{j=1,j\neq i}^{4} p_i p_j(1-\cos\theta_{ij})}$.

$$
\sigma_m = \sqrt{\sum_{i=1}^{4}\left(\frac{1}{2m}\sum_{j=1,j\neq i}^{4} 2p_j(1-\cos\theta_{ij})\right)^2 \sigma_{p_i}^2} \tag{6.15}
$$

$$
= \frac{1}{m}\sqrt{\sum_{i=1}^{4}\left(\sum_{j=1,j\neq i}^{4} p_j(1-\cos\theta_{ij})\right)^2 \sigma_{p_i}^2}, \tag{6.16}
$$

The muon momentum can be independently measured by the inner detector and the muon system. These measurements can be used to cross check each other, or they are combined to determine a single muon trajectory. The momentum resolution of the muons is dependent on the coordinates of the trajectory given in η and ϕ. For a fixed η, the momentum resolution in the muon system is

$$
\frac{\sigma(p)}{p} = \frac{p_0^{MS}}{p_T} \oplus p_1^{MS} \oplus p_2^{MS}\cdot p_T. \tag{6.17}
$$

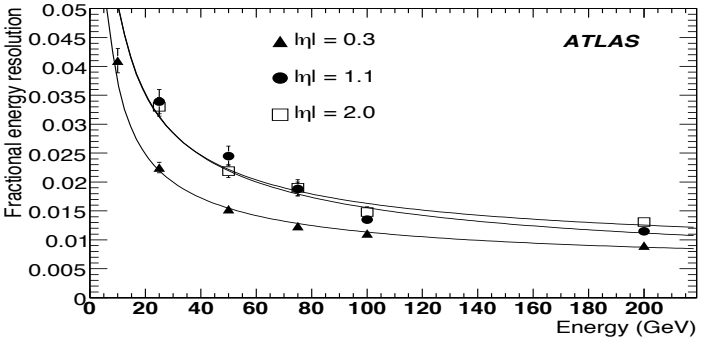


Figure 6.14: The fractional energy resolution is shown for electrons with different energies detected in the inner barrel ($|\eta| = 0.3$), the outer barrel ($|\eta| = 1.1$) and the end-cap ($|\eta| = 2.0$) [36].

The uncertainty on the energy loss in the calorimeter material is given by p_0^{MS} [136]. The coefficient p_1^{MS} takes into account the multiple scattering and p_2^{MS} denotes the intrinsic detector resolution. A dependence on p_T is also observed for the muon momentum resolution in the inner detector

$$\frac{\sigma(p)}{p} = p_1^{ID} \oplus p_2^{ID} \cdot p_T \quad \text{for} \quad |\eta| < 1.9 \tag{6.18}$$

$$\frac{\sigma(p)}{p} = p_1^{ID} \oplus p_2^{ID} \cdot p_T \frac{1}{\tan\theta^2} \quad \text{for} \quad |\eta| > 1.9. \tag{6.19}$$

The coefficient p_1^{ID} describes the effect of multiple scattering on the resolution and p_2^{ID} stands for the intrinsic resolution [137]. The momentum resolution of the ID worsens outside the TRT coverage ($|\eta| > 1.9$). The experimentally determined values for the coefficients can be obtained from reference [136].

The electron energy is measured by the calorimeter with a resolution depending on the energy and pseudorapidity. In equation 3.3, the electron energy resolution is given as a function of the energy, where the sampling, noise and constant term depend on η. In figure 6.14 the fractional electron resolution is shown for different energies in the inner barrel, the outer barrel and the end-cap. At high η more material is in front of the calorimeter decreasing the energy resolution due to bremsstrahlung as shown by the dependence of the CB resolution function on the detector region in figure 6.11.

The Higgs mass resolution can be calculated as the sum of the detector resolution, consisting of the error propagation of the muon momentum and electron energy resolution, and the final state radiation, where the emitted low-energetic photons are very difficult to detect. If the Z-mass constrained is applied, it also affects the mass and error distribution.

With the obtained values for the mass error, the pdfs for signal and background now depend on two observables, the reconstructed four-lepton mass and the respective error resulting in the following fitting function

$$L = \prod_{i}^{N} \left(\sum_{k=S,B} N_k \mathcal{P}_k(m_{4\ell}|m_{4\ell err}) \mathcal{P}_k(m_{4\ell err}) \right) \tag{6.20}$$

where $\mathcal{P}_k(m_{4\ell err})$ is the pdf of the error and $\mathcal{P}_k(m_{4\ell}|m_{4\ell err})$ is the distribution of the reconstructed mass given the error [24]. The distribution of the per-event needs to be handled correctly for background and signal events to avoid biases described by Punzi [131]. If all error distributions are identical, they do not need to be included in the likelihood. In the $H \to ZZ^* \to 4\ell$, the error distributions differ as shown in figure 6.15.

In this case, an event with a specific mass error has a different probability to be a signal or a background event. If the correlation is not included, the event will enter both terms of the likelihood during the calculation of both event categories with the same probability. Therefore, a wrong probability is assumed and biases are introduced (also referred to as Punzi-bias) [131].

The additional observable, $m_{4\ell err}$, provides more rejection power with additional information about the different mass error pdfs in the background and signal category. This is expected to improve the resolution of the parameters of interest in the fit.

The dependence of the two observables results in a 2-dimensional function as shown by the smoothed histogram in figure 6.16. The joint probability of $m_{4\ell}$ and $m_{4\ell err}$ is defined as

$$P_k(m_{4\ell}, m_{4\ell err}) = P_k(m_{4\ell}|m_{4\ell err}) P_k(m_{4\ell err}) = P_k(m_{4\ell err}|m_{4\ell}) P_k(m_{4\ell}). \tag{6.21}$$

$P_k(m_{4\ell}, m_{4\ell err})$ is normalised as

$$\int \int P_k(m_{4\ell}, m_{4\ell err}) dm_{4\ell} dm_{4\ell err} \equiv 1$$

and $P_k(m_{4\ell}|m_{4\ell err})$ is normalised as

$$\int P_k(m_{4\ell}|m_{4\ell err}) dm_{4\ell} \equiv 1$$

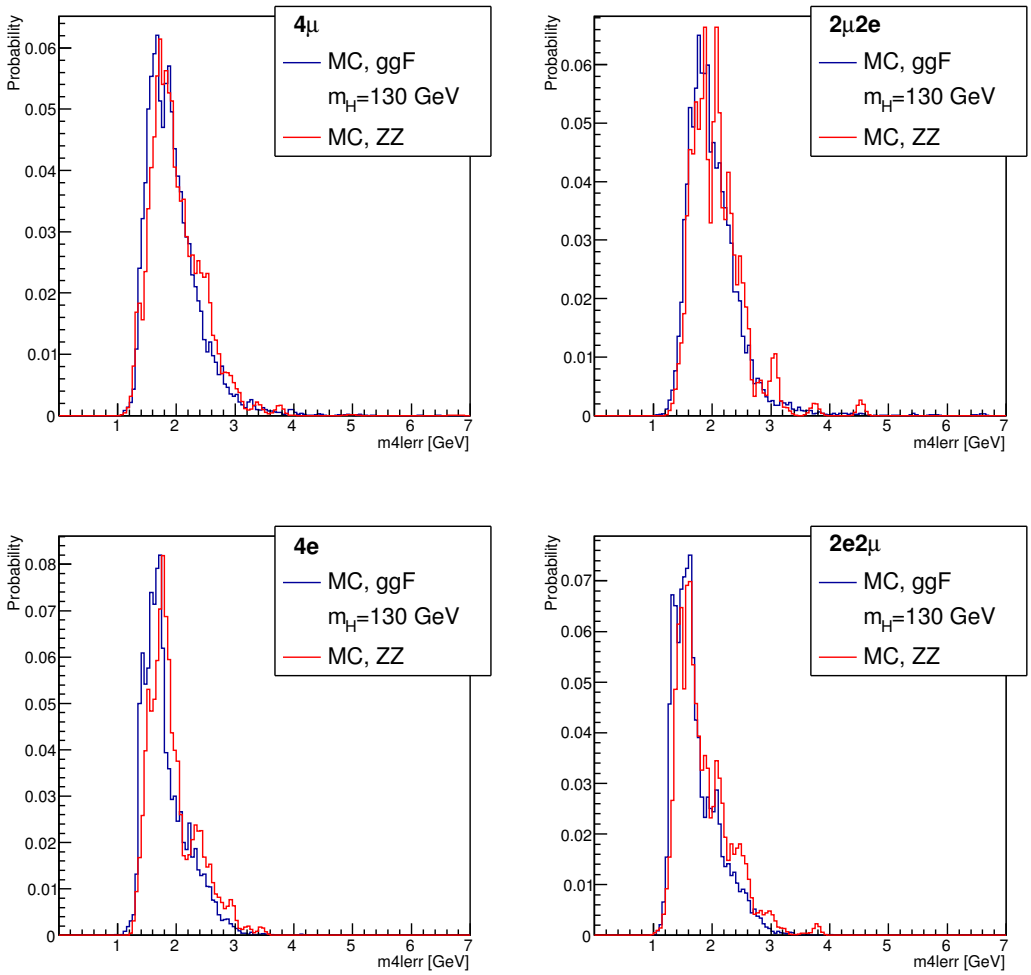


Figure 6.15: The MC distributions of the mass error are shown in the four final states for the ggF signal at $m_H = 130\,\text{GeV}$ and the ZZ background with a cut on $110\,\text{GeV} < m_{4\ell} < 150\,\text{GeV}$.

for each $m_{4\ell err}$-value [133]. Given the product of the conditional pdf of $m_{4\ell}$ given $m_{4\ell err}$ and the pdf of $m_{4\ell err}$, it follows

$$\begin{aligned} &\int\int P_k(m_{4\ell}|m_{4\ell err})P_k(m_{4\ell err})dm_{4\ell}dm_{4\ell err} \\ &= \int\left(\int P_k(m_{4\ell}|m_{4\ell err})dm_{4\ell}\right)P_k(m_{4\ell err})dm_{4\ell err} \\ &= \int 1\cdot P_k(m_{4\ell err})dm_{4\ell err} = 1. \end{aligned}$$

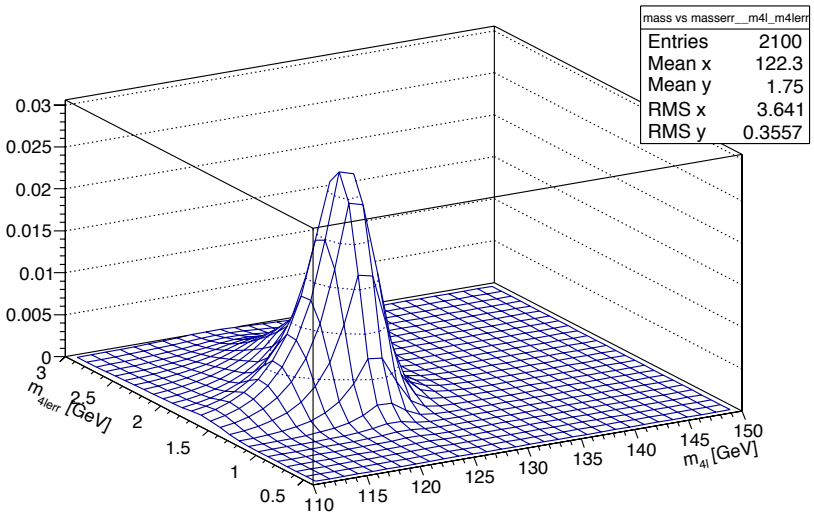
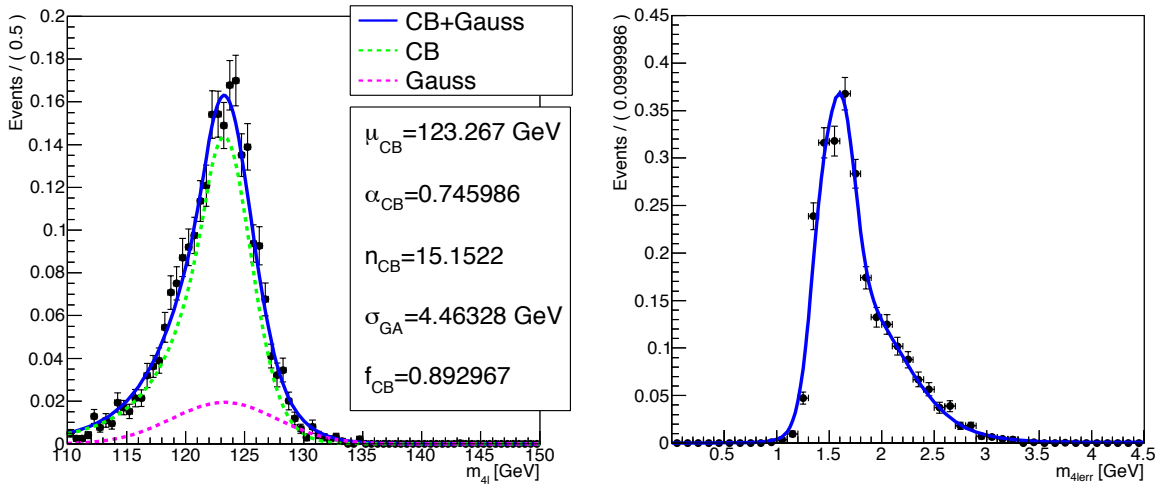


Figure 6.16: 2D smoothed histogram is shown for the $H \to ZZ^* \to 4e$ channel at 125 GeV.

6.5.2 Per-event error pdfs

Several signal models were studied to model the per-event error in H$\to ZZ^{(*)} \to 4\ell$. Besides a non-parametric approach, a study was performed whereby a function fitted to the generator level was convoluted with the detector resolution function. In this thesis the modelling using a conditional pdf is further investigated and the applied pdfs provide a solution for more limited CPU time.



(a) **(b)**

Figure 6.17: The $H \to ZZ^{(*)} \to 4e$ signal model is shown with the sum of a Crystal ball and a Gaussian function for $P_k(m_{4\ell}|m_{4\ell err})$ 6.17a and smoothed histogram for $P_k(m_{4\ell err})$ 6.17b.

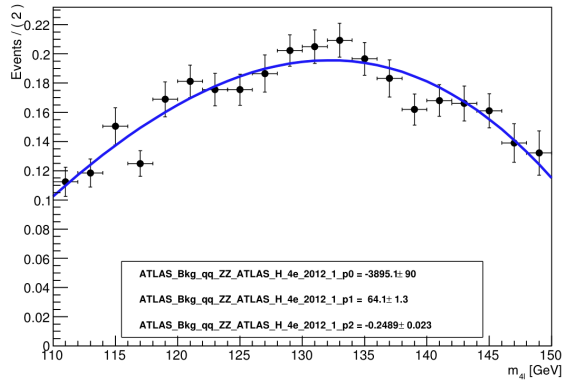
For the conditional signal pdf $P_k(m_{4\ell}|m_{4\ell err})$, a single Crystal ball function and the sum of a Crystal ball and a Gaussian function were studied. The corresponding error distribution $P_k(m_{4\ell err})$ was fitted by a Pearson Type IV distribution [138] or smoothed histogram. The Pearson Type IV distribution is a continuous probability function where k is a normalisation constant and m, ν, a and λ are real-valued parameters:

$$f(x) = k\left[1 + \left(\frac{x-\lambda}{a}\right)^2\right]^{-m} \exp\left[-\nu \arctan\left(\frac{x-\lambda}{a}\right)\right]$$
$$\text{for} \quad -\infty < x < \infty \quad \text{where} \quad m < \frac{1}{2}$$

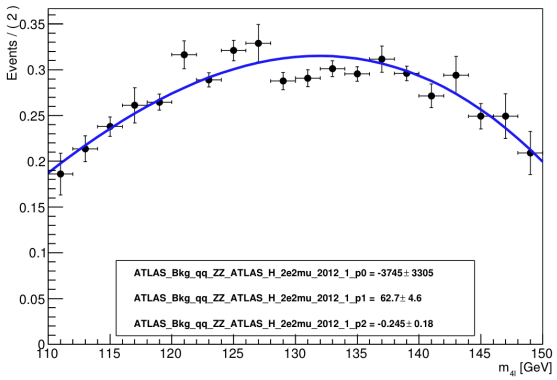
The Pearson Type IV distribution models the error of the invariant mass of the 4 leptons allowing for an asymmetric tail. This function describes the $H \to ZZ^{(*)} \to 4\mu$ signal well when no Z-mass constraint is applied. For the electron channels the error distribution is modelled by a smoothed histogram as shown in figure 6.17b. The conditional pdf shown in figure 6.17a is modeled by the sum of a Crystal ball and a Gaussian function with the same mean for the two distributions. The components of this model are shown in figure 6.17a where the Gaussian function accounts for a fraction of 9% of the full model.

The width of the Crystal ball is the event-by-event error, $m_{4\ell err}$, multiplied by a global scale factor. If the estimated size of the errors is in general too small or too large the global scale factor can account for this and the physics parameter σ_{CB} is at first order not affected. It can also be checked with the scale factor whether undesired general biases of the error modelling are present which would pull the scale factor away from its ideal value of 1. If the pull-distribution of the error estimates is not Gaussian, higher order dependencies are acting between σ_{CB} and $m_{4\ell err}$ which the scale factor can not absorb [133].

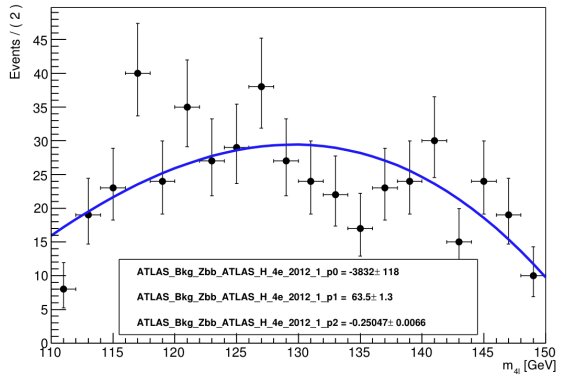
For the background modelling, the $m_{4\ell}$ distribution does not change significantly depending on $m_{4\ell err}$. The mean of the $m_{4\ell err}$ distribution of the background increases proportionally to $m_{4\ell}$. Therefore, a modelling of $P_k(m_{4\ell err}|m_{4\ell})P_k(m_{4\ell})$ is recommended for the background resulting in the same overall model as given in equation 6.21. A polynomial function is studied for $P_k(m_{4\ell})$ and a Pearson Type IV distribution has been considered for $P_k(m_{4\ell err}|m_{4\ell})$. A second order polynomial function is fitted to the $m_{4\ell}$ background distribution as shown for the $qqZZ$ and Zbb background in the $4e$ and $2e2\mu$ final state in figure 6.18. A similar shape is expected for the $qqZZ$ and Zbb background over the mass range of [110 GeV, 150 GeV]. The second order polynomial function models the $m_{4\ell}$ distributions well. Some fluctuations are seen in the $4e$ final state of the Zbb



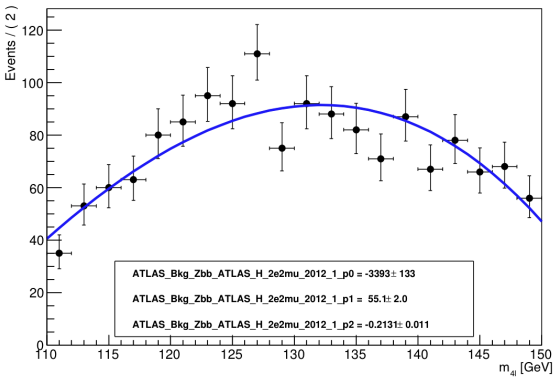
(a) $qqZZ$ background for $4e$ final state



(b) $qqZZ$ background for $2e2\mu$ final state



(c) Zbb background for $4e$ final state



(d) Zbb background for $2e2\mu$ final state

Figure 6.18: Invariant mass distribution for the irreducible $qq \to ZZ \to 4e$ (6.18a) and $qq \to ZZ \to 2e2\mu$ (6.18b) background and the reducible $Zbb \to 4e$ (6.18c) and $Zbb \to 2e2\mu$ (6.18d) background. The $qqZZ$ events simulated with PowHeg and the Zbb events simulated with Alpgen are fitted by a second order polynomial.

background which are however not significant given the limited number of events. The $m_{4\ell err}$ distributions were not modelled well by the test functions including the Pearson Type IV distribution. Therefore, besides this parametric approach, also a smoothed 2-dimensional histogram was studied and applied in the analysis framework used in the following chapters. The smoothing of the 2-dimensional histogram was optimised to include all essential structure, but to avoid binning artefacts as shown in figure 6.19 for the $qq \to ZZ \to 4e$ background.

For the reducible background estimated by data-driven techniques the shape in m_{4l} and m_{4lerr} is determined by varying the applied selection cuts as described in section 5.4. Applying the full selection, only few events are left in the MC of this background as shown in figure 6.18c and 6.18d with a projection in m_{4l}. The cuts are relaxed gaining a larger number of events to build the shape of this background.

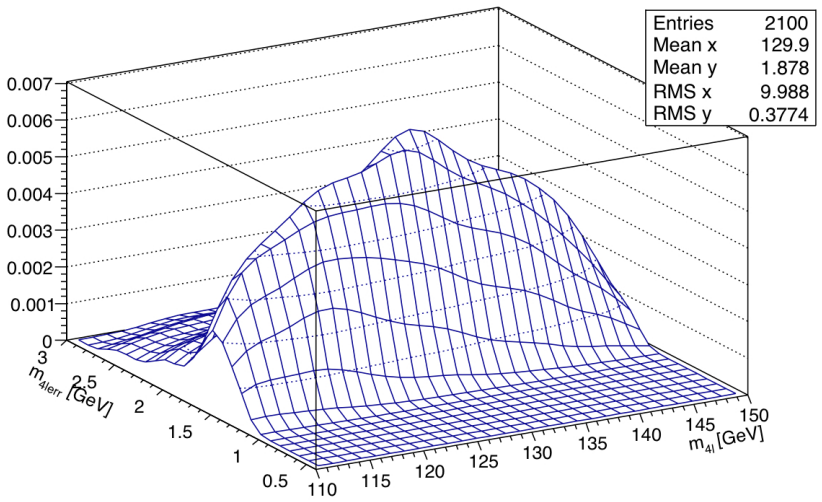


Figure 6.19: The simulated $ZZ^{(*)}$ background in the $4e$ channel is modeled by a smoothed function in $m_{4\ell}$ and $m_{4\ell err}$.

Besides the shape in m_{4l} and m_{4lerr}, the shape systematics are needed for the reducible background. To determine the shape systematics, variables are selected for which changing the value of the cut changes the reducible background shape. The track isolation and impact parameter cuts, which are described in section 5.3.4, were relaxed to determine two additional 2-dimensional histograms for the reducible background. The ratio of each of this histogram over the nominal histogram was built. Figure 6.20 shows the ratio of the histogram with relaxed track isolation cuts. The variations of the ratio in $m_{4\ell}$ and

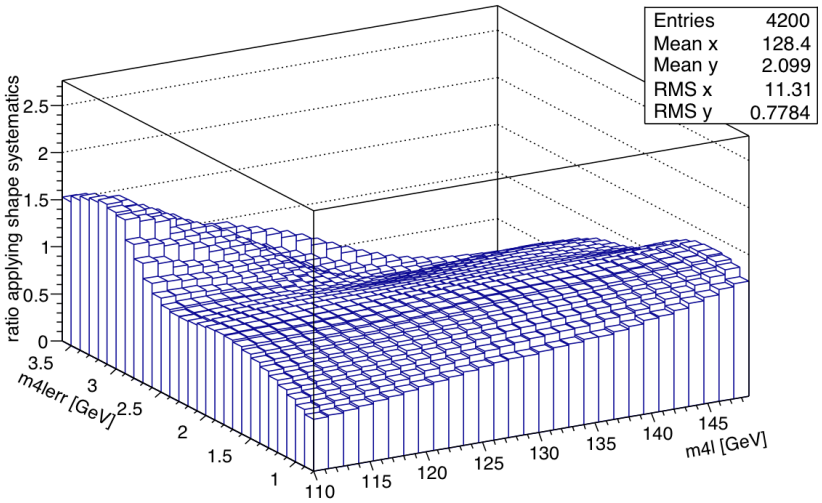


Figure 6.20: The ratio of the reducible background shape with relaxed track isolation cuts over the nominal shape of the reducible background is shown in $m_{4\ell}$ and $m_{4\ell err}$.

$m_{4\ell err}$ motivate the implementation of the shape systematics in two dimensions which has been implemented in the fitting framework.

6.6 Conclusion

In this chapter the parametric and non-parametric signal models are discussed. Several functions are studied and among these the recommended parametric signal model is the sum of a Crystal ball and Gaussian function. The development of a categorisation by detector regions is presented as a stepping stone towards the per-event error approach.

A fitting framework has been developed to accomplish the statistical analysis. The presented per-event models are implemented in this overall fitting infrastructure resulting in a workspaces with two observables, m_{4l} and m_{4lerr}. Additionally the parametric model consisting of a sum of a Crystal ball and a Gaussian function is implemented for m_{4l} without using the per-event error. Both workspaces are discussed in the following chapter.

Chapter 7

Fitting validation & results of the H$\rightarrow ZZ^{(*)} \rightarrow 4\ell$ mass measurement

In the following chapter the approaches with a signal model consisting of a non-parametric and a parametric pdf depending on the $m_{4\ell}$ observable are compared. Additionally, the per-event error implementation is studied.

7.1 Parametric models

To compare the parametric and non-parametric models introduced in section 6.1 and 6.2, the results of the non-parametric method, denoted as the template approach, are presented first. Then, the results of parametric model are given and a comparison is drawn. The Z-mass constraint is applied for both models.

7.1.1 Results of the non-parametric model

The model consisting of only templates has been published as the main result of the ATLAS H$\rightarrow ZZ^{(*)} \rightarrow 4\ell$ analysis over the full mass range. Here this model is studied for the low mass region around the mass of the new observed boson: 110 GeV$< m_H <$ 150 GeV. The fit results are shown in figure 7.1 with 4.6 fb^{-1} collected at $\sqrt{s} = 7$ TeV in 2011 and 20.7 fb^{-1} collected at $\sqrt{s} = 8$ TeV in 2012. Figure 7.1 shows the flat background component by a green dashed line, the signal peak by a blue dashed line and the combination by a blue solid line given the data presented by black data points. Figure 7.2 shows the different categories divided into the four final states and two years of data-taking. The template signal shape is asymmetric due to the radiative tail, but also has in the region of about 10 GeV around the peak a substructure deviating from a Gaussian peak. This is in particular visible in the $4e$ and $2e2\mu$ channel of the

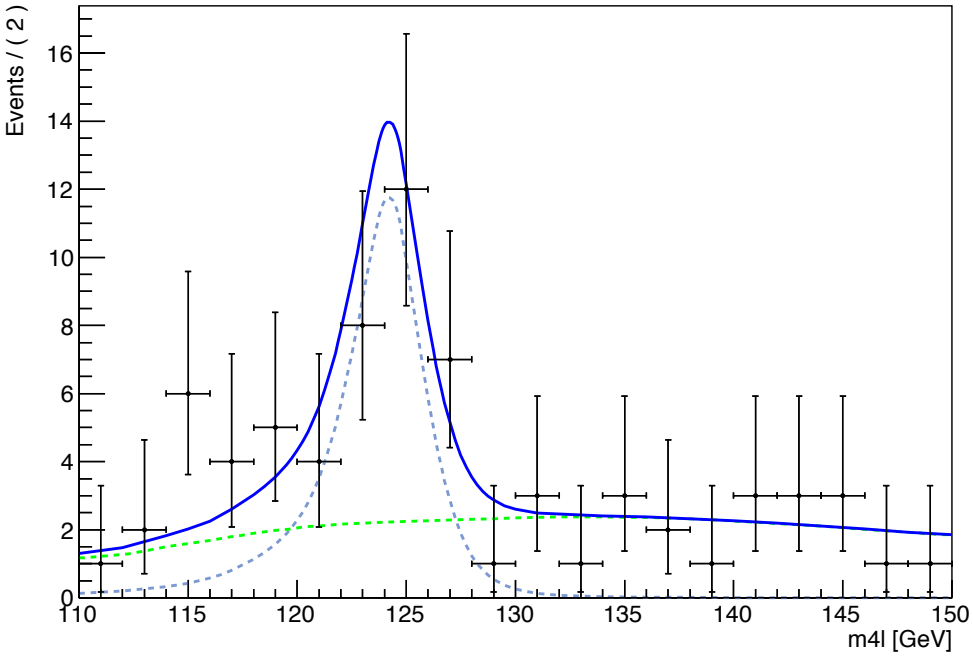


Figure 7.1: Overall H→ $ZZ^{(*)} \to 4\ell$ candidates (black data points) fitted by the template pdfs (blue solid line) consisting of a signal (blue dashed line) and background (green dashed line) component.

2012 dataset given the solid blue line in figure 7.2. The best fit value of the mass is $\hat{m}_H = 124.27^{+0.62}_{-0.52}(\text{stat})^{+0.46}_{-0.33}(\text{sys})\,\text{GeV}$ and of the signal strength is $\hat{\mu} = 1.69^{+0.51}_{-0.43}$ for all four final states combined.

Profile likelihood

Given the likelihood function in equation 6.10, these are the values minimising the negative log-likelihood function corresponding to the observed data sample. The profile likelihood is obtained as the ratio

$$\Lambda(m_H) = \frac{L(\text{data}|m_H, \hat{\hat{\theta}}(m_H))}{L(\text{data}|\hat{m_H}, \hat{\theta})}, \tag{7.1}$$

where m_H is the tested parameter and θ are the other remaining parameters [132]. In this equation only m_H is treated as a parameter of interest and all parameters θ are nuisance parameters in the profile likelihood of m_H. Here, for the m_H scan, also the signal strength is treated as a nuisance parameters.

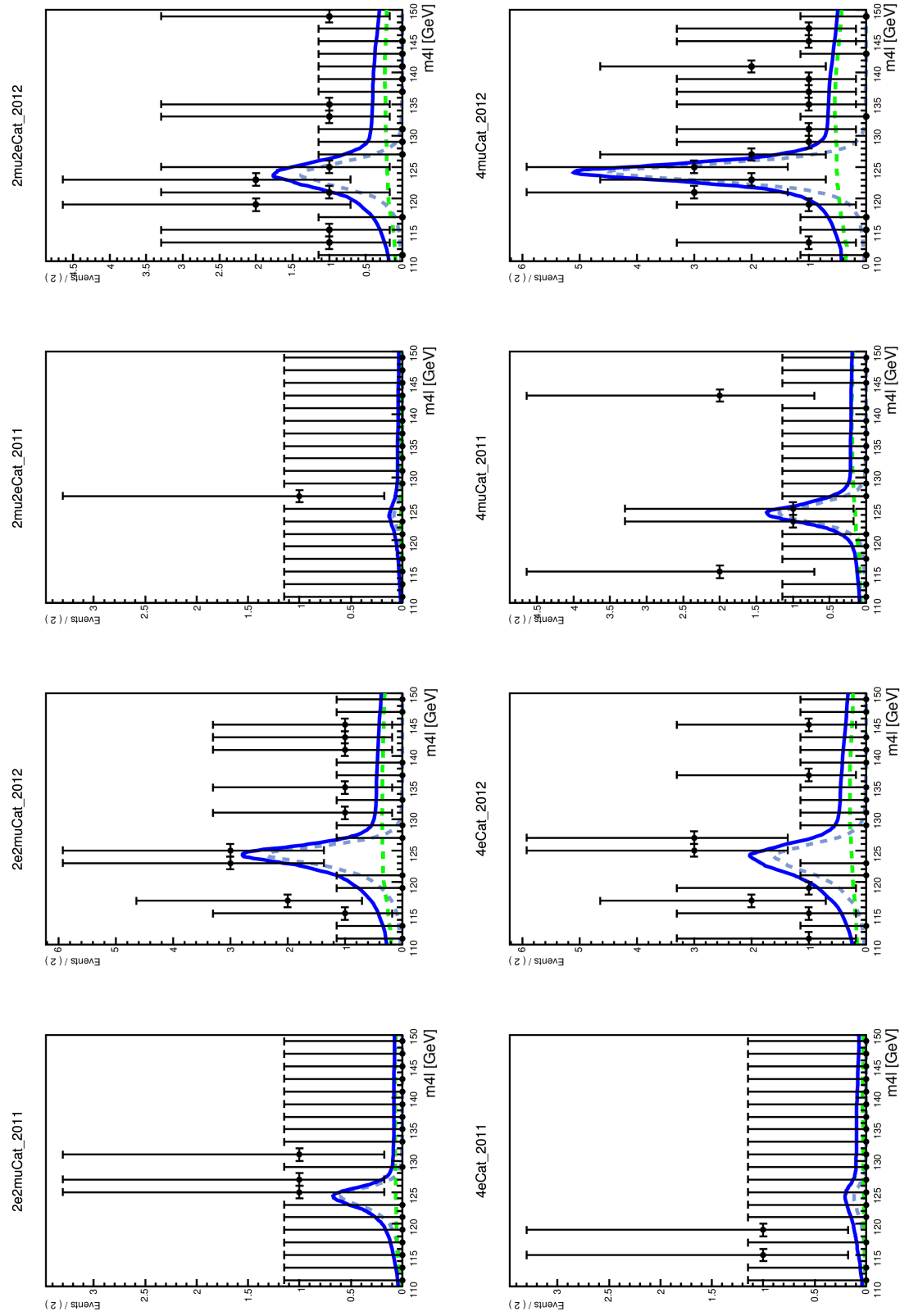


Figure 7.2: Four-lepton invariant mass distribution shown for the template pdfs (blue solid line) consisting of the signal (blue dashed line) and background (green dashed line) component fitted to data (black data points).

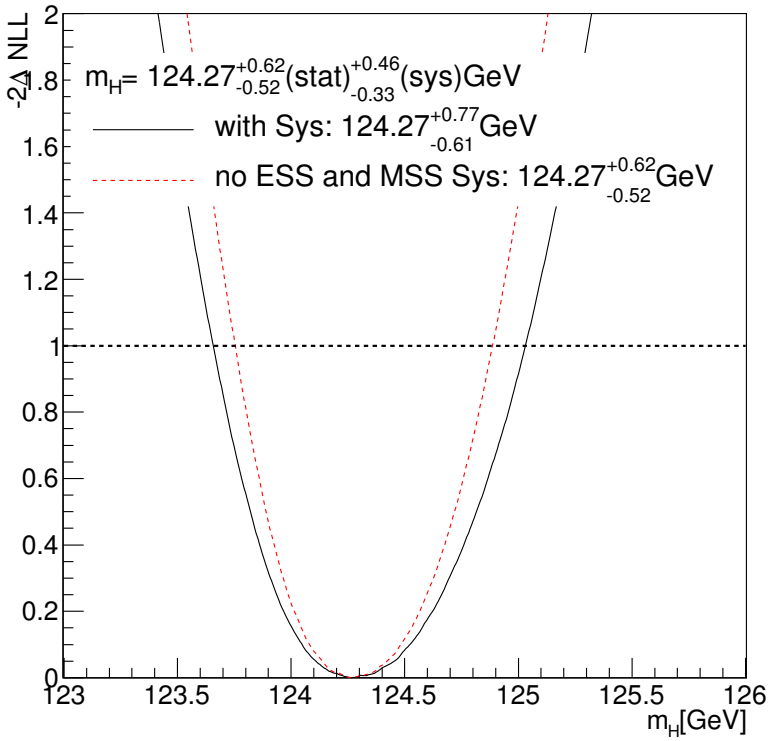


Figure 7.3: The profile likelihood is shown for the template pdfs with and without momentum (MSS) and energy scale systematic (ESS) fixed.

The denominator is the likelihood function evaluated with the best fit values of all parameters, $\hat{m_H}$ and $\hat{\theta}$, for the obtained data. In the numerator, $\hat{\hat{\theta}}(m_H)$ are the best fit values of θ for a fixed value of m_H, so $\hat{\hat{\theta}}$ depends on m_H.

The range of values of $\Lambda(m_H)$ is $0 \leq \Lambda \leq 1$, where Λ is close to one if the model with this value for m_H agrees well with data. Therefore, $-2\ln\Lambda(m_H)$ has only positive values and the better the model (with its value for m_H) agrees with data the smaller the value of $-2\ln\Lambda(m_H)$.

In figure 7.3, the test parameter is m_H and all the remaining parameters, including μ, are treated as nuisance parameters. The profile likelihood is illustrated with a solid black line and the y-axis labelled with -2ΔNLL denotes $-2\ln\Lambda$. This graph is obtained by fixing m_H over 450 equal steps to values between 123 and 126 GeV and fitting the nuisance parameters to evaluate the likelihood function. The total error obtained from the intersection of the likelihood curve at one is $\hat{m}_H = 124.27^{+0.77}_{-0.61}$ GeV.

The main systematic effects for the mass measurement are the momentum (MSS) and energy scale systematic (ESS) as discussed in section 8.2. Both nuisance parameters are fixed to their best fit values in the fit performed to obtain the dashed red line in

figure 7.3. The increased width of the likelihood curve, when keeping more parameters free in the fit, corresponds to the loss of discrimination power by floating additional parameters treating them as nuisance parameters [132].

Fixing the main nuisance parameters reduces the width of the profile likelihood distribution and the errors obtained at the intersection of the new likelihood curve and one. As the other systematic effects are negligible for the mass measurement, this error is denoted the statistical error. The scale systematics shift the mean of the signal mass distribution, whereas the other systematics affect the signal strength by varying the normalisation or the background shape.

As the systematic and the statistical error are quadratically summed to obtain the total variance, the systematic and statistical error can be obtained from the two profile likelihood curves shown in figure 7.3 to be $\hat{m}_H = 124.27^{+0.62}_{-0.52}(\text{stat})^{+0.46}_{-0.33}(\text{sys})\,\text{GeV}$.

Pseudo-experiments

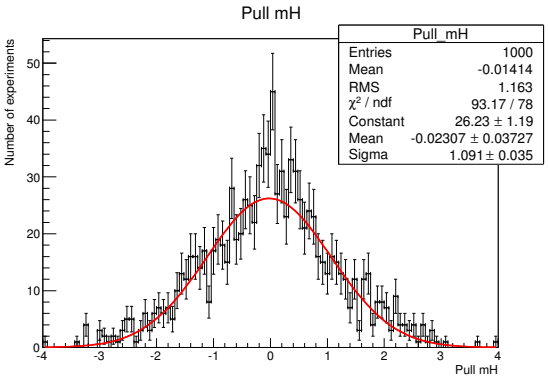
To study the template model, one thousand toy Monte Carlo experiments are generated from the signal and background pdfs with Poissonian fluctuations applied in the generation. These are fitted by the template model and the pull distributions for m_H and μ are shown in figure 7.4a and 7.4b. Asymmetric errors are calculated for the toys and depending on whether $\hat{m_H}$ is smaller than 125 GeV or larger the according asymmetric error is used to calculated the pull. The same applies to the fit of the signal strength. In addition, one thousand toy experiments have been sampled from the MC and fitted by the template pdfs as shown in figure 7.4c and 7.4d. The toy experiments use pdfs and MC samples for the 2012 dataset and do not include the modelling of the systematics. The toys experiments are created for $\mu = 1$ and $m_H = 125\,\text{GeV}$.

To cross check the fitting framework toys are generated from the pdfs which are the same pdfs as those fitted to the toy experiments. It checks the consistency of the model and detects intrinsic biases due to fit problems, e.g. the probability of non converging fits. By sampling from MC, it can be tested how the model performs on example datasets with full detector simulation and subsequent observable correlations. The pull distributions are ideally expected to be Gaussianly distributed with a mean of zero and a sigma of one. As shown in figure 7.4, all pull-distributions are fitted by Gaussian functions. The number of entries per bin follows a Poissonian distribution with an uncertainty of $\sqrt{\lambda}$ where λ is the mean of the distribution. The fluctuations observed in the pull distributions are compatible with a Gaussian distribution given the limited number of events. This can be also observed by the χ^2/ndf which is close to one determining the quality of the

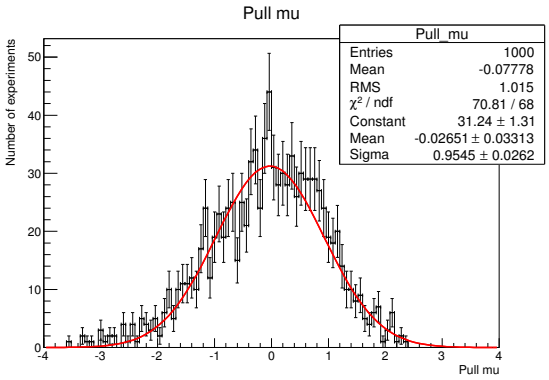
fit. Pull-distributions with ten times the amount of toy experiments have also shown a compatibility with the Gaussian distribution. As this requires large resources of CPU time, the pull distributions have been produced with 1000 toy experiments by default and the results are summarised in table 7.1.

	m_H-pull distribution		μ-pull distribution	
	Gaussian mean	Gaussian sigma	Gaussian mean	Gaussian sigma
pdf toys	-0.023 ± 0.037	1.091 ± 0.035	-0.027 ± 0.033	0.955 ± 0.026
MC toys	-0.044 ± 0.038	1.106 ± 0.034	-0.028 ± 0.035	1.014 ± 0.029

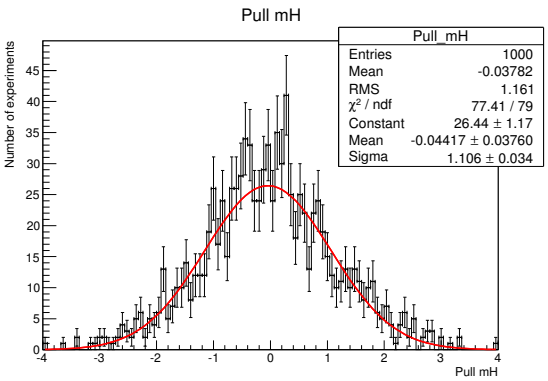
Table 7.1: This table summarises the results obtained for thousand toy experiments generated from pdf (pdf toys) and sampled from MC (MC toys) for $m_H = 125\,\text{GeV}$ and $\mu = 1$ and fitted by the template model as given in figure 7.4.



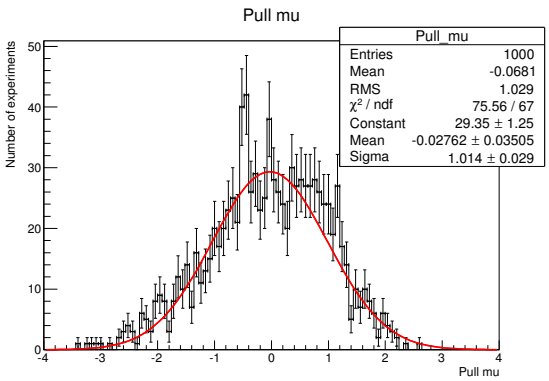
(a) m_H-pull distribution when generating from the pdf



(b) μ-pull distribution when generating from the pdf



(c) m_H-pull distribution when sampling from MC



(d) μ-pull distribution when sampling from MC

Figure 7.4: Pull distributions for m_H and μ for the toys generated from the pdf and sampled from MC for the template approach.

For the toys generated from the pdf, the mean values of the m_H and μ-pull distribution are compatible with zero, so no bias is observed when using the template approach. The shape of the pull-distribution is not absolutely Gaussian given the constraint $\mu \geq 0$ and the Poissonian bias due to low signal yields resulting in a slightly asymmetric $\hat{\mu}$ distribution. The sigma of the m_H-pull distribution is about 10% larger than the expected value of one when generating from the pdf (figure 7.4a). This is currently being investigated and a possible explanation is that the uncertainty on $\hat{m}_H$ is underestimated. In previous so far unpublished studies of the template model over the full mass range, it was observed that the statistical uncertainty is underestimated which is consistent with the too broad m_H-pull distribution. The sigma of the μ-pull distribution is consistent with the expected value of one within 1.74 standard deviations.

For the toys sampled from MC, the Gaussian mean of the m_H and μ-pull distribution are both consistent with zero and no bias is observed. The sigma of this m_H-pull distribution is about 10% larger than the expected value of one, similar to the sigma of the m_H-pull distribution obtained for thousand toys generated from the pdf. As mentioned before this is being investigated and possibly due to underestimation of the uncertainty. The sigma of this μ-pull distribution is compatible with the value one.

7.1.2 Results of the parametric model

A model comprising of a sum of a Crystal ball and Gaussian function for the ggF signal is studied. This model is a good cross-check given the possible error underestimation with the template model. This parametric function for ggF consists of a broad Gaussian function with a fraction of less than 10% as described in section 6.2. The Crystal ball and the Gaussian function have the same mean and all other pdfs besides the ggF signal are kept as templates.

Profile likelihood

The results of the maximum-likelihood fit are shown in figure 7.5. The signal shapes look much smoother applying the parametric model than for the template model which is particularly striking when comparing the peak region of the $4e$ and $2\mu 2e$ final states for 2012 (figure 7.1 and 7.5). The best fit value of the mass is $\hat{m}_H = 124.36^{+0.62}_{-0.60}(\text{stat})^{+0.43}_{-0.37}(\text{sys})$ GeV for the CB+GA approach as shown in figure 7.6. The best fit value of the signal strength is $\hat{\mu} = 1.84^{+0.53}_{-0.45}$. The smoother signal shape observed in the invariant four lepton distribution for the parametric model in comparison to the non-parametric model affects

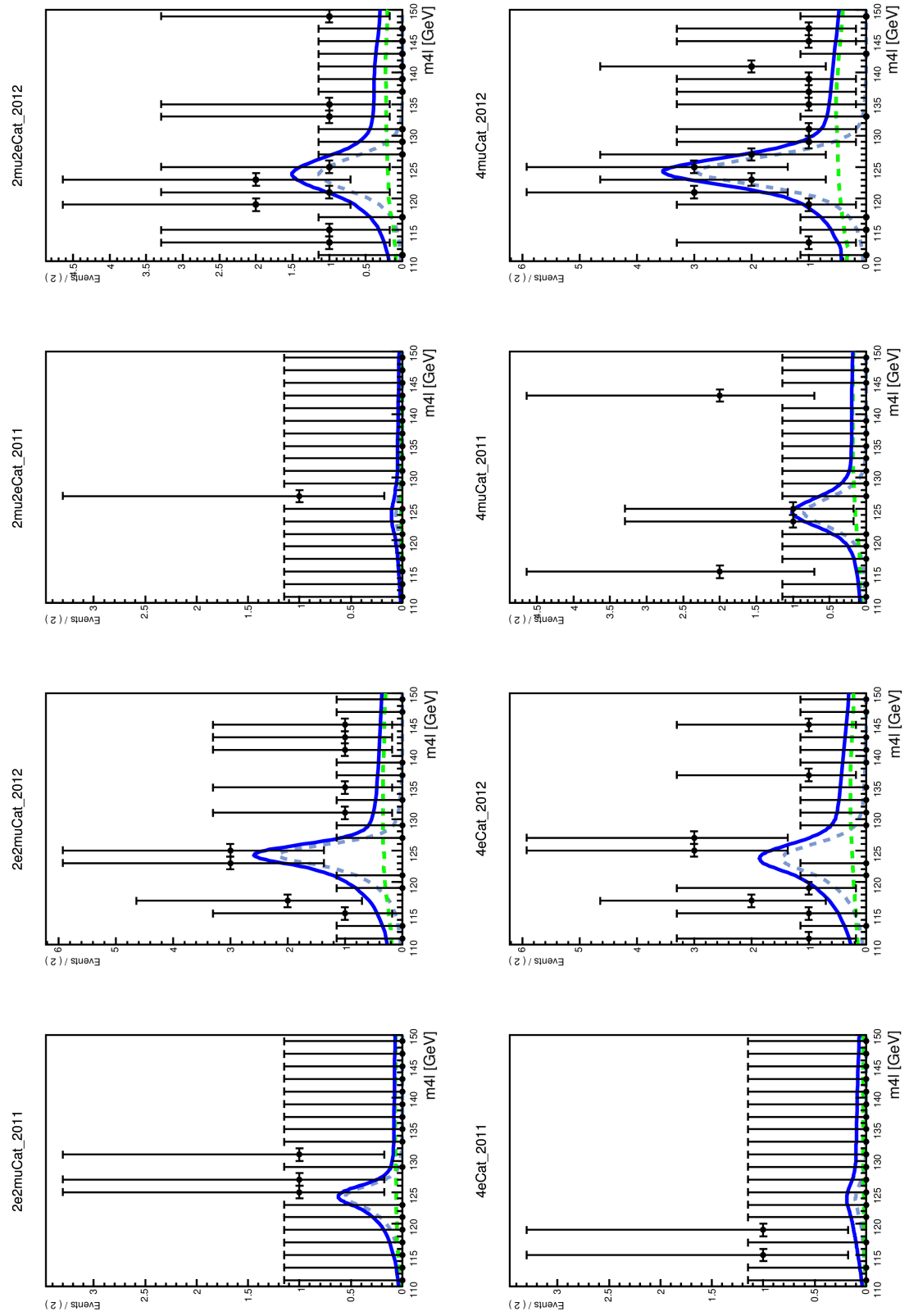


Figure 7.5: Four-lepton invariant mass distribution is shown for the model including the sum of a Crystal ball and a Gaussian function as the ggF signal pdf. The combination pdfs (blue solid line) consisting of the signal (blue dashed line) and background (green dashed line) component fitted to data (black data points).

the smoothness of the profile likelihood curve. The curve containing the parametric model (figure 7.6) is smoother than the curve for the template signal model (figure 7.3), in particular close to the minimum where the curve wiggles slightly with 1 GeV steps corresponding to the intervals between the interpolated signal samples.

The mass measurement result obtained by the CB+GA model is compatible with the results obtained with the template approach ($\hat{m}_H = 124.27^{+0.62}_{-0.52}(\text{stat})^{+0.46}_{-0.33}(\text{sys})$ GeV, $\hat{\mu} = 1.69^{+0.51}_{-0.43}$). The errors on the mass measurement are of similar size and the parametric ones are more symmetric than the non-parametric. A difference is observed in the signal strength, where the best fit value of the CB+GA result is 9% larger than the result of the template approach. This lies well within the uncertainties on the signal strength, but further investigation whether this is a difference observed in general or just by chance for this dataset is useful.

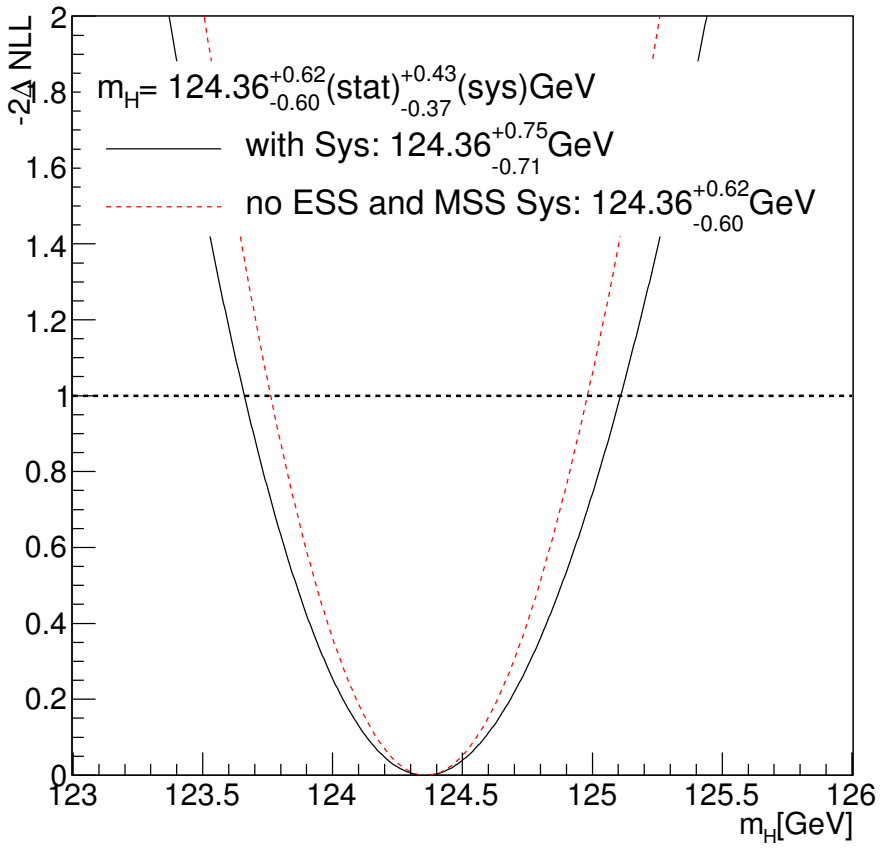
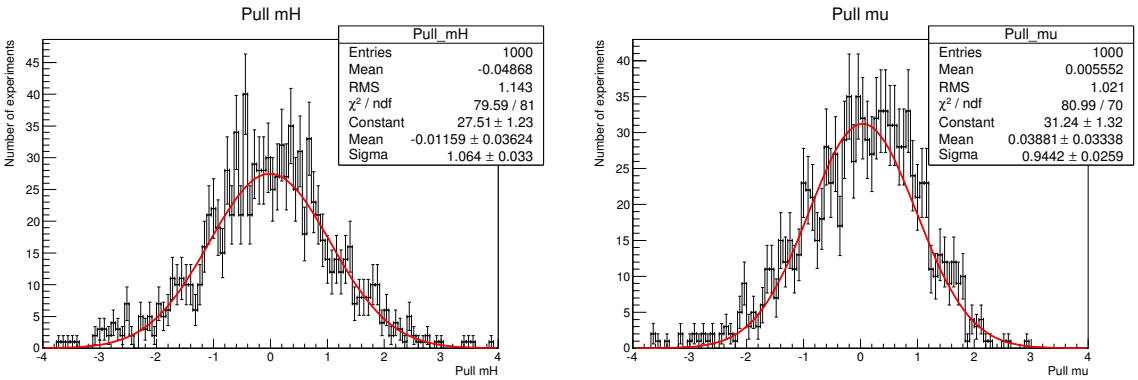


Figure 7.6: The profile likelihood is shown for the fit of the signal and background pdfs including the sum of a Crystal ball and a Gaussian function as a model for the ggF signal.

Pseudo-experiments

To study the CB+GA model, a thousand toy experiments have been generated from its pdfs and sampling from MC for initial values of $m_H = 125\,\text{GeV}$ and $\mu = 1$ as shown in figure 7.7. This and other studies can be done to see if the asymmetric error on m_H is a feature of the template model.



(a) m_H-pull distribution when generating from the pdf

(b) μ-pull distribution when generating from the pdf

(c) m_H-pull distribution when sampling from MC

(d) μ-pull distribution when sampling from MC

Figure 7.7: Pull distributions for m_H and μ for the toys generated from the pdf and sampled from MC for the approach with the sum of a Crystal ball and a Gaussian function as a model for the ggF signal.

For the toys generated from the pdf, the mean values of the m_H and μ-pull distribution are both consistent with the expected value of zero, i.e. no bias is observed as summarised in table 7.2. The sigma of the m_H-pull distribution is shifted to larger values by 1.93 standard deviations than the expected value of one. The sigma of the μ-pull distribution lies within 2.15 standard deviations from the expected value one. This shows that the CB+GA does not contain an intrinsic bias on the mass and signal strength measurement.

	m_H-pull distribution		μ-pull distribution	
	Gaussian mean	Gaussian sigma	Gaussian mean	Gaussian sigma
pdf toys	-0.012 ± 0.036	1.064 ± 0.033	0.039 ± 0.033	0.944 ± 0.026
MC toys	-0.064 ± 0.030	0.886 ± 0.026	-0.178 ± 0.034	0.951 ± 0.028

Table 7.2: This table summarises the results obtained for thousand toy experiments generated from pdf and sampled from MC for $m_H = 125\,\text{GeV}$ and $\mu = 1$ and fitted by the CB+GA model as given in figure 7.7.

For the toys sampled from MC, the mean values of the m_H-pull distribution is shifted by 2.16 standard deviations from the value zero. The mean of the μ-pull distribution is shifted to 0.178 ± 0.034. This shows that the increase of $\hat{\mu}$ between the template and the CB+GA approach, observed for the combined dataset, is reproduced when running thousand toy experiments of sample datasets. As observed in section 6.2, the parametric models, including the CB+GA, have difficulties to model the peak-region of the signal. The Crystal ball model with an additional broad Gaussian function covering the outliers is able to capture the peak-region better than the other studied parametric models. This is a main reason why this model was chosen for more detailed studies within the workspace. The overestimation of the signal strength indicates that the CB+GA model is picking up background events with the large tails. The peak-region is slightly underestimated as shown in figure 6.10 when studying the model. In particular for the mass points around 125 GeV the pdf undershoots significantly the MC in the peak.

When sampling toy experiments from MC, the m_H-pull distribution has a sigma that is 11% smaller than one and shifted by 4.32 standard deviations. This indicates that the errors of the best fit value of m_H obtained from the CB+GA model are overestimating the actual fluctuations of the best fit values of m_H. The sigma of the μ-pull distribution when sampling from toy experiments lies within 1.76 standard deviations from the expected value of one.

7.1.3 Detailed comparison of the results

The parametric and non-parametric signal model are compared using their performance on data and pseudo-experiments. For both models, the best fit values for m_H are plotted for thousand experiments together. They follow a normal distribution and are fitted by a Gaussian function. The means and sigmas of the Gaussian functions are summarised for the different toy experiments in table 7.3.

	Toys generated from the pdf		Toys sampled from MC	
	mean [GeV]	sigma [GeV]	mean [GeV]	sigma [GeV]
Template	124.982 ± 0.026	0.780 ± 0.024	125.014 ± 0.025	0.730 ± 0.022
CB+GA	124.984 ± 0.039	1.166 ± 0.038	124.923 ± 0.028	0.829 ± 0.023

Table 7.3: Fit result for m_H obtained for thousand toy experiments generated from pdf and sampled from MC for $m_H = 125\,\text{GeV}$.

In table 7.3, the width of the fitted Gaussian to the mass distribution is given in the third column for toys generated from the pdf and in the fifth column for toys sampled from MC. Applying the CB+GA approach, the sigma is about 0.3 GeV (1.166 GeV−0.829 GeV) larger for the toy experiments generated from pdf than the experiments sampled from MC. This indicates that the signal shape of the CB+GA is broader than in MC. Applying the template approach, the difference of the sigma using for toys generated from pdf and sampled from MC are significantly smaller given the uncertainties on sigma.

The sigma obtained with the template and the CB+GA approach are compatible for the same input of toy experiments sampled from MC given the uncertainties on sigma. It can be concluded that the CB+GA approach slightly overestimates the uncertainty on a single mass measurement as the fluctuation observed for multiple pseudo-experiments are smaller than predicted by the model.

Primarily, different signal models were studied and the CB+GA model was determined as a suitable signal model with an old signal MC version as shown in chapter 6. This CB+GA model is compared to a template model which is created from the latest signal MC version and the CB+GA model has shown a significantly broader signal shape than the template model. By rescaling the width of the CB+GA model to correspond to the latest signal MC, a closer agreement between the CB+GA and template model is expected. This applies in particular to a better mass resolution of the CB+GA model given by the width of the fitted Gaussian to the mass distribution listed in the third column of table 7.3.

Using the template approach, the uncertainty of the mass measurement is possibly underestimated as the toy studies (figure 7.4) are indicating with a too broad m_H-pull distribution.

The results are summarised for the separate and combined 2011 and 2012 dataset in table 7.4. It contains the two different signal models for the fits applying the Z-mass constraint.

	Template		CB+GA	
dataset	$\hat{m}_H$ [GeV]	$\hat{\mu}$	$\hat{m}_H$ [GeV]	$\hat{\mu}$
2011	$125.60^{+1.84}_{-1.40}(\text{stat})^{+0.84}_{-0.37}(\text{sys})$	$1.62^{+1.22}_{-0.84}$	$125.39^{+1.97}_{-1.71}(\text{stat})^{+0.39}_{-0.31}(\text{sys})$	$1.83^{+1.33}_{-0.90}$
2012	$124.16^{+0.56}_{-0.49}(\text{stat})^{+0.38}_{-0.28}(\text{sys})$	$1.69^{+0.54}_{-0.44}$	$124.25^{+0.65}_{-0.62}(\text{stat})^{+0.44}_{-0.35}(\text{sys})$	$1.83^{+0.56}_{-0.48}$
Combined	$124.27^{+0.62}_{-0.52}(\text{stat})^{+0.46}_{-0.33}(\text{sys})$	$1.69^{+0.51}_{-0.43}$	$124.36^{+0.62}_{-0.60}(\text{stat})^{+0.43}_{-0.37}(\text{sys})$	$1.84^{+0.53}_{-0.45}$

Table 7.4: Results are summarised for the template approach and the model using a sum of a Crystal ball and a Gaussian function for the ggF signal. The results are shown for the datasets 2011, 2012 and 2011+2012 applying the Z-mass constraint.

Some of the errors on the mass measurement obtained in 2012 are smaller than for the analysis of 2011 and 2012 combined. This is likely due to a combination of facts. Most importantly, the number of collected events in this channel is very limited so that statistical fluctuations have a large impact on the result. Additionally, the signal reconstruction and selection efficiency at $m_H = 125\,\text{GeV}$ has changed between the 2011 and 2012 dataset from 21% to 26% in the mixed channels ($2\mu 2e$ and $2e2\mu$) and from 15% to 19% in the $4e$ channels. For the 4μ channel the signal reconstruction and selection efficiency remained 39%. These changes are due to a looser electron identification and improved kinematic cuts reducing the mis-pairing for the 2012 dataset which is neither applied in the 2011 dataset, nor in the 2011 component of the combined (2011+2012) dataset [41]. As the datasets have a small number of events, single events affect the best fit value and the error on m_H and μ considerably. Therefore, the toy experiments are important to support the conclusions drawn for different models.

As concluded from the toy experiments, the models do not bias the mass measurement. Fitting to data, the obtained best fit values for m_H are compatible between the template and CB+GA approach. The errors given on m_H are larger for the CB+GA than the template approach where the errors on m_H of the CB+GA approach are an overestimation as concluded by the toy studies sampling from MC. The broad Gaussian picks up outliers from the background. A future study could look for a function that can capture the tails and at the same time model the peak region even better than the sum of a Crystal ball and a Gaussian function. A better approach will be using a per-event error discussed in the next section which provides a possibility to model the resolution at the level of individual events.

The bias in μ of the CB+GA approach affects the best fitted value of the signal strength by an increase of the order of 10% in comparison to the template approach. This difference between the CB+GA and template approach is compatible within one

sigma, but is a systematic shift as shown by the result of the toy studies in figures 7.4d and 7.7d.

	Template		CB+GA	
dataset	$\hat{m}_H$ [GeV]	$\hat{\mu}$	$\hat{m}_H$ [GeV]	$\hat{\mu}$
2011	$124.89^{+1.98}_{-1.27}(\text{stat})^{+0.68}_{-0.43}(\text{sys})$	$2.09^{+1.38}_{-1.02}$	$124.81^{+1.78}_{-2.32}(\text{stat})^{+0.33}_{-0.26}(\text{sys})$	$2.40^{+1.67}_{-1.10}$
2012	$124.27^{+0.59}_{-0.67}(\text{stat})^{+0.56}_{-0.41}(\text{sys})$	$1.54^{+0.52}_{-0.43}$	$124.02^{+0.98}_{-0.98}(\text{stat})^{+0.28}_{-0.22}(\text{sys})$	$1.74^{+0.58}_{-0.48}$
Combined	$124.33^{+0.52}_{-0.56}(\text{stat})^{+0.50}_{-0.47}(\text{sys})$	$1.63^{+0.50}_{-0.41}$	$124.14^{+0.89}_{-0.88}(\text{stat})^{+0.31}_{-0.22}(\text{sys})$	$1.84^{+0.56}_{-0.47}$

Table 7.5: Results are summarised for the template approach and the model using a sum of a Crystal ball and Gaussian function for the ggF signal. The results are shown for the datasets 2011, 2012 and 2011+2012 without applying the Z-mass constraint.

Table 7.5 shows the results of both approaches for the 2011, 2012 and combined dataset without the Z-mass constraint applied. The results obtained with and without Z-mass constraint are consistent and the expected increased mass resolution by applying the Z-mass constraint discussed in subsection 5.3.5 is observed increasing the mass measurement resolution for the combined dataset by $^{+0.11}_{-0.27}$ GeV for the template approach and by $^{+0.30}_{-0.20}$ GeV for the CB+GA model.

7.1.4 Conclusion

The template approach as a non-parametric model provides accurate results with no bias in m_H and μ. The results have been cross-checked with a parametric approach using the sum of a Crystal ball and a Gaussian function for the ggF signal. With both approaches a similar mass resolution is obtained. The template approach tends to underestimate the error whereas the CB+GA overestimates the error on the mass measurement. The consistent results provide confidence in the statistical infrastructure and the chosen signal model.

7.2 Per-event error

The per-event error approach uses conditional pdfs for the signal and two-dimensional smoothed histograms for the background components as described in section 6.5.

7.2.1 Applied models and their profile likelihood results

A Crystal ball function is used as a conditional pdf to model the $m_{4\ell}$ distribution where the sigma is a global scale factor multiplied by $m_{4\ell err}$. For the 4μ channel, the $m_{4\ell err}$ distribution is modelled by a Pearson Type IV distribution, whereas for the electron channels an interpolation of smoothed histograms is used as substructure in the distribution deviates form the shape of a Person Type IV function. Studying the $m_{4\ell err}$ distributions with and without Z-mass constraint applied, the unconstrained distributions were smoother and better to model. The Z-mass constraint also uses the per-event error to calculate the corrected mass of the leading lepton-pair. This study concentrates on the analysis without the Z-mass constraint applied, to avoid spiky distributions which are extremely difficult to model, and additional correlations due to double use of the per-event error. For the signal, $\mathcal{P}_k(m_{4\ell}|m_{4\ell err})$ is given in figure 7.8 showing Crystal ball functions with the mean linearly depending on the Higgs mass. The parameters α and n of the Crystal ball function, defined in equation 6.2, are fixed to constants.

In figure 7.9, $\mathcal{P}_k(m_{4\ell err})$ is shown for different Higgs masses. For the electron channels the histograms are interpolated by basis splines of the third order to obtain a continuous dependence on the Higgs mass. The basis splines, also known as B-Splines, are also used for the systematics modelling and further described in section 8.2.3.

For the Pearson Type IV function (used in the 4μ channel), λ depends linearly on m_H, and m, ν and a are constants. The $m_{4\ell err}$ distribution of the electron channels was studied with several functions to obtain a parametric model, but none of the functions fitted reasonably well. Therefore, the smoothed MC histogram is used for the $m_{4\ell err}$ shape in the electron channels. In figure 7.9 the $m_{4\ell err}$ shapes can be compared for different mass points. The changes between the mass points are very smooth for the 4μ channel using a Pearson Type IV function whereas the changes between the mass points of the electron channels are not very smooth. For example, the shape has the feature of a shoulder at $m_{4\ell err} = 2\,\text{GeV}$ for some mass points in the $2e2\mu$ channel. The distributions shown in figure 7.8 and 7.9 are the results of an analysis selection without the Z-mass constraint applied. The pdfs of the background components are all modelled as two-dimensional smoothed histograms in $m_{4\ell}$ and $m_{4\ell err}$ as described in section 6.5.

The fit of the per-event error model to the 2012 dataset is shown by the profile likelihood in figure 7.10 without a Z-mass constraint applied. The best fitted values are $\hat{m}_H = 124.10^{+0.71}_{-0.66}(\text{stat})^{+0.27}_{-0.22}(\text{sys})\,\text{GeV}$ and $\hat{\mu} = 1.53^{+0.52}_{-0.43}$.

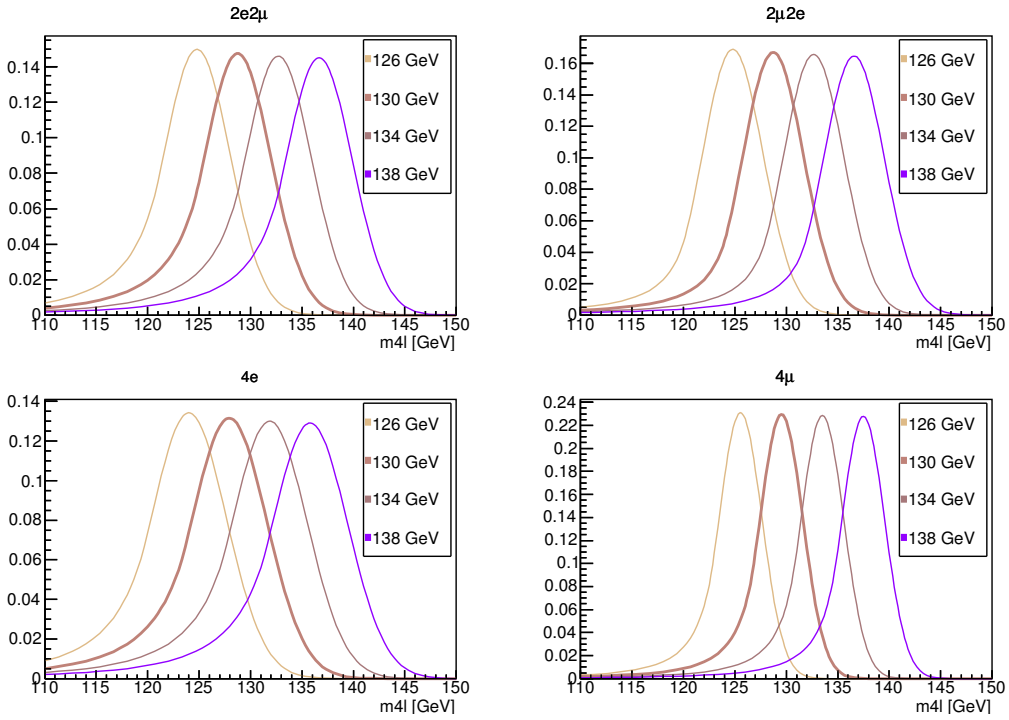


Figure 7.8: The Crystall ball signal distribution $\mathcal{P}_k(m_{4\ell}|m_{4\ell err})$ is shown for the four final states with its dependence on the Higgs mass (given in different colours) without the Z-mass constraint applied.

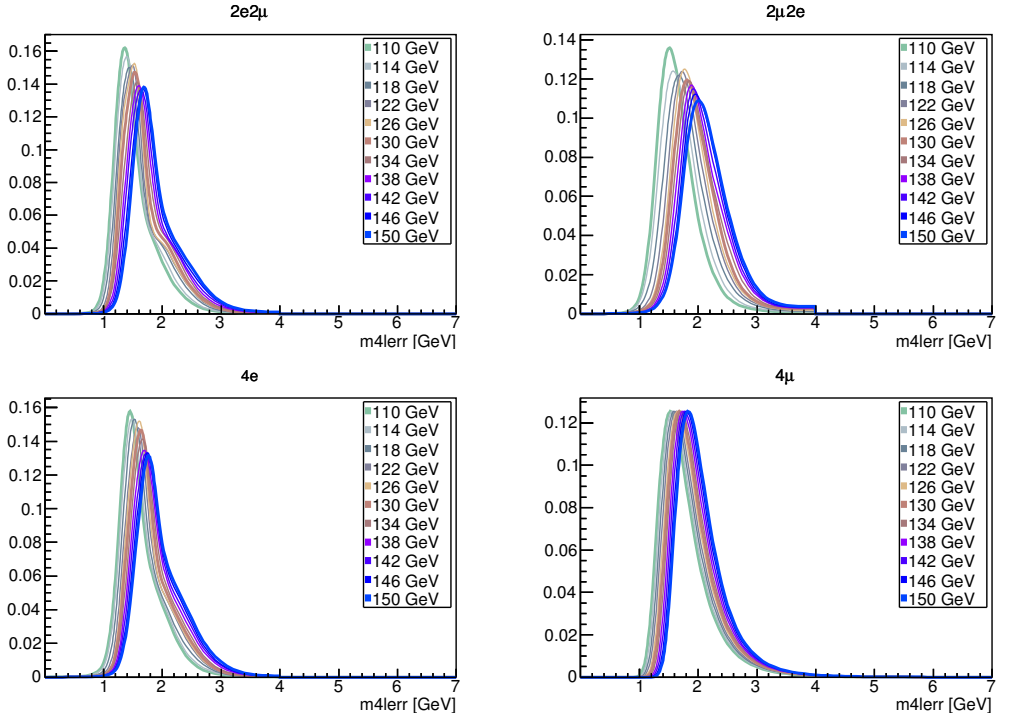


Figure 7.9: The signal distribution $\mathcal{P}_k(m_{4\ell err})$ is shown for the four final states with its dependence on the Higgs mass (given in different colours) without the Z-mass constraint applied.

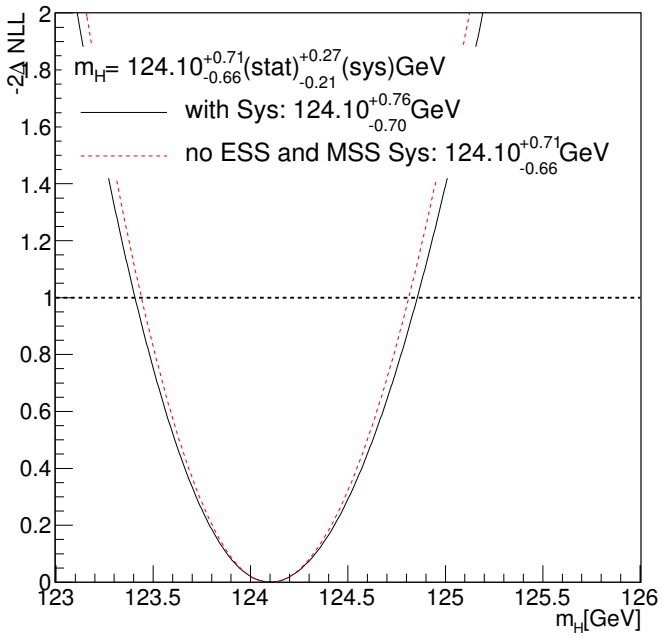


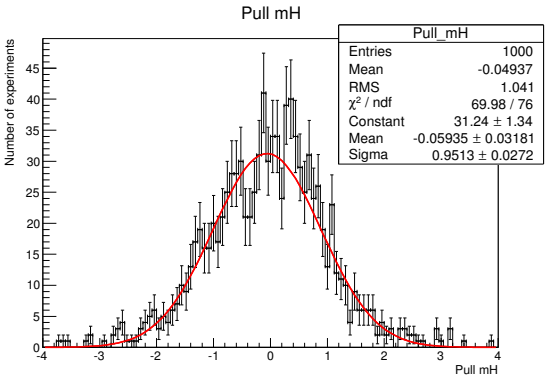
Figure 7.10: Profile likelihood is shown for the per-event error workspace fitted to the 2012 dataset without Z-mass constraint applied.

7.2.2 Pseudo-experiments

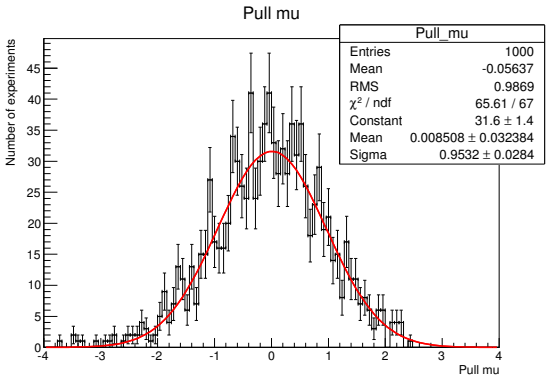
One thousand toys are generated from the pdfs, and fitted by the same pdfs with the m_H and μ-pull distributions shown in figure 7.11a and 7.11b. The m_H and μ-pull distributions for the toys sampled for MC are shown in figure 7.11c and 7.11d. All pull distributions follow a Gaussian function and the results of the pseudo-experiments are summarised in table 7.6.

For the toys generated from the pdf, the mean values of the m_H and μ-pull distribution are consistent with the expected value of zero and no bias is observed. The sigma of the m_H-pull distribution lies 1.79 standard deviations from the expected value of one. The sigma of the μ-pull distribution is shifted by 1.65 standard deviations from one.

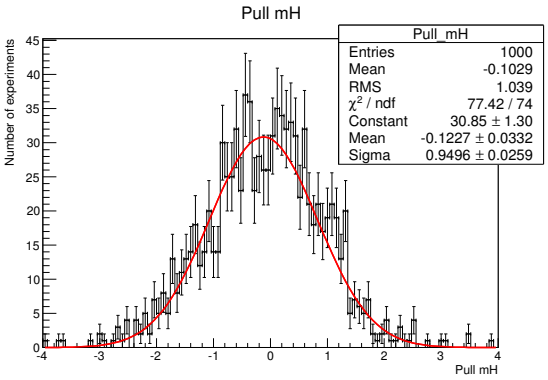
For the toys sampled from MC, the mean of the m_H-pull distribution lies 3.7 standard deviations away from zero. The bias is towards lower best fit values of m_H than the initial value of 125 GeV. As shown in figure 6.1 in section 6.2, the Crystal ball function has difficulties capturing the tails and the peak region at the same time. It is pulled towards the low energetic tail to model outliers. The high mass side of the Crystal ball function is not as steep as the MC signal distribution. This results in a small offset of the peak of the Crystal ball function towards lower energies in comparison to the peak



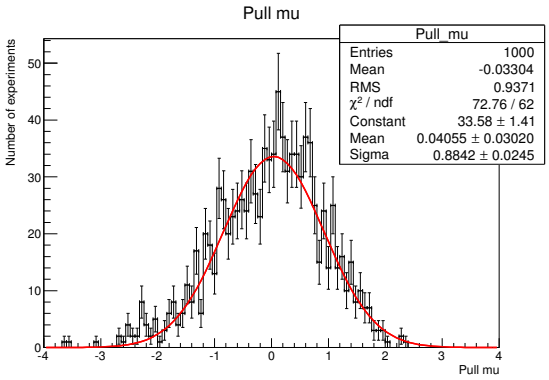
(a) m_H-pull distribution when generating from the pdf



(b) μ-pull distribution when generating from the pdf



(c) m_H-pull distribution when sampling from MC



(d) μ-pull distribution when sampling from MC

Figure 7.11: Pull distributions for m_H and μ for the toys generated from the pdf and sampled from MC for the per-event workspace with a Crystal ball as a signal model.

	m_H-pull distribution		μ-pull distribution	
	Gaussian mean	Gaussian sigma	Gaussian mean	Gaussian sigma
pdf toys	-0.059 ± 0.032	0.951 ± 0.027	0.009 ± 0.032	0.953 ± 0.028
MC toys	-0.123 ± 0.033	0.950 ± 0.026	0.041 ± 0.030	0.884 ± 0.025

Table 7.6: This table summarises the results obtained for thousand toy experiments generated from pdf and sampled from MC for $m_H = 125\,\text{GeV}$ and $\mu = 1$ and fitted by the per-event model as given in figure 7.11.

of the MC signal distribution. The mean of the μ-pull distribution are compatible with zero which means that no bias in μ is observed when sampling from MC. The sigma of the m_H-pull distribution lies 1.95 standard deviations from the expected value of one. The sigma of the μ-pull distribution is with 0.88 ± 0.02 significantly smaller than one.

	Toys generated from pdf		Toys sampled from MC	
	mean [GeV]	sigma [GeV]	mean [GeV]	sigma [GeV]
Template	125.002 ± 0.033	0.972 ± 0.031	125.023 ± 0.030	0.907 ± 0.025
Per-event error	124.959 ± 0.027	0.781 ± 0.022	124.918 ± 0.029	0.874 ± 0.024

Table 7.7: Mass measurement fit result obtained for thousand toy experiments generated from pdf and sampled from MC for an initial value of $m_H = 125\,\text{GeV}$.

This could be due to an overestimation of the error on the signal strength and future studies could look into this.

7.2.3 Comparison of per-event error to template approach

As given in table 7.5, the best fit values for the template approach using only $m_{4\ell}$ as an observable are $\hat{m}_H = 124.27^{+0.59}_{-0.67}(\text{stat})^{+0.56}_{-0.41}(\text{sys})\,\text{GeV}$ and $\hat{\mu} = 1.54^{+0.52}_{-0.43}$ for the 2012 dataset without applying the Z-mass constraint. These values are compatible with the results observed with the per-event error implementation where $\hat{m}_H = 124.10^{+0.71}_{-0.66}(\text{stat})^{+0.27}_{-0.22}(\text{sys})\,\text{GeV}$ and $\hat{\mu} = 1.53^{+0.52}_{-0.43}$. The total uncertainty on the mass measurement for the 2012 dataset is $^{+0.81}_{-0.79}\,\text{GeV}$ for the template approach and $^{+0.76}_{-0.70}\,\text{GeV}$ for the per-event model. Subtracting these numbers a decrease in the error of $^{+50}_{-90}\,\text{MeV}$ is observed with the per-event model. This can also be seen in table 7.7 where the mean and sigma of the best fit values of m_H are compared using thousand toy experiments. The sigma using the per-event error model is in both cases significantly smaller than for the template approach. The value of the mean for the per-event approach shows a bias of 41 MeV to lower best fit values of m_H. The error on this m_H-bias can be calculated with the mean of the m_H-pull distribution for toy experiments sampled from MC, -0.1227 ± 0.0332, given in figure 7.11c. This results in a m_H-bias of $41 \pm 11\,\text{MeV}$.

7.2.4 Conclusion

The results of the mass and signal strength measurement with the per-event error implementation are compatible with the one-dimensional template approach performed for the 2012 dataset without the Z-mass constraint applied. A m_H-bias of $41 \pm 11\,\text{MeV}$ is observed for the per-event model which could be improved by studying further signal models, for example the convolution approach discussed in section 6.2. This first version of the per-event error model improves the resolution of the mass measurement by $^{+50}_{-90}\,\text{MeV}$.

Chapter 8

Statistical interpretation of the H$\rightarrow ZZ^{(*)} \rightarrow 4\ell$ analysis

In this chapter the main results published at the Moriond conference in 2013 are summarised. Additionally, the systematics treatment is discussed in more detail and the results are presented in the context of the statistical models studied in chapter 7.

8.1 Results and interpretation of the main non-parametric analysis

The main results of the H$\rightarrow ZZ^{(*)} \rightarrow 4\ell$ analysis in ATLAS consist of the template approach studied over a four-lepton invariant mass range of 80 GeV$< m_{4\ell} <$ 1 TeV as shown in figure 8.1 with the Z-mass constraint applied. The combined (signal+background) pdf represented by the blue solid line has three peaks: one at the Z-mass of around 91 GeV from the continuum $(Z^{(*)}/\gamma^*)(Z^{(*)}/\gamma^*)$ with one Z on-shell, a signal peak for the best fitted mass and a peak at $\sim$182 GeV from the $ZZ^{(*)}$ background. The best fitted value of the signal strength is $\hat{\mu} = 1.71^{+0.51}_{-0.43}$ for the combined (2011+2012) dataset. The best fit value of the mass is $\hat{m}_H = 124.26^{+0.61}_{-0.52}(\text{stat})^{+0.45}_{-0.33}(\text{sys})$ GeV as shown in figure 8.2.

In figure 8.3 the probability, local p_0, is given which states how unlikely it is assuming a background-only hypothesis to observe the test statistic seen in data or greater[1].

[1]This is further discussed in section 6.4.1.

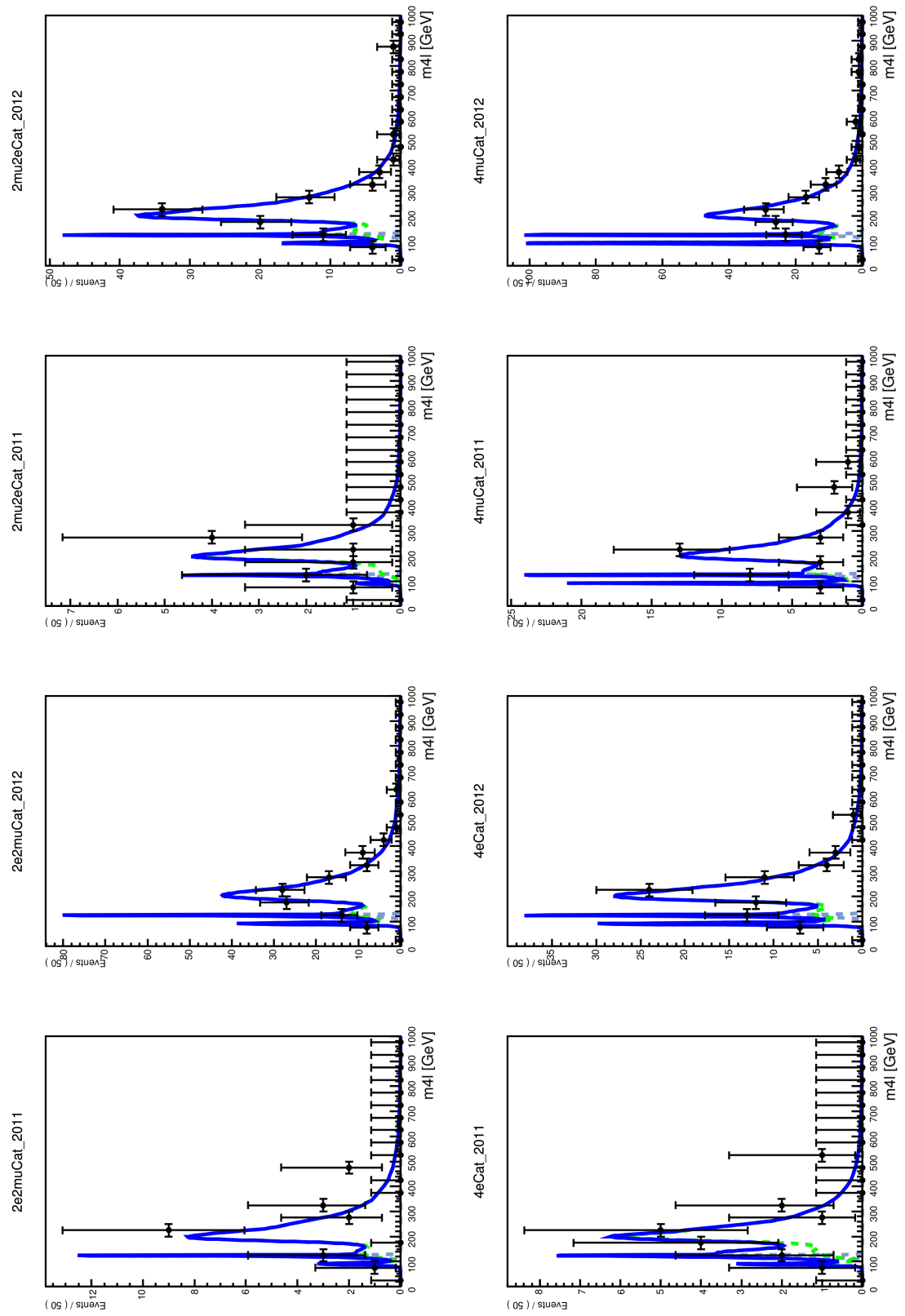


Figure 8.1: Four-lepton invariant mass distribution for the template approach and the 2011 and 2012 dataset studied over the full mass range. The combined (signal+background) pdfs are illustrated by the blue solid line with the signal component given by blue dashed line and background component by the green dashed line.

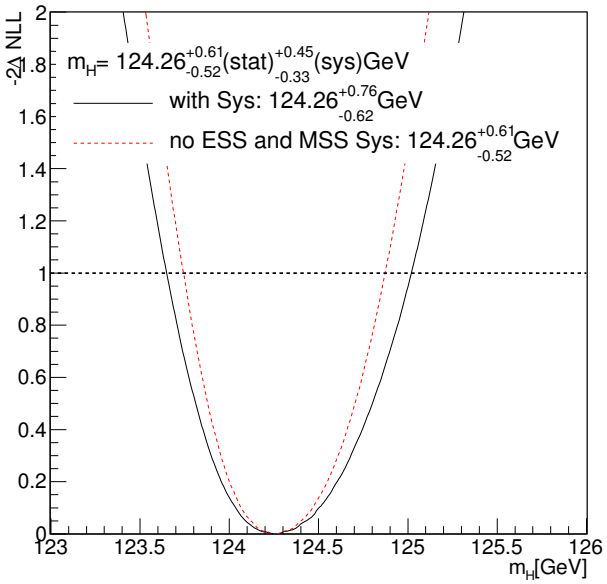
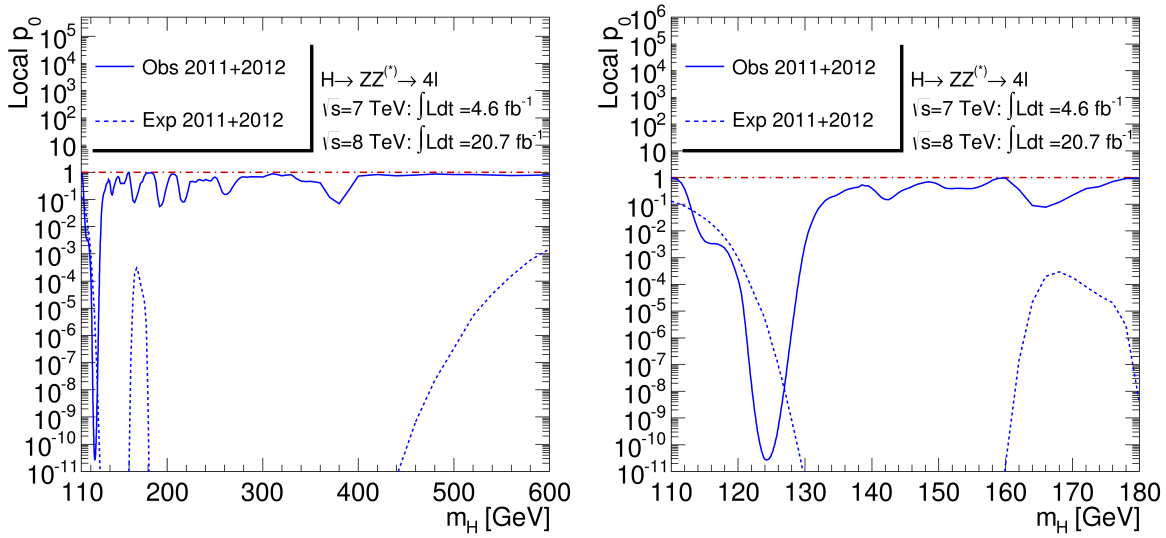


Figure 8.2: Profile likelihood of m_H for the template approach studied over the full mass range with the best fit value of $\hat{m}_H = 124.26^{+0.61}_{-0.52}(\text{stat})^{+0.45}_{-0.33}(\text{sys})\,\text{GeV}$.



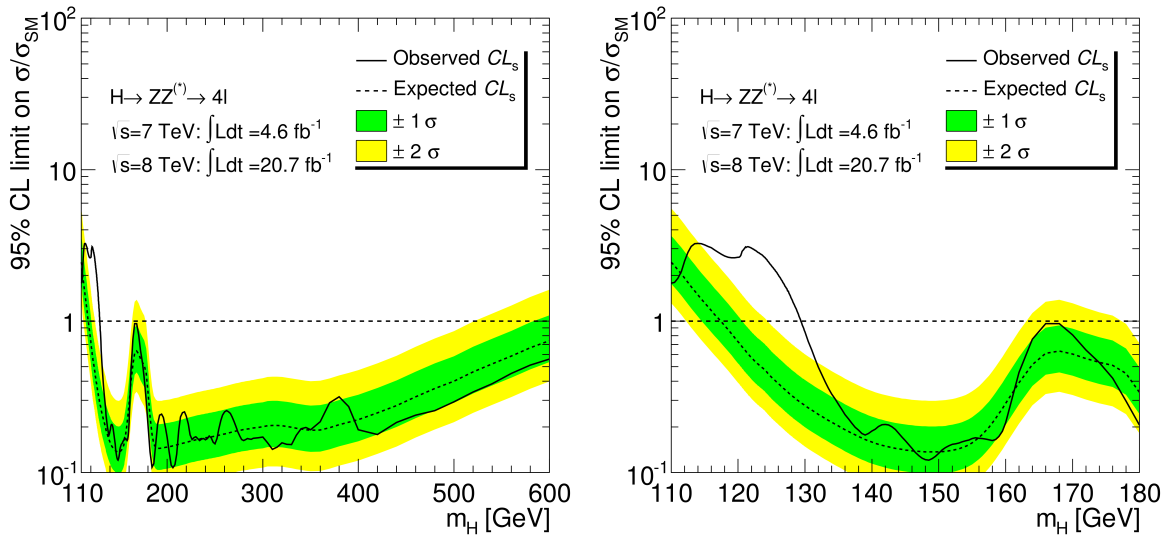
(a) Mass range 110 GeV$\leq m_H \leq$ 600 GeV **(b)** Mass range 110 GeV$\leq m_H \leq$ 180 GeV

Figure 8.3: Distribution of the local p_0 for different mass ranges using the combined dataset.

As discussed in section 6.4.1, the local p-value is defined as $1 - CL_b$ which is given for every mass point. The observed local p_0 value is close to one for most of the mass range, as shown by the blue solid line in figure 8.3a, while the expected median of the local p_0 value for a signal hypothesis at the corresponding mass is smaller than 10^{-3} for most of

the mass range shown by the blue dashed line. A zoomed in region for $110 - 180\,\text{GeV}$ in figure 8.3b reveals that an excess with a local p_0 of the order of 10^{-10} is observed. With the combined dataset the observed excess at $\hat{m}_H = 124.26^{+0.6}_{-0.5}(\text{stat})^{+0.5}_{-0.3}(\text{sys})\,\text{GeV}$ exceeds a 5σ significance giving an observation of new boson in the H$\rightarrow ZZ^{(*)} \rightarrow 4\ell$ channel [5]. The typical discovery criterion is a probability of an upward fluctuation of maximal 2.87×10^{-7}, corresponding to the tail on one side of a Gaussian distribution beyond 5σ.

A SM Higgs is excluded with a 95% confidence level by the H$\rightarrow ZZ^{(*)} \rightarrow 4\ell$ channel for a mass range of $129.4\,\text{GeV} \leq m_H \leq 600\,\text{GeV}$ as shown in figure 8.4. As defined in section 6.4.1, the signal strength with $CL_{s+b} \leq 0.05$ are excluded for every mass point (of the range $129.4\,\text{GeV} \leq m_H \leq 600\,\text{GeV}$). Due to the observed excess at $m_H = 124.26^{+0.76}_{-0.62}$, the observed exclusion starts at 129.4 GeV even though the expected exclusion goes down to 117.5 GeV.



(a) Mass range 110 GeV$\leq m_H \leq$ 600 GeV **(b)** Mass range 110 GeV$\leq m_H \leq$ 180 GeV

Figure 8.4: Exclusion limits for different mass ranges using the combined dataset.

In figure 8.5 the best fit value and the profile likelihood contours at 68% and 95% confidence level are shown for μ and m_H. The results are shown with and without the scale systematics free in the fit. This has a strong impact on the contours obtained in the m_H dimensions with the scale systematics being the main systematics for the mass measurement. The best fit value is $\hat{\mu} = 1.71^{+0.51}_{-0.43}$ with $\hat{m}_H = 124.26\,\text{GeV}$. As shown in figure 5.1, the cross-section times branching ratio rises sharply over the studied mass range. Therefore, observing a similar amount of events at different mass points results

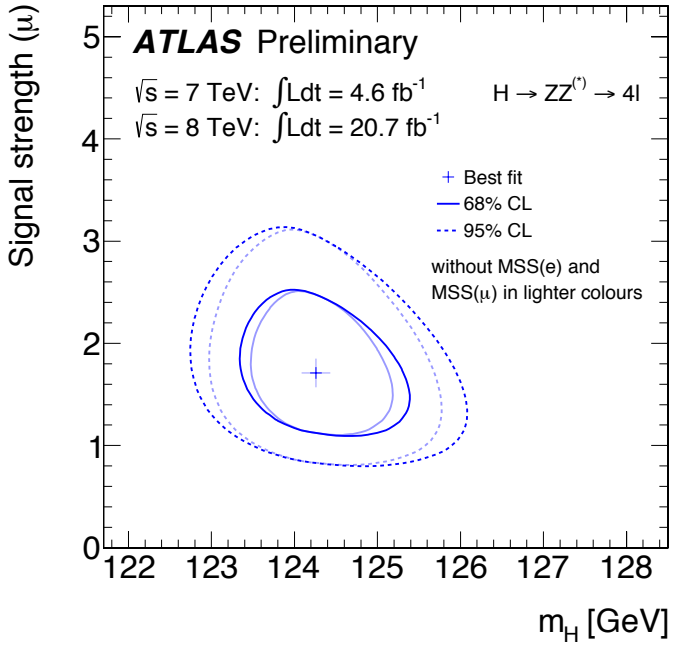


Figure 8.5: Best fit values for μ and m_H are shown together with their profile likelihood contours at 68% (dark blue solid line) and 95% (dark blue dashed line) confidence levels. The results are shown with (dark blue) and without (light blue) momentum and energy scale systematics [5].

in a larger signal strength for lower m_H. This can be seen in figure 8.5 where the best fit value is, for example, $\hat{\mu} = 1.84 \pm 0.43$ when fixing $m_H = 123.5\,\text{GeV}$, and the signal strength is $\hat{\mu} = 1.54 \pm 0.35$ when fixing $m_H = 125\,\text{GeV}$. These two mass point have approximately the same number of events, given they are at about the same distance from the best fit value, and if one assumes an approximately symmetric signal shape.

8.2 Systematics

The likelihood function depends on a set of parameters $\vec{\theta} = \theta_{1,\ldots,m}$ where the parameters which are of direct interest in the measurement are called parameters of interest (POI). In the H→ $ZZ^{(*)} \to 4\ell$ analysis the POI are the mass and the signal strength. The remaining parameters are called nuisance parameters and they are needed to model the unknown aspects of our data. In the H→ $ZZ^{(*)} \to 4\ell$ analysis, these can be separated into theoretical and experimental effects. The latter include detector resolution effects.

Systematics	Value [%]
Luminosity	1.8 (2011)/3.6 (2012)
Muon efficiency	0.4-0.8
Muon momentum scale	0.1-0.2
Electron efficiency	1.6-9.4[2]
Electron energy scale	0.2-0.4

Table 8.1: A selection of important systematic uncertainties is summarised for experimental systematic effects.

8.2.1 Experimental systematic effects

The signal rate is influenced by the electron and muon efficiency systematics which include the identification and reconstruction efficiency. The effect of the muon efficiency systematics on the uncertainty of the signal and irreducible background, $ZZ^{(*)}$ is estimated to be $\pm 0.8\%$ in the 4μ and $\pm 0.4\%$ in the mixed channels.

The electron efficiency systematics, consisting of uncertainties in the electron identification and reconstruction efficiency, amounts to $\pm 2.4\%$ for $4e$, $\pm 1.8\%$ for $2\mu 2e$ and $\pm 1.6\%$ for $2e2\mu$ for $m_H = 1\,\text{TeV}$. As shown in figure 8.6, the electron efficiency depends strongly on the mass. It increases to $\pm 9.4\%$ for $4e$, $\pm 8.7\%$ for $2\mu 2e$ and $\pm 2.4\%$ for $2e2\mu$ at $m_H = 125\,\text{GeV}$. This is further discussed in subsection 8.2.3.

The scale factors have to be taken into account which arise from the calibration uncertainties of the devices determining the energy and momentum. The mass measurement is affected by the electron energy scale (EES) which is evaluated using $Z \to ee$ and for $E_T < 15\,\text{GeV}$ using $J/\psi \to ee$ samples. It results in a systematic uncertainty of $\pm 0.4\%$ for $4e$, $\pm 0.2\%$ for $2e2\mu$ and is negligible for $2\mu 2e$ due to the low momentum of the electrons.

The muon momentum scale (MMS) is determined by using $J/\psi \to \mu\mu$, $\Upsilon \to \mu\mu$ and $Z \to \mu\mu$ samples. The uncertainty is estimated to be $\pm 0.2\%$ in the 4μ and 0.1% in the mixed channels.

The uncertainty on the integrated luminosity is $\pm 1.8\%$ on the 2011 and $\pm 3.6\%$ on the 2012 dataset. The systematic uncertainty estimated for the reducible data-driven background is at most $\pm 1\%$ at 7 TeV and $\pm 0.25\%$ at 8 TeV. A summary of the most important experimental systematic uncertainties is given in table 8.1.

[2]The electron efficiency systematics depend strongly on the Higgs mass as further discussed in subsection 8.2.3.

8.2.2 Theoretical systematic effects

The theoretical systematic uncertainties affect the cross section of the signal and background. The QCD scale uncertainty is for the ggF production mode $^{+7}_{-8}\%$, for the VBF and Higgsstrahlung production modes $\pm 1-2\%$, and for the ttH production mode $^{+4}_{-9}\%$ at $m_H = 125\,\text{GeV}$ and varies slightly over the mass range. The uncertainty for the signal cross section due to the parton distribution function (PDF) and the strong coupling constant, α_S, is $\pm 8\%$ for gluon-initiated and $\pm 4\%$ quark-initiated processes. The QCD scale and PDF uncertainty are the same for $\sqrt{s} = 7\,\text{TeV}$ and $\sqrt{s} = 8\,\text{TeV}$. The percentages of the QCD scale and PDF uncertainty result in the cross section shown in table 8.2 where the uncertainty is a linear sum of the QCD scale and PDF+α_s uncertainty. The production cross sections and branching ratios applied for the H$\to ZZ^{(*)} \to 4\ell$ analysis are given with their corresponding theoretical uncertainty at $m_H = 125\,\text{GeV}$.

The QCD scale uncertainty on the $ZZ^{(*)}$ background is $\pm 5\%$. The PDF+α_s uncertainty for this background accounts to $\pm 8\%$ for gluon-initiated and $\pm 4\%$ quark-initiated processes. For the $t\bar{t}$ background the QCD scale uncertainty accounts to $^{+4}_{-9}\%$ and the PDF+α_S uncertainty is $\pm 7\%$. The Z+jets background is normalised to control samples from data. The mass dependence of the theoretical uncertainties, as shown in figure 8.8, is further discussed in the subsection 8.2.3 together with several other systematic effects shown in more detail.

8.2.3 Modelling of systematics

The POI of $\vec{\theta}$ are denoted $\vec{\theta} = \theta_{1,\ldots,h}$ and the nuisance parameters are referred to as $\vec{\alpha} = \alpha_{1,\ldots,l}$ where $n = h + l$. According to equation 6.10, the likelihood function is

$$L_{s+b}(\vec{x}|\mu,\vec{\theta}) = \frac{1}{n!}\int e^{-(\mu s(\vec{\theta},\vec{\alpha})+b(\vec{\theta},\vec{\alpha}))}\prod_{i=1}^{n}\Big(\mu s(\vec{\theta},\vec{\alpha})f_s(\vec{x_i};\vec{\theta},\vec{\alpha}) + b(\vec{\theta},\vec{\alpha})f_b(\vec{x_i};\vec{\theta},\vec{\alpha})\Big)\,d^l\alpha$$

$\sqrt{s}$ [TeV]	$\sigma\,(gg\to H)$ [pb]	$\sigma\,(qq'\to Hqq')$ [pb]	$\sigma\,(q\bar{q}\to WH)$ [pb]	$\sigma\,(q\bar{q}\to ZH)$ [pb]	$\sigma\,(q\bar{q}/gg\to t\bar{t}H)$ [pb]	BR $\left(H\to ZZ^{(*)}\to 4\ell\right)$ [10^{-3}]
7	15.3 ± 2.3	1.22 ± 0.03	0.57 ± 0.02	0.32 ± 0.02	$0.09^{+0.01}_{-0.02}$	0.125
8	19.5 ± 2.9	$1.58^{+0.04}_{-0.05}$	0.70 ± 0.03	0.39 ± 0.02	0.13 ± 0.02	0.125

Table 8.2: The Higgs production cross sections are shown with their theoretical systematic uncertainties at $m_H = 125\,\text{GeV}$. The systematic uncertainties are a linear sum of the QCD scale and the PDF+α_S uncertainties and they vary with Higgs mass [32].

Looking at a systematic effect on the number of background events, the pdf of the background estimate can be modelled by the measurement of the number of background events

$$L_{s+b}(n, b'; s, b) = \frac{(s+b)^n}{n!} e^{-(s+b)} P(b'; b) \text{ [132]}. \tag{8.1}$$

The nuisance parameter b is eliminated by integrating over it

$$L_{s+b}(n, b'; s, b) = \int_0^\infty \frac{(s+b)^n}{n!} e^{-(s+b)} P(b'; b) db. \tag{8.2}$$

In case of a Gaussian $P(b'; b)$ term an analytical solution can be derived. To avoid negative values in the integration, other often used assumptions for $P(b'; b)$ are log-normal or Gamma functions which are only defined for positive values [139].

This is called a hybrid Bayesian approach as a Bayesian procedure would suggest the multiplication with a prior assumption about b and the Frequentist approach would imply a multiplication with an auxiliary measurement [140].

In a generalised form, the expected number of events for the signal $s(\vec{\theta}, \vec{\alpha})$ and the background $b(\vec{\theta}, \vec{\alpha})$ depend on the term $\eta_j(\alpha)$ giving the relative changes in the overall normalisation. For a nominal expectation, the values are $\alpha_i = 0$ and $\eta_j(0) = 0$. A $\pm 1\sigma$ variation of the systematic effect is represented by $\alpha_i = \pm 1\sigma$ [141]. The relative change on the overall normalisation is determined for several Higgs mass points at $\alpha = \pm 1\sigma$ and the dependence is interpolated by basis splines as a function of the Higgs mass. Basis splines, abbreviated by B-Splines, is a parametric curve $S(t) = \sum_{i=0}^{m-n-2} P_i b_{i,n}(t)$ where P_i is a set of control points and $b_{i,n}$ are basis polynomials. These polynomials of order n are defined depending on the knots t_i

$$b_{i,0}(t) = \begin{cases} 1, & t_i \leq t < t_{i+1}, \\ 0, & \text{otherwise}, \end{cases} \qquad i = 0, ..., m-2$$

$$b_{i,n}(t) = \frac{t - t_i}{t_{1+n} - t_i} b_{i,n-1}(t) + \frac{t_{i+n+1} - t}{t_{1+n+1} - t_{i+1}} b_{i+1,n-1}(t) \quad i = 0, ..., m-n-2$$

where the values of t_i increase from $i = 0$ to $i = m$ [142]. The control points are defined for each knot for $t_n \leq t \leq t_{m-n-1}$. B-Splines of the third order are used for the modelling of the systematics as a function of the Higgs mass.

In figure 8.6, the electron efficiency systematic is parametrized versus m_H using B-splines. Going from high to low m_H values, the electron efficiency systematic strongly increases at $m_H \sim 180\,\text{GeV}$ for the $4e$ and $2\mu 2e$ channel where ZZ changes to ZZ^*. This

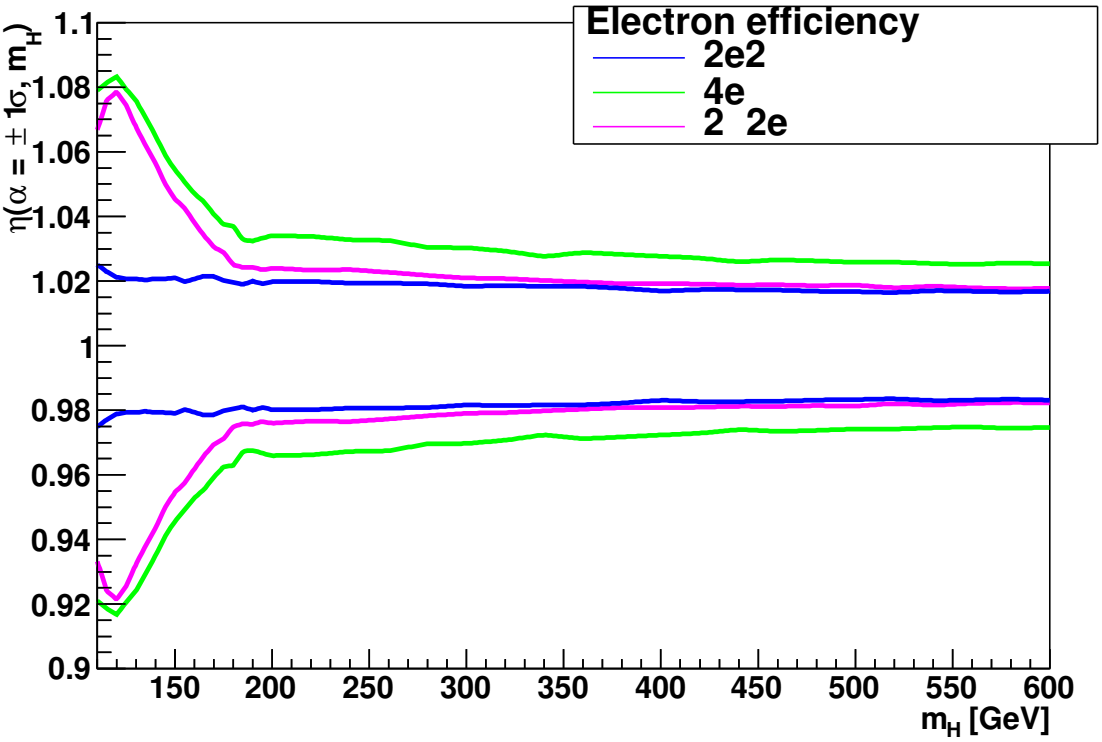


Figure 8.6: Relative change in the overall normalisation is shown as a response to the nuisance parameter of the electron efficiency $\alpha = \pm 1\sigma$ as a function of the Higgs mass for the 2012 dataset.

rise is not visible in the $2e2\mu$ channel as this systematic concerns only the on-shell Z_1 in this channel. With the Z_2 being off-shell the E_T of $\ell_{3,4}$ is smaller due to less phase space which increases the relative effect of the electron efficiency systematic. At around 120 GeV most of the Z_1 are off-shell so the change from ZZ^* to Z^*Z^* occurs. This kinematic change also affects the E_T of the electrons coming from Z_2. The mean E_T is larger at $m_H = 110\,\text{GeV}$ than at $m_H = 120\,\text{GeV}$ as the probability of Z_1 being off-shell is larger allowing a larger phase-space for E_T of Z_1. Therefore, the systematic effect of the electron efficiency decreases below 120 GeV in the $4e$ and $2\mu2e$ channel. A slight increase of the systematic effect of the electron efficiency is observed for $2e2\mu$ below 120 GeV. This is caused by a small decrease of the E_T of $\ell_{1,2}$ due to the Z_1 going off-shell.

The response of the muon efficiency is modelled as a function of m_H as shown in figure 8.7. The overall shape of the dependence is very similar to the the electron efficiency as the effect of the muon efficiency on the overall normalisation also increases for low p_T. The p_T decrease of $\ell_{3,4}$ for Z_2 going off-shell is visible by an increase in the response at about $m_H = 180\,\text{GeV}$ in the 4μ and $2e2\mu$ channel. The slight decrease below

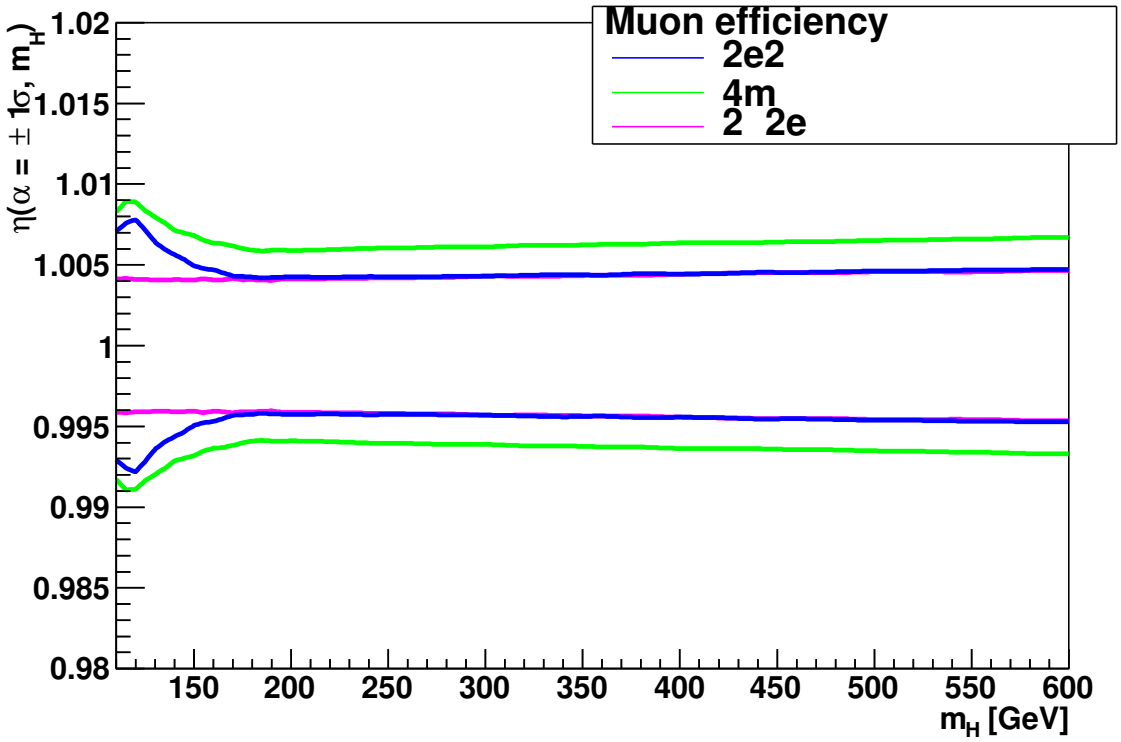


Figure 8.7: Response on the muon efficiency systematic is given as a function of the Higgs mass for the 2012 dataset. The scale of the y-axis is chosen to be the same as in figure 8.6 to show the relative importance.

$m_H = 120\,\text{GeV}$ is caused by a small increase in the p_T of $\ell_{3,4}$ with Z_1 going off-shell. In the $2\mu 2e$ channel the muon efficiency response is approximately constant and increases slightly below $m_H = 120\,\text{GeV}$ with Z_1 going off-shell.

In figure 8.8 the response of the QCD scale and PDF+α_s uncertainty is shown as a function of m_H. Some steps are observed due to rounded input of the reference points provided by theoretical calculations [143, 144].

8.3 Comparison of (non-)parametric and per-event models

The template approach is studied in the low mass region ($110\,\text{GeV} < m_H < 150\,\text{GeV}$) with the aim to improve the results obtained for the mass measurement. These studies can be directly compared to the main analysis which applies the template approach over the full mass range because the change of the mass range has a minor effect on the mass

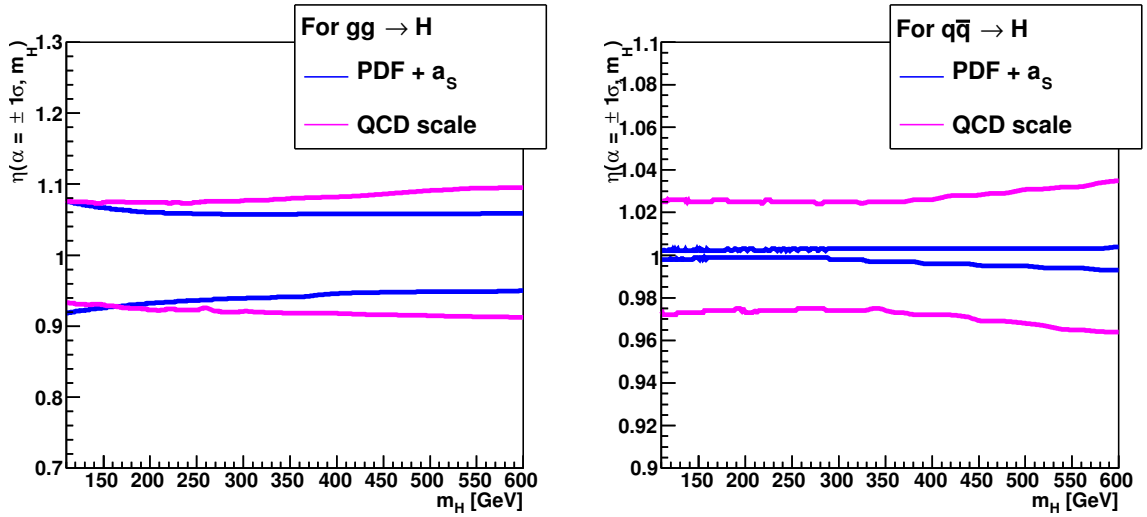


Figure 8.8: The response in the overall normalisation is shown as a response to the QCD scale and the PDF+α_s uncertainty for the Higgs production modes gluon-gluon fusion and vector boson fusion. The response for the 2012 dataset is modelled as a function of the Higgs mass by third order B-Splines.

measurement. It influences slightly the fitting of the reducible background and the overall fitting results change only insignificantly from $\hat{m}_H = 124.26^{+0.61}_{-0.52}(\text{stat})^{+0.45}_{-0.33}(\text{sys})\,\text{GeV}$ and $\hat{\mu} = 1.71^{+0.51}_{-0.43}$ to $\hat{m}_H = 124.27^{+0.62}_{-0.52}(\text{stat})^{+0.46}_{-0.33}(\text{sys})\,\text{GeV}$ and $\hat{\mu} = 1.69^{+0.51}_{-0.43}$.

As shown in figure 7.4, no bias was observed for the model of the main analysis. As expected very similar results are obtained when comparing this model to a parametric approach with a sum of a Crystal ball and a Gaussian function for the ggF signal. This CB+GA model has a bias in μ of 0.09 ± 0.01 and overestimates the error on m_H resulting in a m_H-pull distribution with a sigma of 0.89 ± 0.03 given in figure 7.7c. The overestimation of the error in m_H by 11% would decrease the error on the mass measurement results of the CB+GA model for the combined dataset of $\hat{m}_H = 124.36^{+0.75}_{-0.70}\,\text{GeV}$ to $\hat{m}_H = 124.36^{+0.67}_{-0.69}\,\text{GeV}$. This adjusted resolution is of similar size than the results obtained for the template $\hat{m}_H = 124.27^{+0.77}_{-0.62}\,\text{GeV}$. The uncertainties on the mass measurement using the parametric model are more symmetric than the uncertainties of the non-parametric approach.

The main analysis is performed with the Z-mass constraint as this results in an improvement of the mass resolution of 1.9% in the $4e$ channel and 1.3% in the 4μ channel at 125 GeV, determined by a Gaussian fit in the earlier section 5.3.5. It exploits information obtained from the per-event error to rescale the mass of the leading Z boson.

Analysis	Dataset	$\hat{m}_H$ [GeV]	$\hat{\mu}$
full mass range 80 GeV$< m_H <$ 1 TeV			
Template approach (with Z constraint)	2011+2012	$124.26^{+0.76}_{-0.62}$	$1.71^{+0.51}_{-0.43}$
low mass range 110 GeV$< m_H <$ 150 GeV			
Template approach (with Z constraint)	2011+2012	$124.26^{+0.77}_{-0.61}$	$1.71^{+0.51}_{-0.43}$
CB+GA (with Z constraint)	2011+2012	$124.36^{+0.75}_{-0.71}$	$1.84^{+0.53}_{-0.45}$
Template approach (without Z constraint)	2012	$124.27^{+0.81}_{-0.79}$	$1.54^{+0.52}_{-0.43}$
Per-event error (without Z constraint)	2012	$124.10^{+0.76}_{-0.70}$	$1.53^{+0.52}_{-0.43}$

Table 8.3: This table contains the results of the analysis performed with their best fit values for m_H and mu.

Using the per-event error as an additional observable results in a consistent mass measurement with $\hat{m}_H = 124.10^{+0.76}_{-0.70}$ GeV and $\hat{\mu} = 1.53^{+0.52}_{-0.43}$. A Crystal ball function was used as a conditional pdf for the signal and a small bias in m_H of 41 ± 11 MeV was observed. The resolution is improved by the per-event error by $^{+50}_{-90}$ MeV compared to the one-dimensional template approach for the 2012 dataset without applying a Z-mass constraint. An overview of the obtained results is given in table 8.3.

8.4 Outlook

The parametric and per-event model have both shown successful cross checks of the main analysis and improved the resolution. Further studies could optimize the parametric model applied, for example changing to a convolution approach where the signal is modelled on the generator level and convoluted by a detector response function. This is in particularly interesting for the muon channels, whereas the shape of the electron channels is dominated by a radiative tail due to bremsstrahlung. Therefore, the shape of the generator level function has only a marginal impact on the final shape of the electron channels. The convolution approach can be combined with an improved modelling of the per-event error to exploit the full discrimination power of the $m_{4\ell}$ and $m_{4\ell err}$ observables. Besides the per-event error, additional dimensions as for example m_{34} are studied and can

be combined with the per-event model. For this multidimensional analysis a restructuring of the systematics implementation in the workspace building code is recommended using the systematic m_H parametrization discussed in the subsection 8.2.3.

By including additional variables in the multi-variant analysis, further discrimination power can be exploited, for example, by using m_{34}. Currently the application of a boosted decision tree (BDT) is studied for the H$\rightarrow ZZ^{(*)} \rightarrow 4\ell$ analysis using the p_T and η distributions. The error on the four-lepton invariant mass is dependent on the p_T and the detector region defined by η. Therefore, the BDT approach exploits part of the per-event error approach. These improvements can result in even more precise mass measurements with the recorded data. Studies to prepare the analysis for the next data-taking period are performed too where the mass measurement will stop to be statistically limited.

Chapter 9

Conclusion

This thesis presents performance studies for the current inner detector comparing the results obtained with data to the predictions made by MC simulation. Given the difference in the cluster size, the Bragg-Peak model for the energy deposition of secondaries was added to the simulation. Additionally, the simulation of the cross talk generation was enabled for every hit pixel and the value of the Lorentz angle and cross talk were adjusted in simulation given the results of *in-situ* measurements affected by radiation.

These improvements of the cluster size modelling have a direct effect on the accuracy of the simulated channel occupancy which was compared to data at pile-up of 26. The occupancy in the different ID regions is modelled well by MC. No saturation was observed in the inner detector for up to twenty-eight reconstructed vertices where the largest occupancy was obtained in the TRT with 40%.

The occupancy studied in high p_T jets ($p_T > 280\,\text{GeV}$) increases in the centre of the jet by an order of magnitude in the case of studying all clusters and only clusters on track. This is linked to the track separation in high p_T jets which was studied, demonstrating the needs of a neural network based cluster reconstruction algorithm to split merged clusters.

The silicon cluster size, channel occupancy and track separation in jets were studied for several possible upgraded tracker layouts for phase II. It is demonstrated that the LoI layout accomplished the design target of an occupancy $< 1\%$ throughout the whole upgrade tracker layout. This concluded in the proposal of the LoI layout for the high luminosity upgrade planned for 2021. Until then further studies of the performance, and prospects for physics analysis, will be performed.

The implementation of an insertable B-layer in 2014 will result in a commissioning phase with continuous performance studies evaluating the cluster size and the implementation of an adapted neural network cluster algorithm. As the luminosity will increase by another factor of ten with a reduced bunch spacing of 25 ns, the occupancy has to be

further monitored and studied. This also accounts for the radiation damage which is expected to change the cluster size.

The other main focus of the thesis is the H$\to ZZ^{(*)} \to 4\ell$ analysis. Given the preselection, the leading lepton-pair invariant mass distributions of the MC simulation were compared to the data to cross-check the selections applied in the analysis. It was verified that no possible mismatching of the leading and sub-leading lepton pair was present by varying the energy scale systematic and restricting the four lepton invariant mass.

Furthermore, the systematic effects present in the H$\to ZZ^{(*)} \to 4\ell$ analysis were studied and modelled as a function of the Higgs mass by interpolating between the mass points with basis splines. The main electron efficiency systematic varies by 7% over the mass range of up to 1 TeV.

Datasets were used with integrated luminosities of $4.6\,\text{fb}^{-1}$ collected at $\sqrt{s} = 7\,\text{TeV}$ in 2011, and $20.7\,\text{fb}^{-1}$ at $\sqrt{s} = 8\,\text{TeV}$ in 2012, respectively. For the template approach an excess of events was observed where the probability of an observation at least as signal-like as obtained is 2.7×10^{-11} assuming a background-only hypothesis. This corresponds to a significance of 6.6 standard deviations appearing at $m_H = 124.3\,\text{GeV}$ with a signal strength of $\mu = 1.71^{+0.51}_{-0.43}$.

The Higgs mass measurement of $m_H = 124.3^{+0.8}_{-0.6}\,\text{GeV}$ in the H$\to ZZ^{(*)} \to 4\ell$ channel was verified by applying parametric signal models. The implementation of the per-event error achieved a decrease of the total mass uncertainty by 9% exploiting additional discrimination power.

The H$\to \gamma\gamma$ analysis, studying the other sensitive channel in the low mass region, obtained a best fit value of $m_H = 126.6 \pm 0.3(\text{stat}) \pm 0.7(\text{syst})\,\text{GeV}$. Combining the H$\to ZZ^{(*)} \to 4\ell$ with the H$\to \gamma\gamma$ channel results in a best fitted Higgs mass of $m_H = 125.5 \pm 0.2(\text{stat})^{+0.5}_{-0.6}(\text{syst})\,\text{GeV}$ for $4.6\,fb^{-1}$ ($4.8\,\text{fb}^{-1}$ for H$\to \gamma\gamma$) at $\sqrt{s} = 7\,\text{TeV}$ and $20.7\,\text{fb}^{-1}$ at $\sqrt{s} = 8\,\text{TeV}$. The mass difference is

$$\Delta\hat{m} = \hat{m}_H^{\gamma\gamma} - \hat{m}_H^{4\ell} = 2.3^{+0.6}_{-0.7}(\text{stat}) \pm 0.6(\text{syst})\,\text{GeV}$$

with the signal strength treated as an independent nuisance parameter. The probability of a single Higgs boson-like particle to produce these values is $\sim 1.5\%$ (2.4σ) with Gaussian pdfs for the systematic uncertainties, and $\sim 8\%$ with rectangular pdfs used for the systematic energy scale uncertainties calibrated with $Z \to ee$, the uncertainty on the material in front of the electromagnetic calorimeter and the energy scale of the presampler

detector [145]. The rectangular pdf provides a uniform probability distribution within the $\pm 1\sigma$ range and a probability of 0 outside this range.

Besides this mass difference which has to be studied with a larger number of events, the combination of the signal strength from the different decay channels will be investigated with the new data obtained during the next data-taking period (run 2). The following channels in table 9.1 are combined for a signal strength measurement.

	$\sqrt{s} = 7\,\text{TeV}$	$\sqrt{s} = 8\,\text{TeV}$
W/ZH$\rightarrow b\bar{b}$	4.7 fb^{-1}	13.0 fb^{-1}
H$\rightarrow \tau^-\tau^+$	4.6 fb^{-1}	13.0 fb^{-1}
H$\rightarrow \gamma\gamma$	4.8 fb^{-1}	20.7 fb^{-1}
H$\rightarrow WW^{(*)} \rightarrow \ell\nu\ell\nu$	4.6 fb^{-1}	20.7 fb^{-1}
H$\rightarrow ZZ^{(*)} \rightarrow 4\ell$	4.6 fb^{-1}	20.7 fb^{-1}

Table 9.1: This table summarises the Higgs channel with the according datasets which were use for the latest combination [22].

The latest result for the best fitted signal strength combining these channels is $\mu = 1.3 \pm 0.13(\text{stat}) \pm 0.14(\text{syst})$ at $m_H = 125.5\,\text{GeV}$, which is the best fit m_H value for the combination of H$\rightarrow \gamma\gamma$ and H$\rightarrow ZZ^{(*)} \rightarrow 4\ell$. This is shown by figure 2.3 giving the μ values for each channel and the result is consistent with the SM Higgs boson hypothesis at $\sim 9\%$ [22].

The other main result for the H$\rightarrow ZZ^{(*)} \rightarrow 4\ell$ analysis is produced by the CMS collaboration with an excess of the background by a significance of 6.7 standard deviations using $5.1\,\text{fb}^{-1}$ taken in 2011 at $\sqrt{s} = 7\,\text{TeV}$ and $19.6\,\text{fb}^{-1}$ taken in 2012 at $\sqrt{s} = 8\,\text{TeV}$. The best fitted Higgs mass is $m_H = 125.8 \pm 0.5(\text{stat}) \pm 0.2(\text{syst})\,\text{GeV}$ with a signal strength of $\mu = 0.91^{+0.30}_{-0.24}$ and Higgs exclusion limits at 95% CL in the range from 130 GeV to 827 GeV [146]. These results are consistent with the results of the ATLAS H$\rightarrow ZZ^{(*)} \rightarrow 4\ell$ channel.

Besides the mass measurement, the determination of the other properties of the observed particle are of great interest. In the H$\rightarrow ZZ^{(*)} \rightarrow 4\ell$ analysis, the two Z bosons masses, a production angle θ^* and four decay angles Φ_1, Φ, θ_1 and θ_2 are used to measure the spin and parity. Compatible results for the spin and parity measurement are obtained by the Matrix element based likelihood analysis (MELA) and the boosted decision tree (BDT). The spin-parity analysis is performed for $115\,\text{GeV} < m_H < 130\,\text{GeV}$ for the combined dataset. The SM state 0^+ is favoured and 0^- and 1^+ are excluded at 97.8% confidence level or higher using MELA or BDT [5].

In run 2 the variations of the mass measurement observed in the different Higgs channels can be studied with an expected additional $50.0\,\mathrm{fb}^{-1}$ of data at $\sqrt{s} = 13-14\,\mathrm{TeV}$. This will also give the opportunity to investigate the difference observed in the mass measurement between the ATLAS and CMS experiment. This data-taking period with the new insertable b-layer in place will profit from the improvements made modelling the inner detector, e.g., by adjusting the cross-talk generation. The high luminosity run (phase II) planned to start after 2021 is intended to include a new inner detector with the occupancy studied to be $< 1\%$. During this run, the self-coupling of the Higgs is expected to be measured to obtain a first complete picture of the properties of the newly discovered particle currently consistent with the SM Higgs boson.

Appendix A

Appendices

A.1 Crystal ball model with all parameters floating

$$\begin{aligned}
\mu_{CB}(m_H) &= p_0 + p_1 m_H \\
\sigma_{CB}(m_H) &= p_0 + p_1 \sqrt{m_H} \\
\alpha_{CB}(m_H) &= p_0 + p_1 m_H + p_2 m_H^2 \\
n_{CB}(m_H) &= p_0 + p_1 m_H + p_2 m_H^2
\end{aligned} \tag{A.1}$$

A.2 Crystal ball model with n fixed

$$\begin{aligned}
\mu_{CB}(m_H) &= p_0 + p_1 m_H \\
\sigma_{CB}(m_H) &= p_0 + p_1 \sqrt{m_H} \\
\alpha_{CB}(m_H) &= p_0 + p_1 m_H + p_2 m_H^2
\end{aligned} \tag{A.2}$$

The value for n is fixed to a constant value for each final state. This constant p_0 is determined by performing the fit presented in section A.1 with $n_{CB}(m_H) = p_0$.

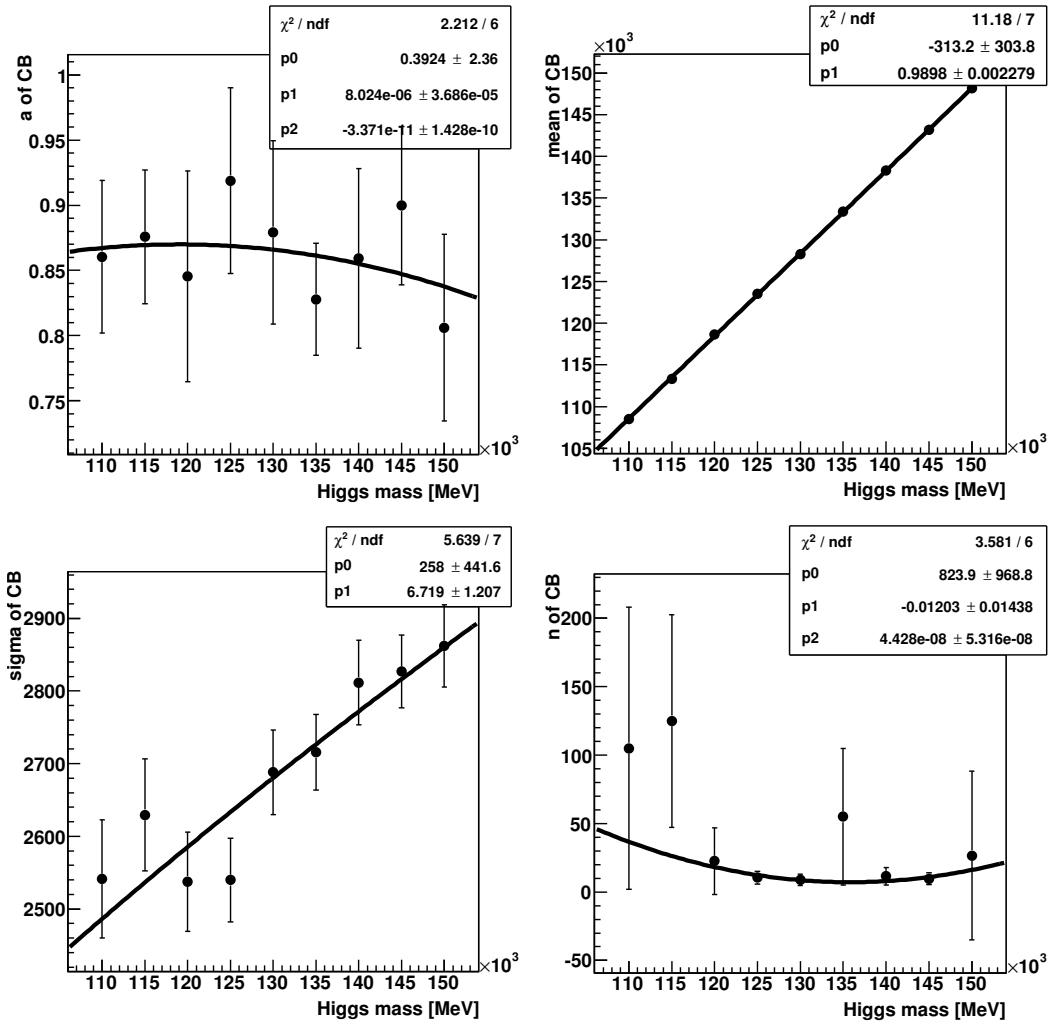


Figure A.1: Fit results for the Crystal ball parameters shown for $4e$ final state as a function of the Higgs mass. Besides the mean and the sigma describing the Gaussian component of the Crystal ball function, n, is the free parameter of the power law and a determines the transition between the power law and the Gaussian component.

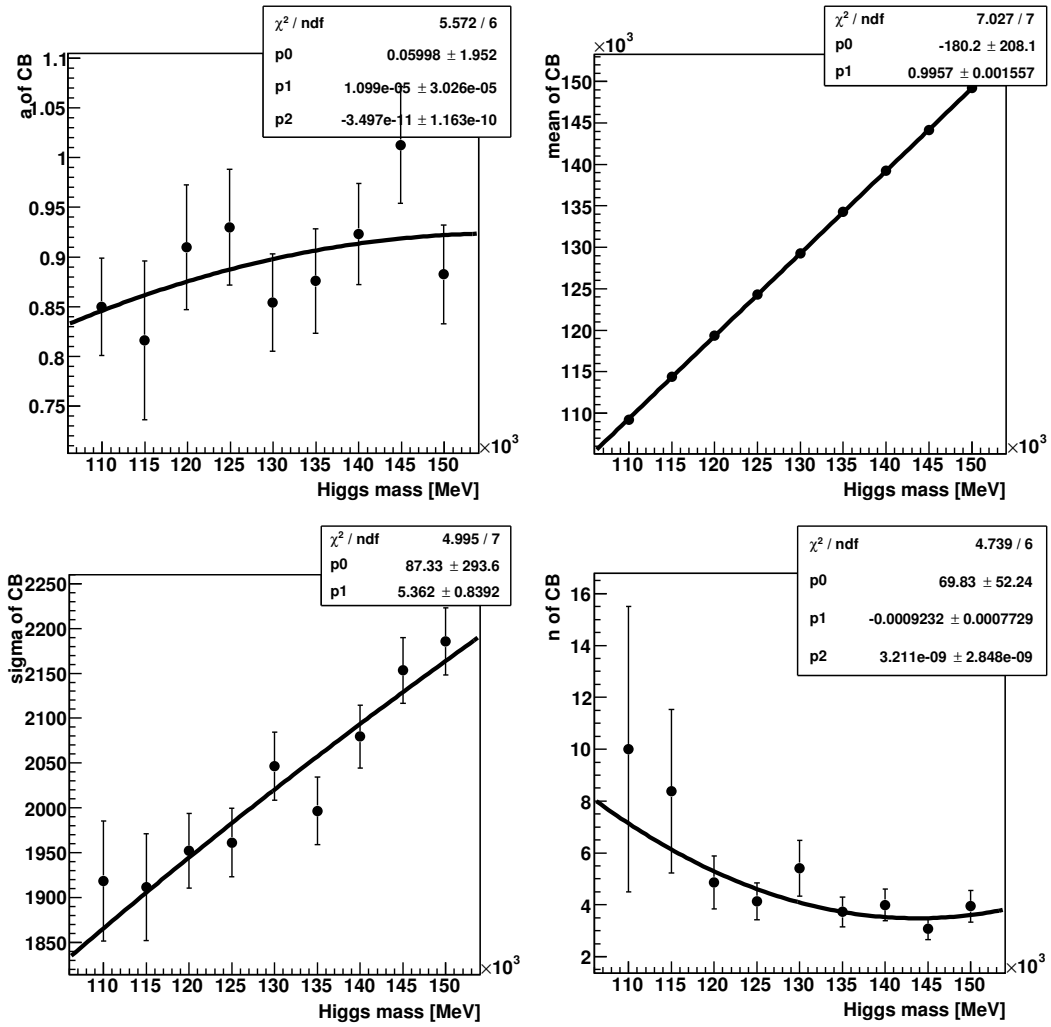


Figure A.2: Fit results for the Crystal ball parameters shown for $2e2\mu$ final state as a function of the Higgs mass.

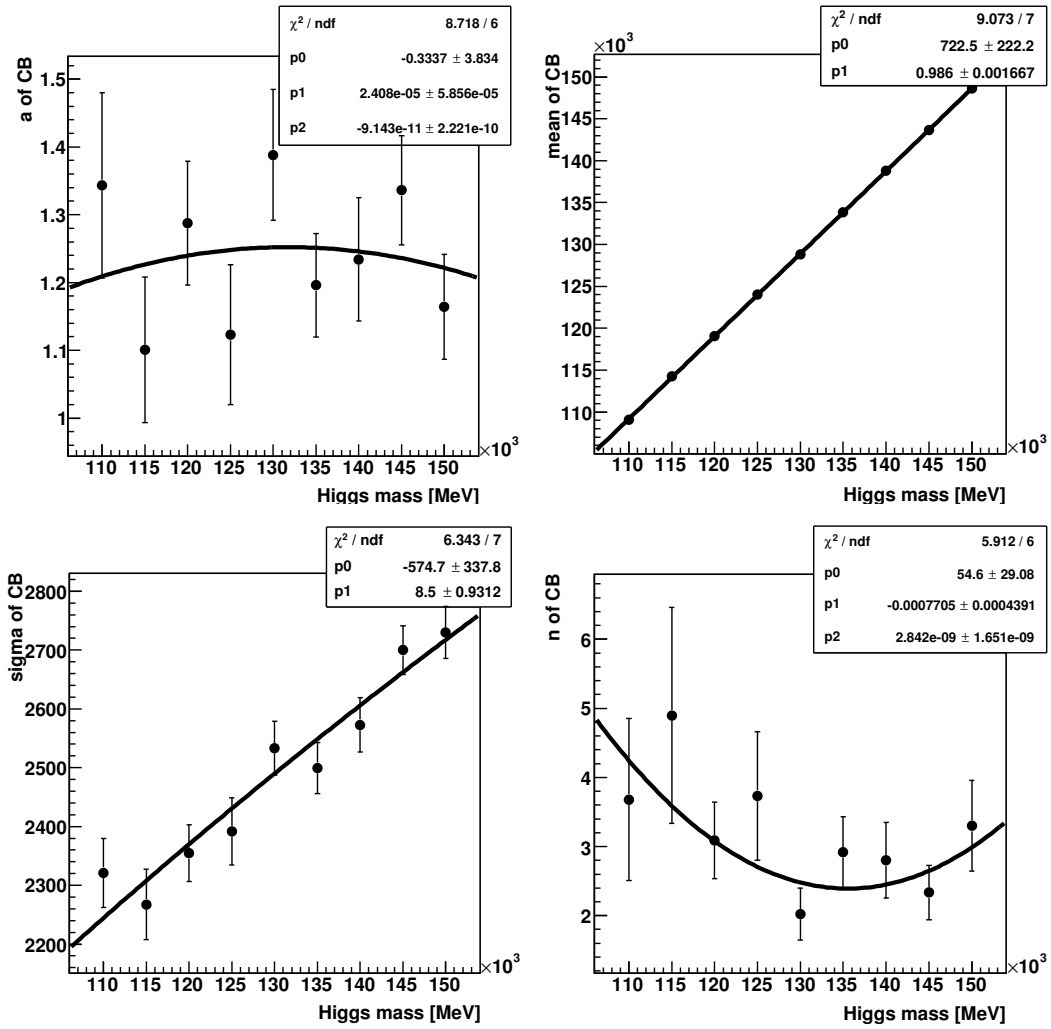


Figure A.3: Fit results for the Crystal ball parameters shown for $2\mu 2e$ final state as a function of the Higgs mass.

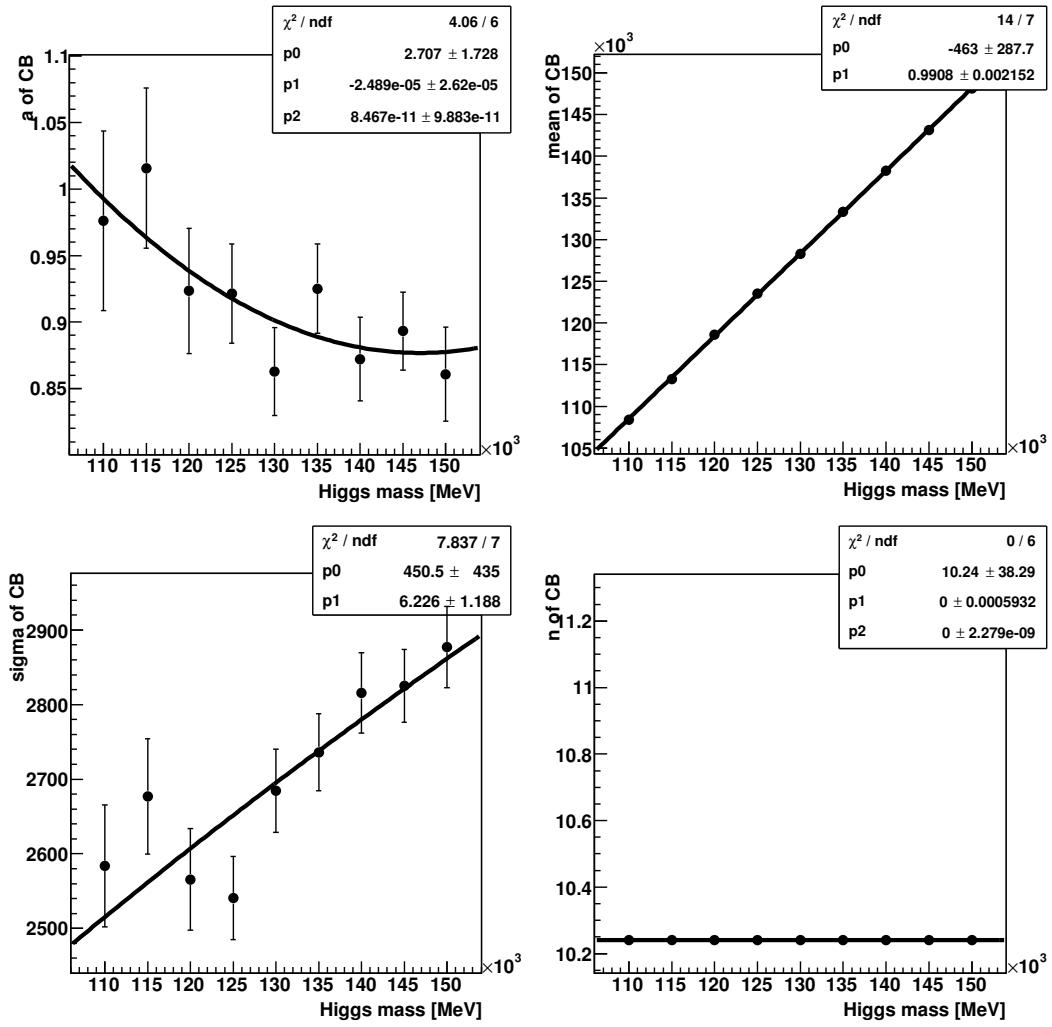


Figure A.4: Fit results for the Crystal ball parameters with n fixed are shown for $4e$ final state as a function of the Higgs mass.

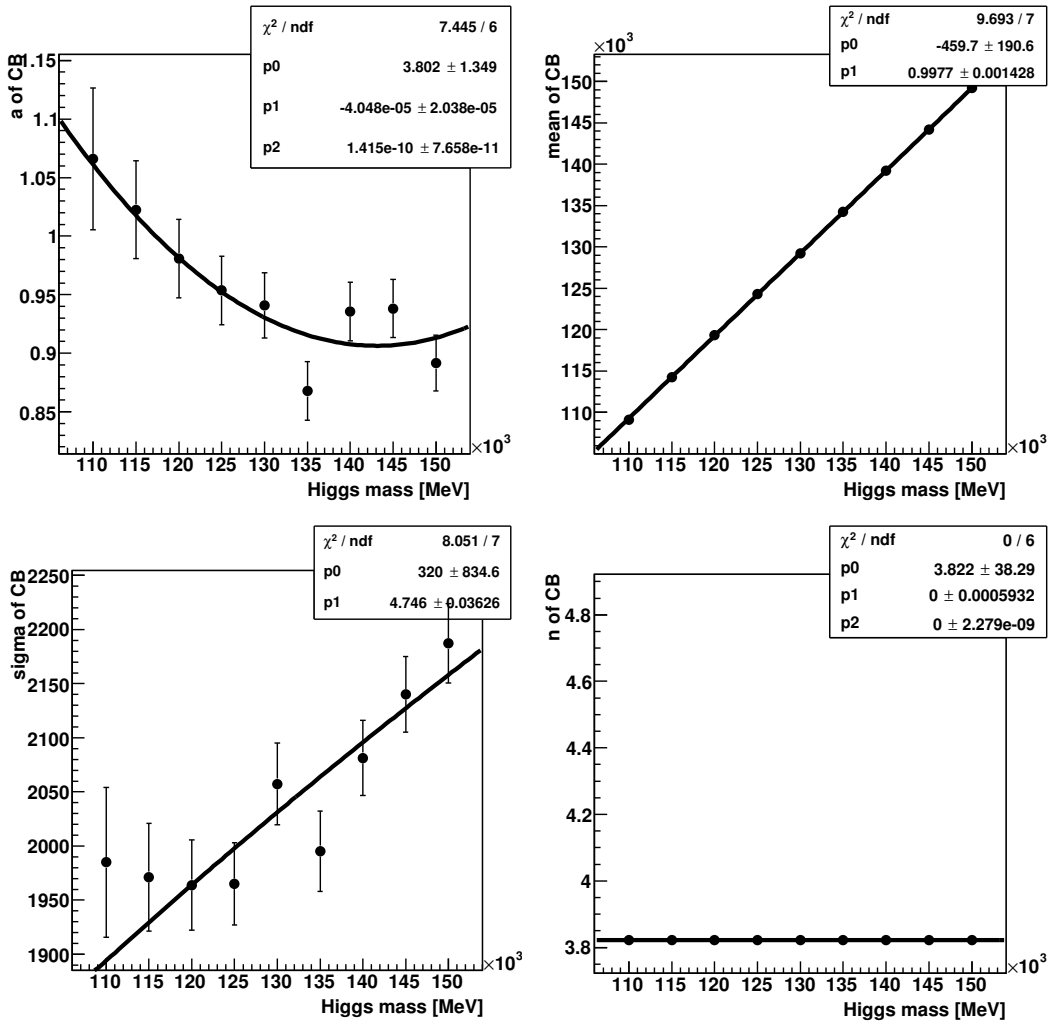


Figure A.5: Fit results for the Crystal ball parameters with n fixed are shown for $2e2\mu$ final state as a function of the Higgs mass.

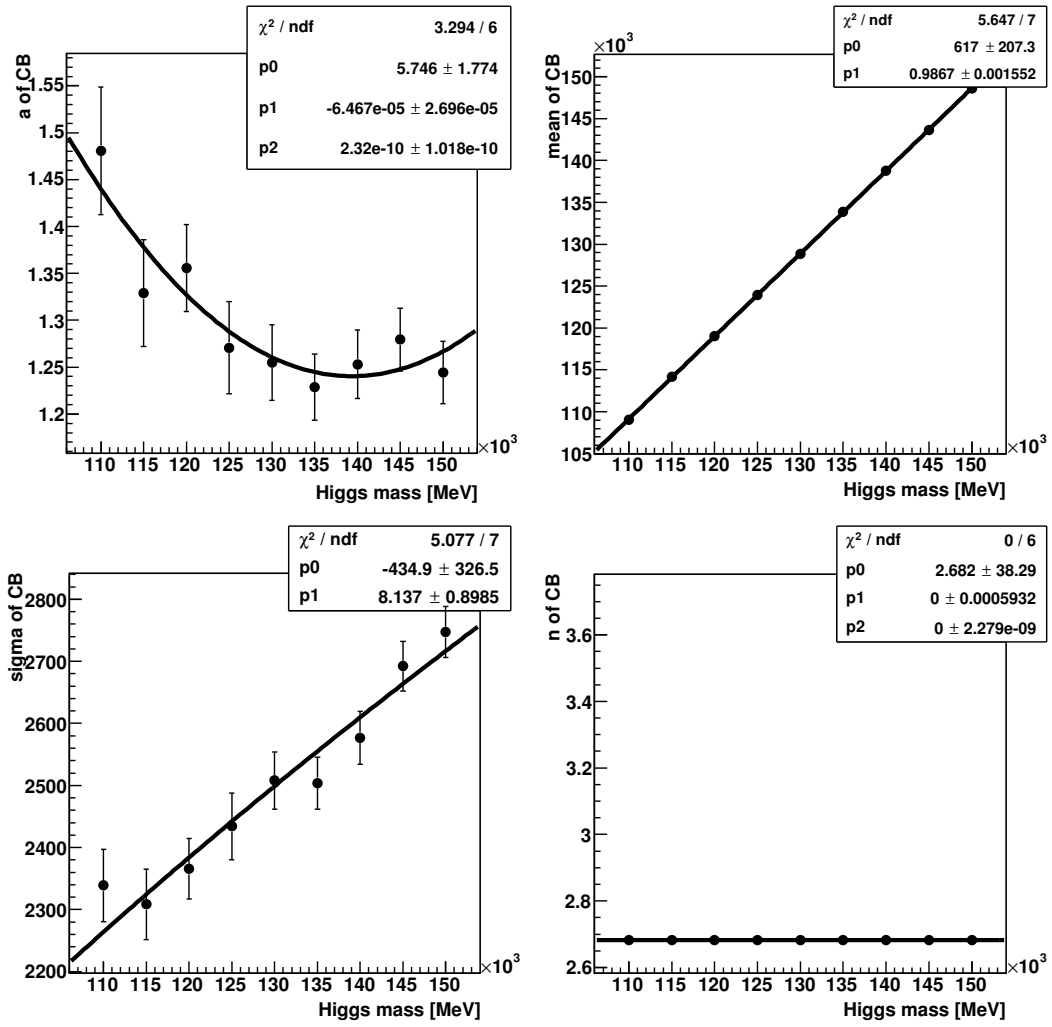


Figure A.6: Fit results for the Crystal ball parameters with n fixed are shown for $2\mu 2e$ final state as a function of the Higgs mass.

Bibliography

[1] D. Griffiths, *Introduction to Elementary Particles,* Physics Textbook (Wiley, 2008).

[2] P. W. Higgs, Broken symmetries and the masses of gauge bosons, Phys. Rev. Lett. **13**, 508 (1964).

[3] F. Englert and R. Brout, Broken symmetry and the mass of gauge vector mesons, Phys. Rev. Lett. **13**, 321 (1964).

[4] G. S. Guralnik, C. R. Hagen, and T. W. B. Kibble, Global conservation laws and massless particles, Phys. Rev. Lett. **13**, 585 (1964).

[5] ATLAS Collaboration, Measurements of the properties of the Higgs-like boson in the four lepton decay channel with the ATLAS detector using 25 fb^{-1} of proton-proton collision data, ATLAS-CONF-2013-013 (2013).

[6] ATLAS Collaboration, Letter of Intent for the Phase-II Upgrade of the ATLAS Experiment, CERN-LHCC-2012-022. LHCC-I-023 (2012).

[7] R. Ellis, W. Stirling, and B. Webber, *QCD and Collider Physics,* (Cambridge University Press, 1996).

[8] F. Mandl and G. Shaw, *Quantum Field Theory* (Wiley, 2010).

[9] F. Halzen and A. Martin, *Quarks and leptons: an introductory course in modern particle physics* (Wiley, 1984).

[10] L. Ryder, *Quantum Field Theory* (Cambridge University Press, 1996).

[11] S. Heinemeyer, Higgs and Electroweak Physics, at SUSSP65, St. Andrews, www.ifca.es/users/heinemey/uni/lectures/2009/sussp/SUSSPLecturePart1.pdf.

[12] P. Langacker, Introduction to the Standard Model and Electroweak Physics, arXiv:0901.0241 , 3 (2009).

[13] A. Bettini, *Introduction to Elementary Particle Physics* (Cambridge University Press, 2008).

[14] Particle Data Group, J. Beringer *et al.*, Review of particle physics, Phys. Rev. D **86**, 010001 (2012).

[15] A. Djouadi, The Anatomy of electro-weak symmetry breaking. I: The Higgs boson in the standard model, Phys.Rept. **457**, 1 (2008).

[16] K. Nikolopoulos, D. Fassouliotis, C. Kourkoumelis, and V. Polychronakos, *Discovery Potential for the Standard Model Higgs $\to ZZ^{(*)} \to 4\ell$ and Contributions to Muon Detection in ATLAS*, PhD thesis, Athens U., Athens, 2010.

[17] Gfitter Group, Constraints on the electroweak symmetry breaking sector from global fits with Gfitter, https://indico.cern.ch/getFile.py/access?contribId=81&sessionId=18&resId=1&materialId=slides&confId=141983.

[18] CDF and D0 Collaborations, Combined CDF and D0 Search for Standard Model Higgs Boson Production with up to 10.0 fb^{-1} of Data, arXiv:1203.3774 (2012).

[19] CMS Collaboration, Observation of a new boson at a mass of 125 GeV with the CMS experiment at the LHC, CMS-HIG-12-028 (2012).

[20] ATLAS Collaboration, Observation of a new particle in the search for the Standard Model Higgs boson with the ATLAS detector at the LHC, Phys.Lett. **B716**, 1 (2012).

[21] ATLAS Collaboration, Updated results and measurements of properties of the new Higgs-like particle in the four lepton decay channel with the ATLAS detector, ATLAS-CONF-2012-169 (2012).

[22] ATLAS Collaboration, Combined coupling measurements of the Higgs-like boson with the ATLAS detector using up to 25 fb^{-1} of proton-proton collision data, ATLAS-CONF-2013-034 (2013).

[23] Edited by T. Binoth, C. Buttar and P. J. Clark, *LHC Physics* (CRC Press, 2012).

[24] K. Ecker, H. Kroha, and O. Kortner, Search for the Standard Model Higgs Boson in Decays into Four Charged Leptons with the ATLAS Detector at the LHC, Master thesis, Tech. U. Munich, Munich (2013).

[25] ATLAS Collaboration, Higgs production cross section times branching ratio, https://twiki.cern.ch/twiki/bin/view/LHCPhysics/CrossSections.

[26] A. Pich, The Standard Model of Electroweak Interactions, arXiv:1201.0537 (2012).

[27] J. R. Ellis, M. K. Gaillard, and D. V. Nanopoulos, A Phenomenological Profile of the Higgs Boson, Nucl.Phys. **B106**, 292 (1976).

[28] Y. Gao *et al.*, Spin determination of single-produced resonances at hadron colliders, Phys.Rev. **D81**, 075022 (2010).

[29] V. Barger *et al.*, Higgs bosons: Intermediate mass range at e+e- colliders, Phys Rev D Part Fields **49**, 79 (1994).

[30] L. D. Landau, The moment of a 2-photon system, Dokl. Akad. Nauk. SSSR **60**, 207 (1948).

[31] C. N. Yang, Selection Rules for the Dematerialization of a Particle into Two

Photons, Physical Review Online Archive (Prola) **77**, 242 (1950).

[32] LHC Higgs Cross Section Working Group, Handbook of LHC Higgs Cross Sections: 1. Inclusive Observables, CERN-2011-002 (2011).

[33] G. Burdman, New solutions to the hierarchy problem, Braz. J. Phys. **37**, 506 (2007).

[34] D. Perkins, *Introduction to High Energy Physics* (Cambridge University Press, 2000).

[35] C. Quigg, Unanswered questions in the electroweak theory, Annu. Rev. Nucl. Part. Sci. **59**, 505 (2009).

[36] ATLAS Collaboration, Expected performance of the ATLAS experiment: detector, trigger and physics, CERN-OPEN-2008-020 (2009).

[37] L. Evans and P. Bryant, LHC Machine, Journal of Instrumentation **3**, S08001 (2008).

[38] ATLAS Collaboration, Measurement of the total ZZ production cross section in proton-proton collisions at $\sqrt{s} = 8\,\text{TeV}$ in $20\,\text{fb}^{-1}$ with the ATLAS detector, ATLAS-CONF-2013-020 (2013).

[39] ATLAS Collaboration, G. Aad *et al.*, Search for dark matter candidates and large extra dimensions in events with a jet and missing transverse momentum with the ATLAS detector, JHEP **1304**, 075 (2013).

[40] C. Ohm, D. Milstead, and T. Moa, *Searches for exotic stable massive particles with the ATLAS experiment*, PhD thesis, Stockholm U., Stockholm, 2011.

[41] E. Mountricha, T. Alexopoulos, C. Guyot, and S. Hassani, *Search for the Standard Model Higgs boson in the $H \to ZZ^{(*)} \to 4\ell$ channel with the ATLAS experiment at the LHC leading to the observation of a new particle compatible with the Higgs boson*, PhD thesis, Natl. Tech. U., Athens and Orsay, 2012.

[42] ATLAS Collaboration, ATLAS: technical proposal for a general-purpose pp experiment at the Large Hadron Collider at CERN, CERN-LHC-94-43 (1994).

[43] CMS Collaboration, CMS: Technical proposal, CERN-LHC-94-38, LHCC-P-1 (1994).

[44] LHCb Collaboration, LHCb: Technical Proposal, CERN-LHCC-98-004, LHCC-P-4 (1998).

[45] ALICE Collaboration, ALICE: Technical proposal for a Large Ion collider Experiment at the CERN LHC, CERN-LHCC-95-7, LHCC-P-3 (1995).

[46] TOTEM Collaboration, TOTEM, Total Cross Section, Elastic Scattering and Diffraction Dissociation at the LHC: Technical Proposal, CERN-LHCC-99-007,

LHCC-P-5 (1999).

[47] LHCf Collaboration, LHCf: Technical Design Report, CERN-LHCC-2006-004, LHCF-TDR-001 (2006).

[48] MoEDAL Collaboration, Technical Design Report of the MoEDAL Experiment, CERN-LHCC-2009-006, MoEDAL-TDR-001 (2009).

[49] ATLAS Collaboration, Results related to ATLAS luminosity measurements, https://twiki.cern.ch/twiki/bin/view/AtlasPublic/LuminosityPublicResults.

[50] ATLAS Collaboration, Letter of Intent for the Phase-I Upgrade of the ATLAS Experiment, CERN-LHCC-2011-012. LHCC-I-020 (2011).

[51] O. Brüning *et al.*, LHC Design Report, CERN-2004-003 (2004).

[52] ATLAS Collaboration, The ATLAS Experiment at the CERN Large Hadron Collider, Journal of Instrumentation **3**, S08003 (2008).

[53] ATLAS Collaboration, Performance of Missing Transverse Momentum Reconstruction in Proton-Proton Collisions at 7 TeV with ATLAS, CERN-PH-EP-2011-114 (2011).

[54] M. Morii, Magnetic Field in the ATLAS Muon Spectrometer, http://lppc.physics.harvard.edu/annual_reports/doe_site_visit_2008/ATLAS/ATLAS_6_Magnet.pdf.

[55] ATLAS Collaboration, documentation of magnetic field parameters, http://atlas.web.cern.ch/Atlas/GROUPS/MUON/magfield/geometry/MagFieldParam-03-06-08.pdf.

[56] D. Froidevaux and P. Sphicas, General-purpose detectors for the large hadron collider, Annual Review of Nuclear and Particle Science **56**, 375 (2006).

[57] ATLAS Collaboration, dE/dx measurement in the ATLAS Pixel Detector and its use for particle identification, ATLAS-CONF-2011-016 (2011).

[58] ATLAS Collaboration, Public TRT Plots for Collision Data, https://twiki.cern.ch/twiki/bin/view/AtlasPublic/TRTPublicResults.

[59] ATLAS Collaboration, dE/dx measurement in the ATLAS SCT detector and particle identification with the Time-Over-Threshold method, www.zeuthen.desy.de/∼stanescu/DEDX/dEdx_note.pdf.

[60] ATLAS Collaboration, The ATLAS Inner Detector commissioning and calibration, Eur. Phys. J. C **70**, 787 (2010).

[61] D. Green, *At the leading edge* (World Scientific, 2010).

[62] A. Alonso, O. Smirnova, and A. Torsten, *Transition Radiation Tracker calibration, searches beyond the Standard Model and multiparticle correlations in ATLAS*, PhD thesis, Lund U., 2012.

[63] ATLAS Collaboration, Measurement of Lorentz angle and depletion depth in the ATLAS Pixel Detector with cosmic rays data, ATL-INDET-INT-2010-014 (2010).

[64] D. A. Dobos, C. Gssling, and R. Klingenberg, *Commissioning Perspectives for the ATLAS Pixel Detector*, PhD thesis, U. Dortmund, Dortmund, 2007.

[65] ATLAS Collaboration, The ATLAS TRT Electronics, Journal of Instrumentation **3**, P06007 (2008).

[66] ATLAS collaboration, E. Abat *et al.*, The atlas transition radiation tracker (trt) proportional drift tube: design and performance, Journal of Instrumentation **3**, P02013 (2008).

[67] C. Berger, *Elementarteilchenphysik* (Berger, 2006).

[68] K. Kleinknecht, *Detectors for Particle Radiation* (Cambridge University Press, 1998).

[69] H.-C. Schultz-Coulon, Calometry I: Electromagnetic Calorimeters, (2011), www.kip.uni-heidelberg.de/ ∼coulon/Lectures/Detectors/Free_PDFs/Lecture9.pdf.

[70] ATLAS Collaboration, Readiness of the ATLAS Liquid Argon Calorimeter for LHC collisions, Eur. Phys. J. C **70**, 723 (2010).

[71] ATLAS Collaboration, Readiness of the ATLAS Tile Calorimeter for LHC collisions, Eur. Phys. J. C **70**, 1193 (2010).

[72] S. Palestini, The muon spectrometer of the ATLAS experiment, ATL-MUON-2004-001, ATL-COM-MUON-2003-005 (2003).

[73] ATLAS Collaboration, ATLAS Muon Spectrometer Technical Design Report, CERN/LHCC/97-22 (1997).

[74] B. Bittner *et al.*, Development of fast high-resolution muon drift-tube detectors for high counting rates, Nuclear Instruments and Methods in Physics Research Section A **628**, 154 (2011).

[75] L. Fabbri, Forward Detectors in ATLAS: ALFA, ZDC and LUCID, ATL-COM-LUM-2009-008 (2009).

[76] J. Pinfold, The ATLAS Forward Physics Program, ATL-COM-LUM-2009-012 (2009).

[77] R. Jones and D. Barberis, The ATLAS computing model, Journal of Physics: Conference Series **119**, 072020 (2008).

[78] A. Robichaud-Vronneau and A. G. Clark, *Measurement of the Production Cross-Section of J/psi Mesons Decaying into Electron-Positron Pairs in Proton-Proton Interactions at a Collision Energy of 10 TeV, using a detailed Simulation of the ATLAS Detector at the CERN LHC*, PhD thesis, Geneva U., Geneva, 2010.

[79] A. Earl, P. J. Clark, and S. Thorn, ScotGrid: A Prototype Tier 2 Centre, arXiv:cs/0412093 (2004).

[80] S. R. Whitehead and A. R. Weidberg, *A Measurement of the W Boson Charge Asymmetry with the ATLAS Detector*, PhD thesis, Oxford U., Oxford, 2012.

[81] ATLAS, G. Aad *et al.*, The ATLAS Simulation Infrastructure, Eur. Phys. J. **C70**, 823 (2010).

[82] T. Sjostrand, S. Mrenna, and P. Z. Skands, PYTHIA 6.4 physics and manual, JHEP **05**, 026 (2006).

[83] T. Sjostrand, S. Mrenna, and P. Z. Skands, A brief introduction to PYTHIA 8.1, Comput. Phys. Commun. **178**, 852 (2008).

[84] D. P. L. Moroni, Study of the correlated noise in the microvertex detector, www.hep.uiuc.edu/e687/memos/memo_cornoise.ps.

[85] F. Djama, Private communication with Fares Djama working on the Pixel detector, (2013).

[86] K. Nakamura *et al.*, Particle Physics Booklet, Journal of Physics G 37, 075021 (2010).

[87] N. I. of Standards and T. of the United States, Stopping-power and range tables for electrons, http://physics.nist.gov/PhysRefData/Star/Text/ESTAR.html.

[88] P. Behera, T. Lari, and A. L. Schorlemmer, Measurement of Lorentz angle and depletion depth in the ATLAS Pixel Detector with cosmic rays data, ATL-INDET-INT-2010-041 (2010).

[89] A. L. Schorlemmer, Monitoring radiation damage in the atlas pixel detector, ATL-INDET-PROC-2012-014 (2012).

[90] M. Keil *et al.*, Studies of Radiation Effects in the NA60 Silicon Pixel Detectors, Nucl. Instrum. Methods Phys. Res., A **546**, 448 (2005).

[91] ATLAS Collaboration, Luminosity Determination in pp Collisions at $\sqrt{s} = 7$ TeV using the ATLAS Detector in 2011, ATLAS-CONF-2011-116 (2011).

[92] G. Antchev *et al.*, First measurement of the total proton-proton cross section at the LHC energy of $\sqrt{s}$ =7 TeV, Europhys.Lett. **96**, 21002 (2011).

[93] ATLAS Collaboration, G. Aad *et al.*, Measurement of the Inelastic Proton-Proton Cross-Section at $\sqrt{s} = 7$ TeV with the ATLAS Detector, Nature Commun. **2**, 463 (2011).

[94] L. A. Tompkins, *A Measurement of the proton-proton inelastic scattering cross-section at $\sqrt{s}$ =7 TeV with the ATLAS detector at the LHC.*, PhD thesis, UC, Berkeley, 2011.

[95] A. R. Baden, Jets and kinematics in hadronic collisions, International Journal of Modern Physics A **13**, 1817 (1998).

[96] ATLAS Collaboration, Performance of the ATLAS Inner Detector Track and Vertex Reconstruction in the High Pile-Up LHC Environment, ATLAS-CONF-2012-042 (2012).

[97] M. Capeans *et al.*, ATLAS Insertable B-Layer Technical Design Report, CERN-LHCC-2010-013. ATLAS-TDR-019 (2010).

[98] S. Consonni, H. Gray, G. Piacquadio, K. Selbach, and A. Salzburger, Pixel Cluster Taskforce Plots for Approval, ATL-COM-PHYS-2012-476 (2012).

[99] ATLAS Collaboration, Making the super-LHC super safe, http://slhcpp.web.cern.ch/SLHCPP/upgrade_pages/upgrade_wp5.php.

[100] S. Gibson, Monitoring radiation damage in the ATLAS Silicon Tracker, ATL-INDET-PROC-2011-014, ATL-COM-INDET-2011-073 (2011).

[101] S. Gibson, Radiation damage at the LHC and silicon detector upgrades, www.rhul.ac.uk/physics/documents/pdf/events/particlephysicsseminars/12-13-stephengibson-27feb2013.pdf.

[102] A. Clark, M. Elsing, and P. Wells, Performance Specifications of the Tracker Phase II Upgrade, ATL-UPGRADE-PUB-2012-003 (2012).

[103] ATLAS Collaboration, Tracking Performance of the Proposed Inner Tracker Layout for the ATLAS Phase-II Upgrade, ATL-UPGRADE-PUB-2013-001 (2013).

[104] A. Clark *et al.*, ATLAS Phase II Letter of Intent: Backup Document, ATL-UPGRADE-PUB-2012-004 (2012).

[105] ATLAS Collaboration, Search for the Standard Model Higgs boson in the decay channel H$\to ZZ^{(*)} \to 4\ell$ with $4.8\,\mathrm{fb}^{-1}$ of pp collision data at $\sqrt{s} = 7\,\mathrm{TeV}$ with ATLAS, Physics Letters B **710**, 383402 (2012).

[106] R. R. T. Melia, P. Nason and G. Zanderighi, $\mathrm{W}^+\mathrm{W}^-$, WZ and ZZ production in the POWHEG BOX, JHEP **1111**, 078 (2011).

[107] N. Kauer and G. Passarino, Inadequacy of zero-width approximation for a light Higgs boson signal, JHEP **1208**, 116 (2012).

[108] C. Anastasiou, L. J. Dixon, K. Melnikov, and F. Petriello, High precision QCD at hadron colliders: electroweak gauge boson rapidity distributions at NNLO, Phys. Rev. **D69**, 094008 (2004).

[109] J. M. Butterworth, J. R. Forshaw, and M. H. Seymour, Multiparton interactions in photoproduction at HERA, Z. Phys. **C 72**, 637 (1996).

[110] S. Agostinelli *et al.*, GEANT4: a simulation toolkit, Nucl. Instrum. Meth. **A 506**,

250 (2003).

[111] ATLAS Collaboration, Improved electron reconstruction in ATLAS using the Gaussian Sum Filter-based model for bremsstrahlung, ATLAS-CONF-2012-047 (2012).

[112] ATLAS Collaboration, Updated ATLAS results on the signal strength of the Higgs-like boson for decays into WW and heavy fermion final states, ATLAS-CONF-2012-162 (2012).

[113] W. Lampl *et al.*, Calorimeter clustering algorithms: Description and performance, ATL-LARG-PUB-2008-002. ATL-COM-LARG-2008-003 (2008).

[114] Reconstruction of collinear final-state-radiation photons in Z decays to muons in $\sqrt{s} = 7\,\text{TeV}$ proton-proton collisions., ATLAS-CONF-2012-143 (2012).

[115] ATLAS Collaboration, G. Aad *et al.*, Measurement of ZZ production in pp collisions at $\sqrt{s} = 7$ TeV and limits on anomalous ZZZ and $ZZ\gamma$ couplings with the ATLAS detector, JHEP **1303**, 128 (2013).

[116] CMS Collaboration, Measurement of the ZZ production cross section and search for anomalous couplings in 2l2l' final states in pp collisions at $\sqrt{s}$=7 TeV, J. High Energy Phys. **01**, 063. 29 p (2012).

[117] CMS Collaboration, Measurement of the ZZ production cross section and anomalous trilinear gauge couplings in $\ell\ell\ell'\ell'$ decays at $\sqrt{s} = 8\,\text{TeV}$ at the LHC, CMS-PAS-SMP-13-005 (2013).

[118] D. Scott, *Multivariate Density Estimation: Theory, Practice, and Visualization* (John Wiley and Sons Inc., 1992).

[119] K. Cranmer, Kernel Estimation in High-Energy Physics, Comput. Phys. Commun. **136**, 198 (2001).

[120] L. Skinnari, A. Morley, and S. Marti, Inner Detector Alignment Performance Plots using $Z \to \mu\mu$, ATL-COM-PHYS-2011-865 (2011).

[121] J. Gaiser, *Charmonium spectroscopy from radiative decays of the J/ψ and ψ'*, PhD thesis, Stanford University, SLAC-0255, 1982.

[122] R. Nikolaidou, Private communication with Rosy Nikolaidou working on the FSR, (2013).

[123] Y. Pan, Studies on Higgs Mass Resolutions and Mass Fitting with Four-lepton Final States with the ATLAS Experiment, www.lsa.umich.edu/UMICH/physics/Home/Academics/Undergraduate%20Program/Current%20Students/Senior%20Honor%20Theses/Yutong%20Pan.pdf.

[124] W. H. Press, B. P. Flannery, S. A. Teukolsky, and W. T. Vetterling, *Numerical*

recipes in C: the art of scientific computing (Cambridge University Press, 1988).

[125] ATLAS Collaboration, Observation and study of the Higgs boson candidate in the two photon decay channel with the ATLAS detector at the LHC, ATLAS-CONF-2012-168 (2012).

[126] ATLAS Collaboration, Search for the Standard Model Higgs boson in the two photon decay channel with the ATLAS detector at the LHC, Phys. Lett. B **705**, 452 (2011).

[127] ATLAS Collaboration, Combined Muon Performance Public Results, https://twiki.cern.ch/twiki/bin/view/AtlasPublic/MuonPerformancePublicPlots.

[128] T. Alexopoulos *et al.*, Search for the Standard Model Higgs boson in the decay channel $H \to ZZ^{(*)} \to 4\ell$ with $4.8\,\mathrm{fb}^{-1}$ of pp collisions at $\sqrt{s} = 7$ TeV, ATL-COM-PHYS-2011-1715 (2011).

[129] ATLAS Collaboration, Observation of an excess of events in the search for the Standard Model Higgs boson in the $H \to ZZ^{(*)} \to 4\ell$ channel with the ATLAS detector, ATLAS-CONF-2012-092 (2012).

[130] W. Eadie and F. James, *Statistical Methods in Experimental Physics* (World Scientific Publishing Company Incorporated, 2006).

[131] G. Punzi, Comments on Likelihood fits with variable resolution, arXiv:0401045 (2004).

[132] L. Lista, Statistical Methods for Data Analysis in Particle Physics, http://people.na.infn.it/ ∼ lista/Statistics/paper.pdf.

[133] D. K. W. Verkerke, Roofit users manual v2.91, 2008, ftp://root.cern.ch/root/doc/RooFit_Users_Manual_2.91-33.pdf.

[134] A. Read, Presentation of search results: the CLs technique, Journal of Physics G: Nuclear and Particle Physics **28**, 2693 (2002).

[135] T. R. Junk, Confidence level computation for combining searches with small statistics, Nucl. Instrum. Methods Phys. Res., A **434**, 435 (1999).

[136] ATLAS Collaboration, Muon Momentum Resolution in First Pass Reconstruction of pp Collision Data Recorded by ATLAS in 2010, ATLAS-CONF-2011-046 (2011).

[137] A. Salvucci, Measurement of muon momentum resolution of the ATLAS detector, arXiv:1201.4704 (2012).

[138] J. Heinrich, A Guide to the Pearson Type IV Distribution, CDF/MEMO/STATISTICS/PUBLIC/6820 (2004).

[139] K. Cranmer, Statistical Combination of ATLAS and CMS Higgs Searches, http://atlas.physics.arizona.edu/ ∼ kjohns/downloads/roostats/ATL-

PHYS-SLIDE-2011-067.pdf.

[140] L. M. K.Cranmer, G. Schott and W. Verkerke, CERN RooStats Userguide, (2010), http://root.cern.ch/viewcvs/branches/dev/roostats/roofit/roostats/doc/users guide/RooStats_UsersGuide.pdf.

[141] K. Cranmer, G. Lewis, L. Moneta, A. Shibata, and W. Verkerke, HistFactory: A tool for creating statistical models for use with RooFit and RooStats, CERN-OPEN-2012-016 (2012).

[142] A. Armbruster and J. Qian, *Discovery of a Higgs Boson with the ATLAS Detector*, PhD thesis, Michigan U., 2013.

[143] R. T. Chiara Mariotti, SM Higgs production cross sections at $\sqrt{s} = 7\,\text{TeV}$, https://twiki.cern.ch/twiki/bin/view/LHCPhysics/CERNYellowReportPageAt7TeV.

[144] R. T. Chiara Mariotti, SM Higgs production cross sections at $\sqrt{s} = 8\,\text{TeV}$, https://twiki.cern.ch/twiki/bin/view/LHCPhysics/CERNYellowReportPageAt8TeV.

[145] ATLAS Collaboration, Combined measurements of the mass and signal strength of the Higgs-like boson with the ATLAS detector using up to 25 fb^{-1} of proton-proton collision data, ATLAS-CONF-2013-014 (2013).

[146] CMS Collaboration, Properties of the Higgs-like boson in the decay $H \to ZZ \to 4\ell$ in pp collisions at $\sqrt{s} = 7$ and $8\,\text{TeV}$, CMS-PAS-HIG-13-002 (2013).

List of Figures

2.1 The Higgs potential is shown as a function of the magnitude of the two complex entries of the scalar field [11]. 6

2.2 The Feynman diagrams for the scattering of longitudinal W bosons are shown without the contribution of the Higgs boson (2.2a) and the ones involving the Higgs boson (2.2b) [11]. 10

2.3 Signal strength shown for the different Higgs decay channels measured at the ATLAS experiment [22]. 12

2.4 SM Higgs boson production modes with gluon-gluon fusion (ggF) 2.4a, vector-boson fusion (VBF) 2.4b, W/Z-bremsstrahlung 2.4c and associated production with a top-quark pair 2.4d [24]. 12

2.5 SM Higgs boson production cross section times branching ratio at E_{cm}= 8 TeV where $H \to ZZ^{(*)} \to 4\ell$ is given in red. Even though many channels have higher $\sigma \times$ BR, the $H \to ZZ^{(*)} \to 4\ell$ is a very sensitive channel due to its clean signature [25]. 13

2.6 The Feynman diagrams are shown for the production of $qq \to ZZ$ 2.6a and $gg \to ZZ$ 2.6b at LHC. 15

2.7 The leading order diagrams are given for the $Zq\bar{q}$ background with $q = b$. 15

2.8 The $t\bar{t}$ production is summarised for the LHC. 15

2.9 This diagram illustrates the process $qq/gg \to X \to ZZ \to 4\ell$ produced by proton-proton collision and defines the angles sensitive to the spin and parity measurement of X [28]. 16

2.10 Total theoretical width of the Higgs boson shown on a Higgs mass range from 100 GeV to 1 TeV [32]. 17

3.1 The chain of accelerators and synchrotrons that is used to produce proton-proton collisions at CERN is shown [41]. 20

3.2 Schematic of the ATLAS detector [52]. 23

3.3 The ATLAS inner detector is shown as a 3D model with detector sections cut away for a view inside [52]. 27
3.4 Schematic of the ATLAS inner detector [52]. 28
3.5 A simulated geometry of the ATLAS calorimetry system is shown as a 3D model [52]. 31
3.6 Momentum resolution shown as a function of p_T for the ID, MS and combined for $|\eta| < 2.5$ [72]. 33
3.7 Two dimensional model of the muon spectrometer showing all four technologies: RPC, MDT, CSC and TGC [16]. 35
3.8 Simulated Higgs event at $m_H = 130\,\text{GeV}$ is shown in the ATLAS detector [64]. 39

4.1 Average cluster size versus transverse incidence angle of the track using 2010 data and Monte Carlo showing the discrepancy in the Pixel cluster size; the minimum cluster size corresponds to the Lorentz angle. 43
4.2 Average cluster size versus transverse incidence angle of the track using 2010 data and Monte Carlo samples with different G4 range cuts. 43
4.3 Shape of energy deposition of secondaries as it is implemented in usual digitization and the new Bragg-peak modelling. 44
4.4 The energy deposition of electrons in silicon is shown as a function of the energy of the passing through electron for the total stopping power and its two components, the collision and radiative stopping power [87]. 45
4.5 Cluster size of Monte Carlo 10 samples digitized with the flat profile and with Bragg-peak modelling. 45
4.6 Average cluster size versus track incidence angle of data 10 and Monte Carlo 10 samples provided by default digitization and with the Bragg-peak modelling. 46
4.7 Drift of charge carriers in the magnetic and electric field for a particle passing perpendicularly through the detector (upper figure) and with an incidence angle equal to the Lorentz angle (lower figure) [88]. 47
4.8 The average cluster width as a function of the track incidence angle. The distribution is plotted for 2010 data, the default MC09 sample, and the improved MC09 sample with the scaled Lorentz angle. 48
4.9 The Pixel sensor design is shown before 4.9a and after 4.9b type inversion. The depletion zone grows from the bias side in an n^+np^+-type sensor as indicated by the arrows. After type inversion the bulk is p-doped and the depletion zone develops from the pixel side [90]. 49

4.10 Average cluster size in ϕ is shown versus the track incidence angle in the $r\phi$ plane for data10 and Monte Carlo samples digitized with different cross-talk. 50
4.11 The average cluster size versus track incidence angle is shown with MC processed with and without new tags. The modelling of the average cluster size is clearly improved with the new value for the cross-talk, the Lorentz angle scaling and the removal of threshold for the cross-talk. 51
4.12 The average cluster size versus track incidence angle is shown with MC processed with each change of the new tags undone. 51
4.13 Size of clusters on track for 2011 data and Pythia 8 MC simulation. . . . 52
4.14 Distribution of the mean occupancy obtained from data is shown for different silicon detector sections of the current ATLAS detector. 56
4.15 The mean occupancy is shown for different silicon detector sections of the current ATLAS detector modelled with Pythia 6. 57
4.16 The mean occupancy modelled with Pythia 8 is shown for different silicon detector sections of the current ATLAS detector. 58
4.17 The mean number of reconstructed primary vertices shown as a function of the pileup for data taken in 2011 (consisting of three datasets with $\langle\mu\rangle = 15$, 29 and 32) using the default track requirements[96]. 60
4.18 The occupancy in the inner detector is shown separately for the Pixel, SCT and TRT using all clusters. The dependence on the number of reconstructed vertices is displayed for the data taken during a high-pileup run in 2011 with $\langle\mu\rangle = 26$ (solid markers) and MC Pythia 8 simulation samples (line). The mean occupancy of each barrel layer is shown for the Pixel and SCT. For the TRT, the average over the three straws with the highest and the lowest occupancy is determined indicating the occupancy range observed. 61
4.19 The occupancy simulated for the technical design report of the Insertable B-layer is shown depending on the pileup in the three Pixel barrel layers (left) and the four SCT barrel layers (right) of the current detector. The pileup conditions of up to hundred interactions are expected after inserting the Insertable B-layer[97]. 62
4.20 Occupancy in boosted jets (p_T >280 GeV) as a function of the distance R from the jet axis is shown for the three Pixel barrel layers for a selection of events using the run 182726 of the 2011 data taking. 63

4.21 Simulated mean minimum separation between two charged particles in a jet for the innermost layer of the current ATLAS pixel barrel ($|\eta|$<2.77 with 50 µm × 400 µm pixels) in simulated dijet events. The mean minimum particle separation in z, d_Z^{min}, is shown after requiring the separation in $r\phi$<50 µm. The mean minimum particle separation in $r\phi$, $d_{r\phi}^{min}$, is shown after requiring the separation in z<400 µm. 65
4.22 Distribution of the minimal track separation in jets as a function of the jet p_T where the number of entries is shown with a colour code. The median for each column is displayed with black data points. The results are obtained for the current three Pixel barrel layers with radius 50.5 mm, 88.5 mm and 122.5 mm using simulation. 66
4.23 3D approach showing the dependence of the track separation on the position in a jet cone. 67
4.24 A cluster shown with charges deposited in each pixel represented by the colour scale and with the particle's true positions (pink marker) and their true directions (red line). Additionally, the NN probabilities for the particle multiplicity (lower left corner) and the estimated positions (blue marker) and their uncertainty (blue dotted line) are displayed[98]. 68
4.25 The cluster residual in the rϕ-direction for 4-pixel clusters reconstructed with the standard algorithm and the NN clustering algorithm for $t\bar{t}$ events[98]. 69
4.26 Simulated transverse impact parameter resolution with and without NN-based clustering for tracks with p_T>100 GeV for $t\bar{t}$ events[98]. 69
4.27 Projection in r-z of the ATLAS inner detector Utopia design given in cm. The Pixel detector is shown in green, the short strips in blue, the long strips in red and the micro-strip disks in purple[102]. 71
4.28 The occupancy given in % of the Utopia is shown for pileup 200 as a function of z [mm] for the SCT (4.13a) and Pixel (4.13b) barrel and as a function of the radius [mm] for the SCT (4.13c) and Pixel (4.13d) disks. . 72
4.29 Distribution of the minimal track separation in jets as a function of the jet p_T where the number of entries (colour code) and the mean (black data points) are shown. The results are obtained for the innermost Pixel layer in the Utopia layout with a radius of 37 mm. 73
4.30 Projection in r-z of the inner detector design for the LoI for phase II consisting of the Pixels detector (red) and the SCT (blue)[103]. 73
4.31 Occupancy map of the inner detector design for the LoI for phase II. . . 75

4.32 The tracking efficiency of muons, pions and electrons is shown depending on the pseudorapidity at upgrade conditions with 140 pileup for the LoI layout. The efficiency is shown for 5 GeV on the left and for 100 GeV on the right[6]. 75

5.1 Feynman diagram with Higgs produced by gluon-gluon fusion and the decay channel $H \to ZZ^{(*)} \to 4\ell$. 78
5.2 Signal resolution for a simulation of $m_H = 125\,\text{GeV}$ without Z-mass constraint applied 5.2a - 5.2c and with Z-mass constraint applied 5.2d - 5.2f[5]. 82
5.3 The m_{12} distribution of the events is shown after the full selection for simulation using a signal sample at $m_H = 125\,\text{GeV}$ and the combined dataset[5]. 84

6.1 A Crystal ball function is fitted to the MC SM Higgs signal samples produced with ggF. 90
6.2 The results of the Crystal ball fit are shown with the MC SM Higgs signal samples on a logarithmic scale. 91
6.3 Fit results for the Crystal ball parameters shown for 4μ final state as a function of the Higgs mass. Besides the mean and the sigma describing the Gaussian component of the Crystal ball function, n, is the free parameter of the power law and a determines the transition between the power law and the Gaussian component. 92
6.4 Fit results for the Crystal ball parameters shown for 4μ with n set to constant. 93
6.5 The convolution of a Crystal ball and a Breit-Wigner function is fitted to signal MC with $m_H = 120\,\text{GeV}$. 96
6.6 Fit results and residual of a Crystal ball function fitted to signal MC at $m_H = 110\,\text{GeV}$. In the residuals a periodic fluctuation can be observed where the pdf underestimates MC in the peak region and overestimates MC in region of the steep tails. 98
6.7 The fit of the sum of a Crystal ball and a Gaussian function is shown at $m_H = 110\,\text{GeV}$. The residual of the fitted function and the signal MC is well distributed without a systematic effects. 99
6.8 The signal model discussed consists of the sum of a Crystal ball and a Gaussian function. 100

6.9 The composition of a signal model is shown consisting of the sum of a Crystall ball and a Gaussian function where the colours represent the changes on the z-axis. . . . 101
6.10 Signal resolution for a simulation of $m_H = 125\,\text{GeV}$ without Z-mass constraint applied using the sum of a Crystal ball and a Gaussian function. This signal model describes the MC simulated samples well over the mass range $110\,\text{GeV} \leq m_H \leq 150\,\text{GeV}$. . . . 102
6.11 The invariant mass distribution is shown for the $J/\psi \to e^+e^-$ analysis using the standard reconstruction (6.11a) and using GSF-refitted electrons (6.11b) for the simulated signal samples. The signal shape depends strongly on the detector region and the mean is stabilised applying the GSF algorithm[111]. . . . 103
6.12 Fits results for the Crystal ball parameters are shown for 4μ with n set to constant and all muons detected at $|\eta| < 1.05$. . . . 104
6.13 Expected and observed exclusion limit shown for a SM Higgs boson at $m_H = 125\,\text{GeV}$ using $4.8\,\text{fb}^{-1}$. The expected exclusion limit is 7% smaller if the combined exclusion limit is determined by fitting the four final states separately 6.13a than without this discrimination 6.13b. . . . 107
6.14 The fractional energy resolution is shown for electrons with different energies detected in the inner barrel ($|\eta| = 0.3$), the outer barrel ($|\eta| = 1.1$) and the end-cap ($|\eta| = 2.0$)[36]. . . . 110
6.15 The MC distributions of the mass error are shown in the four final states for the ggF signal at $m_H = 130\,\text{GeV}$ and the ZZ background with a cut on $110\,\text{GeV} < m_{4\ell} < 150\,\text{GeV}$. . . . 112
6.16 2D smoothed histogram is shown for the $H \to ZZ^* \to 4e$ channel at 125 GeV. . . . 113
6.17 The $H \to ZZ^{(*)} \to 4e$ signal model is shown with the sum of a Crystal ball and a Gaussian function for $P_k(m_{4\ell}|m_{4\ell err})$ 6.17a and smoothed histogram for $P_k(m_{4\ell err})$ 6.17b. . . . 113
6.18 Invariant mass distribution for the irreducible $qq \to ZZ \to 4e$ (6.18a) and $qq \to ZZ \to 2e2\mu$ (6.18b) background and the reducible $Zbb \to 4e$ (6.18c) and $Zbb \to 2e2\mu$ (6.18d) background. The $qqZZ$ events simulated with PowHeg and the Zbb events simulated with Alpgen are fitted by a second order polynomial. . . . 115

6.19 The simulated $ZZ^{(*)}$ background in the $4e$ channel is modeled by a smoothed function in $m_{4\ell}$ and $m_{4\ell err}$. 116
6.20 The ratio of the reducible background shape with relaxed track isolation cuts over the nominal shape of the reducible background is shown in $m_{4\ell}$ and $m_{4\ell err}$. 116

7.1 Overall H$\rightarrow$ $ZZ^{(*)}$ $\rightarrow$ 4ℓ candidates (black data points) fitted by the template pdfs (blue solid line) consisting of a signal (blue dashed line) and background (green dashed line) component. 119
7.2 Four-lepton invariant mass distribution shown for the template pdfs (blue solid line) consisting of the signal (blue dashed line) and background (green dashed line) component fitted to data (black data points). 120
7.3 The profile likelihood is shown for the template pdfs with and without momentum (MSS) and energy scale systematic (ESS) fixed. 121
7.4 Pull distributions for m_H and μ for the toys generated from the pdf and sampled from MC for the template approach. 123
7.5 Four-lepton invariant mass distribution is shown for the model including the sum of a Crystal ball and a Gaussian function as the ggF signal pdf. The combination pdfs (blue solid line) consisting of the signal (blue dashed line) and background (green dashed line) component fitted to data (black data points). 125
7.6 The profile likelihood is shown for the fit of the signal and background pdfs including the sum of a Crystal ball and a Gaussian function as a model for the ggF signal. 126
7.7 Pull distributions for m_H and μ for the toys generated from the pdf and sampled from MC for the approach with the sum of a Crystal ball and a Gaussian function as a model for the ggF signal. 127
7.8 The Crystall ball signal distribution $\mathcal{P}_k(m_{4\ell}|m_{4\ell err})$ is shown for the four final states with its dependence on the Higgs mass (given in different colours) without the Z-mass constraint applied. 133
7.9 The signal distribution $\mathcal{P}_k(m_{4\ell err})$ is shown for the four final states with its dependence on the Higgs mass (given in different colours) without the Z-mass constraint applied. 133
7.10 Profile likelihood is shown for the per-event error workspace fitted to the 2012 dataset without Z-mass constraint applied. 134

7.11 Pull distributions for m_H and μ for the toys generated from the pdf and sampled from MC for the per-event workspace with a Crystal ball as a signal model. 135

8.1 Four-lepton invariant mass distribution for the template approach and the 2011 and 2012 dataset studied over the full mass range. The combined (signal+background) pdfs are illustrated by the blue solid line with the signal component given by blue dashed line and background component by the green dashed line. 138

8.2 Profile likelihood of m_H for the template approach studied over the full mass range with the best fit value of $\hat{m}_H = 124.26^{+0.61}_{-0.52}(\text{stat})^{+0.45}_{-0.33}(\text{sys})$ GeV. 139

8.3 Distribution of the local p_0 for different mass ranges using the combined dataset. 139

8.4 Exclusion limits for different mass ranges using the combined dataset. . . 140

8.5 Best fit values for μ and m_H are shown together with their profile likelihood contours at 68% (dark blue solid line) and 95% (dark blue dashed line) confidence levels. The results are shown with (dark blue) and without (light blue) momentum and energy scale systematic$[5]. 141

8.6 Relative change in the overall normalisation is shown as a response to the nuisance parameter of the electron efficiency $\alpha = \pm 1\sigma$ as a function of the Higgs mass for the 2012 dataset. 145

8.7 Response on the muon efficiency systematic is given as a function of the Higgs mass for the 2012 dataset. The scale of the y-axis is chosen to be the same as in figure 8.6 to show the relative importance. 146

8.8 The response in the overall normalisation is shown as a response to the QCD scale and the PDF+α_s uncertainty for the Higgs production modes gluon-gluon fusion and vector boson fusion. The response for the 2012 dataset is modelled as a function of the Higgs mass by third order B-Splines. 147

A.1 Fit results for the Crystal ball parameters shown for $4e$ final state as a function of the Higgs mass. Besides the mean and the sigma describing the Gaussian component of the Crystal ball function, n, is the free parameter of the power law and a determines the transition between the power law and the Gaussian component. 155

A.2 Fit results for the Crystal ball parameters shown for $2e2\mu$ final state as a function of the Higgs mass. 156

A.3 Fit results for the Crystal ball parameters shown for $2\mu 2e$ final state as a function of the Higgs mass. 157
A.4 Fit results for the Crystal ball parameters with n fixed are shown for $4e$ final state as a function of the Higgs mass. 158
A.5 Fit results for the Crystal ball parameters with n fixed are shown for $2e2\mu$ final state as a function of the Higgs mass. 159
A.6 Fit results for the Crystal ball parameters with n fixed are shown for $2\mu 2e$ final state as a function of the Higgs mass. 160

List of Tables

3.1 Table showing the main LHC design parameters[23, 37]. 21
3.2 The table contains the ATLAS performance goals for the different detector devices where the units for E and p_T are in GeV[52]. 22
3.3 The table shows the position and number of channels of the ID components. 29

4.1 Samples used for the cluster size study are listed with their full names. . 41
4.2 Samples used for the occupancy studies are listed with their full names. . 55
4.3 Summary of the mean occupancy in different detector regions of the Pixel and SCT detector for data, Pythia 6 and Pythia 8 shown in figures 4.14, 4.15 and 4.16. The mean occupancy is given in per mill. 59
4.4 Samples used for the track separation studies in jets are listed with their full names. 64
4.5 Summary of critical jet p_T values for a mean [median] calculation of the minimal separation in $r\phi$ and z. 65
4.6 Samples used for the ID upgrade studies are listed with their full names. 72

5.1 The trigger types used for the H$\to ZZ^{(*)} \to 4\ell$ analysis are summarised where p_{T1}/E_{T1} [p_{T2}/E_{T2}] means first [second] lepton in di-lepton pair. . . 79
5.2 The number of events are summarised the expected signal with $m_H = 125\,\text{GeV}$, the expected background and the observed data for $120\,\text{GeV} < m_{4\ell} < 130\,\text{GeV}$. Additionally, the ratio of expected signal over background events is given by S/B. The results are listed for $20.7\,\text{fb}^{-1}$ at $\sqrt{s} = 8\,\text{TeV}$, $4.6\,\text{fb}^{-1}$ at $\sqrt{s} = 7\,\text{TeV}$ and the combined dataset[5]. 85

6.1 Samples used for the $H \to ZZ^{(*)} \to 4\ell$ signal studies are listed with their full names. 91
6.2 Percentage error at 125 GeV for a gluon-gluon fusion signal model of the sum of a Crystal ball and a Gaussian function for the 4μ channel as a representative example. 102

7.1 This table summarises the results obtained for thousand toy experiments generated from pdf (pdf toys) and sampled from MC (MC toys) for $m_H = 125\,\text{GeV}$ and $\mu = 1$ and fitted by the template model as given in figure 7.4. . . . 123
7.2 This table summarises the results obtained for thousand toy experiments generated from pdf and sampled from MC for $m_H = 125\,\text{GeV}$ and $\mu = 1$ and fitted by the CB+GA model as given in figure 7.7. . . . 128
7.3 Fit result for m_H obtained for thousand toy experiments generated from pdf and sampled from MC for $m_H = 125\,\text{GeV}$. . . . 129
7.4 Results are summarised for the template approach and the model using a sum of a Crystal ball and a Gaussian function for the ggF signal. The results are shown for the datasets 2011, 2012 and 2011+2012 applying the Z-mass constraint. . . . 130
7.5 Results are summarised for the template approach and the model using a sum of a Crystal ball and Gaussian function for the ggF signal. The results are shown for the datasets 2011, 2012 and 2011+2012 without applying the Z-mass constraint. . . . 131
7.6 This table summarises the results obtained for thousand toy experiments generated from pdf and sampled from MC for $m_H = 125\,\text{GeV}$ and $\mu = 1$ and fitted by the per-event model as given in figure 7.11. . . . 135
7.7 Mass measurement fit result obtained for thousand toy experiments generated from pdf and sampled from MC for an initial value of $m_H = 125\,\text{GeV}$. 136

8.1 A selection of important systematic uncertainties is summarised for experimental systematic effects. . . . 142
8.2 The Higgs production cross sections are shown with their theoretical systematic uncertainties at $m_H = 125\,\text{GeV}$. The systematic uncertainties are a linear sum of the QCD scale and the PDF+α_S uncertainties and they vary with Higgs mas$[32]. . . . 143
8.3 This table contains the results of the analysis performed with their best fit values for m_H and mu. . . . 148

9.1 This table summarises the Higgs channel with the according datasets which were use for the latest combination[22]. . . . 152